

University de Granada

Department of Electronics and Computer Technology



Desarrollo de capacidades sensoras en Tecnología RFID

**Development of sensing capabilities in RFID
Technology**

Tesis Doctoral

José Fernández Salmerón

Editor: Editorial de la Universidad de Granada
Autor: José Fernández Salmerón
D.L.: GR 2272-2014
ISBN: 978-84-9083-333-9

Alberto J. Palma López, Miguel Ángel Carvajal Rodríguez y Jesús Banqueri Ozáez, profesores del Departamento de Electrónica y Tecnología de Computadores de la Universidad de Granada,

CERTIFICAMOS:

Que el trabajo de investigación recogido en la presente memoria, titulada “Desarrollo de capacidades sensoras en Tecnología RFID”, y presentada por José Fernández Salmerón para optar al grado de Doctor por la Universidad de Granada, ha sido realizado en su totalidad bajo nuestra dirección en el Departamento de Electrónica y Tecnología de Computadores de la Universidad de Granada.

Granada, Septiembre de 2014

Dr. Alberto J. Palma López

Dr. Miguel A. Carvajal Rodríguez



Dr. Jesús Banqueri Ozáez

El doctorando José Fernández Salmerón y los directores de la tesis Alberto J. Palma López, Miguel Ángel Carvajal Rodríguez y Jesús Banqueri Ozáez, garantizamos, al firmar esta tesis, que el trabajo ha sido realizado por el doctorando bajo la dirección de los directores de la tesis y de acuerdo con nuestra información, en la realización del trabajo, se han respetado los derechos de otros autores a ser citados, cuando se han utilizado sus resultados o publicaciones

Granada, Septiembre de 2014

Director/es de la Tesis

Doctorando

Fdo.: Alberto J. Palma López

Fdo.: José Fernández Salmerón

Miguel A. Carvajal Rodríguez



Jesús Banqueri Ozáez

*A mi tita Mari, espero que allá donde
esté se pueda sentir orgullosa.*

Agradecimientos

En primer lugar agradecer a mis directores de Tesis Alberto, Jesús y Migue el haberme dado la oportunidad de trabajar con ellos estos años brindándome todo su apoyo y confianza. Ellos son los que me han ayudado a superar las múltiples dificultades encontradas. No puede olvidarme de los demás compañeros de departamento, Fernando, Sofía, Antonio, Nuria, Diego, Miguel y Antonio. Son ya muchos desayunos juntos para no formar parte importante de mi vida.

Este trabajo se ha realizado en estrecha colaboración con el Departamento de Química Analítica de la Universidad de Granada, de ahí mi más sincero agradecimiento al profesor Luis Fermín Capitán y a Manuel, María, Alfonso, Alejandro, Inma, Miguel... No ha sido fácil el desarrollo de esta línea de investigación, y el posible éxito conseguido es en gran parte mérito suyo.

Agradecer al Laboratorio SAMLAB de EPFL su grata acogida durante la estancia realizada en Suiza, especialmente a Paco, Andrés, Giorgio y Danick por abrirme los ojos al mudo de la electrónica imprimible y a sus muchas posibilidades.

Agradecer a mis padres el trabajo y esfuerzo, a lo largo de muchos años, para poder ofrecerme la oportunidad de llegar hasta aquí. Espero que ese esfuerzo se vea recompensado ahora y en el futuro.

Para finalizar, esta tesis sería muy diferente sin la contribución de dos personas. Manuel, ese madrileño “malafollá” sin que él no se hubiera podido imprimir ni una solo gota de plata y Almu, cuya ilusión y ganas de trabajar se contagian irremediabilmente. Sin ella no habría podido llegar hasta aquí.

Resumen

Usualmente las etiquetas RFID son empleadas para identificación básica de objetos, pero en el contexto de Redes de Sensores Inalámbricos (Wireless Sensor Networks, WSNs) o del Internet de las cosas (Internet of Things, IoT) hay una creciente demanda de sistemas capaces no solo de identificar un objeto, sino de monitorizar las condiciones ambientales a las que está expuesto. Esta información es de un gran interés en una amplia variedad de aplicaciones como en las cadenas de producción o distribución de bienes, preservación de los alimentos empaquetados, asistencia sanitaria o con propósitos de garantizar la seguridad de los bienes. Para esta información en tiempo real de los objetos, una alternativa sería la integración de sensores en las etiquetas RFID, consiguiendo la meta de crear una red inteligente de etiquetas RFID con capacidades sensoras.

El rápido surgimiento en los últimos años de las técnicas de fabricación de electrónica imprimible ha propiciado el desarrollo de una nueva generación de sensores fabricados en sustratos plásticos flexibles. Además de un gran potencial para reducir los costes de fabricación, los beneficios de los dispositivos impresos presentan ventajas como reducido peso, facilidad para ser enrollados o deformados, transparentes, de espesores muy finos, susceptibles de ser producidos a gran escala y capaces de adaptarse a la geometría del objeto en el que sería incluidos.

En este trabajo las técnicas de impresión han sido utilizadas por un lado para la fabricación de etiquetas RFID de bajo coste y por otro lado para fabricar sensores impresos directamente en estas etiquetas. De esta forma se demuestra el concepto de etiquetas RFID sensoras con un gran potencial para aplicaciones donde la información relativa al estado del objeto monitorizado sea de importancia, demostrando el potencial que presentan estos sistemas fabricados completamente mediante electrónica imprimible. Por lo tanto, el objetivo de este trabajo es el diseño, simulación, desarrollo y validación de etiquetas RFID para monitorización ambiental y empaquetado inteligente. Más aún, las etiquetas deben aportar características de valor añadido y

II

proveer de esta información útil al productor, distribuidor, vendedor o consumidor final.

En un primer capítulo, se han caracterizado dos procesos de fabricación mediante técnicas de electrónica imprimible: inyección por chorro de tinta y serigrafía. Distintas combinaciones de materiales y tintas han sido caracterizadas a través del diseño y fabricación de distintos patrones impresos. La finalidad es obtener por un lado las principales características geométricas y eléctricas para cada caso estudiado y por otro lado, establecer una comparación entre los distintos materiales en términos de rendimiento en radiofrecuencia para la fabricación de etiquetas RFID impresas. En el caso de impresión por chorro de tinta, dos tintas de nano partículas de plata, DGP y Suntronic, se han impreso sobre tres sustratos diferentes, PET, PEI y PI. Adicionalmente, se ha mostrado un modelo simple para estimar el espesor en patrones impresos mediante esta técnica. Las medidas experimentales muestran una gran concordancia con los datos predichos por el modelo. El espesor obtenido con la tinta de plata DGP es de $0.105\text{-}0.180\ \mu\text{m}$ mientras que con la tinta Suntronic es de $0.355\text{-}0.430\ \mu\text{m}$, si bien existen ligeras diferencias dependiendo del sustrato empleado. Los resultados experimentales muestran que varias capas se pueden imprimir consecutivamente sin degradar la reproducción del patrón ni la rugosidad superficial obtenida. La resolución de esta técnica viene determinado por el diámetro de gota, $\sim 50\ \mu\text{m}$ para la tinta Suntronic y $\sim 100\ \mu\text{m}$ para DGP. La combinación de la tinta DGP junto con el sustrato PEI presentan la menor resistividad, $8.6\pm 0.8\ \mu\Omega\cdot\text{cm}$, comparado con el resto de casos analizados aunque el mejor resultado en términos de rendimiento, resolución y espesor alcanzado por una única capa impresa corresponde a la combinación de tinta Suntronic en sustrato PEI con una resistividad de $24.4\pm 1.1\ \mu\Omega\cdot\text{cm}$. Más aún, se ha observado un incremento en la resistividad obtenido para patrones impresos con un espesor menor a las $0.3\ \mu\text{m}$, probablemente debido a un incremento de la contribución de los mecanismos de dispersión, el denominado “grain boundary scattering” que se produce en las fronteras de grano.

En el caso de serigrafía, una única tinta ha sido impresa en los tres sustratos propuestos: PET, PEI y PI. Para ello se han empleado mallas con distintas densidades, es decir, distinto número de hilos por centímetro. Los espesores

obtenidos han sido $9.2 \mu\text{m}$ para 140 hilos por centímetro (h/cm), $19 \mu\text{m}$ para 90 h/cm y $30 \mu\text{m}$ para 43 h/cm. Los límites de impresión para serigrafía obtenidos experimentalmente son $800 \mu\text{m}$ en el caso de la malla de 90 h/cm y $600 \mu\text{m}$ para 140 h/cm. La resistividad mínima medida es de $39 \pm 4 \mu\Omega \cdot \text{cm}$ obtenida en los sustratos PEI y PI. Como se esperaba, estos patrones con un mayor espesor presentan una resistencia laminar menor que la obtenida con inyección de tinta. Las resistencias laminares en el caso de serigrafía son $15.0 \pm 0.7 \text{ m}\Omega/\square$ para 43 h/cm, $21 \pm 2 \text{ m}\Omega/\square$ para 90 h/cm y $41 \pm 4 \text{ m}\Omega/\square$ para 140 h/cm, mientras que en los mejores casos de inyección de tinta la menor resistencia laminar encontrada es de $54 \pm 6 \text{ m}\Omega/\square$ (12 capas impresas con la tinta DGP) y $153 \pm 8 \text{ m}\Omega/\square$ (4 capas impresas con la tinta Suntronic) ambas en el sustrato PEI. No obstante, los patrones de serigrafía presentan peor resolución, bordes de los patrones impresos más irregulares y una mayor rugosidad superficial que los patrones fabricados mediante inyección.

Para estudiar el rendimiento a las frecuencias de operación de la tecnología RFID, se han diseñado y fabricado líneas de transmisión de tipo coplanar con las distintas combinaciones de materiales y técnicas. Dichas líneas de transmisión se han fabricada en cada caso concreto con dos diferentes longitudes presentando los resultados finales como pérdidas por unidad de longitud. Los resultados demuestran que en el caso de inyección, Suntronic presenta menores pérdidas que DGP, demostrando que en el caso de patrones impresos solo el estudio de la resistividad no es suficiente para asegurar un buen rendimiento en radiofrecuencia. La printabilidad, es decir, la correcta reproducción de los patrones en términos de resolución y precisión, también juega un papel muy importante. La comparación entre sustratos muestra el compartimiento esperado de acuerdo a la información de pérdidas indicada para cada sustrato por los fabricantes: PEI presenta las menores pérdidas seguido de PI y PET. En resumen, se ha demostrado que el sustrato PEI con la tinta Suntronic es la combinación indicada para la fabricación de antenas RFID mediante técnica de chorro de tinta mientras que en el caso de serigrafía ambos sustratos, PEI y PI pueden ser empleados para este fin donde la elección de la densidad de malla determina de la resolución y espesor obtenidos.

IV

Partiendo de la caracterización previa de ambas técnicas de fabricación, a continuación se han fabricado etiquetas RFID completas. Usando las condiciones óptimas de fabricación, diversas antenas RFID para las bandas HF y UHF han sido diseñadas, simuladas y validadas. En el caso de la simulación numérica, los parámetros introducidos en el simulador numérico son aquellos obtenidos en la caracterización de la tecnología.

Debido a la mejor printabilidad y mejor rendimiento en radiofrecuencia, la combinación de tinta Suntronic impresa en el sustrato PEI ha sido usado para la fabricación de antenas por medio de chorro de tinta. Se ha presentado la optimización del proceso de curado, obteniéndose que los mejores resultados se producen cuando la temperatura de curado se eleva gradualmente desde la temperatura ambiente, ~ 25 °C, hasta 180 °C con una rampa de 3°C/min. Los cambios abruptos de la temperatura de curado conllevan a que el solvente de la tinta no se evapore homogéneamente, acarreando problemas como el “coffee ring” en líneas estrechas o una gran rugosidad superficial. Para las antenas fabricadas mediante serigrafía, se ha usado una malla de 120 h/cm en sustrato PI debido a su mejor printabilidad en comparación con otras densidades de malla.

En el caso de antenas para la banda HF, el número de capas impresas de las bobinas fabricadas debe ser suficiente para obtener un espesor mínimo. El espesor logrado debe ser suficiente para no degradar el factor de calidad Q de la antena debido al alto valor de la resistencia serie asociada con el inductor. En nuestro caso particular, 4 capas impresas han sido suficientes para conseguir un factor de calidad de 1.68 ± 0.12 . Las antenas HF fabricadas mediante serigrafía con mallas de 90 h/cm y 140 h/cm obtienen mejores factores de calidad y, por lo tanto, mejor rendimiento como antenas RFID.

En el caso de antenas UHF, se ha presentado una nueva técnica para la medida de la impedancia de entrada diferencial de dichas antenas. Esta medida es crítica en el diseño de las etiquetas UHF para garantizar la condición de máxima transferencia de potencia entre el chip RFID y la antena. Para realizar esta medida se han fabricado de forma personalizada una sonda diferencial con conectores U.FL y un kit de calibración SOLT para dicha sonda que, junto con un analizador de redes de gama media, permite obtener la impedancia de entrada a partir del estudio de los parámetros de dispersión (S-parameters). Para obtener dicha medida no es necesario ningún

post-procesado de los datos obtenidos, pudiendo realizarse las medidas directamente. En todos los casos investigados, las medidas experimentales y las simulaciones numéricas muestran una gran concordancia y respuestas en frecuencia muy similares, si bien la parte real de la impedancia presenta mayores diferencias con los valores simulados que la parte imaginaria. Esto sugiere que la parte real de la impedancia es el factor crítico para obtener la condición de adaptación de impedancias y que una correcta caracterización de las resistencia laminar (resistividad y espesor) de las capas metálicas impresas conlleva unos resultados con menores errores. Dos diseños de antenas han sido mostrados, un dipolo tradicional con los brazos doblados para optimizar el área ocupada, usando una inductancia SMD con red de adaptación, y un nuevo diseño compuesto por una estructura dipolo modificado en forma de pajarita junto con un inductor “loop” impreso para la adaptación. Ambos diseños de antenas presentan rangos de lectura comparables.

En cuanto a comparación de técnicas de fabricación, las antenas serigrafiadas presentan rangos de lectura mayores que las realizadas por medio de técnicas de inyección aunque sufren de un rango ligeramente menor que las realizadas con cobre de 35 μm de espesor, en cualquier caso los rangos obtenidos de las antenas serigrafiadas son comparables a las de cobre. La razón para el menor rendimiento de las antenas inyectadas es su mayor resistencia laminar por lo que las pérdidas óhmicas degradan las características de radiación de las antenas. De cualquier forma, las antenas de inyección pueden obtener rangos comprables siempre que se impriman suficientes capas para mejorar su rendimiento. En nuestro caso particular, la impresión de 20 capas conlleva que el rendimiento entre las antenas de inyección y serigrafía sean equiparables, si bien la fabricación mediante de las mismas implica tiempos de impresión muy largos, entorno a varias horas.

Una vez diseñadas y validadas las etiquetas RFID, la integración de sensores en dichas etiquetas se ha llevado a cabo mediante el diseño, prototipado y validación de distintas arquitecturas. Se han mostrado arquitecturas pasivas y semi-pasivas de bajo coste que pueden ser utilizadas para la integración de sensores en etiquetas RFID en distintas aplicaciones. La lectura de la información de los sensores se ha realizado mediante lectores RFID comerciales compatibles con los protocolos ISO o EPC, ampliamente

usados en RFID. De esta forma no es necesario ningún lector RFID especial para estas aplicaciones.

Primero, se ha demostrado como el uso de chips RFID junto con microcontroladores de ultra bajo consumo puede ser explotado para integrar sensores en las etiquetas. En un primer prototipo valores de temperatura y humedad ambiental han sido obtenidos por un microcontrolador de un sensor comercial STH15. Esta información es almacenada en el chip RFID gracias a la interfaz I2C que puede ser utilizada por el microcontrolador para acceder a la memoria EEPROM. Se ha mostrado tanto la realización de la etiqueta en la banda HF en substrato flexible como el desarrollo del software necesario del lector RFID para la correcta adquisición de los datos mediante el protocolo ISO15693.

Ya en la banda de UHF se han presentado dos arquitecturas. Ambas hacen uso del chip RFID SL900A. Las configuración y acceso a las funciones especiales de este chip son controladas mediante comandos del estándar EPC Gen2. De forma similar el primer prototipo, un microcontrolador ha sido integrado junto con un sensor de presión ambiental MEMS. Las mejoras de esta arquitectura semi-pasiva frente al primer prototipo descrito son: menor número de componentes, empaquetados de los chips de menores dimensiones, la arquitectura ha sido integrada en un área menor y se hace uso de baterías flexibles. La segunda arquitectura utiliza las ventajosas características del chip RFID SL900A para crear arquitecturas pasivas. Valores de temperatura y luz ambiental han sido obtenidos mediante una etiqueta RFID pasiva, sin necesidad de baterías. La etiqueta integra una antena tipo dipolo junto con un fotodiodo. Los valores de temperatura son obtenidos del sensor integrado en el chip RFID. El convertidor analógico-digital integrado también en el chip RFID es utilizado para medir la fotocorriente generada. Esta etiqueta representa una solución de reducido coste compuesta por un fotodiodo y un chip RFID como únicos elementos no impresos.

Por último, se ha mostrada una aproximación al cosechado de energía o “harvesting”. Una placa solar junto con la circuitería necesaria para el acondicionamiento de la señal entregada se ha integrado en un prototipo de etiqueta RFID en la banda UHF. Los beneficios frente a la solución han sido un rango de lectura de la etiqueta incrementado incluyendo las funciones

sensoras. Además dicha fuente de energía puede ser aprovechada para alimentar las arquitecturas sensoras cuando las etiquetas RFID pasivas no están en presencia del lector RFID y, por lo tanto, no pueden estar operativas.

Como parte final de esta tesis, se han utilizado las arquitecturas previamente presentadas para la integración de sensores impresos en las etiquetas. Estas etiquetas, por lo tanto, integran sensores y las arquitecturas RFID descritas demostrando ser dispositivos de bajo coste capaces de aportar información de los sensores impresos de forma digital. Así se demuestran las ventajas de esta aproximación para el campo de investigación de etiquetas RFID con capacidades sensoras.

Se ha fabricado y validado una etiqueta RFID semi-pasiva para la determinación de la concentración de oxígeno. Una membrana sensible al oxígeno es excitada ópticamente por un LED mientras que un detector de color analiza la intensidad de la señal generada por luminiscencia en dicha membrana. El sistema es de alta resolución y con un tiempo de vida largo permitiendo al usuario (productor, distribuidor, vendedor o consumidor) monitorizar el contenido de O₂ dentro de un contenido empaquetado. La lectura del oxígeno es realizada mientras el paquete permanece completamente cerrado sin necesidad de perforaciones para sondas. Además la alta resolución conseguida permite detectar concentraciones de oxígeno muy bajas, en torno a 40 ppm de O₂ con un error del orden de 0.01 ppm de O₂. La deriva térmica del sensor ha sido estudiada y corregida gracias al sensor de temperatura integrado en el chip RFID. Por lo tanto este sistema está especialmente indicada para aplicaciones de envasado inteligente donde la atmosfera ha sido modificada para que la concentración de oxígeno presente sea extremadamente baja.

Se han fabricado y caracterizado dos etiquetas RFID UHF para la medida de humedad relativa en el ambiente. Las etiquetas han sido completamente impresas sobre una poliamida, Kapton HN, cuya permitividad eléctrica se incrementa con la humedad. Dos tipos diferentes de sensores capacitivos, fabricados por inyección y serigrafía respectivamente, han sido caracterizados completamente en de temperatura y humedad. Los valores de capacidad son obtenidos por el chip RFID SL900A. Aparte del chip RFID, la arquitectura está formada por una antena dipolo impresa por serigrafía, una inductancia SMD como red de adaptación y una capacidad SMD de

VIII

referencia necesaria para la medida de la capacidad. . Ambas etiquetas presentan una arquitectura pasiva con un único chip, capaz de devolver a un lector RFID estándar valores de humedad y temperatura ambientales de forma digital (10 bits) usando comandos EPC Gen 2.

La etiqueta con los sensores impresos por inyección está formada por 12 estructuras serpentinadas en paralelo mientras que la etiqueta fabricada por serigrafía por 6 estructuras interdigitales. El número que componen estos arrays ha sido elegido para alcanzar un valor nominal de capacidad en torno a 30 pF. La etiqueta con los sensores fabricados por inyección presenta un mejor rendimiento que la etiqueta fabricada por serigrafía. La primera cubre un rango de 800 cuentas de las 1024 posibles para un cambio de humedad relativa del 37% al 70%. La segunda cubre un rango de 220 cuentas de 1024 para un cambio de humedad relativo del 57% al 86%. Entre estos valores de humedad la resolución y el rendimiento obtenidos son aceptables, fuera de estos límites se ven degradados. La diferencia obtenida entre las etiquetas puede ser explicada por el distinto número de dispositivos, 12 en el caso de inyección y 6 en el caso de serigrafía, que afectan directamente a la sensibilidad de cada array de sensores. La diferencia en el rango de humedad obtenido puede explicarse por el distinto valor de la capacidad de referencia usada, 36 pF para los sensores fabricados por inyección y 39 pF por serigrafía, por lo que este valor puede ser escogido para monitorizar un rango de humedad concreto. La falta de rendimiento fuera de estos rangos puede ser explicada porque las interfaces capaces de medir sensores del chip RFID no están diseñadas específicamente para medir capacidad, sino que son de propósito general.

La desventaja de la aproximación con sensores impresos por inyección es la necesidad de usar dos técnicas de fabricación distintas elevando la complejidad de la fabricación con más procesos de sinterizado y necesidad de alineamiento. En cambio, la etiqueta por serigrafía se realiza con un solo paso de fabricación aunque el área ocupada por los sensores es mucho mayor. Por lo tanto dependiendo de los requerimientos de sensibilidad y área uno de las dos aproximaciones sería la más adecuada para una aplicación en concreto.

Una etiqueta RFID en la banda de HF ha sido estudiada como sensor de humedad umbral. La idea es estudiar el cambio en la frecuencia de

resonancia de la etiqueta pasiva sintonizada en 13.56 MHz al introducir en el circuito LC resonante que constituye la antena los sensores de humedad capacitivos. Sintonizando apropiadamente las etiquetas se podría conseguir que estas etiquetas fueran detectadas por un lector RFID solo si la humedad relativa es inferior o superior a un valor umbral. Para ello primero se ha estudiado el comportamiento en frecuencia de las inductancias fabricadas tanto por inyección como para distintos niveles de humedad relativa. El cambio en el valor nominal de las inductancias a distintos niveles de humedad ha sido despreciable pero los factores de calidad de las bobinas se ven seriamente afectados, posiblemente debido a un aumento de la resistividad de la capa de plata impresa. Este efecto se aprecia aun de forma más severa en la bobina fabricada por inyección, por lo que se rechazó esta opción para la etiqueta final. La caracterización de una etiqueta RFID fabricada completamente fabricada por serigrafía incluyendo un sensor interdigital capacitivo y el chip RFID conectado mostró un cambio de la frecuencia de resonancia de 100 kHz para el rango completo de humedad relativa estudiado. En las mismas condiciones pero con un array de sensores serpentina fabricado por inyección en lugar del sensor interdigital serigrafiado el cambio de resonancia fue de 300 kHz. Es necesario un estudio en mayor profundidad para sintonizar las etiquetas en las frecuencias deseadas a valores concretos de humedad, si bien se ha obtenido un significativo cambio en la frecuencia de resonancia fácilmente detectable. De hecho, este último diseño podría ser utilizado como un sensor de humedad de tipo resonante.

Se ha diseñado y fabricado una etiqueta UHF RFID pasiva impresa directamente en una caja de mensajería comercial. La etiqueta presenta una arquitectura pasiva con un único chip, el SL900A, siendo capaz de adquirir de forma digital los valores de varios sensores. Dos sensores resistivos se han usado. Uno es un sensor de fuerza directamente integrado en la parte superior cuya función es detectar el peso depositado encima del paquete. El segundo es una línea de plata impresa atravesando la línea pre-perforada de apertura del paquete para detectar si este ha sido abierto. Para conectar ambos sensores a al chip RFID que en principio es hábil para un único sensor, un simple conmutador se ha diseñado e integrados en el diseño. Se ha demostrado el correcto funcionamiento de la etiqueta, si bien el sensor de

peso está más indicado para operar como sensor umbral que para adquirir medidas absolutas.

Así pues, el objetivo principal de esta tesis, la creación de etiquetas RFID de bajos costes capaces de proporcionar información de sensores para monitorización ambiental o empaquetado inteligente, ha sido conseguido. Se han mostrado etiquetas capaces de medir parámetros ambientales de gran interés en una gran variedad de aplicaciones como temperatura, humedad, luz ambiental o presión atmosférica. Además, se ha mostrado el diseño de una etiqueta para la medida de concentración de oxígeno en atmósferas modificadas con una gran resolución para concentraciones bajas de este gas, por lo que es altamente recomendable en aplicaciones de empaquetado inteligente. En definitiva, estas etiquetas RFID abren nuevas vías para el desarrollo de Redes de Sensores con tecnología RFID.

Motivation and objectives	17
1. Introduction.....	21
1.1 RFID Technology.....	21
1.1.1 RFID History.....	21
1.1.2 RFID Systems	22
1.1.3 RFID Standards.....	27
1.1.4 RFID Chip.....	29
1.1.5 RFID Antennas.....	32
1.2 Printed Electronics	35
1.2.1 Inkjet Printing.....	37
1.2.2 Screen Printing.....	38
1.2.3 Printed Sensors.....	39
1.3 Smart Packaging.....	41
2. Study of materials and techniques for RFID tag prototyping. 45	45
2.1 Material and Methods.....	45
2.1.1 Inkjet printing.....	47
2.1.2 Screen printing	50
2.1.3 Milling FR-4.....	51
2.1.4 RF Numerical Simulation	52
2.2 Experimental Results.....	54
2.2.1 Geometrical and DC Characterization of Inkjet Printed patterns.....	54
2.2.2 Geometrical and Electrical of Screen Printed patterns.....	57
2.2.3 RF Simulation and Characterization	60
2.3 Conclusions	63
3. Design, numerical simulation and experimental characterization of RFID tags.....	65
3.1 Material and Methods.....	65
3.1.1 Fabrication process.....	65
3.1.2 Inkjet Printing Optimization	67
3.1.3 High Frequency Band (13.56 MHz) RFID tags	68
3.1.4 Ultra High Frequency Band RFID tags.....	74
3.1.5 Comparison of fabrication techniques for UHF RFID tags ..	78
3.2 Calibration method of UHF RFID tags	80
3.3 Results and discussion.....	84
3.3.1 Inkjet Printig Optimization	84
3.3.2 High Frequency Band Antennas	85
3.3.3 Ultra High Frequency Band Antennas	90

3.3.4	Comparison of fabrication techniques for UHF RFID tags ..	98
3.4	Conclusions	102
4.	Design and characterization of smart RFID Tags	103
4.1	Smart RFID tags with commercial sensors	103
4.1.1	Material, methods and designs	103
4.1.2	Experimental Results	110
4.2	Smart RFID tag with harvesting capabilities	114
4.2.1	Material, methods and design	114
4.2.2	Experimental Results	116
4.3	Conclusions	120
5.	Design and characterization of smart RFID tags with printed sensors.....	121
5.1	Smart HF tag: Oxygen Monitoring	121
5.1.1	Material and methods	121
5.1.2	Tag architecture.....	123
5.1.3	Experimental Results	127
5.1.4	Conclusions.....	136
5.2	Single-chip passive UHF tag for humidity monitoring	136
5.2.1	Experimental Results	142
5.2.2	Conclusions.....	147
5.3	Single-chip passive HF tag for humidity monitoring.....	148
5.3.1	Material, methods and design	149
5.3.2	Experimental Results	150
5.3.3	Conclusion	160
5.4	Single-chip passive UHF RFID tag with multiple sensors capabilities.....	160
5.4.1	Material, methods and design	161
5.4.2	Experimental Results	164
5.4.3	Conclusion	167
6.	Conclusiones.....	169
7.	Scientific Contributions.....	179
	Appendix I. Smart RFID Chip SL900A.....	183
	Appendix II. Smart RFID Chip SL13A	187

Figures Index

Figure 1. Diagram showing the three main components of a RFID system.	23
Figure 2. Diagram showing the two coupling mechanism on RFID: (a) inductive coupling and (b) propagation or capacitive coupling.....	23
Figure 3. Scheme of a simple passive tag showing the rectifier, the antenna interface and the backscattering mechanism.....	25
Figure 4. Some examples of RFID tags: passive on the HF band (left), passive (center-up) and semi-passive (center-down) on UHF band and active on microwave band.	26
Figure 5. Block diagram of a generic RFID IC Circuit.....	31
Figure 6. Schema of screen printing fabrication (Suganuma 2014).....	39
Figure 7. Schematic diagram of the inkjetted meandered structure for DC study (a) and image of the meandering patterns inkjetted with DGP silver ink on PI substrate (b).	47
Figure 8. Sketch of the size of a printed line of real width W' compared with the size established in the layout with width W	49
Figure 9. Schematic diagram of the screen printed structure for DC study (a) and image of the screen-printed patterns for study of minimum dimensions; each square is composed of lines of constant width ranging from 0.2 mm to 1.0 mm (b).....	51
Figure 10. Drawing showing the structure and relevant dimensions of the designed CPWs transmission lines.....	52
Figure 11. Image of the fabricated FR-4 CPW transmission lines (a). Capture image with the Dimatix printer fiducial camera showing the 150 μm gap of the printed CPW. The green and orange lines are references axis and measurement distance line, respectively, generated by the camera. (b) Image of the inkjetted CPW transmission lines showing the two different lengths of 2 and 4 cm printed on the three different substrates.	53
Figure 12. Thickness of DGP (a) and SunTronic (b) patterns as a function of the number of printed layers. Experimental and modeled data are shown....	54
Figure 13. Sheet resistances (a) and resistivity (b) of inkjetted patterns as a function of thickness for different conductive inks and substrates. Lines are only eye guides.....	56
Figure 14. Microphotographs of screen printed lines with a mesh of 43 T/cm (a) and 140 T/cm (b). (c) The “saw tooth” effect (solid line) and the	

measured geometrical parameters: minimum and maximum width. The screen printing mesh is also outlined to explain this effect.	59
Figure 15. Measured frequency response of the transmission parameter S_{21} for inkjet printed coplanar waveguide with Anapro DGP and Suntronic U5603 silver inks (a) and screen printed coplanar waveguide with Suntronic CRSN 2442 silver ink and FR-4 (b).....	61
Figure 16. Illustration showing the chip assembly process.....	66
Figure 17. Patterns for printing optimization study.	67
Figure 18. Diagram showing the coupling mechanism on RFID HF band (13.56 MHz).....	69
Figure 19. Non-ideal LC resonator schematics.....	70
Figure 20. Antenna band-pass characteristic showing how a high value quality factor can cause conflict with the sub-carrier signals generated by the RFID protocol.	72
Figure 21. Definition of the structure for ADS simulator. Blue layer is the substrate, defining relative permittivity, thickness and loss tangent (frequency dependent). Yellow layer represents the deposited silver ink, defining thickness and conductivity.....	73
Figure 22. Inductor frequency response showing the effective range of operation and the self-resonant frequency.	74
Figure 23. Measured chip impedances versus frequency evaluated at -15 dBm, minimum operating power level for the employed RFID chip. Results are displayed for the two substrates: 35 μm thick copper on 1.5 mm thick FR-4 substrate and 13 μm silver paste on 50 μm thick PI substrate.....	77
Figure 24. Input impedance RFID chip measurement showing the RF probe and, in-detail, the electrical contact of the 800 μm pitch point probes.	78
Figure 25. Layout of the (a) thin propeller design and (b) basetta design prototyped for fabrication techniques benchmarking. Red line indicates the studied line-thickness profiler through profilometer study.	79
Figure 26. Diagram of the measurement setup for antenna impedance measurements showing the different connections and calibration planes.....	81
Figure 27. a) Picture of the differential test fixture showing the N-SMA adaptors, the SMA-U.FL interconnection cables and a straight arms dipole antenna. b) Picture of the custom calibration kit showing Short-Open-Load and Thru standards and c) Measurement setup showing the screen printed	

bow-tie antenna measurement and the smith chart representation on the VNA.....	82
Figure 28. Measurement setup in an anechoic chamber to validate the proposed RFID system. The reader antenna can be seen on the tripod and the smart RFID tag can be observed attached to the foam structure.....	84
Figure 29. Images showing surfaces from the interferometry study. On the right side, Suntronic ink on PEI after sintering with a ramp temperature profile (RMS roughness=13.99 nm). On the left side, Suntronic ink on PEI substrate after sintering at constant temperature (RMS roughness=1.4 um) after abrupt change.....	85
Figure 30. Layouts of the final antenna designs for milling on FR-4 substrate (a) (b), screen printing (c) and inkjet printing (d).	86
Figure 31. Pictures of the fabricated coil inductors on FR-4 substrate.	87
Figure 32. (a) Printed coil for 13.56 MHz RFID tag. (b) Simulated and measured frequency response of the 4 layers inkjet printed coil.	87
Figure 33. (a) Screen-printed coil for 13.56 MHz RFID tag. Simulated and measured frequency response of the screen printed coil with 90 T/cm (b) and 140 T/cm (c).....	89
Figure 34. Smith chart representation showing the S-differential parameter measurement of the standards using the proposed test fixture. Short standard in red, load in green and open in blue. a) no-calibration b) port-extension calibration c) calibration proposed in this work.....	91
Figure 35. Schematic layout of the two proposed RFID Antennas for the UHF band.....	91
Figure 36. Pictures showing a) bow-tie antenna fabricated on FR-4 substrate, b) screen printed dipole including RFID chip and SMD inductance for matching and screen printed dipole showing the U.FL connectors on antenna feed point and c) Inkjet printed loop antenna showing the U.FL connectors and the U.FL-SMA cable adaptor.	93
Figure 37. Measured and simulated power reflection coefficient for the set of fabricated dipole antennas: FR-4 substrate using milling techniques and Kapton PI substrate using screen printing techniques.....	94
Figure 38. Measured and simulated responses of the UHF bow-tie antennas: a) S-parameter response of the antenna fabricated on FR-4 substrate, b) S-parameter response of the screen printed antenna, c) impedance of the	

antenna fabricated on FR-4 substrate and d) impedance of the screen printed antenna.	96
Figure 39. Thickness line-profiles of the bassetta antennas along the red line depicted in Figure 25 for the four fabrication techniques.	99
Figure 40. Smith Chart representation showing the impedance frequency response for the set of prototyped RFID tags. Red point indicated the designed antenna impedance.	100
Figure 41. Block diagram of smart RFID tag with temperature and humidity sensors.	104
Figure 42. Schematic layout of the designed RFID Smart tags number 1..	104
Figure 43. Block Diagram of the developed RFID sensing systems showing the two different tag architectures. a) RFID reader and PC application, b) light and temperature passive smart tag, manufactured in this work by screen printing technique and c) semi-passive smart tag showing the pressure sensor and the microcontroller interfaces, manufactured in this work by screen and inkjet printing techniques.	106
Figure 44. Schematic layout of the designed RFID Smart tags: a) a passive temperature and a light sensor tag based on dipole antenna; b) a semi-passive pressure and a temperature sensor tag based on loop antenna.	108
Figure 45. (a) Capture image of the Visual Basic application to configure and read-out the Smart RFID tag and (b) picture of the prototype number 1, a HF RFID tag capable of measuring temperature and humidity manufactured on PI substrate by screen printing.	111
Figure 46. Images showing the fabricated RFID smart tags: a) smart tag number 2, passive dipole-based antenna tag fabricated by screen printing with temperature and light sensors, b) the smart tag number 3, a semi-passive loop-based tag also fabricated by screen printing with pressure and temperature sensors and showing the test interface retractile probes and c) the semi-passive tag number 4 as in b) but inkjet-printed and showing the mounted thin battery.	112
Figure 47. Block diagram of the setup for testing the Smart RFID tag with harvesting capabilities.	114
Figure 48. Schematics of the harvester module.	116
Figure 49. RFID tag with energy harvesting module.	116
Figure 50. Temperature monitoring in 3 different scenarios of power providing.	117

Figure 51. Monitoring battery level with the harvester module operating until 1.5 min, then battery capacitor discharges in one minute.	119
Figure 52. Temperature and battery level monitoring in autonomous mode.	119
Figure 53. Side view of the sensing module.	124
Figure 54. Block diagram of the developed RFID tag. Black connections represent data lines, red connections are principal power lines and blue connections are secondary power lines.	126
Figure 55. Photography of the system. The sensing module has been uncovered to show its structure.	128
Figure 56. Response curve of the oxygen RFID tag (21 °C).	129
Figure 57. Calibration curve of the oxygen RFID tag.	130
Figure 58. Response curves for different integration times.	131
Figure 59. Thermal dependence of the oxygen RFID tag.	133
Figure 60. Simulated (lines) and measured (symbols) frequency response of the antenna.	134
Figure 61. Impedance of the tag as a function of the frequency.	135
Figure 62. Schematics of the two RFID tags with (a) array of capacitive humidity sensors by inkjet printing and (b) array of capacitive sensor by screen printing (highlighted in red). Both tags include the same antenna design (in yellow) and the same chip RFID (in green). The external matching network has been remarked in purple and the reference capacitance in blue.	137
Figure 63. Diagram showing the external capacitive sensor mode of the RFID chip with AC signal excitation.	138
Figure 64. (a) Layout of the designed SRE capacitor indicating the notation of the dimensions and the Cartesian axes and (b) Layout of the designed IDE sensor (w = width, s = distance, i = interspacing, t = thickness).	140
Figure 65. (a) RFID tag with inkjetted serpentine sensors and (b) RFID tag with interdigitated sensors by screen printing.	143
Figure 66. (a) Capacitance vs. Relative humidity for a single inkjetted printed serpentine capacitor and (b) Capacitance vs. Relative humidity for a single screen printed interdigitated capacitor.	144
Figure 67. (a) ADC counts of tag with inkjetted serpentine sensor and (b) ADC counts of screen printed tag with IDE sensors.	146
Figure 68. Printed coil inductor by (a) screen printing, (b) inkjet printing.	151

Figure 69. Coil impedance by screen printing as function of frequency at different values of RH.....	151
Figure 70. Coil resonance frequency by screen printing as a function of relative humidity.	152
Figure 71. Coil impedance by screen printing as a function of frequency at different temperature values.	152
Figure 72. Coil resonance frequency by screen printing as a function of temperature.	153
Figure 73. Coil impedance by inkjet printing as a function of frequency at different values of RH.....	154
Figure 74. Screen printed capacitance as a function of frequency at different RH values.....	154
Figure 75. Screen printed capacitance as a function of frequency at different temperature values.	155
Figure 76. LC tag by screen printing.	156
Figure 77. Impedance of the screen printed LC tag as a function of frequency for different RH values.	156
Figure 78. Normalized impedance as a function of frequency for two RH values.	157
Figure 79. Resonance frequency of the screen printed LC circuit as a function of RH.....	157
Figure 80. Hybrid LC tag by screen printing (coil) and inkjet printing (capacitors).....	158
Figure 81. Impedance of the hybrid LC tag as a function of frequency for different RH values.....	158
Figure 82. Normalized impedance of hybrid LC tag as a function of frequency for two RH values.....	159
Figure 83. Resonance frequency of the hybrid printed LC circuit as a function of RH.	159
Figure 84. Schematics of the RFID tag with the dipole antenna (in yellow) and the chip RFID (in green). The external matching network has been remarked in purple. The resistors and transistors to switch the sensors are highlighted in orange and blue, respectively. The opening sensor is shown in grey and the pads for the force sensor are presented in red.	161
Figure 85. Diagram showing the external resistive sensor mode of the RFID chip, including the extra circuitry to read each resistive sensor.	163

Figure 86. Fabricated RFID tag with all components.	164
Figure 87. a) Close cardboard with RFID tag; (b) view of the RFID tag before closing the box.	166
Figure 88. ADC counts for the force sensor measurements.	166

Table Index

Table 1. Advantages and disadvantages of the different RFID bands.	24
Table 2. RFID ISO Standards.	28
Table 3. Some characteristics of the substrates.	46
Table 4. Technical specifications of the analyzed conductive inks for inkjet printing (a) and paste for screen printing (b) and FR-4 clad laminate Copper (c).	46
Table 5. Experimental results from the physical characterization of printed patterns with different inks, substrates and printing techniques.	55
Table 6. Experimental results from the characterization screen printed patterns.	58
Table 7. Experimental results from the characterization screen printed patterns.	58
Table 8. Coplanar waveguide dimensions for the printed transmission lines.	60
Table 9. Measured transmission parameters of the coplanar waveguides at 13.56 MHz (HF band) and 868 MHz (UHF band) frequencies.	60
Table 10. Calculated relevant dimension of the designed HF antenna.	86
Table 11. Simulated and measured inductance (L) and quality factor (Q) at 13.56 MHz.	88
Table 12. Main Characteristic of the designed RFID antennas.	97
Table 13. Maximum read ranges for the set of fabricated RFID tags showing pictures of all prototype obtained with each design/technique.	101
Table 14. Summary of Main Characteristic of the fabricated smart RFID.	103
Table 15. Main characteristics of the sensor capabilities of the fabricated smart tags.	110
Table 16. Read range for identification and temperature measurement in passive mode and active (harvester powered) modes.	118
Table 17. Theoretical resolution of the system in ppm at different O ₂ concentrations.	132
Table 18. Physical dimensions of each of the inkjet-printed serpentine structures.	141
Table 19. Physical dimensions of each of the screen printed interdigitated structures.	141

Table 20. Physical dimensions of the screen printed interdigitated structure	155
---	-----

Acronyms

ASIC	Application Specific Integrated Circuit
AC	Alternate Current
ADS	Advanced Design System
CAB	Cellulose Acetate Butyrate
CPW	Coplanar Waveguide
CST	Computer Simulation Technology
DC	Direct Current
DTD	Drop to Drop
EEPROM	Electrically Erasable Programmable Read-Only Memory
EH	Energy Harvester
EPC	Electronic Product Code
FR-4	Flame Retarded Type 4
HF	High Frequency
I2C	Inter-Integrated Circuit
IC	Integrated Circuit
IDE	Interdigitated Electrodes
IEC	International Electrotechnical Commission
ISO	International Organization for Standardization
LED	Light Emitting Diode
MAP	Modified Atmosphere Packaging
MCU	Microcontroller Unit

MIT	Massachusetts Institute of Technology
PCB	Printed Circuit Board
PE	Printed Electronics
PEI	Polyetherimide
PET	Polyethylene terephthalate
PI	Polyimide
PMMA	Polymethylmethacrylate
PS	Polystyrene
PtOEP	Platinum Octaethylporphyrin
PVC	Polyvinylchloride
RFID	Radiofrequency Identification
RFID	Radiofrequency
RGB	Red Green Blue
RH	Relative Humidity
SER	Serpentine Electrode
SFE	Sensor Front End
SMA	Subminiature version A
SMD	Surface Mount device
SOLT	Short-Open-Load-Thru
SPI	Serial Port Interface
SRF	Self Resonant Frequency
TGME	Triethylene Glycol Monoethyl Ether

THF	Tetrahydrofuran
TTI	Time–Temperature Indicators
UHF	Ultra High Frequency
UTC	Universal Time Coordinate
UV	Ultra Violet
VNA	Vector Network Analyzer
WDT	Watch Dog Timer

Motivation and objectives

Motivation

Usually RFID tags only provide basic identification of objects, but in the context of Wireless Sensors Networks (WSNs) and Internet of Things (IoT), there is a growing demand to create systems that are capable of not only tracking, but also monitoring environmental parameters of significant interest in different fields: supply-chain monitoring, food safety, comfort health or security purposes. With this real-time cognition, the status of a certain object will be made possible by integrating sensors into the RFID tag, achieving the ultimate goal of creating an “intelligent network of RFID-enabled sensors.”

The emergence of the printed electronics industry has propiciated the development of sensing technologies on flexible substrates such as plastic foils. Printed electronics are becoming a more and more mature technology every day. Besides a strong potential for cost-effective production based on additive processes with a reduced infrastructure, the benefits of printing devices on plastic foil include their potential to be light weight, foldable/rollable, transparent, thin and conformal, wearable, and produced on a large scale.

On one hand, printed electronics are being considered as a production means for very low-cost RFID tags. On the other hand, there is a need for a variety of cost-effective sensors that could be manufactured directly on RFID labels to make them smarter showing how powerful the system can be if these electronic devices are embedded in RFID.

Objectives

The aim of this work is the design, simulation, development and validation of smart Radiofrequency Identification (RFID) tags for environmental monitoring and smart packaging. These sensors systems must be simply and low-cost devices with feasibility to be attached on different objects surfaces or be integrated on food packaging. Moreover, the smart tags must provide “value-add” characteristics in aspect regarding with consumer products, security or environmental information that can be accessed by the

manufacturer, distributor or final consumer. In this work different possibilities to include these capabilities on RFID tags will be studied in three different ways:

- Inclusion of commercial sensors on ultra low-power architectures using RFID mechanism to transmit sensor information on digital form.
- Inclusion of new-developed printed sensors on ultra low-power architectures with conditioning stages using RFID mechanism to transmit sensor information on digital form.
- Inclusion of printed sensors that causes a variation on tag antenna response as resonance frequency, measured reflected power or maximum read range variation.

Inkjet and screen printing techniques will be employed for manufacturing the tags on flexible foils, using conductive pastes to integrate the non-printed electronic components. These techniques will be used as well to manufacture sensors structures on the same substrate, integrating in this way sensor systems with wireless communication interfaces based on RFID technology. Magnitudes of interest are temperature, relative humidity and different gas concentration.

Outline of the thesis

The first chapter describes the basic functionality and the related principles of RFID technology as well as an introduction to printing techniques for electronics device manufacturing.

Chapter two explains in detail inkjet and screen printing, two techniques employed in this work. Geometrical and electrical properties of different patterns are reported setting a comparison among materials and techniques. The outcome of this study is the optimal conditions to manufacture RFID tags with each technique.

On the basis of the performed characterization, chapter three demonstrates the realization of several printed RFID tags on two frequency bands, HF and UHF. Numerical simulations are compared with experimental measurements,

and validation of the manufactured tags is performed using commercial RFID readers on anechoic chambers.

With the aim of manufacturing sensor-enhanced RFID tags, chapter four presents and discusses different smart RFID tags architectures targeting low-power operation. These architectures provide sensor data on digital form to be reliably transmitted to the reader using RFID standards protocols communications.

Finally, in Chapter five, fully-integrated RFID tags including printed sensors are shown. These tags integrates sensors, communication capabilities and power resources on flexible foil to monitor temperature, humidity and oxygen gas concentration demonstrating the revolutionary effect of this approach in low-cost RFID and RFID-enabled sensors fields.

1. Introduction

1.1 RFID Technology

Radio Frequency Identification (RFID), also called non-contact IC cards or ID tags, are devices that make it possible to detect the presence of objects and verify their identification without contacting them. Identification is possible by means of a unique number that identify objects, people or information stored on the tag. The vast majority of radio frequency identification (RFID) tags consist of an antenna and an application-specific integrated circuit (ASIC). Most RFID tags are low-cost passive tags which take advantage of the reader induced signal to supply the RFID chip with power. Compared to traditional identification techniques such as barcodes, RFID presents the advantages of simultaneous tag reading, wider reading range and faster data transfer (Finkenzeller and Müller 2010). The great disadvantage is its comparative higher cost. However, the increase in cost is justified by the added value that RFID technology is able to bring such as, for instance, including sensing capabilities (Zhu, Mukhopadhyay and Kurata 2012). The possibility of monitoring the environmental conditions of objects and the interconnection/communication between them leads to Wireless Sensor Network (WSNs) and the paradigm of the Internet of Things (IOT) (Atzori, Iera and Morabito 2010, Akyildiz et al. 2002).

1.1.1 RFID History

RFIDs have been used since the 1980's but initially their use was limited to maritime transports, traffic information systems, and other special applications. The birth of this technology was in October 1948 after publication of the work "Communications by Means of reflected power" by Harry Stockman. Regarding the first know application, the British Royal Air Force used airplanes with radio transponder that responds when interrogates, allowing British pilots to distinguish between allies and enemies.

Until 1960s significant progress in RFID was not possible, it was in this decade when the electromagnetic theory related to RFID was developed. One example of application is Electronic Article Surveillance (EAS). It consists in

a single-bit tag to detect or not the presence of an object. A rapid development of RFID technology was produced on 1970s, when practical applications appeared as animal tracking or factory automation. In the decade on 1980s the mass deployment of RFID was produced by laboratories, companies and universities engaged for the RFID technology development. Examples of applications are access control, public transport, toll roads... Since 1990s, the advances on microelectronic, embedded software and microwave devices have dramatically expanded the functionality and possibilities of RFID technology. Today, RFID is deployed across different sectors and services, increasing its efficiency and visibility (Finkenzeller and Müller 2010).

1.1.2 RFID Systems

All RFID systems are comprised of three main components as illustrated in Figure 1:

- RFID tag, or transponder, which is located on the object to be identified.
- RFID reader, or transceiver, which may be able to both read data from and write data to a transponder
- Data processing subsystem, which utilizes the obtained information from the transceiver in some useful manner

The readers can stand at fixed-position or be mobile while the tags are attached to the object to be identified. A reader communicates with the tag only if the tag is in its coverage zone, this area is known as interrogation zone. Typically the reader includes external interfaces for communicate with other devices, e. g., a personal computer where the control application is running. The wireless link between reader and tag establishes the communication and, optionally, power up the tag...

It is really important to point out the importance of the cost of each tag. The industry adoption of this technology is strongly conditioned by its implementation cost. Manufacturers are not ready to pay a high cost for smart tags although they provided more functionalities than other traditional methods.

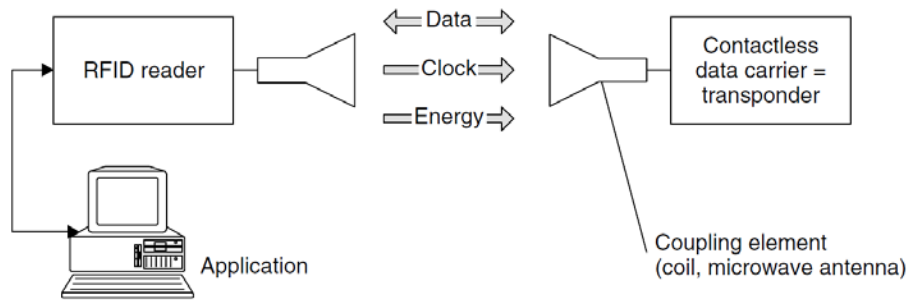


Figure 1. Diagram showing the three main components of a RFID system.

The RFID systems have evolved along the decades. The operating frequency conditions the system characteristics as the coupling mechanism, maximum read range or immunity to external interferences. The use of higher frequency provides larger read ranges although other problems appears, as metal or moisture affecting the RF link performance. Table 1 shows the most relevant frequency bands as well as their main advantages and disadvantages.

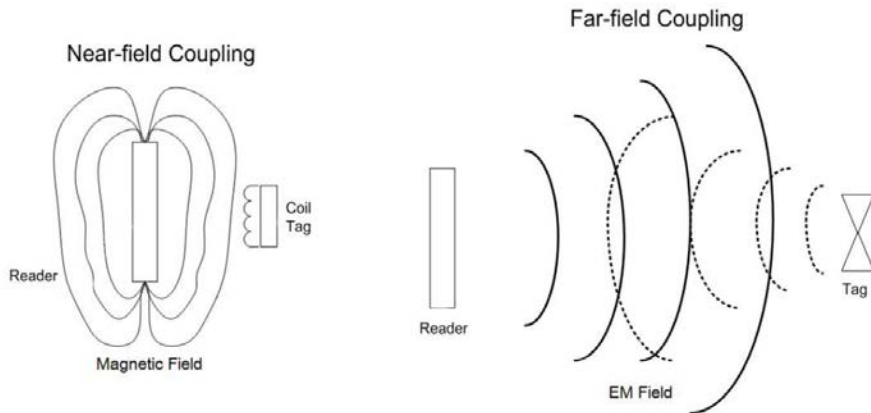


Figure 2. Diagram showing the two coupling mechanism on RFID: (a) inductive coupling and (b) propagation or capacitive coupling.

There are two coupling mechanism depending of the operating frequency. In Figure 2 both mechanism can be observed. The frequency band of HF uses the coupling mechanism: the reader generates a magnetic field due to the current flowing on the reader inductor. When the tag is on the vicinity of the reader, a voltage is induced on the coil antenna that is employed for

powering up the tag. In these systems, the design of the inductors acting as antennas is critical.

Table 1. Advantages and disadvantages of the different RFID bands.

Band/Frequency / System	Advantages	Disadvantages
High Frequency (HF)/ 13.56 MHz / Inductive	<ul style="list-style-type: none"> -Frequency band available worldwide -Well for application with small read ranges and small amount of data -ISO15693, ISO14443 and HF EPC standards -Robust communication with reader -Excellent immunity to environmental and electrical noise -Well-defined and localized interrogation zones -Minimal effects of shielding objects -Penetrates in water -Freedom of environmental reflections that affect propagation coupling -Good data transfer rate -Low power RF transmission for EM compliance 	<ul style="list-style-type: none"> -Does not penetrate on metals -Large antennas -Larger tag size -Short Reading Range
Ultra High Frequency (UHF)/ 865-954 MHz / Propagation	<ul style="list-style-type: none"> -Read range up to 6 meters -Significant higher data rates than HF -Widespread use in the last decade -Suitable for inventory tracking due the large read range -Penetration in metals with proper antenna design. 	<ul style="list-style-type: none"> -Absorbed by liquids -Unpredictable performance near metal surfaces, although is susceptible of antenna design -Common sources of interference (ISM band) -Non-robust communication: some tags closer to the reader are non-detected than those further due to little power reception from reader.
Microwave/2.4-2.5 GHz / Propagation	<ul style="list-style-type: none"> -Worldwide unlicensed band -Wider bandwidth: higher data rate and more channels to avoid collisions -Good reflection on metal surfaces -Reasonable propagation thru non-conductive materials as wood or plastic 	<ul style="list-style-type: none"> -More expensive components -More current consumption -Reduced propagation distance compare to other bands with the same power -Suffer from energy-absorption when working moisture-containing material -Multipath effects and fading due the propagation mechanism -More susceptible to electrical noise than UHF band

The propagation mechanism belongs to the far-field radiated electromagnetic field study. It is employed on UHF band and microwave. The reader generates an EM field at the operating frequency and the tag is able to detect this radiation, harvest energy from the radiated field and sent back information to the reader through backscattering mechanism.

The operating principle of a passive RFID tags is illustrated on Figure 3. The antenna harvest energy from the EM field radiated by the reader. The induced voltage on antenna is rectified and energy is stored thanks to the internal capacitance, in this stable voltage is provided for powering purposes. Another rectifier with a smaller capacitor is used to demodulate the information sent from the reader.

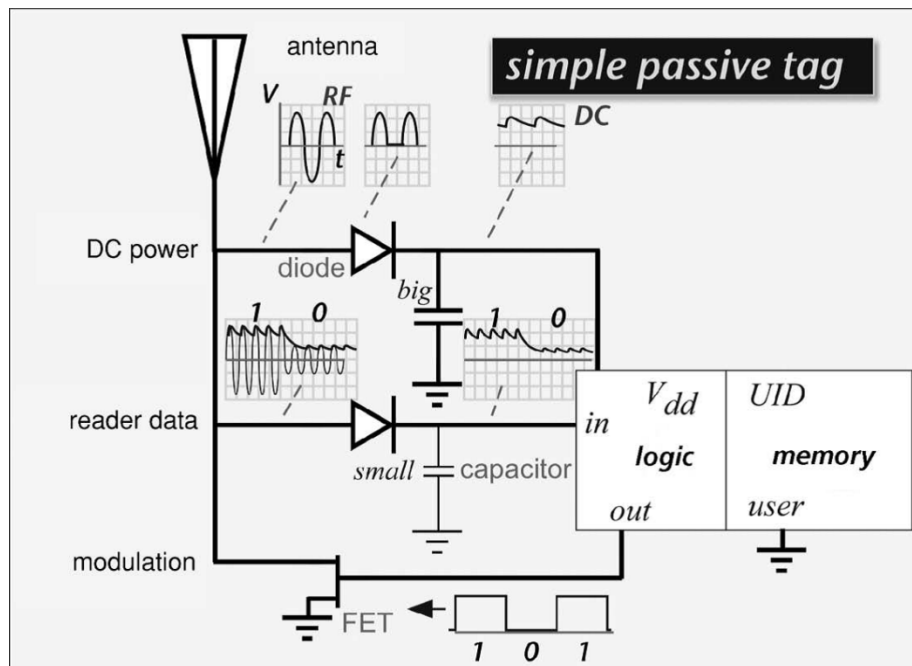


Figure 3. Scheme of a simple passive tag showing the rectifier, the antenna interface and the backscattering mechanism.

Finally, RFID backscatter coupling or RFID backscattering, see Figure 3, is the mechanism used by the tags to send back information to the reader. When the signal from reader reaches the RFID tag, some energy is reflected back towards the RFID reader. The way in which the signal is reflected back depends upon the properties of the tag. In particular the antenna will harvest

and re-radiate energy, and the way this energy is re-radiated is dependent upon the antenna properties. Therefore by changing factors the re-radiated signal properties can be changed. This can be used to drive an electronic switch, e.g., a FET that can switch an antenna load resistor in and out of circuit. This will effectively modulate the returned signal and allow data to be passed back to the reader.

Attending to power source there are three types of RFID tags:

- Actives. Use internal batteries to power their circuits and to transmit radio waves to a reader.
- Passive. Use entirely the radiated field by the reader as their power source implying lower production costs
- Semi-passive. Internal batteries are used to provide energy to extra-circuitry whilst the communication with the reader remains passive

Attending to the type of functionalities provided by the RFID chip:

- Read-only. Tags contain only an identification number that can be accessed by the reader. The identification code is written on the fabrication process and cannot be modified.
- Write-once read many (WORM). It is possible to write the identification code but only once. This code can be accessed by the reader
- Read/write. In this case the information stored on the RFID chip can be modified. This requirement is critical on production chains due to the objects suffers from constant changes. These are the most expensive chips.

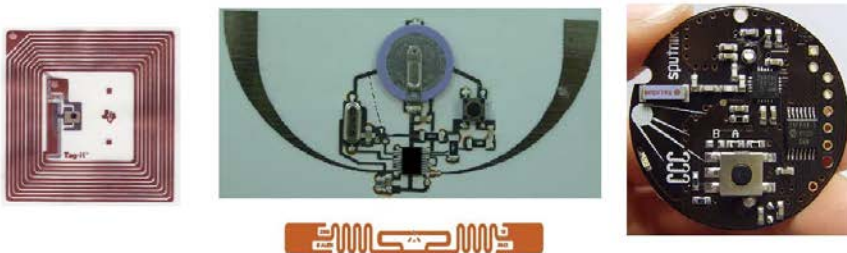


Figure 4. Some examples of RFID tags: passive on the HF band (left), passive (center-up) and semi-passive (center-down) on UHF band and active on microwave band.

1.1.3 RFID Standards

Standardization is crucial for the RFID technology due to enable manufacturers to make compatible the same products for a variety of markets and products from different manufacturers to operate together. One example may be for tags which are used in very large quantities and manufacturers may want to source from suppliers to provide reliability.

There are two main international RFID standards bodies:

- ISO - International Standards Organization
- EPCGlobal - Electronics Product Code Global Incorporated

Although these two organizations provide the main RFID standards organizations, there are also other standards that apply to different areas of RFID. In terms of the standardization organizations ISO is the longest established. In 1996 it set up a joint committee with International Electrotechnical Commission (IEC) to look at standardization for RFID technology. The ISO RFID standards regard different categories according to the aspect of RFID that they are addressing: air interface and associated protocols; data content and the formatting; conformance testing; applications; and various other smaller areas.

In addition to these standards, there are also the standards from EPC Global. In 1999 a number of industrial companies with Massachusetts Institute of Technology (MIT) make the Auto-ID consortium with the aim of researching and standardizing RFID technology. In 2003 this organization was split with the majority of the standardization activities coming under a new entity called EPCGlobal. The Auto-ID Center retained its activities associated with the research into RFID technologies.

The Auto-ID Center set a series of classes for RFID tags in order to be able to standardize the RFID tags. This classification forms the basis for RFID tag classes seen today:

- Class 0: Basic read-only passive tag using backscatter where the tag was programmed at the time the tag chip was made.
- Class 1: Basic read-only passive tag using backscatter with one-time non-volatile programmer capability.

- Class 2: Passive backscatter tag with up to 65k of read-write memory.
- Class 3: Semi-passive tag with up to 65 k read-write memory and a battery incorporated to provide increased range.
- Class 4: Active tag using a battery to enable extra functionality within the tag and also to provide power for the transmitter.
- Class 5: An active tag that provides additional circuitry to communicate with other class 5 tags.

The responsibilities for Class 0 and Class 1 RFID tag definitions and standards were handed on to EPC Global in 2003. Although other newer RFID tag standards and now available, reference is still made to these original tag classes. In 2004 EPCGlobal began the creation of a second generation protocol, often referred to as EPCGlobal Gen2. While the EPCGlobal Gen2 RFID standard is not backwards compatible with the Class 0 and Class 1 tags, it aims to provide a worldwide RFID tag standard that is compatible with ISO standards. Some of the main RFID standards are summarized in the table below.

Table 2. RFID ISO Standards.

RFID Standard	Details
ISO 10536	ISO RFID standard for close coupled cards
ISO 11784	ISO RFID standard that defines the way in which data is structured on an RFID tag.
ISO 11785	ISO RFID standard that defines the air interface protocol.
ISO 14443	ISO RFID standard that provides the definitions for air interface protocol for RFID tags used in proximity systems - aimed for use with payment systems
ISO 15459	Unique identifiers for transport units (used in supply chain management)
ISO 15693	ISO RFID standard for use with what are termed vicinity cards
ISO 15961	ISO RFID standard for Item Management (includes application interface (part 1), registration of RFID data constructs (part 2), and RFID data constructs (part 3).
ISO 15962	ISO RFID standard for item management - data encoding rules and logical memory functions.
ISO 16963	ISO RFID standard for item management - unique identifier of RF tag.

ISO 18000	ISO RFID standard for the air interface for RFID frequencies around the globe
ISO 18001	RFID for item management - application requirements profiles.
ISO 18046	RFID tag and interrogator performance test methods.
ISO 18047	The ISO RFID standard that defines the testing including conformance testing of RFID tags and readers. This is split into several parts that mirror the parts for ISO 18000.
ISO 24710	Information technology, automatic identification and data capture techniques - RFID for item management - Elementary tag license plate functionality for ISO 18000 air interface.
ISO 24729	RFID implementation guidelines - part: RFID enabled labels; part 2: recyclability of RF tags; part 3: RFID interrogator / antenna installation.
ISO 24730	RFID real time locating system: Part 1: Application Programming Interface (API); Part 2: 2.4 GHz; Part 3: 433 MHz; Part 4: Global Locating Systems
ISO 24752	System management protocol for automatic identification and data capture using RFID
ISO 24753	Air interface commands for battery assist and sensor functionality
ISO 24769	Real Time Locating System (RTLS) device conformance test methods
ISO 24770	Real Time Locating System (RTLS) device performance test methods

RFID standards are now widespread in their use, and although EPCglobal and ISO are separate organisations, there are efforts to move towards a single RFID standards scenario, rather than having two sets of competing RFID standards.

1.1.4 RFID Chip

The RFID chip is an integrated circuit implemented in silicon. The RFID circuitry itself consists of an RF front end, some additional basic signal processing circuits, logic circuitry to implement the algorithms required, and EEPROM for storage. The major blocks and their functions of the RFID front end are as follows:

- Rectifier: Generates the power supply voltage for front-end circuits and the whole chip, as well from the coupled EM field;

- Power (voltage) regulator: Maintains the power supply at a certain level and at the same time prevents the circuit from malfunctioning or breaking under large input RF power;
- Demodulator: Extracts the data symbols embedded in the carrier waveforms;
- Clock extraction or generation: Extracts the clock from the carrier (usually in HF systems) or generates the system clock by means of some kind of oscillator;
- Backscattering: Fulfills the return link by alternating the impedance of the chip;
- Power on reset: Generates the chip's power-on reset (POR) signal;
- Voltage (current) reference: Generates some voltage or current reference for the use of front-end and other circuit blocks, usually in terms of a bandgap reference;

Figure 5 is a block diagram for RFID IC circuits and lists many of the circuit's associated function blocks. The RF front end is connected to the antenna, and typically, at UHF, an electric dipole antenna is used, while HF tags use a coil antenna. Passive RF tags have no power source and rely on the signal from the reader to power up; thus, the RF front end implements modulators, voltage regulators, resets, and connections to an external antenna. RFID chips have control logic that typically consists of a few thousand gates. The lowest level chip uses very few gates, on the order of 1,500 gate equivalents. Functions in the logic include the error and parity/CRC checkers, data encoders, anticollision algorithms, controllers, and command decoders. More complex RFID chips may include security primitives and even tamperproofing hardware. The size of the circuit affects the number of mask, metal, and poly layers required in the semiconductor process, and RFID systems usually use CMOS.

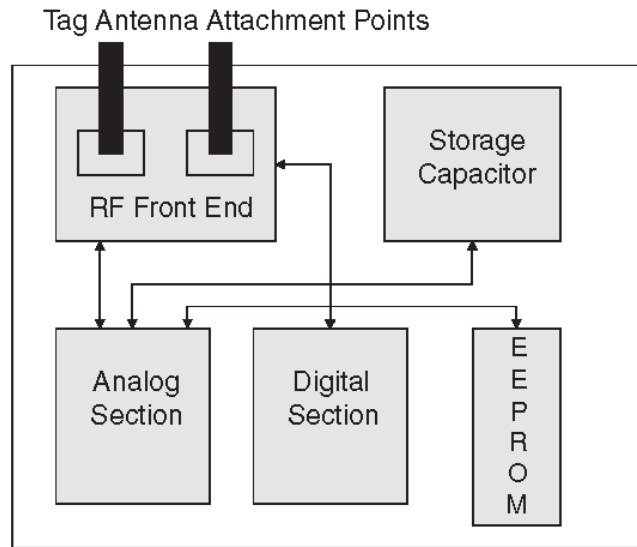


Figure 5. Block diagram of a generic RFID IC Circuit

A certain amount of information is stored on-chip in an EEPROM. The size of this EEPROM increases as more information is required to be on the RFID chip. The size of the required EEPROM is a factor in determining the number of mask, metal, and poly layers required in the semiconductor fabrication process. It is also a factor in determining the size of the final semiconductor die. Silicon cost is directly proportional to both the die size and the number of mask, metal, and poly metal layers. The IC in an RFID tag must be attached to an antenna to operate.

RFID chips usually provide protocol standard compatibility as ISO 15693 on HF band or EPC Gen 2 on UHF band, but some extra functions are required to include sensing capabilities. These functions are mainly:

- Serial Port Interface (SPI) or Inter-Integrated Circuit (I²C) to provide full access to the RFID chip EEPROM memory by other chips, typically microcontrollers.
- Integration of built-in sensors or signal conditional stages to interface external sensors. Examples are on-chip temperature sensors or Analog to Digital Converters (ADC).

There are only few RFID UHF chips that can provide these functions. RFID chips with SPI capability are, for example, the D18BLO1 from Delta

Company. The EM4325 provided by EM Microelectronics-Marin and the WM72016 from Ramtron Corporate count also with on-chip temperature sensor. Besides these features, the RFID chips SL13A and SL900A (AMS AG, Unterpremstaetten, Austria) integrates a very complete SFE. This extra circuitry can be used to interface different type of current-output, resistive and capacitive sensors to be read out easily by a standard RFID reader.

1.1.5 RFID Antennas

An antenna is a conductive structure specifically designed to couple or radiate electromagnetic energy enabling communication in RFID systems. Any conducting structure can be termed to be an antenna, but the efficiency with which the structure can transform the energy is the key determining factor on how well communication can be established in the system. Antennas are reciprocal in their behavior. This means that the antenna behaves in a similar fashion irrespective of its transmission and reception modes

As previously explained, in the HF range with short read distances, the tag is in the near field of the reader antenna, and the power and signals are transferred by means of a magnetic coupling. In the UHF range, in cases where the read distances are larger, the tag is located in the far field of the reader antenna.

Good antenna design is a critical factor in obtaining good range and stable throughput in a wireless application. This is especially true in low-power and compact designs where antenna space is less than optimal. It is important to remember that, in general, the smaller the antenna, the lower the radiation resistance and the lower the efficiency. The tag antenna should be as small as possible and easy to produce.

When designing any antenna we must consider certain characteristics as key parameters such as antenna radiation patterns, bandwidth, gain...They are discussed as follows:

- **Resonant Frequency.** Frequencies where antenna radiates or transmits EM waves in a most efficient way.

- **Bandwidth.** The range of frequency around the resonant frequency where the efficiency of the antenna in transmitting or receiving EM waves is close to 90% (−10 dB).
- **Impedance.** Any antenna has three different resistances: radiative, resistive, and reactive. Together, these are referred to as the impedance of the antenna. Power absorbed by the radiative resistance is transmitted as EM energy. The power absorbed by the resistive resistance is dissipated as heat. The reactive energy is the unwanted energy that does not do any useful work and is composed of inductance and capacitance. It inhibits the transfer of energy and thus acts like a barrier. At resonant frequency, the inductance and capacitance mutually cancel each other to almost zero, and hence the antenna is the most efficient transducer at its resonant frequency.
- **Scattering Parameter.** This is an estimation that shows how efficiently an antenna is transmitting (or receiving). The S_{11} parameter (in decibels) measures the ratio of the reflected wave to the incident wave and it is called the return loss (RL). The industry standard of acceptable RL of 10 dB.
- **Gain.** Gain of any antenna is the ratio of the power transmitted in any given direction with respect to the power transmitted in that direction by an isotropic antenna (unit dBi). An isotropic antenna is an imaginary antenna that radiates in an omnidirectional pattern with equal intensity in all directions. It should be kept in mind that any passive antenna might have higher gain in any given direction, but this has to be compensated by lower gain in another direction..
- **Radiation Pattern.** The graphical three-dimensional view of the power pattern of any antenna is called its radiation pattern. The radiation pattern consists of a main lobe where the intensity is maximum and some side lobes that are pointed at different directions and don't contribute to the antenna performance.
- **Directivity/Beamwidth.** When the radiation pattern of any antenna is plotted in the direction of its main lobe, the angle (three-

dimensional) at which the power level falls to half of maximum power is called the beamwidth (3-dB beamwidth). This determines the directivity of the antenna. In RFID operations, the reader antennas are required to have the maximum gain and directivity, whereas the tag antennas are supposed to achieve (as much as possible) omnidirectional nature in their radiation pattern.

- **Polarization.** The EM wave radiated from any antenna has electric field and magnetic field perpendicular to each other. Based on the orientation of the electric (E) field, the polarization of any antenna is defined which may be either linear or circular. In linear polarized antennas, the E-field is either horizontal or vertical with respect to the ground. In circularly polarized antennas, the antenna is designed in such a way that both vertically and horizontally polarized E-fields add up with 90° phase delay between them. This results in the creation of a rotating E-field with time which may rotate either in clockwise or anticlockwise manner in the direction of the propagation of the EM wave. Two linear polarized antennas gets maximum transfer of energy between them (co-polarized antennas) but if the polarization of one of the antennas is changed (rotating the antenna by 90°), then power is no longer transferred between them (cross-polarized antennas). For this reason typically RFID antenna readers are circular polarized antennas and then a penalization of 3 dB on the transfer of energy takes place the transfer of half (-3 dB) the power takes place.

The size and shape of the tag antenna have a significant effect on tag read rates, regardless of the coupling used for communication. Various types of antennas are available, among which the most commonly used are dipole, folded dipole, printed dipole, printed patch, squiggle, and log-spiral. Among these, the dipole, folded dipole, and squiggle antennas are omnidirectional, thus allowing them to be read in all possible tag orientations, relative to the base antenna. On the other hand, directional antennas have a good read range due to their good resistance to radiation patterns. Care must be taken while choosing an antenna because the antenna impedance must match to the RFID chip and to free space. The four major considerations when choosing an antenna are as follows:

- Antenna type;
- Antenna impedance;
- Nature of the tagged object;
- Vicinity of structures around the tagged object.

Another type of usage involves integration into the object that is to be identified. Parts of the object can be shaped to form an antenna and the antenna can be adjusted optimally to suit the object. This significantly increases readability, while simultaneously protecting against counterfeiting.

1.2 Printed Electronics

Printed Electronics (PE) is a technology based on printing techniques to create electronic circuits. PE continues to gain ground with the constant development of many new functional printed circuits and devices. In this sense, high-quality electronic products can be manufactured providing new features to the traditional electronics, such as the ability to produce thin, flexible, wearable, lightweight, ultra-cost-effective, and environmentally friendly structures. The main benefits of PE technology are summarized below:

1. It must be thin, lightweight, and useable in large electronic devices. Printing can make large products up to several tens of meters wide. This could be applied to, for example, TV, solar, and lighting equipment being larger than those made with conventional silicon technology.
2. It reduces production cost and time. Silicon technology is reaching its ultimate fine pitch resolution, 13 nm, and the establishment of the production foundry requires a huge investment. Printing production requires less than approximately 10 or 100 times the investment, and time is also considerably reduced.
3. It achieves true wearable devices. Traditional “wearable” devices are easily characterized by their size, heavy weight, stiffness, and fast power consumption. But truly wearable devices should be lightweight, thin, and comfortable and must power themselves; these requirements can be fulfilled by PE.

4. All products tend to be smart: they will be equipped with some sort of intelligent device capable of communicating with the outside world wirelessly. Traditional silicon dyes are not profitable in many cases due to their high cost.
5. All electronic devices should be environmentally friendly that means free of toxins and rare earth elements and requiring low energy, both in the manufacturing process and in operation. In conventional production of electronic equipment, complex processes are required in the production of both silicon devices and printed circuit boards, discarding much solid and liquid waste in the environment. The considerable reduction of solid and liquid waste in manufacturing is a key feature of PE technology, as well as the fact that it uses less energy.

Some of the pursued applications for printed electronics include RFID tags as well as various types of wireless sensors (Finkenzeller and Müller 2010). Conductive inks and pastes provide an alternative technology for antenna fabrication in RFID technology (Allen et al. 2011, Allen et al. 2009, Catarinucci, Colella and Tarricone 2013, Koski et al. 2012, Lim et al. 2009, Rida et al. 2009, Virtanen et al. 2012, Vyas et al. 2009, Merilampi et al. 2010a, Sangoi et al. 2005). Antennas can be directly fabricated from digital format by inkjet or screen printing processes, introducing significant savings on design effort and material costs in R&D, and enabling high-volume production under ambient conditions using roll-to-roll printing techniques in the industry.

Geometry and electrical characteristics of printed patterns determine the RF behavior of antennas and conductive tracks for RFID applications. The diversity of commercially available conductive inks and substrates need to be considered in order to study which printing technology would present better performances at high frequencies. The importance of such analysis has been pointed out in previous works: dealing with DC electrical and/or mechanical characterization (Jung et al. 2007, Lee and Oh 2010, Merilampi, Laine-Ma and Ruuskanen 2009, Roberson, Wicker and MacDonald 2012), printed devices fabrication (Kim et al. 2010a) and RF characterization (Chiolerio et al. 2012, Feng et al. 2011, Palukuru et al. 2011, Tanabe et al. 2000).

To compensate this higher cost of RFID, printing technology can be considered. Printing conductive inks and pastes provide an alternative technology for the large area and high throughput fabrication of antennas and connections in RFID technology using roll-to-roll techniques (Merilampi et al. 2010a, Rida et al. 2009, Janeczek et al. 2012, Shin, Lee and Kim 2009, Sangoi et al. 2005, Virtanen et al. 2012, Amin et al. 2012, Amin et al. 2013, Rouse et al. 2013, Siegel et al. 2010, Yang et al. 2007, Koski et al. 2012). In this sense, printed electronics results in a good alternative to produce low-cost systems in large-scale production. Several examples are found of RFID tags developed with different printing techniques: screen printing, gravure, flexography, inkjet printing (Sangoi et al. 2005, Allen et al. 2011, Virtanen et al. 2011). In addition to cost savings, printed electronics can produce thin, wearable, lightweight devices and it can also provide more flexibility by using malleable substrates (Suganuma 2014).

1.2.1 Inkjet Printing

The traditional continuous jet printer used electrostatic plates to deposit drops on the substrate. These have been replaced by drop-on-demand systems. Canon and Hewlett-Packard developed systems where a heated plate causes a vapour bubble to form and eject a droplet of ink through a nozzle. Epson printers use an array of piezoelectric plates which drive the droplet in bend or push mode (Calvert 2001). In order to obtain a wiring homogeneous fine line, the inkjet parameters should be controlled for each nozzle at each step. The droplet size, shape, speed, and uniformity of an inkjet printer differ from one nozzle to another.

The distance between the substrate and a nozzle is usually about 1–2 mm, but during flight, air resistance can affect the droplet shape. Furthermore, the solvent evaporation happens at the same time. Metallic particle inks typically consist of silver, copper or gold particles dispersed in a solvent matrix. Such particles can be microparticles whose diameter typically ranges from 2 μm to 40 μm (Faddoul, Reverdy-Bruas and Blayo 2012, Kattumenu et al. 2009, Kim, Kim and Yoo 2010b, Merilampi et al. 2009, Roberson et al. 2012) or nanoparticles whose diameter ranges from just 2 nm to above 50 nm and are encapsulated with a protective shell (Derby 2010, Magdassi et al. 2010, Perelaer et al. 2010, Roberson et al. 2012, Tao et al. 2008). After printing

nanoparticles, an annealing step is needed in order to loosen up the nanoparticles shells and make them melt together, achieving a continuous conducting structure. Due to the small size of the metallic nanoparticles, the sintering temperatures are significantly lower than melting points of the corresponding bulk materials. The viscosity of the ink should be lower than 5 mPa·s. The pattern resolution is about 20-30 μm and the thickness achieved can be lower than 100 nm.

1.2.2 Screen Printing

In screen printing, the process is performed at low pressure using a screen mesh with the designed pattern with uniform thickness (Figure 6). The image area of a screen is the area of the screen through which the ink will be transferred. To define this area, it has to be all covered using a photosensitive emulsion. The photosensitivity of this emulsion causes its hardening after being exposed to a light source whose exposure time, intensity, distance and wavelength (UV) are properly controlled. This hardened area of the screen becomes impermeable their threads, so that, the ink path is blocked. However, the areas of the emulsion that have not been exposed to light are not hardened and can be removed using water. Thus these threads do not contain any emulsion and the ink can be transferred trough them, thereby defining the image area.

The design of the printed layout is reproduced in a positive photolithography. This positive contains our design in black color and the density must be appropriate to be opaque on a transparent polyester film. The positive is placed on an intermediate position between the exposure light source and the coated screen. Thus, the light passes through the transparent film only (no image area) and will be blocked by the black color of our design (image area). After the completion of the etching, water is applied to the screen in order to remove all of the emulsion that has not been hardened by light exposure. The ink is transferred onto the substrate through the open areas of this mesh. A fill blade or flexible metal squeegee or rubber squeegee is moved across the screen for squeezing paste through the mesh. The typical materials used for the mesh are polyamide, polyester, or stainless steel. The mesh pattern is defined by photolithography of an emulsion on the mesh. A

metal screen can also be used instead of a mesh screen with an emulsion pattern.

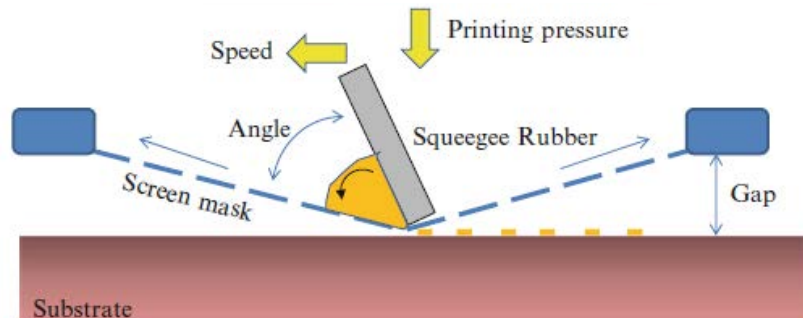


Figure 6. Schema of screen printing fabrication (Suganuma 2014).

The usual thickness of a screen printed pattern is in the range of microns, but in case of a thick screen mesh, the thickness can exceed $100\ \mu\text{m}$ with one layer of printing. This thickness value cannot be achieved by any other printing method. The pattern resolution obtained by screen printing is higher than $100\ \mu\text{m}$. The viscosity of the ink has to be at least $1000\ \text{mPa}\cdot\text{s}$.

1.2.3 Printed Sensors

Great efforts and very valuable advances have been made in the design of flexible and printed sensor (Andersson et al. 2012, Unander and Nilsson 2009, Virtanen et al. 2010b, Briand et al. 2011). Thanks to the requirement of low energy consumption, many gases and humidity printed sensors are capacitive, specifically through changes in the electrical permittivity of some component of the capacitor. Regarding moisture sensors, this transduction mechanism requires the use of chemicals (usually polymers) whose electrical permittivity changes with the relative humidity of the environment. Different approaches have been followed to include the sensing capability in the capacitor. The most frequent strategy has consisted of depositing a sensing layer over the electrodes capacitor (Starke et al. 2011, Weremczuk, Tarapata and Jachowicz 2012, Molina-Lopez, Briand and de Rooij 2012). Some common polymers are cellulose acetate butyrate (CAB), polymethylmethacrylate (PMMA) and polyvinylchloride (PVC), among others. Another method is to directly use the flexible substrate as sensing element, saving fabrication steps compared with the previous strategy. For

this purpose, the use of polyimide (Virtanen et al. 2010b) and photographic paper (Briand et al. 2011) has already been described. Regarding the physical structure for these capacitors, the most used design is the interdigitated electrodes (IDE) because it presents very interesting features such as one-side access, control of signal strength by changing easily its dimensions, multiple physical effects in the same structure (electric, magnetic, acoustic) and a wide frequency spectrum of use (Mamishhev et al. 2004). Recently, a novel serpentine electrode (SRE) has been described by Rivadeneyra et al. whose sensitivity is higher than IDE in the same area conditions (Rivadeneyra et al. 2014b).

In this regard, several RFID tags with sensing capabilities have been already developed following different strategies. Over the last years, several strategies have been applied to include sensing capabilities to RFID systems. On one hand, some authors have studied the analog response of the RFID tag: read range, shift of the antenna resonance frequency, measured level of the backscattered power, etc. These changes have been associated to a variation of the monitored magnitude. Some examples are moisture sensing by means of antenna gain variation (Amin et al. 2013) and strain and crack sensing (Yi et al. 2013), among others (Potyrailo et al. 2012, Merilampi et al. 2011, Manzari et al. 2012, Virtanen et al. 2011, Bhattacharyya, Floerkemeier and Sarma 2010, Jacquemod et al. 2010, Babar et al. 2012, Cazeca et al. 2013, Nilsson et al. 2012, Daliri et al. 2012, Li and Kan 2010). These strategies can be very useful, e. g., for threshold sensor tags (Gao et al. 2013), but lead to uncertainties in the source of these variations because there are many factors that can interfere in the tag performance, for instance the path loss between antenna and reader or the spatial and temporal fading. In addition, extra circuitry must be added to the reader in order to measure these parameters. Other approaches are based on microcontroller architectures with RFID chips and different types of sensors: multisensors approach (Catarinucci et al. 2008, Catarinucci, Colella and Tarricone 2009, De Donno et al. 2013, De Donno, Catarinucci and Tarricone 2014, Yang, Rida and Tentzeris 2009), temperature, light, moisture content (Abad et al. 2009, Mattoli et al. 2010, Atsushi and Kentaro 2006, Chu et al. 2013); chemical sensing (Eom et al. 2012, Kassal, Steinberg and Steinberg 2013, Oprea et al. 2009, Steinberg et al. 2014, Zampolli et al. 2007); printed moisture sensors (Unander and Nilsson 2009, Unander, Siden and Nilsson 2011, Virtanen et

al. 2011, Virtanen et al. 2010b); pressure (Fernandez et al. 2012); or built-in sensors, typically temperature sensors (Yin et al. 2010). There are also some examples of single chip architecture without microcontroller unit already reported (Broutas et al. 2012, Catarinucci et al. 2013, Pletersek, Sok and Trontelj 2012). The main advantage of this strategy compared to the analog reading of the tag is the fact that sensor data are directly processed in the RFID tag. Therefore, the sensor digital data can be transmitted to the reader or stored on the RFID tag for future access. In case of data logging, these strategies require the use of a battery to power periodically the tag. Although the extra components increase the cost of the system, the functionalities incorporated justifies this higher cost.

Regarding smart printed RFID tags, Unander et al. (Unander et al. 2011, Unander and Nilsson 2009) presented a semi-passive RFID tag with a printed moisture sensor. The sensor solution consisted of a passive RFID tag, a microcontroller, a printed resistor, a printed moisture sensor, and two printed batteries to power the microcontroller. The sensors were defined by conductive silver ink on a plastic film laminated onto cellulose-based substrates. The readout of the sensors was measured by charging and discharging the capacitance. Another similar example was a printed UHF RFID tag which indicated whether the tag had been exposed to a certain degree of humidity (Gao et al. 2013). The change of the sensor resistance was used to modulate the properties of a UHF RFID tag antenna by changing antenna input impedance and also introducing or removing ohmic losses in the antenna structure. Both the sensor and the tag antenna are printed horizontally on a paper substrate. Contrary to these strategies, our tags do not require either extra circuitry to obtain data sensor or battery to take measurements.

1.3 Smart Packpaging

In recent years, there is a high interest in converging RFID tags with sensing capabilities. The development of RFID and the Electronic Product Code (EPC) standard has become a substitute of popular barcodes in packaging. This new trend, known as smart packaging, is able to read not only many packages at the same time but also environmental properties detected by sensors included in the RFID tags. In this sense, a special interest is shown in

the capability of tracking the condition of a package through the whole supply chain to certify the product quality has not been degraded. In fact, the field of smart packaging including sensor capabilities opens new challenges in the development of flexible and printed tags compatible with this kind of technologies (Potyrailo et al. 2012, Virtanen et al. 2011, Unander et al. 2011, Schoo and Knoll 2014, Oprea et al. 2009, Rida et al. 2009)

The basis of the modern packaging technology surged in the 19th century with the invention of canning by Nicholas Appert, and the later application of the food microbiology principles established by Louis Pasteur to the canning process (Brody et al. 2008, Wilson 2007). The main objective of packaging is the protection and preservation of food and beverage from external contamination. Food packaging can retard product deterioration, retain the beneficial effects of processing, extend shelf-life, and maintain or increase the quality and safety of food. In this way, packaging protects from three major external influences: chemical, biological and physical (Marsh and Bugusu 2007). Beyond this barrier function, there has been more research and development in the recent years regarding the introduction of new purposes to food packaging systems. Among these innovations, significant new functional packaging systems include smart and active packaging, modified atmosphere packaging (MAP) and edible films/coatings (Han 2005). Active packaging includes additives or components that can participate in a host of packaging applications and by doing so, enhance the preservation function of the primary packaging system. Intelligent or smart packaging is packaging that somehow senses some properties of the food it encloses or the environment in which it is kept and is able to inform the manufacturer, retailer and consumer of the state of these characteristics (Kerry, O'Grady and Hogan 2006). Intelligent packaging is an extension of the communication function of traditional packaging, and communicates information to the consumer based on its ability to sense, detect, or record external or internal changes in the product's environment. Basically, there are two types of intelligent packaging: one based on measuring the condition outside the package, the other directly measuring the quality of the food product, i.e. inside the packaging. In the latter case, there is direct contact with the food or with its headspace and there is always the need for an indicative marker of the quality and/or safety of the packed food. Examples

include time–temperature indicators (TTI), gas leakage indicators, ripeness indicators, toxin indicators, biosensors, and RFID (Restuccia et al. 2010).

One of the most interesting parameter to be sensed in smart packaging is the concentration of oxygen within the package, since it is the main cause of food spoilage (Rooney 1995). The presence of oxygen facilitates processes such as promotion of microbial growth, lipid oxidation, protein decomposition and discoloration (Mills et al. 2012). Therefore, it is common to seal the food in an ambient atmosphere that is low in oxygen, usually in the 0.5-2% range (Blakistone 1998) or even less (Faustman and Cassens 1990). Different types of oxygen sensors and indicators for MAP have been reported in the literature, being the most popular the -visual indicators (Evans et al. 2006, Mills 2005, Smolander, Hurme and Ahvenainen 1997). In this kind of indicators, a color change is observed, in most cases, due to either an oxygen-binding reaction, a redox reaction or a light-activated redox reaction (Mills 2005, Mills and Hazafy 2008). Apart from these colorimetric indicators, luminescence-based sensors offer an alternative to a purely visual response (O'Riordan et al. 2005, Papkovsky et al. 2000, Reininger et al. 1996). This optical technique can be used for the quantitative measurement of the O₂ concentration in a non-destructive manner, and has the advantage of addressing misreading due to the sensitivity limitations of human eyesight. Nevertheless, additional electronics is required, thus, increasing the cost of the system.

2. Study of materials and techniques for RFID tag prototyping

In this chapter, a comparative study of the materials and techniques employed for RFID tags prototyping is presented. Three fabrication techniques are characterized: two printing techniques, inkjet and screen printing, and milling copper on FR-4 substrate. Thickness prediction for inkjet patterns was performed with a simple model based on printing parameters and the ink specifications. The geometrical characterization of the printed lines has been correlated with their measured DC electrical conductivity. On the basis of the latter analysis, numerical simulations have been carried out for the design of coplanar waveguide transmission lines in order to evaluate and compare the real RF performances of the different studied cases.

2.1 Material and Methods

The characteristics of the substrates are shown in Table 3. The flexible polymeric substrates are Kapton® HN PI from Dupont TM, Melinex® ST506 PET from Dupont Teijin Films TM and ULTEM® PEI from Ajedium TM. Two different conductive inks composed by silver nanoparticles have been printed by inkjet and one silver paste by screen printing. Some specifications of such conductive inks are shown in Table 4. The ranges of the electrical resistivities related to the sintering conditions are those given by the manufacturers.

These set of substrate and inks have been combined to prototype test patterns. Apart from that, Flame-Retarded class 4 (FR-4) copper clad laminate rigid substrate from LPKF A.G. has been studied for comparison purposes. This material is widely used on electronic devices manufacturing. For the geometrical characterization, the roughness of substrates and printed patterns as well as the thickness of the patterns were measured with a Wyko NT1100 optical profiling system (VEECO, Tucson, AZ, USA) in all cases at three different spots. The optical measurements were carried out with 50x magnification objective in phase shift interference (PSI) mode with withe

light. The optical resolution is 0.55 μm . According to manufacturer specifications the repeatability is less than 3 nm (Metrology 1999). The roughness and thickness of each inkjet or screen printed pattern are represented as the mean of the three measured values with the standard deviation.

Table 3. Some characteristics of the substrates.

Substrate	Chemical composition	Dielectric constant	Dissipation factor	Glass transition temperature ($^{\circ}\text{C}$)
PI	Polyimide	3.5 (1kHz)	0.002 (1kHz)	360-410
PET	Polyethylene terephthalate	2.9 (1MHz)	0.002 (1kHz)	70
PEI	Polyetherimide	3.1 (1kHz)	0.001 (1kHz)	217
FR-4	Fiberglass Epoxy	4.6 (1kHz)	0.015 (1kHz)	-

Table 4. Technical specifications of the analyzed conductive inks for inkjet printing (a) and paste for screen printing (b) and FR-4 clad laminate Copper (c).

Conductive ink	Resistivity ($\mu\Omega\cdot\text{cm}$)	Solid content (Ag)	Solvent	Curing temperature ($^{\circ}\text{C}$)	Viscosity (cPs)
^a Suntronic U5603	5-30	20 %	Ethanol, ethanediol	150-300	10-13@25 $^{\circ}\text{C}$
^a ANP DGP 40LT-15C	11-12	30-35%	Triethylene Glycol Monomethyl Ether (TGME)	120-150	10-17@25 $^{\circ}\text{C}$
^b Suntronic CRSN 2442	25-50	70%	Thermoplastic Resin	120-150	20-30@25 $^{\circ}\text{C}$
^c Copper	1.68	-	-	-	-

The DC measurements have been recorded using the four-wires measurement technique with an 8 1/2-bit digital multimeter 3158A (Agilent Tech., Santa Clara, CA, USA). Values of resistivity and sheet resistance have been obtained in that way in all the mentioned patterns for different combinations of substrate/ink. The number of printed layers and mesh densities has been also considered for inkjet and screen printing respectively. The obtained values were compared with the bulk-Ag resistivity and the ink manufacturer datasheet.

2.1.1 Inkjet printing

The DMP-2831™ Dimatix printer (Fujifilm Dimatix Inc, Santa Clara, USA) has been used for inkjet printing. This printed works with piezo-based inkjet print cartridges. The printable area depends on the substrate thickness. Below 0.5 mm, this area is about 210 mm x 315 mm; between 25 mm and 0.5 mm it is 210 mm x 260 mm. The repeatability is $\pm 25 \mu\text{m}$. The substrate holder contains a vacuum platen to fix the substrate. Furthermore, the temperature is adjustable from ambient value to 60°C . The pattern, printed by inkjet, for DC characterization is shown in Figure 7b. It consists of twelve meander-shaped devices, each of them composed by twelve parallel segments of $200 \mu\text{m}$

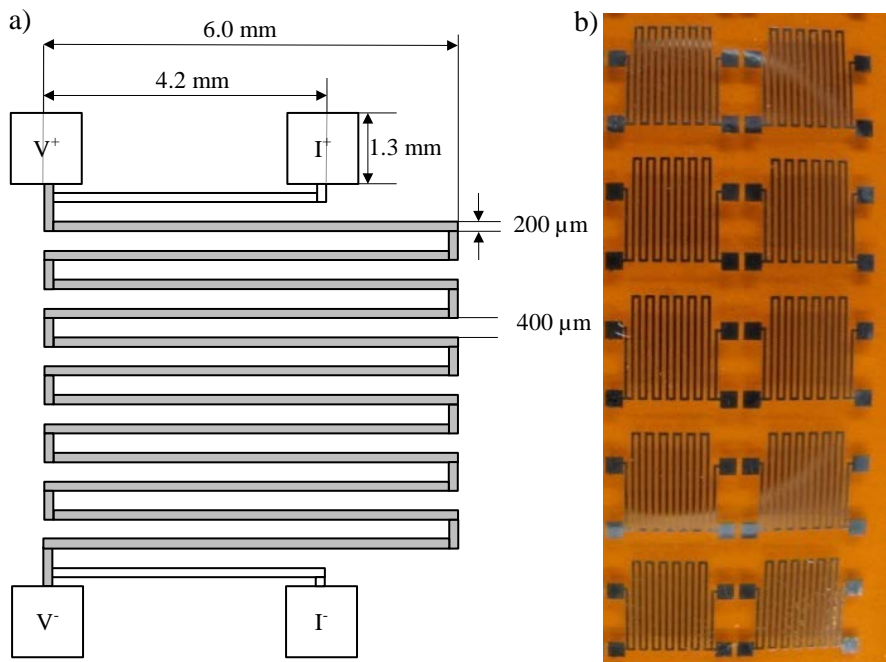


Figure 7. Schematic diagram of the inkjetted meandered structure for DC study (a) and image of the meandering patterns inkjetted with DGP silver ink on PI substrate (b).

width separated by $400 \mu\text{m}$, making the total length of 76.36 mm as can be seen shadowed in Figure 7a. Two squares with 1.3 mm side and separated with 4.2 mm were printed at both ends of the meandered lines to provide the four electrical contacts for DC measurements. Depending on the used conductive ink, this pattern was printed with up to 16 layers, all of them without intermediate curing for alignment improvement and with a single final curing

in a convection air oven. In the case of DGP 40LT15C ink (Advanced Nano Products Co., Chungcheongbuk-do, South Korea), a drop-to-drop space of 50 μm was used for around 100 μm diameter landed drops and sintering took place at 160 $^{\circ}\text{C}$ during 30 min. On the other hand, a drop space of 25 μm was used for around 50 μm diameter landed drops following by a sintering at 160 $^{\circ}\text{C}$ during 60 min for SunTronic U5603 ink (Sun Chemical, New Jersey, USA). The substrate temperature was fixed at 40 $^{\circ}\text{C}$ while printing. The reason for the difference in curing time is due to the different Ag content of each ink (see Table 2).

Inkjet Printing Model

Thickness is a crucial dimension to understand and predict the DC and RF behaviour of printed patterns. Whereas length and width are mainly determined by the printing conditions (which are under our control), thickness is more difficult to estimate. In this chapter, the theoretical model based on the one reported in (Molina-Lopez et al. 2012) has been validated with our experimental measurements. In the case of inkjet printing, the theoretical thickness of a printed layer of dry silver can be estimated as the ratio of the volume of dry silver, V_{Ag} , to the surface area, S , that it occupies as:

$$t = \frac{V_{Ag}}{S} \quad (1)$$

Knowing that one single inkjetted drop volume, V_D , is composed by a certain volume of silver, V_{Ag} , and certain of solvent, V_S , then:

$$V_D = V_{Ag} + V_S = \frac{m_{Ag}}{\rho_{Ag}} + \frac{m_S}{\rho_S} \quad (2)$$

where ρ_{Ag} (m_{Ag}) and ρ_S (m_S) are the density (mass) of the silver and solvent, respectively. The total volume of every drop is fixed by the cartridge used in the printing process and is set to 10 pL in the present work. Inks suppliers usually provide the solid ratio or mass fraction, χ_{Ag} , of silver inside a total ink mass, m_T , from where it is possible to establish the relationship between total mass and the mass of each ink component as follow:

$$m_{Ag} = \chi_{Ag} m_T \quad (3)$$

$$m_S = \chi_S m_T = (1 - \chi_{Ag}) m_T \quad (4)$$

Dividing both equations by the corresponding density and replacing them in equation (2) the following expression is found for the volume contained in one jetted drop in terms of its mass:

$$V_D = \frac{\chi_{Ag} m_T}{\rho_{Ag}} + \frac{(1 - \chi_{Ag}) m_T}{\rho_S} \quad (5)$$

Isolating m_T in the equation (5) and introducing it in the term we obtain:

$$V_{Ag} = \frac{V_D}{1 + \frac{\rho_{Ag} (1 - \chi_{Ag})}{\rho_S \chi_{Ag}}} \quad (6)$$

The total number of drops deposited on a certain surface area, S , at every printed layer can be estimated from the drop to drop space, dtd . The printed head deposits one drop every dtd distance in both x and y directions, thus every surface area equal to dtd^2 accommodates the volume of one single drop. This relation is fulfilled everywhere except at the edge of the printed line where the amount of ink is smaller (see Figure 8). This irregularity in the contribution of the outer part of the lines to the average thickness has to be taken into account only if the printed element is comparable in size with the diameter of one printed drop. In the case of the meandered lines, the width, W , and length, L , of the printed lines are $200 \mu\text{m}$ and 76.36 mm respectively, whereas the diameter of a printed dot is $100 \mu\text{m}$ for DGP ink and $50 \mu\text{m}$ for

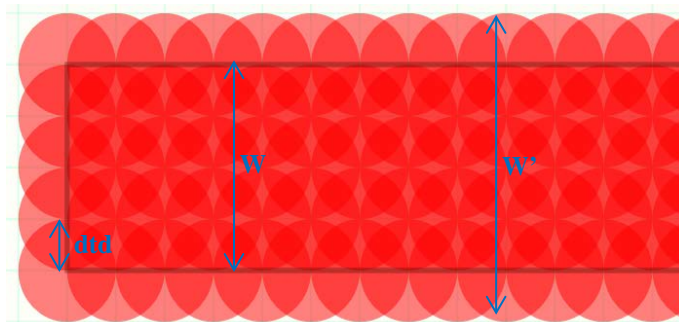


Figure 8. Sketch of the size of a printed line of real width W' compared with the size established in the layout with width W .

SunTronic ink. Therefore, special care has to be taken to the amount of ink deposited along the width of the lines. We can still consider a linear drop density of one drop per dtd distance along the length direction. The number of drops printed along the line width are $(W/dtd + 1)$, with W the width established on the layout of the pattern, so that a surface $S=W'dtd$, where W' is the real measured width, would correspond to a number of $(W/dtd + 1)$ drops. Then, combining (1) and (6) and assuming that the thickness of dry silver adds up linearly at every printed layer, the total theoretical thickness of a line composed of n layers is given by the following expression where all the parameters are known.

$$t = n \frac{\left(\frac{W}{dtd} + 1\right)}{S} V_{AG} = n \frac{\left(\frac{W}{dtd} + 1\right)}{W'dtd} \frac{V_D}{1 + \frac{\rho_{Ag}(1 - \chi_{Ag})}{\rho_S \chi_{Ag}}} \quad (7)$$

All the parameters in the expression above are known or can be estimated. If layers are printed with different dtd space, the total thickness is easily calculated by using equation (7) independently for each layer. This model has been checked with the experimental data obtained from the interferometry study of the meandered lines thickness.

2.1.2 Screen printing

A Serfix III screen printing machine (Seglevint SL, Barcelona, Spain) has been used for screen printing prototyping. In our case, an emulsion of a hardened diazo-photopolymer (Kopimask S. A., Barcelona, Spain) have been used to manufacture the mask. The screens used to manufacture the patterns are aluminum rectangular structures of 50 cm of width and 35 cm of length to fabricate them with only a single-layer screen printed. Three different screens have been used to manufacture the screen printed patterns for DC characterization with mesh densities of 43, 90 and 140 Nylon thread per centimeter (T/cm), respectively. The patterns were printed with SunTronic CRSN 2442 ink (Sun Chemical, New Jersey, USA) and consisted of one layer straight lines of 1.0 mm width and 5.0 cm length. Two circles with 4.0 mm diameter and separated by 1.0 cm were printed at both ends of the screen printed lines to provide electrical contacts for DC measurements, see Figure 9a. In order to evaluate if the pattern orientation had an influence on physical

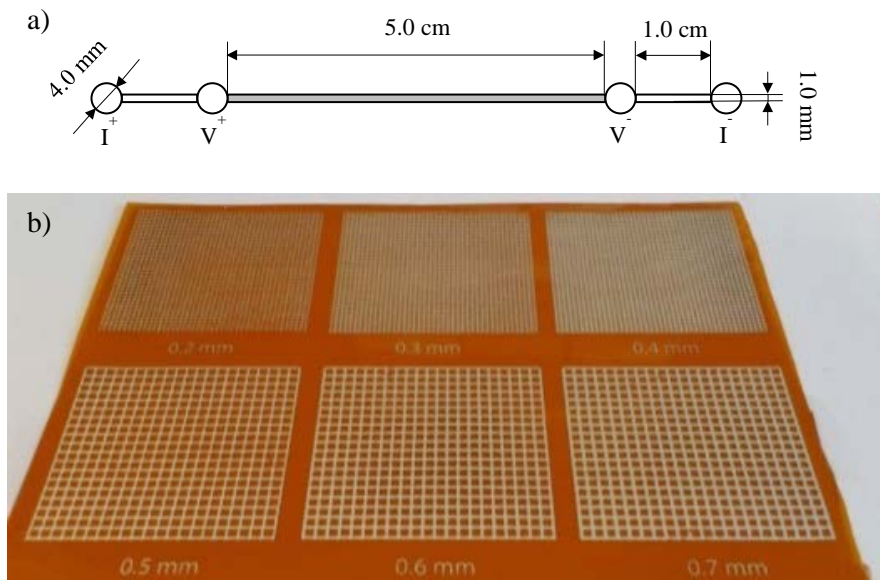


Figure 9. Schematic diagram of the screen printed structure for DC study (a) and image of the screen-printed patterns for study of minimum dimensions; each square is composed of lines of constant width ranging from 0.2 mm to 1.0 mm (b).

dimensions or electrical properties, the test lines were screen printed along three different directions: vertical, horizontal and diagonal. Furthermore, several horizontal and vertical lines with widths ranging from 0.2 mm to 1.0 mm were printed, as shown in Figure 9a, to find the minimum achievable width for every utilized mesh.

2.1.3 Milling FR-4

A milling machine model S100 (LPKF Laser & Electronics AG, Garbsen, Germany) was employed for prototyping on FR-4 substrate. Metallization layer was Copper 35 μm thick whilst the substrate was 1.5 mm thick. Conductivity and substrate parameters were provided by the manufacturer and can be seen in Tables 3 and 4. Accuracy on fabrication plays an important role on RF circuits so specific RF tools were employed on the milling process. RF tools get more vertical clean edge finish compare with standards ones. According to the manufacturer, the minimum conductor width that is possible to be fabricated is 100 μm . Repetition accuracy with the employed tools is $\pm 2.5 \mu\text{m}$ and positioning accuracy $\pm 5 \mu\text{m}$.

2.1.4 RF Numerical Simulation

The Advanced Design System (ADS) software (Agilent Technologies, Santa Clara, CA, USA) based on momentum method was used for simulating the RF electrical behavior of the printed patterns, including their surface area, roughness and the influence of the substrate.

Coplanar waveguide refers to a special case of a transmission line commonly used for RF characterization of materials. The structure (Figure 10) is composed by an inner conductor separated from a pair of ground planes, all on the same plane. The distance between the central conductor and the ground planes is denoted as gap. The characteristic impedance of CPW depends on the gap and the central conductor width. In this work the gap has been fixed to $150\ \mu\text{m}$. Line Calculator tool from ADS simulator was thus used for each combination of substrate and ink to find the width dimensions leading to the desired 50 Ohms characteristic impedance. The substrate properties, such as relative permittivity and dissipation factor, were provided by the supplier whereas the metal characteristics, thickness and effective conductivity, were obtained in the performed DC study. In the case of the set of CPWs fabricated on FR-4 substrate, the same process was performed but

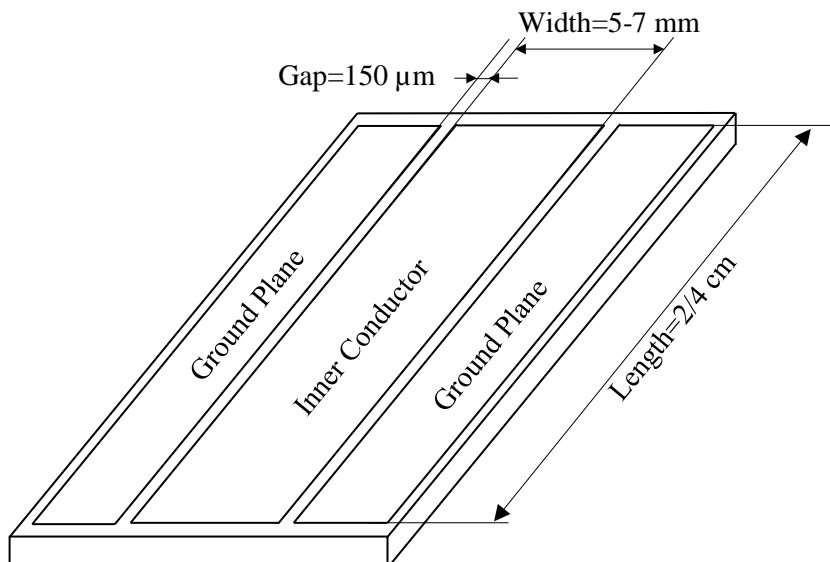


Figure 10. Drawing showing the structure and relevant dimensions of the designed CPWs transmission lines.

substrate and metallization layer parameters were supplied by the manufacturer, see Table 1 and Table 2. Once the geometrical parameters were obtained, full S-parameters simulation was carried out and optimized to validate the different fabricated CPW. The measured frequency range was extended to 1.2 GHz covering not only the RFID HF band but also the RFID UHF band of 858-930 MHz.

For each substrate/ink pair, two different lengths were printed: 2.0 cm and 4.0 cm. In the case of screen printed lines, only the highest mesh density of 140 (T/cm) has been used in order to get a well-defined gap distance along the entire length of the lines. Special care has to be taken while printing the gap because any irregularity on this separating distance will lead to a mismatching that will perturb the measurements. The CPW transmission lines characterization was carried out using an E5071C network analyzer for the S-parameter study with a N4431A kit for calibration purposes (Agilent Tech., Santa Clara, CA, USA). The designed layout includes the space to accommodate the subminiature version A (SMA) edge connectors on both ends of the printed lines. The N4431A kit performs an electronic calibration setting the reference plane on these SMA connectors as shown in Figure 11

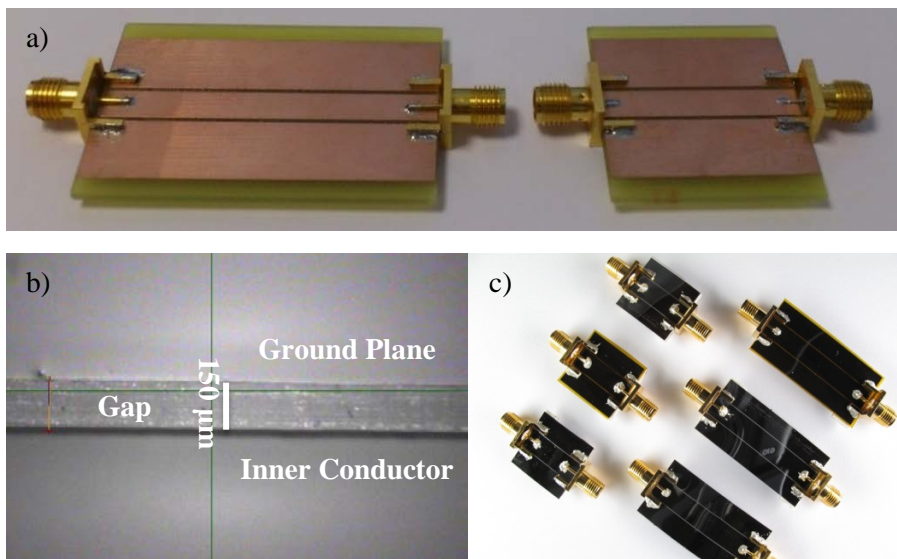


Figure 11. Image of the fabricated FR-4 CPW transmission lines (a). Capture image with the Dimatix printer fiducial camera showing the 150 µm gap of the printed CPW. The green and orange lines are references axis and measurement distance line, respectively, generated by the camera. (b) Image of the inkjetted CPW transmission lines showing the two different lengths of 2 and 4 cm printed on the three different substrates.

where a complete set of inkjetted CPW lines are shown: three different substrates and two different length forms a total number of six pieces.

2.2 Experimental Results

2.2.1 Geometrical and DC Characterization of Inkjet Printed patterns

The main results of the geometrical characterization of the printed patterns using different substrates, inks, number of layers and printing technique are summarized in Table 5. This table includes the measurements of thickness, roughness and sintering conditions. The data and their uncertainties come

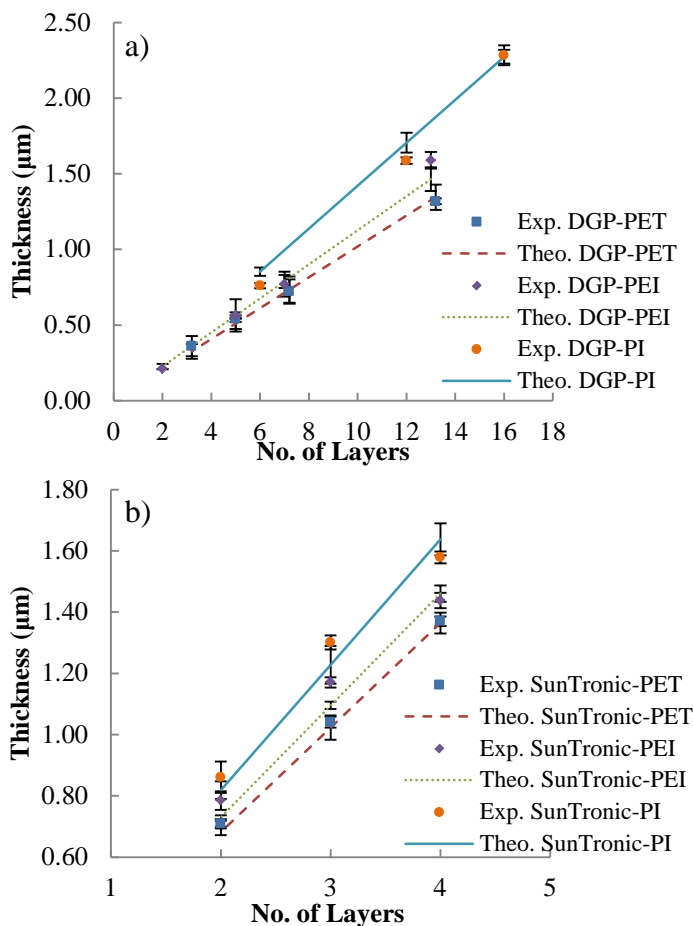


Figure 12. Thickness of DGP (a) and SunTronic (b) patterns as a function of the number of printed layers. Experimental and modeled data are shown.

from five different specimens and their standard deviations. We have applied the above model (Eq.7) for the theoretical estimation of the thickness of the inkjet printed patterns.

Table 5. Experimental results from the physical characterization of printed patterns with different inks, substrates and printing techniques.

Substrates		Thickness (μm)	RMS Roughness
PI		130.0	86.7 nm
PET		100.0	26.8 nm
PEI		130.0	22.1 nm
Inkjet patterns	Layers	Thickness (μm)	RMS Roughness
DGP / PI (160°/30 min)	6	0.76 \pm 0.02	
	12	1.58 \pm 0.02	
	16	2.28 \pm 0.06	
DGP / PET (160°/30 min)	2	0.36 \pm 0.02	32.5 nm
	5	0.54 \pm 0.07	–
	7	0.72 \pm 0.08	43.9 nm
DGP / PEI (160°/30 min)	13	1.32 \pm 0.02	46.0 nm
	2	0.21 \pm 0.01	
	5	0.56 \pm 0.09	
Suntronic / PI (160°/60 min)	7	0.77 \pm 0.08	
	13	1.59 \pm 0.05	
	2	0.86 \pm 0.05	63.3 nm
Suntronic / PET (160°/60 min)	3	1.30 \pm 0.02	76.6 nm
	4	1.51 \pm 0.03	81.2 nm
	2	0.71 \pm 0.09	
Suntronic / PEI (160°/60 min)	3	1.04 \pm 0.02	
	4	1.37 \pm 0.02	
	2	0.78 \pm 0.03	
Suntronic / PEI (160°/60 min)	3	1.17 \pm 0.02	
	4	1.43 \pm 0.03	

The comparison between the experimental data (symbols) and the model results (line) is displayed in Figure 12a for the DGP ink, showing a very good agreement. The error bars in the theoretical thickness come from the standard deviation of the measured width W . This model provided very good agreement with experiments, making it a very useful tool. The jetted drop has a volume of $V_D = 10$ pL and according with the ink supplier, the mass fraction of silver in the ink is $\chi_{Ag} = 0.3$ -0.35 and the solvent is triethylene glycol monoethyl ether (TGME) based. TGME's density is $\rho_S \approx 1$ g/cm³. Finally, ρ_{Ag} can be taken as the silver bulk density 10.49 g/cm³ as a first approximation. Due to the different meandered pattern widths measured on the different substrates, the estimated thickness obtained is different for each substrate. In order to fit the experimental and the theoretical results, the solid content of Ag has been used as the only fitting parameter, resulting in 0.35

for the three substrates. Despite the different assumptions and approximations taken when introducing the numerical values (mainly bulk silver density instead of porous inkjet printed one and lack of exact composition of the ink), the experiments fit well the theoretical prediction.

In an analogous way, the content solid for SunTronic provided by the manufacturer is 20% and the solvent is ethylene glycol with a density of $\rho_s \approx 1.11 \text{ g/cm}^3$. The best fit of the solid ratio on silver for the SunTronic ink is goes from 0.17 to 0.18 (see Figure 12b). In addition, experimental DC measurements of the resistivity and sheet resistance as a function of the thickness of inkjet patterns are shown in Figure 13. The resistivity has been calculated from the expression $R=\rho L/Wt$, being ρ the resistivity, R the measured resistance, W the measured width line, L the length line and t the

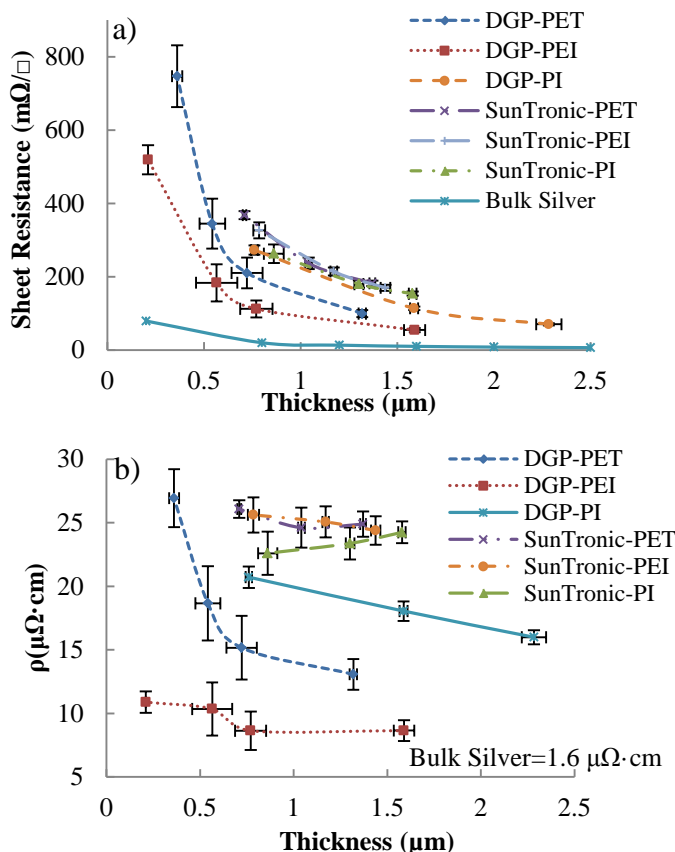


Figure 13. Sheet resistances (a) and resistivity (b) of inkjetted patterns as a function of thickness for different conductive inks and substrates. Lines are only eye guides.

measured thickness line. The sheet resistance, R_{\square} , is derived from $R_{\square}=\rho/t$. Bulk silver resistivity and sheet resistance has been included on the graphs for comparative purposes. The obtained resistivity for DGP ink is around 8 times the bulk silver resistivity (9-15 $\mu\Omega\cdot\text{cm}$ vs. 1.6 $\mu\Omega\cdot\text{cm}$) depending on the substrate. These results are in good agreement with the resistivity of 11-12 $\mu\Omega\cdot\text{cm}$ indicated on the ink manufacturer datasheet. Similarly, SunTronic ink offers a resistivity of around 15 times the bulk silver (24-25 $\mu\Omega\cdot\text{cm}$ vs. 1.6 $\mu\Omega\cdot\text{cm}$) whereas the manufacturer given resistivity ranges from 5 to 30 $\mu\Omega\cdot\text{cm}$ on their datasheet. Both, the sheet resistance and the electrical resistivity increase when the thickness for the printed lines decrease, as depicted in Figure 13. The behavior of the sheet resistance was expected considering that $R_{\square}=\rho/t$ (see in Figure 13a). Regarding the electrical resistivity ρ , printed silver presents higher porosity and smaller grain size than bulk silver. As a consequence, the electrons scatter more at the grain boundaries of printed silver than on bulk silver and a higher resistivity is generally observed (Jung et al. 2007, Kim et al. 2010b, Merilampi et al. 2009). Moreover, it is known that the resistivity depends only on the material if no boundaries exist at distances comparable to the mean free path of the electrons in the material. In the case of bulk silver, the electrons mean free path is ~ 53 nm. Hence, an increase in the resistivity is observed in silver films thinner than 300 nm due to significant extra scattering of electrons on the surface of the lines (Artunc, Bilge and Utlü 2007, Lacy 2011, Sondheimer 2001, Zhang et al. 2004). However, according to Figure 13b, the increase of resistivity in DGP ink lines is observed when their average thickness falls below 500 nm. The reason for that mismatch is that the thickness of printed lines is not totally homogeneous along the whole pattern. If one takes into account the standard deviation of the thickness and the RMS roughness of the line surface (see Table 5), some zones are only ~ 300 nm-thick for an average thickness of 500 nm.

2.2.2 Geometrical and Electrical of Screen Printed patterns

Regarding measurements of the patterns obtained by screen printing, the results of the geometrical characterization, resistivity and sheet resistance are presented in Table 6 for two substrates, PI and PET, and the different

analyzed meshes. Data are from eleven replicas and their variation is given by the standard deviation. No influence on the direction of the patterns has been observed. The images of screen printed lines for different meshes are displayed in Figure 14a and b, presenting the lowest roughness for the 140 T/cm mesh. This is also pointed out in the lowest standard deviation data of the thicknesses showed in Table 6. Measured resistivity ranges from 40 to 50 $\mu\Omega\cdot\text{cm}$ depending on mesh densities and are in concordance with the resistivity indicated by the manufacturer, 25-50 $\mu\Omega\cdot\text{cm}$.

Table 6. Experimental results from the characterization screen printed patterns.

Substrate	Mesh density (T/cm)	Thickness (μm)	RMS Roughness	Resistivity ($\mu\Omega\cdot\text{cm}$)
PI	43	30.0 \pm 3.0	7.75 μm	50 \pm 2
	90	19.0 \pm 1.0	4.58 μm	44 \pm 7
	140	9.3 \pm 0.2	1.61 μm	39 \pm 4
PET	43	29.0 \pm 4.1	-	46 \pm 2
	90	17.0 \pm 2.2	-	41 \pm 4
	140	8.9 \pm 0.5	-	39 \pm 3

Table 7. Experimental results from the characterization screen printed patterns.

Width Layout (μm)	Mesh 90 T/cm		Mesh 140 T/cm	
	Min. (μm)	Max. (μm)	Min. (μm)	Max. (μm)
1000	970	990	980	990
900	860	880	880	890
800	760	780	790	800
700	660	690	680	690
600	530	600	580	600
500	410	500	470	490
400	280	380	370	400
300	180	270	-	-
200	-	-	-	-

The minimum width achieved by screen printing is shown in Table 7 for two mesh densities. This work was carried out for 140 T/cm and 90 T/cm mesh densities with horizontal and vertical lines (see Figure 9b), 43 T/cm mesh density was not used due to the poor resolution obtained on the preliminary test. The study of the pattern geometry showed a “saw tooth” effect on the edge of the printed lines. This effect could be caused by the mismatch between mesh threads and pattern orientation as illustrated in Figure 14c,

where this effect is represented through a solid line outlined over a sketch of the screen printing mesh.

The misalignment between test line direction and screen mesh threads orientation causes that the ideally straight lines present a variable width along the whole line length. This width ranges from the minimum to the maximum values that are presented in Table 7. As the line width to be transferred becomes smaller, the “saw tooth” effect increases yielding more irregular edges. For each mesh density, we highlighted the minimum line width related to a “saw tooth” size smaller than 5% of the real printed width (see bold font in Table 7). Those dimensions are 800 μm for 90 (T/cm) mesh density and 600 μm for 140 (T/cm). There is a minimum width, 400 μm for 90 (T/cm) and 300 μm for 140 (T/cm) meshes, under which the lines are no longer continuous due to this “saw tooth” effect.

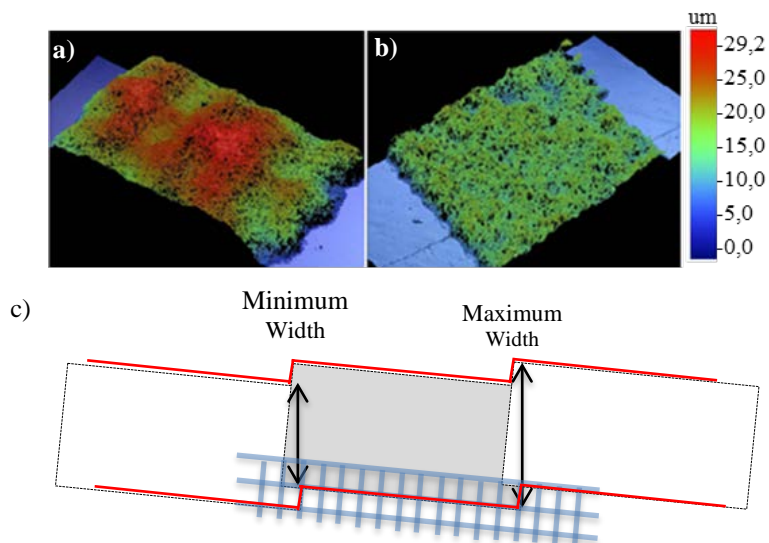


Figure 14. Microphotographs of screen printed lines with a mesh of 43 T/cm (a) and 140 T/cm (b). (c) The “saw tooth” effect (solid line) and the measured geometrical parameters: minimum and maximum width. The screen printing mesh is also outlined to explain this effect.

Furthermore, contrary to the inkjet printed patterns, the real width of the screen printed lines is always smaller than the designed one, as shown in Table 7, and the mismatch increases with decreasing the line width. This effect is linked to the nature of the fabrication process for the photosensitive emulsion mask. During the development step the non-exposed part of the

photosensitive emulsion dries slightly at the edges before is removed. Nevertheless, screen printed patterns also presented worse resolution, more irregular edge profiles and higher RMS roughness than inkjet printed patterns.

2.2.3 RF Simulation and Characterization

The electrical response of the CPWs transmission lines corresponding to the different combinations of inks and substrates have been used to compare their RF loss. As previously explained in the section on simulation, for each combination of substrate and ink, the width of the central conductor has been calculated to get the desired 50 Ohms characteristic impedance fixing the gap at 150 μm with the Line Calculator tool of ADS simulator. Table 8 shows the obtained dimensions for each case. A detail of the inter-spacing gap can be appreciated in Figure 11b where the ground plane and inner conductor have been also labeled. In the case of FR-4 substrate the width of inner conductor is fixed to 5 mm and Line Calculator tool is used to calculate the gap that is 650 μm as can be seen in Figure 11a.

Table 8. Coplanar waveguide dimensions for the printed transmission lines.

Calculated width central conductor (mm) for CPW's transmission lines			
Substrate	Screen printing 140 T/cm 9.30 μm thick	Inkjet SunTronic 2 layers-0.77 μm thick	Inkjet DGP 6 layers-0.85 μm thick
PEI	5.596	6.412	6.366
PI	5.151	6.277	5.790
PET	6.609	6.998	6.664

Table 9. Measured transmission parameters of the coplanar waveguides at 13.56 MHz (HF band) and 868 MHz (UHF band) frequencies.

Transmission loss parameter (dB/mm) for CPW's transmission lines				
Frequency	Substrate	Screen printing 140 T/cm 9.30 μm thick	Inkjet SunTronic U5603 2 layers-0.77 μm thick	Inkjet DGP ANP 6 layers-0.85 μm thick
High frequency band (HF) (13.56 MHz)	PEI	0.0016 \pm 0.0012	0.0022 \pm 0.0012	0.0036 \pm 0.0012
	PI	0.0016 \pm 0.0012	0.0025 \pm 0.0012	0.0051 \pm 0.0012
	PET	0.0018 \pm 0.0012	0.0029 \pm 0.0012	0.0072 \pm 0.0012
Ultra high frequency	PEI	0.0100 \pm 0.0014	0.0130 \pm 0.0014	0.0300 \pm 0.0014
	PI	0.0100 \pm 0.0014	0.0190 \pm 0.0014	0.0340 \pm 0.0014

band (UHF) (868 MHz)	PET	0.0130±0.0014	0.0200±0.0014	0.0400±0.0014
-------------------------	-----	---------------	---------------	---------------

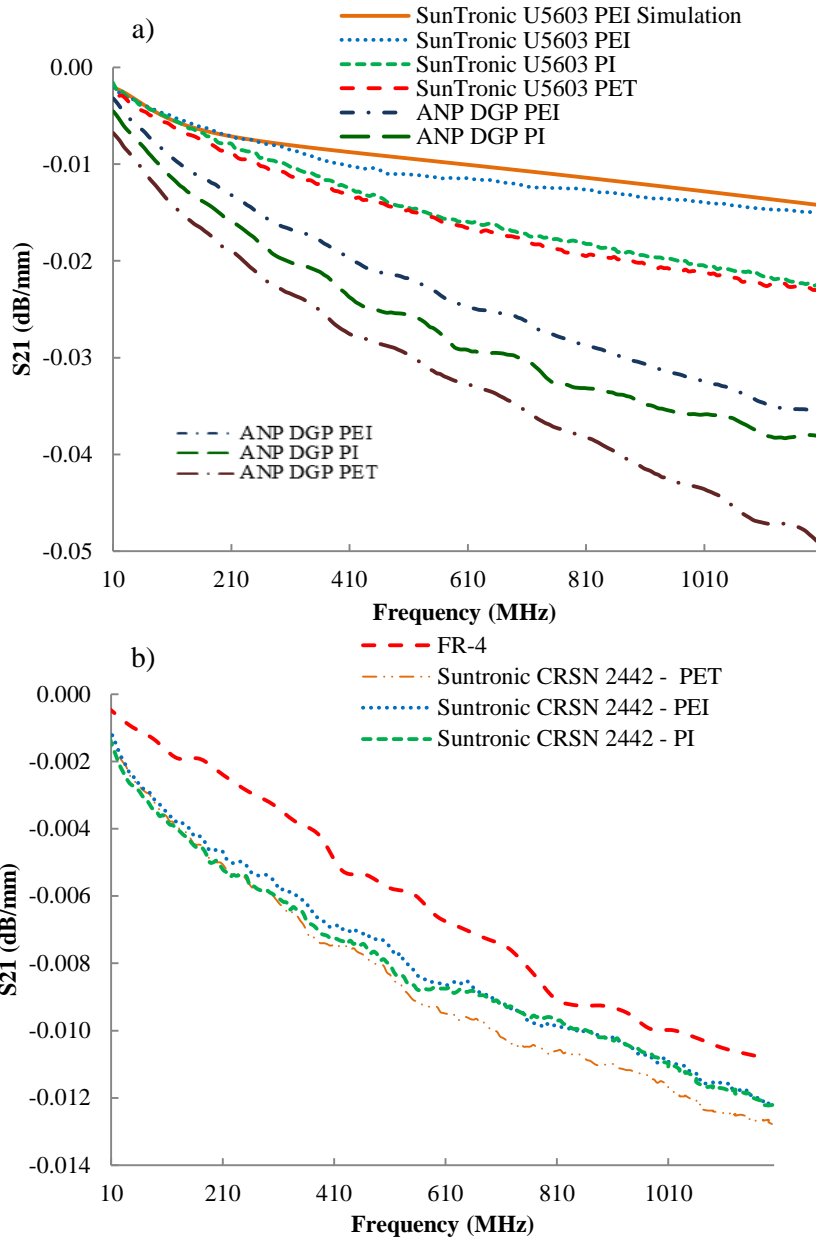


Figure 15. Measured frequency response of the transmission parameter S_{21} for inkjet printed coplanar waveguide with Anapro DGP and Suntronic U5603 silver inks (a) and screen printed coplanar waveguide with Suntronic CRSN 2442 silver ink and FR-4 (b).

Figure 15 illustrates the frequency response for inkjetted and screen printed CPWs. The transmission parameter S_{21} is presented per length unit combining the 2.0 cm and 4.0 cm transmission lines response. Table 9 shows the measured response at 13.56 MHz and 868 MHz corresponding to the HF and UHF RFID frequencies bands. On one hand, minimum transmission losses of 0.0022 ± 0.0012 dB/mm and 0.0016 ± 0.0012 dB/mm measured at HF band have been achieved by inkjet printing on PEI and screen printing on PI, respectively. On the other hand, those minimum values are 0.0130 ± 0.0014 dB/mm by inkjet printing on PEI and 0.0100 ± 0.0014 dB/mm by screen printing on PI at UHF band. The difference in the transmission losses at HF band is not statistically significant owing to the high data scatter (see Table 9). Therefore the comparison between patterns is more relevant at higher frequencies (UHF band). Simulation results obtained by ADS for the pair PEI/SunTronic ink are included in Figure 15 for comparison purposes showing good agreement with the experimental data. The decay of the obtained value for the S_{21} parameter as frequency rises is related to the loss phenomena. There are two types of losses in a transmission line: the dielectric substrate loss and the ohmic loss in the conductors due to the skin effect (Pozar 2009). The latter becomes more significant as the frequency increases and is normally larger than the former for the typical substrates thickness used in this work. Therefore, we could attribute the decay in S_{21} mainly to losses in the conductor. This behavior is fulfilled for all the lines at the measured frequency range. As expected, screen printed transmission lines present less loss than the inkjetted ones due to the thicker patterns achieved with this technique (see thickness of the fabricated transmission lines in Table 8). The transmission losses on each substrate present similar behavior on both inkjetted and screen printed transmission lines. The differences of losses among substrates can be associated to the dissipation factor presented in Table 1: PEI presents the smallest loss factor of 0.0010, compared to PI (0.0020) and PET (0.0024). As depicted in Figure 15a and Table 9, the lines printed with SunTronic ink exhibited better transmission parameter S_{21} than those printed with DGP ink for all the substrates, despite the fact that the measured DC conductivity was lower for the former. Apart from the DC conductivity of each metallization layer and substrate losses, there are two other main factors that play a role in RF performance: line thickness and printability, i.e., printing quality in terms of resolution, layout accuracy and

well-defined edges. A key parameter in inkjet printing printability is the deposited drop diameter. Smaller printed drops, as in the case of SunTronic ink, allow better resolution and permit the use of smaller drop-to-drop space, resulting in fewer printed layers and associated alignment errors to obtain the same line thickness. However, special care needs to be taken to ensure good substrate wettability with small ink droplets due to the smaller substrate affinity. Finally, fabricated FR-4 CPW lines shows minor losses than inkjetted or screen printing ones. By one hand, FR-4 substrate is 1.5 mm thick whilst the thin films employed on printed transmission lines are ~ 100 μm thick. By other side, copper conductivity and thickness are larger in this case than in printed lines. These results show that the ohmic loss associated with metallization layers characteristics are crucial role on performance for RF applications.

2.3 Conclusions

Geometrical and electrical, both DC and RF, characterization of inkjet and screen printed silver lines has been carried out on different plastic substrates for RF applications. A simple model to calculate the thickness of a metallic pattern printed by inkjet has been tested with our experimental measurements. This model provided very good agreement with experiments, making it a very useful tool. The obtained thickness for one single layer was 0.105-0.180 μm for DGP ink and 0.355-0.430 μm for SunTronic ink depending on the substrate utilized, PET, PI or PEI. Thicker inkjet printed patterns can be obtained by sequentially printing of several layers with no significant degradation of the surface area RMS roughness. DGP ink on PEI substrate provided the minimum result of DC resistivity, 8.6 ± 0.8 $\mu\Omega\cdot\text{cm}$, compared to the rest of the analyzed samples, although the best performance in terms of resolution and thickness per single layer was provided by SunTronic ink on PEI substrate with a DC resistivity of 24.4 ± 1.1 $\mu\Omega\cdot\text{cm}$. Moreover, an increase of resistivity has been observed for thinner patterns, probably due to a dominant contribution of the grain boundary scattering.

For screen printing, only one ink has been tested and the thickness and conductivity of the patterns have been measured as a function of the mesh density. Thickness patterns were 9.2 μm for 140 (T/cm), 19 μm for 90 (T/Cm) and 30 μm for 43 (T/Cm). Printing limits for screen printing were

found to be 800 μm for 90 (T/cm) mesh and 600 μm for 140 (T/cm) mesh. The minimum resistivity obtained was $39\pm 4 \mu\Omega\cdot\text{cm}$ on PI and PET substrates with 140 (T/cm) mesh. As expected, thicker patterns provides lower sheet resistances than the best cases of inkjet printing. Sheet resistances for screen printing were $15.0\pm 0.7 \text{ m}\Omega/\square$ for 43 (T/cm), $21\pm 2 \text{ m}\Omega/\square$ for 90 (T/cm) and $41\pm 4 \text{ m}\Omega/\square$ for 140 (T/cm), whereas in the case of inkjet printing the best achieved sheet resistances were $54\pm 6 \text{ m}\Omega/\square$ for twelve printed layers of DGP ink and $153\pm 8 \text{ m}\Omega/\square$ for four printed layers of SunTronic ink, both on PEI substrate. Nevertheless, screen printed patterns also presented worse resolution, more irregular edge profiles and higher RMS roughness than inkjet printed patterns.

Inkjet and screen printed coplanar waveguides have been fabricated to study the RF performances of the printed lines. The results demonstrate that for inkjet, SunTronic ink showed better RF performance than DGP ink for the three considered substrates due to its better printability. This fact showed that only DC characterization is not enough to ensure an adequate RF behavior. Substrate comparison showed similar behavior for RF losses in inkjet and screen printed transmission lines: PEI substrate is the best one followed by PI and PET. This result was in agreement with the manufacturer substrate information. The comparison of both techniques showed that PEI is the most suitable for inkjetted patterns and both PI and PEI are similar for screen printed patterns.

3. Design, numerical simulation and experimental characterization of RFID tags

Once that the physical and electrical characterization of the materials and techniques for RFID prototyping has been detailed in the previous chapter, we will use them to manufacture RFID tags. Therefore, this chapter covers the design, fabrication, measurement and validation of several RFID tags for two frequency bands: HF at 13.56 MHz and UHF at 868 MHz. Moreover, a novel methodology will be presented to perform impedance measurements of UHF RFID tags. This experimental procedure will present a better performance in comparison with previous methods. At this point, no sensing capability will be included in the tag design. These matters will be treated in following chapters.

3.1 Material and Methods

3.1.1 Fabrication process

The combinations of substrates and inks have been chosen according to the demonstrated best case in performances. For the screen printing technique, we used a Serfix III screen printing machine (Seglevint SL, Barcelona, Spain). The screens used to manufacture the antennas have a mesh density of 90 and 140 T/cm. All the patterns were printed on a polyimide substrate with 75 μm thickness (Kapton® HN, Dupont™, Wilmington, DE, USA) with SunTronic CRSN 2442 ink (Sun Chemical, New Jersey, USA). In the case of UHF antennas, a 120 thread per centimeter mesh was used to manufacture the single-layer screen printed tags that, according to our previous characterization process, the thickness is 13.3 μm and the resistivity $39 \pm 4 \mu\Omega\text{-cm}$.

For inkjet printing, a DMP-2831™ Dimatix printer (Fujifilm Dimatix Inc, Santa Clara, USA) was used for printing of patterns on PEI substrate. The used ink has a solid content of 20% of silver nanoparticles dispersed in

ethanol/ethanediol (U5603 SunTronic Technology, San Diego, USA). A drop-to-drop space of 25 μm was used for around 50 μm diameter landed drops. Sintering took place in two different stages; a ramping of the temperature from room temperature to 160 $^{\circ}\text{C}$ at 3 $^{\circ}\text{C}/\text{minute}$, followed by an hour at constant 180 $^{\circ}\text{C}$ temperature. For the UHF antennas, twelve layers were printed without intermediate curing for alignment improvement. According to the thickness model presented in chapter 2, the obtained thickness is $4.3 \pm 0.1 \mu\text{m}$ and the resistivity $8.6 \pm 0.8 \mu\Omega\cdot\text{cm}$.

A milling machine model S100 (LPKF Laser & Electronics AG, Garbsen, Germany) was employed for prototyping the antenna designs on FR-4 substrate. Placement and soldering of the chips were carried out using an infrared solder station model IR/PL 550 (Kurtz Holding GmbH & Co., Kreuzwertheim, Germany).

The three-step process to do the assembly of the chips and external components to the foil is illustrated in Figure 16. First a conductive resin, H20E (Epoxy Technology Inc., Billerica, United States), was used to make the interconnections between IC and silver pads. Double layer 50 μm - thick dry adhesive, AR Clear 8932 (Adhesives Research, Inc. Glen Rock, Pennsylvania, United States), has been placed on the bottom part of the chips to fix them to the substrate. The last step was heating up in an oven at 120 $^{\circ}\text{C}$ for 20 minutes to cure the conductive resin. Furthermore, the dry film adhesion improved with temperature so the heat treatment served also to fix better the chips to the substrate. The inner and outer ends of the coils have been connected through a small “bridge” manufactured by ink-jet printing

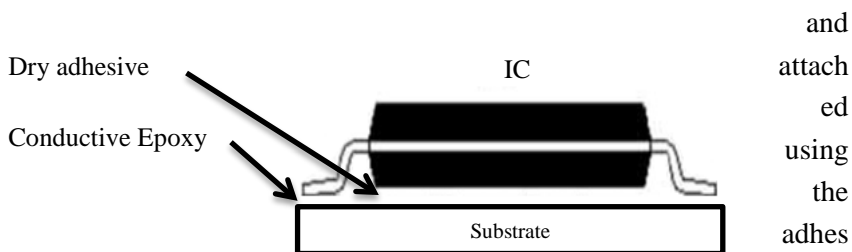


Figure 16. Illustration showing the chip assembly process.

y EPO-TEK H20E (Epoxy Technology, Inc., Billerica, USA).

3.1.2 Inkjet Printing Optimization

The main objective of this study is to obtain the optimal parameters to get well-defined profiles and smooth surfaces with inkjet printing technology. Printing antennas involve two main challenges: optimizing printing for narrow lines (width in a range of 25-50 μm until 1 mm) and optimizing printing for large surface. Narrow lines are commonly used in the matching networks, inductors and in the interconnections between the different integrated circuits, such as common PCB traces. Large surfaces are commonly printed for the antenna main radiator arms on modified dipole antennas.

The test pattern, Figure 17, is composed by two narrow lines of 200 μm and 600 μm of width with a length of 1 mm. For large surface study, two squares of 1 mm and 3 mm respectively were printed.

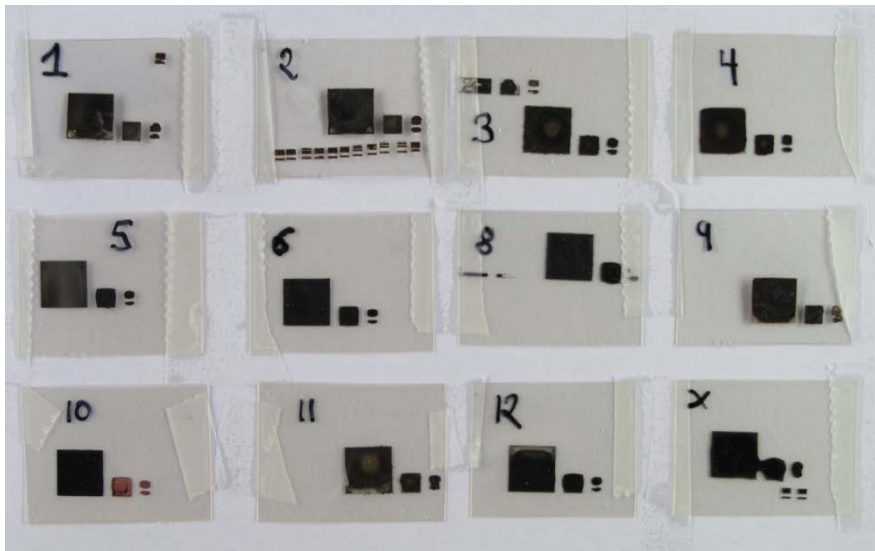


Figure 17. Patterns for printing optimization study.

The entire patterns were printed with 3 layers in case of Suntronic to get around 1 μm of thickness. The drop-space was fixed at the half of the drop diameter, being this 25 μm for Suntronic ink. PEI substrate was chosen due to his best printability. Dimatix printer plate temperature was fixed at room temperature to avoid fast evaporation of the solvent during the printing. Several patterns were printed changing the following parameters:

- Two types of sintering:
 - Constant temperature 180°C for 1 hour in air.
 - Room temperature (25°C) until 180°C for 1 hour with ramp of 3°C/min plus 1 hour at constant temperature of 180 °C in air.

Number of injectors: only 1 injector; 3 injectors or combination of both (1/3/1 for Suntronic ink).

3.1.3 High Frequency Band (13.56 MHz) RFID tags

¡Error! No se encuentra el origen de la referencia. shows a simplified diagram of a HF RFID system. The coil antenna in the RFID reader communicates with the coil antenna in the RFID tag; these are electromagnetically coupled. The RFID reader plays the same role as the primary of a voltage transformer that powers the secondary. The energy transfer ratio from the reader to the tag is similar to the coupling factor of a voltage transformer. It is a function of:

- how well the RFID tag and its antenna are tuned to carrier frequency
- the distance between the reader and the tag
- the reader power
- the tag antenna orientation related to the reader antenna

Basically, an RFID tag consists of an L-C-R circuit, where “L” stands for a loop antenna, “C” for a chip capacitor, and “R” for the IC chip resistance and parasitic loop antenna resistance. The tag fabrication process involves printing or otherwise forming a loop antenna on the substrate and subsequently placing an IC chip and optionally a matching chip capacitor on the same tag. When the inductive impedance is equal to the capacitive impedance the antenna will be at resonance. The resonant frequency of the LCR tank circuit must be tuned to 13.56 MHz to communicate well with a RFID reader.

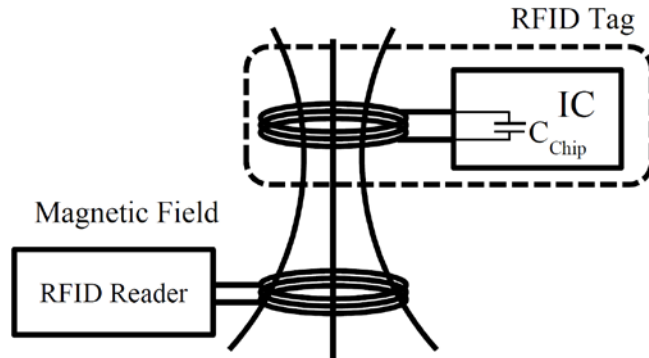


Figure 18. Diagram showing the coupling mechanism on RFID HF band (13.56 MHz).

Two possible models of LCR resonators are shown in Figure 19, differentiated on parasitic resistance placement respect to the loop inductor: series resistance or in shunt configuration. The ideal LC resonator has a negligible parasitic resistance and therefore these two models will be similar (series resistances will be short-circuit and parallel resistance will be an open circuit). In this ideally conditions, since we know the equations for determining the reactance of each element, Equation 8 at a given frequency, and we look for that point where the two reactances are equal to each other, we can set the two reactance formula equal to each other and solve for frequency algebraically:

$$X_L = 2\pi fL \quad X_C = \frac{1}{2\pi fC} \quad (8)$$

Setting the two reactances equal to each other and representing a condition of equal reactance (resonance), we obtain the resonant frequency of a tank circuit, given the values of inductance (L) in Henrys and capacitance (C) in Farads.

$$f_o = \frac{1}{2\pi\sqrt{LC}} \quad (9)$$

But an RFID inductor in our case is essentially just a PCB trace on planar structure comprising several loops whose resistance cannot be non-negligible. Therefore, the LC resonator circuit should include this parasitic resistance, as shown in Figure 19.

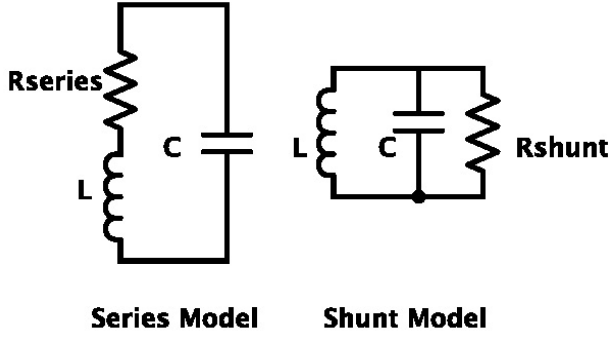


Figure 19. Non-ideal LC resonator schematics.

In order to ease calculations, we work in admittance mode. Let's remember that admittance is the inverse value of impedance. The associated impedance of the LCR series model is presented in Equation 10. In this case, we do not have only reactance parts but also a resistance part in resonance frequency. In order to find the resonance frequency of this circuit, the imaginary parts of the global impedance should be zero.

$$Z_L = R + j2\pi fL \text{ and } Z_C = \frac{1}{j2\pi fC} \quad (10)$$

$$Y_T = j2\pi fC + \frac{1}{R + j2\pi fL} = j2\pi fC + \frac{R - j2\pi fL}{R^2 + (2\pi fL)^2} \quad (11)$$

$$Y_T = \frac{R}{R^2 + (2\pi fL)^2} + j2\pi f \left(C - \frac{L}{R^2 + (2\pi fL)^2} \right) \quad (12)$$

Therefore, if we cancel the imaginary part of Eq. (12)

$$2\pi f_o \left(C - \frac{L}{R^2 + (2\pi f_o L)^2} \right) = 0 \quad (13)$$

Solving for f and simplifying, we obtain the resonant frequency of a tank circuit.

$$f_o = \frac{1}{2\pi} \sqrt{\frac{1}{LC} - \frac{R^2}{L^2}} \quad (14)$$

In non-ideal circuit, we can define the quality factor as the relationship between the maximum stored energy and the dissipated energy in each cycle in the circuit. Taking into account that the energy stored in the capacitor is equal to the energy stored in the inductor at resonance frequency,

$$Q_S = 2\pi \frac{\frac{1}{2}I^2L}{T\frac{1}{2}I^2R} = 2\pi \frac{L}{R}f_o \quad (15)$$

In this case of the shunt LCR circuit, resolution is direct and given by:

$$Y_T = \frac{1}{R} + j2\pi fC + \frac{1}{j2\pi fL} \quad (16)$$

$$f_o = \frac{1}{2\pi} \sqrt{\frac{1}{LC}} \quad (17)$$

$$Q_P = \frac{R}{2\pi f_o L} \quad (18)$$

In general, the higher the Q, the higher the power output for a particular sized antenna. Unfortunately, too high a Q may conflict with the band-pass characteristics of the reader due the protocol specifications, see Figure 20. In RF mode using the ISO15693 protocol, the RFID chip is accessed via a 13.56 MHz carrier electromagnetic wave on which incoming data are demodulated from the received amplitude-modulated signal. Typically, data communications use ASK modulation that generates sub-carrier signals at symmetric frequencies from the carrier signal. The sharpness of resonance (communication bandwidth) is determined by the Q value of the loop antenna. An excessively high sharpness of resonance makes communications difficult when the modulation signal bandwidth is wide; on the other hand, an excessively low sharpness of resonance results in worsened communication distance characteristics.

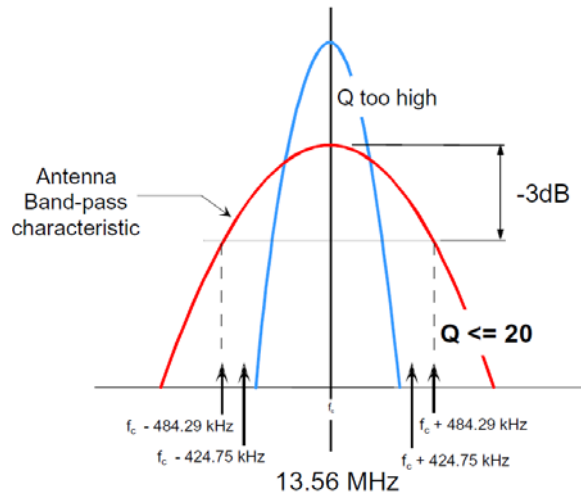


Figure 20. Antenna band-pass characteristic showing how a high value quality factor can cause conflict with the sub-carrier signals generated by the RFID protocol.

As can be seen from the equations, the relative values of the inductance (L) and capacitance (C) are interrelated. For the working frequency of 13.56 MHz frequency though, if the antennas are made too large, the inductance rises to a point where very small capacitor values are required. Once the inductance exceeds $5 \mu\text{H}$, capacitance matching becomes problematic due to required capacitance values in order of the parasitic capacitances.

An M24LR64 (STMicroelectronics, Geneva, Switzerland) was selected as the RFID chip. It has a capacitance of approximately 30 pF at $f_0 = 13.56$ MHz. Without including the parasitic resistance, a value of $4.6 \mu\text{H}$ for the coil antenna must be achieved to enable resonance at the desired frequency without including external matching capacitance.

Coil antennas have been simulated using the Advanced Design System (ADS) software (Agilent Technologies, Santa Clara, CA, USA) based on momentum method. Figure 21 shows the structure introduced on the EM simulator whose parameters were taken from the characterization process on chapter 2.

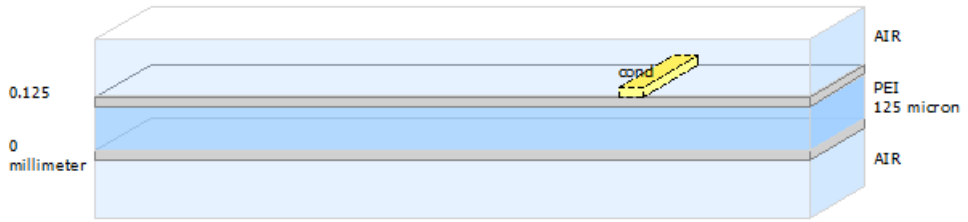


Figure 21. Definition of the structure for ADS simulator. Blue layer is the substrate, defining relative permittivity, thickness and loss tangent (frequency dependent). Yellow layer represents the deposited silver ink, defining thickness and conductivity.

The starting point to design the coil antennas has been taken from (Mohan et al. 1999). The inductance of a square antenna is given by

$$L_{ant} = 2.34\mu_0 N^2 \frac{d}{1 + 2.75p} \quad (1)$$

where $d = \frac{d_{out} - d_{in}}{2}$ and $p = \frac{d_{out} - d_{in}}{d_{out} + d_{in}}$. The outer diameter is d_{out} , the inner diameter is d_{in} , both in millimeters; N is the number of turns, $\mu_0 = 4\pi 10^{-7}$ H/m, L is measured in Henry.

Figure 22 shows the typical frequency response of a real inductance. There is an effective range of operation but, as frequency rises, the effect of parasitic resistance and capacitance increases leading to the coil inductor behaves like a capacitor. These two different regions are separated by the Self Resonant Frequency (SFR), where the inductive and capacitive behaviors of the coil inductor are equal. In our case, these preliminary geometrical parameters were introduced in the simulator. Optimization process was carried out for each fabrication technique (milling on FR-4, inkjet printing and screen printing) to maximize the quality factor taking care of getting the desired value of inductance at the working frequency of 13.56 MHz.

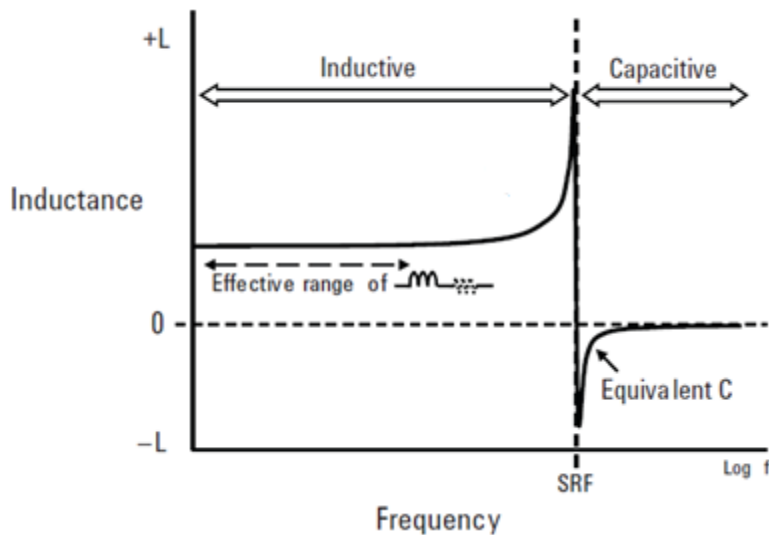


Figure 22. Inductor frequency response showing the effective range of operation and the self-resonant frequency.

The AC electrical characterization for the different fabricated antennas and tags has been performed by measuring their impedance, both magnitude and phase, using the four-wire measurement technique with a precision Impedance Analyser 4294A and an impedance probe kit (4294A1) (Agilent Tech., Santa Clara, CA, USA) that is able to perform in-circuit measurements. The excitation voltage applied in all measurements was $V_{DC} = 0$ and $V_{AC} = 500$ mV from 5 MHz to 40 MHz. After testing each antenna, you can use a probe to measure the resonance characteristics of the entire RFID tag complete with all its components. RFID tag tests were carried out using a commercial RFID reader compatible with ISO 15693, HF TRF7960 (Texas Instruments). The RFID reader power up and drives the tags using ISO15693 commands.

3.1.4 Ultra High Frequency Band RFID tags

An UHF RFID system operates on the frequency band of 860-960 MHz and it is typically composed by an RFID reader radiating an electromagnetic field (EM) and several tags. When the tags are on the vicinity of a RFID reader, the antenna collects the energy from the reader and responds using a backscatter mechanism. In general terms, antennas for RFID tags are

modified dipoles manufactured on planar structures with a highly conductive material. According to the theory of communication in RFID systems (Rao, Nikitin and Lam 2005, Griffin and Durgin 2009), the maximum reading distance can be calculated using:

$$range_{max} = \frac{\lambda}{4\pi} \sqrt{\frac{G_{tag} G_{reader} P_{reader} \tau PLF}{S_{tag}}} \quad (51)$$

where S_{tag} is the RFID chip sensitivity; the minimum received power level to activate the tag. G_{tag} refers to the tag antenna gain. P_{reader} is the effective radiated power by the reader and G_{reader} is the reader antenna gain. In this aspect, two main factors play a role in RFID tags: antenna gain and impedance matching (Nikitin et al. 2005, Rao et al. 2005). The materials, size and geometry of the antenna determines its resonant frequency, gain and input impedance (Marrocco 2008). The τ is a factor that takes into account the losses related to mismatching between the chip and the antenna (Rao et al. 2005). Impedance matching refers to the loss of the received power due to the mismatching between chip and antenna impedances. For this reason, impedance matching severely affects the communication performance between the RFID reader and tags.

The experimental response of an antenna can be calculated through the power reflection coefficient, Γ_{ant} (Meys and Janssens 1998). It describes the quality of power matching between two complex impedances. The power reflection coefficient is defined as:

$$\Gamma_{ant} = \frac{Z_{ant} - Z_{chip}^*}{Z_{ant} + Z_{chip}} \quad (52)$$

being Z_{ant} the differential input impedance of the antenna and Z_{chip} the chip impedance measured at the antenna connections pads. At the frequency of interest the input impedance of the antenna must be complex conjugate of the chip impedance for maximum power transfer. In typical antenna applications, such as the antenna TV, the input impedance of the antenna must be a real value equal to the coaxial wire characteristic impedance used in the feed point of the antenna, normally 50 or 75 Ohms, so the antenna input impedance must be 50 or 75 Ohms too. But the UHF RFID chips has a very

large capacitive part on his input impedance due to the rectifier present at the connections antenna pads, so the main challenge is to design antennas with a large inductive part on his input impedance for getting the complex conjugate impedance of the RFID chip that will maximize the power transfer.

Advanced Design System (ADS) software (Agilent Technologies, Santa Clara, CA, USA) based on momentum method was used for numerical simulation of the antennas performance to get impedance matching with the used RFID chip. Momentum method has been proved to be a good tool for printed UHF RFID tag simulation (Virtanen et al. 2010c). Substrate and metallic layer properties must be precisely included for EM simulation. Substrate thickness, roughness and relative permittivity were set in the EM simulator according to the information provided by the manufacturer. Substrate loss was modeled using a frequency dependent model for the dissipation factor (Svensson and Dermer 2001). Ohmic loss on metallic layers was modeled setting a finite conductivity. Silver printed layers have lower conductivity than these of bulk silver. Conductivity and roughness of printed metallic layer were taken from chapter 2. Instead of setting FR-4 standards parameters, similar work than in chapter 2 was carried out to estimate finite conductivity of the FR-4 copper layer.

Full S-Parameter simulation were carried out from 0-2 GHz and a second span from 700-900 MHz was used to obtain a more detailed response at the RFID band of interest. Finally, the simulator is able to compute radiated far-fields and antenna characteristics (gain, directivity, efficiency among others) from the S-Parameter simulation.

The chosen RFID chip was SL900A (AMS AG, Unterpemstaetten, Austria). RFID chip characterization on both frequency and power level is mandatory for successful RFID tag design (Nikitin et al. 2009). Approximately, imaginary part of the UHF RFID chip impedances ranges from -100 to -400 Ω whilst the real part ranges from a few ohms until 100 Ω when evaluated at minimum operating level (Marrocco 2008). The RFID chip SL900A input impedance provided by the manufacturer is $31.1-j319 \Omega$. However, the fabrication technology involves a mounting capacitance, typically between 0.6-1 pF, thus the chip impedance should be measured using our own bonding process. The RFID chip input impedance (Figure 23) was measured

for all the substrates, FR-4, PI and PEI; and evaluated at the minimum operating power level of the RFID chip, -15 dBm. An Infinity RF probe of 800 μm -pitch (Cascade Microtech Inc, Oregon, USA) was used in conjunction with a PM5 probe station (Cascade Microtech Inc, Oregon, USA). The E5071C Vector Network Analyzer (VNA) (Agilent Tech., Santa Clara, CA, USA) was utilized to check the single-ended input impedance, see Figure 24. A commercial Impedance Substrate Standard (ISS) provided by the RF probe manufacturer was used for calibration purposes. Measured input impedance was $35.4 - j286 \Omega$ for the RFID chip bonded on FR-4 substrate whilst impedance shifted to $29.8 - j226 \Omega$ on PI substrate. Thickness of FR-4 substrate, 1.5 mm, is larger than PI substrate, 150 μm , leading to a different mounting capacitance that explains this difference. No differences on the mounting capacitance were detected for PEI and PI foils. The substrate influence could be negligible at this frequency due to the similar thickness and relative permittivity of both substrates. Therefore, an antenna resonating at 868 MHz with a differential input impedance of $35.4 + j286 \Omega$ on FR-4 and $29.8 + j226 \Omega$ on PI must be designed to get the maximum power transfer and maximize the reading distance.

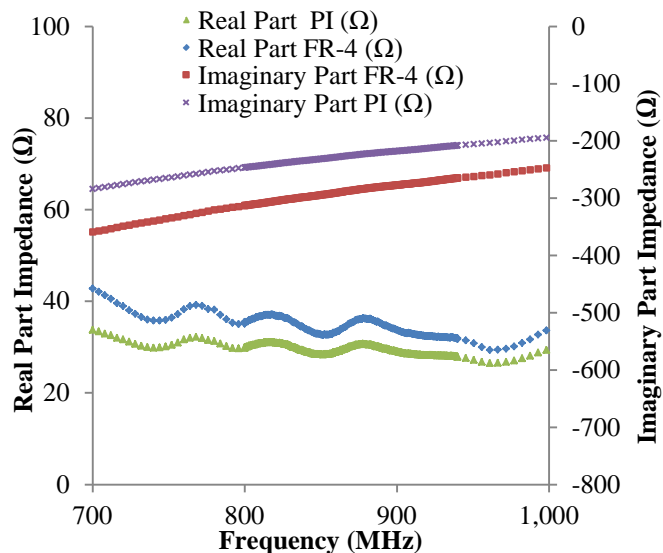


Figure 23. Measured chip impedances versus frequency evaluated at -15 dBm, minimum operating power level for the employed RFID chip. Results are displayed for the two substrates: 35 μm thick copper on 1.5 mm thick FR-4 substrate and 13 μm silver paste on 50 μm thick PI substrate.

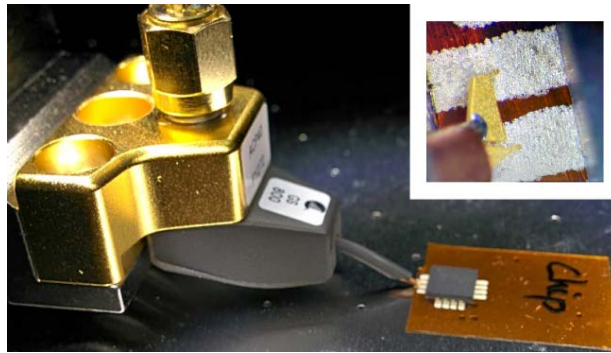


Figure 24. Input impedance RFID chip measurement showing the RF probe and, in-detail, the electrical contact of the 800 μm pitch point probes.

3.1.5 Comparison of fabrication techniques for UHF RFID tags

With the aim to make a comparison of fabrication techniques for prototyping RFID tags, we have benchmarked 4 different fabrication processes. Furthermore this comparison will validate the presented flow fabrication process. Screen and inkjet printing have been tested in the framework of this work. By other side, the other two benchmarked techniques are cutting plotter and solid ink based on flexible PCBs. These latter fabrication techniques have been carried out by the Department of Innovation Engineering of the University of Salento, Italy.

Screen and inkjet printed antennas has been manufactured on PI foil. In the case of screen printing, a mesh density of 120 T/m has been used. For inkjet printing, Suntronic ink has been used to print 20 layers without intermediate curing using the optimal conditions already reported for the sintering process. The number of 20 layers has been chosen to get a thickness comparable to the screen printed antennas.

Cutting Plotter refers to the process where a cutting plotter machine is used for cutting and shaping the antennas layout on an adhesive copper sheet 35 μm -thick. When the shape of the antenna is transferred to the flexible sheet, the extra adhesive copper can be removed manually. This technique is particularly time saving and does not need chemical agents to remove extra

copper. Achieved resolution is around $250\ \mu\text{m}$ and the copper layer presents fragility and low adhesion to the substrate (Catarinucci, Colella and Tarricone 2012).

Solid ink process used a DuPont flexible PCB composed by a foil polyamide with a copper clad laminate layer. Trying to avoid UV exposure process of traditional techniques, this process makes use of a special printer to deposit a wax-based mask on the substrate. The key parameter is this mask that prevents the protected copper from the acid-etching. Therefore, last step is an etching process using on Ferric Chloride to obtain the prototyped RFID tag (Catarinucci et al. 2012).

Two antennas design for the Monza 3 RFID chip (Impinj, Inc., Seattle, USA) has been addressed. The first one, see Figure 25, it is based on thin-propeller design proposed by chip manufacturer while the second one is a novel design denoted “basetta”. Both designs has been designed and optimized to operate at 868.8 MHz resonant frequency targeting RFID chip impedance of $34+j154$ with Computer Simulation Technology (CST) Simulator. In this case, a Perfect Electric Conductor layer has been used to modeling the metallization layer, in this sense we can check differences between prototyping techniques from an ideal model of the antenna.

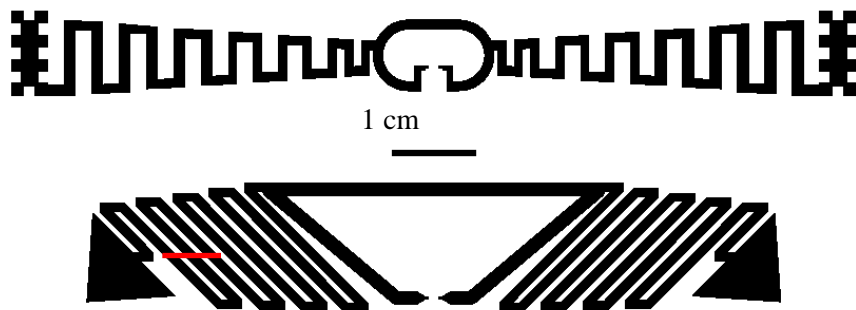


Figure 25. Layout of the (a) thin propeller design and (b) basetta design prototyped for fabrication techniques benchmarking. Red line indicates the studied line-thickness profiler through profilometer study.

The outcome of this study is 8 different RFID tags comprising two designs and four fabrication techniques. The thickness of the thin-propeller design has been measured for the set of fabricated tags along the red line depicted in Figure 25 with a Dektak XT™ Stimulus Surface Profiling System (Bruker Corporation, Coventry, UK).

Finally, the RFID tags were tested to check the maximum read range using a commercial RFID reader compatible with EPC Gen2, DK-UHF RFID HP2 (IDS Microchip AG, Wollerau, Switzerland). The devices were tested in an anechoic chamber attached to a foam structure. The RFID reader antenna patch antenna A0025 (Poynting antenna, Samrad, South Africa) was placed in a tripod at the same height.

3.2 Calibration method of UHF RFID tags

RFID antennas are typically balanced structures fed by a differential signal. S-parameter study can be used to obtain the differential input impedance (Meys and Janssens 1998). There are several methods to do that depending on single-port or two-port network configuration. In case of single-port measurement, two strategies can be employed: mirror theory and balun. According to mirror theory (Balanis 2012), placing one antenna arm above a big ground plane can be used to measure the input impedance. Differential input impedance is twice the measured one whereas accuracy relies on the size of the ground plane compared to antenna dimensions and calibration errors. On the other side, an external balun can be used to transform the unbalanced signal from single-ended port to balanced one. Accuracy relies on balun performance and calibration errors (Balanis 2012, Kuo, Chen and Lin 2008).

If two-port network model is used to evaluate the input impedance, mixed S-parameter mode can be used. The differential scattering matrix is obtained then from measurements using two single-ended ports (da Costa et al. 2013, Grosinger, Mecklenbräuker and Scholtz 2010, Hailong, Ko and Ye 2010, Kuo et al. 2008, Palmer and van Rooyen 2006, Qing, Goh and Chen 2009).

RFID chips usually are surface-mount devices (SMD) so standard connectors, e. g., Sub Miniature Version A (SMA) or coaxial connectors,

cannot be directly employed. A test fixture is normally employed to connect antenna feed point to VNA, see Figure 26. An accurate calibration technique is required to eliminate the impact of the test fixture on antenna measurements. Calibration kits provided by manufacturer only perform calibration until standard test cable. To take into account the impact of the test fixture on antenna measurement, a shift of the calibration plane until the antenna feed point is needed, see Fig. 24. Without regarding single-port or two port configuration, different strategies are followed to shift the calibration plane to antenna feeds point:

- De-embedding can be used to estimate the impact of the test fixture on the measurements. Accuracy relies on simulation of the test fixture. This technique requires post-processing of the measured data, so the result cannot be evaluated during the measurement (Hailong et al. 2010, Ning and Xiuping 2010, Palmer and van Rooyen 2006).
- Port extension can be applied; in this case one or two standards (open and/or short) are used to estimate directly the impact of the test fixture (da Costa et al. 2013, Hailong et al. 2010, Qing et al. 2009).
- Custom calibration kit can be used. It needs to fabricate 3 standards (Open-Short-Load) in case of single port-configuration and 4

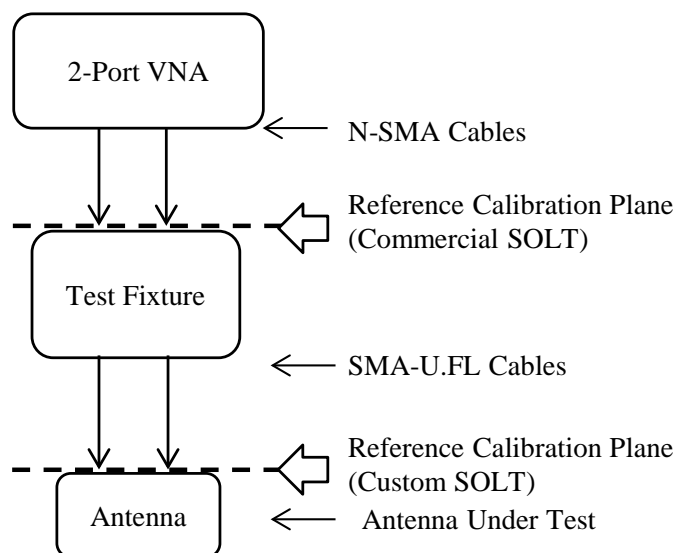


Figure 26. Diagram of the measurement setup for antenna impedance measurements showing the different connections and calibration planes.

standards in two-ports case, Short-Open-Load as single port calibration and Thru standard that estimate the direct connection between the two ports (Grosinger et al. 2010).

To sum up, previous works have probed that two-port network configuration minimizes the error compared to single-ended configuration (Kuo et al. 2008). Comparison between calibration techniques shows that de-embedding is the most accurate technique but needs extra-efforts as post-processing and accurate simulation/measurement of the test fixture. Port extension and custom calibration techniques can be directly applied, but needs the fabrication of the required standards: short and/or open and a full SOLT calibration kit, respectively. Finally, there are interesting studies showing how to verify the matching condition of chip-mounted RFID tags involving indirect measurements (Chen, Lin and Mittra 2010, Mats, Cain and Mickle 2009). However, these techniques are exclusively for RFID tags where other options can be virtually applied to any balanced device.

Here, we propose a direct method without data post-processing that uses two-port network to obtain differential S-parameter and, furthermore, it provides mechanical support to the RFID antennas. In this way, antenna impedance can be tested in different conditions, e.g., detuning when the antenna is attached to different surfaces.

Figure 27 shows the test fixture, the fabricated custom calibration kit and a picture of the measurement setup. The test fixture (Figure 27a) is composed

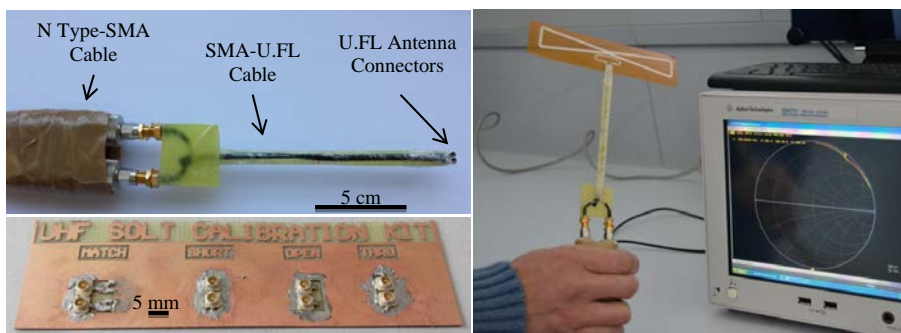


Figure 27. a) Picture of the differential test fixture showing the N-SMA adaptors, the SMA-U.FL interconnection cables and a straight arms dipole antenna. b) Picture of the custom calibration kit showing Short-Open-Load and Thru standards and c) Measurement setup showing the screen printed bow-tie antenna measurement and the smith chart representation on the VNA.

by two U.FL-SMA cables 150 mm length. These cables are attached to a rigid structure to avoid cable movement and provide mechanical support, see Figure 27c. SMA ends are connected to SMA-N type adaptors and finally two cables type N (N6314A from Agilent Technologies) were used to connect the test fixture to the VNA. Short, open, load (50 Ohms) and thru standards were fabricated using the U.FL connectors making up a Short-Open-Load-Thru (SOLT) calibration kit that enables performing full two ports calibration, see Figure 22. Ideal assumptions were taken into account to define the calibration kit on the VNA (lossless devices, zero-delay thru) (Technologies 2002). Trying to avoid the substrate influence, the standards were fabricated on 200 μ m-thick FR-4 substrate instead of 1.5 mm-thick FR-4 substrate employed on FR-4 antenna fabrication. For the load standard fabrication, two high precision RF resistors (Vishay Intertechnology Inc., Malvern, USA) were placed in parallel to get the 50 Ω and, in this way, reducing by half the parasitic inductance associated with SMD resistors. The measurement setup is shown in Figure 27c. Ultra Miniature Coaxial connectors (U.FL) type (Hirose Electric, Tokyo, Japan) were attached on the antenna feed point for characterization purposes, see Figure 36c. Antenna measurements were carried out through a Vector Network Analyzer (VNA), E5071C (Agilent Tech., Santa Clara, CA, USA). Due to the differential character of the measurement, S-parameter differential port between port-1 and port-2 was defined at the VNA through at test fixture. Another test fixture was used to transform the S-Parameter to Z-Parameters, showing the real and imaginary part of the input impedance of the antenna.

Finally, RFID tag tests were performed using a commercial RFID reader compatible with EPC Gen2, DK-UHF RFID HP2 (IDS Microchip AG, Wollerau, Switzerland). This RFID reader was used to check the maximum distance to detect and read out the manufactured RFID tags through a Visual Basic application running in a PC. Maximum reading range measurements took place on anechoic chamber, see Figure 28, the antenna reader was placed on a tripod whilst RFID tags were attached to a foam structure placed at the same height.



Figure 28. Measurement setup in an anechoic chamber to validate the proposed RFID system. The reader antenna can be seen on the tripod and the smart RFID tag can be observed attached to the foam structure.

3.3 Results and discussion

3.3.1 Inkjet Printig Optimization

The conclusions of the inkjet printing study show that the numbers of injectors are related with the definition of the samples. The edge profiles of narrow lines are greater in case of one injector, showing a smooth profile as straight lines. In the case of three injectors, the profile is more irregular, showing a noisily profile. The objective of the different combinations of injectors is to check if the change on injectors number in every layer gets better profiles due to the fact that the local errors of each injectors could be “corrected” between them, so the final profile were better in this case that in the case of three injectors. Unfortunately, the results are quite similar, so we can conclude that the best precision is obtained with only one injector but the disadvantage is a very large time for the whole printing, time that is roughly inversely proportional to the number of injectors used.

The sintering process is the key parameter to get smooth surface in both cases: narrow lines and large surfaces. Regarding the sintering process at constant temperature, the coffee ring effect appears in narrow lines owing to the abrupt change in temperature. In case of large surfaces, similar effect was observed forming craters as shown in Figure 29 (Derby 2010).

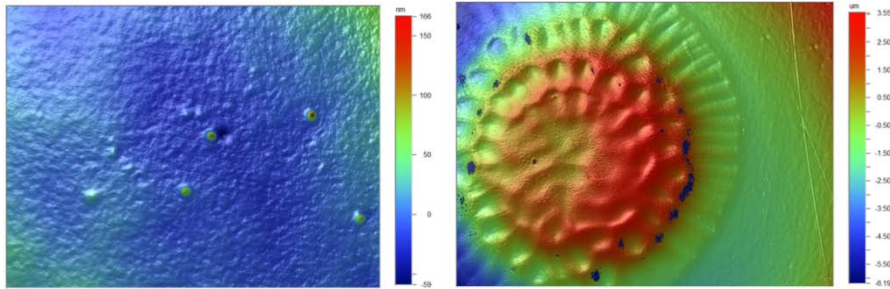


Figure 29. Images showing surfaces from the interferometry study. On the right side, Suntronic ink on PEI after sintering with a ramp temperature profile (RMS roughness=13.99 nm). On the left side, Suntronic ink on PEI substrate after sintering at constant temperature (RMS roughness=1.4 μm) after abrupt change.

The sintering process composed by two different steps (a slow ramp at the beginning until getting the maximum temperature for 1 hour followed by another hour of sintering at this maximum temperature) obtains smooth surface and well defined narrow lines without coffee-ring effect.

More parameters were tested, such as the delay between layers in which the printer wait a time, maximum 10 minutes, between the ending of one layer and the starting of the next one. Another interesting parameter is the plate temperature which could be fixed at 60°C as maximum value. These two parameters could be chosen to do an “inter-curing” between layers waiting, for example, 10 minutes at maximum temperature. The benefit of this curing process is to avoid ink accumulation that could lead to bad profile definition.

3.3.2 High Frequency Band Antennas

The layout of the final designs of the coil antennas for each technique can be seen in Figure 30. Pictures of the FR-4 fabricated prototypes are shown in Figure 31. The relevant dimensions and the number of turns (N) obtained after optimization process with EM simulation are those shown in Table 10.

Table 10. Calculated relevant dimension of the designed HF antenna.

Calculated relevant dimension of the designed inductors				
Design	Dimensions (mm)	Trace width (mm)	Gap (mm)	N
FR-4 (a)	75 x 45	0.6	0.6	6
FR-4 (b)	40 x 20	0.3	0.1	9
PI (Screen) (c)	75 x 45	0.6	0.6	6
PEI (Inkjet)(d)	77 x 49	0.9	0.3	6

There are two different designs for FR-4 substrate denoted as (a) and (b) on both Table 10 and Figure 30. The main difference between them is the overall size. In the smallest design (b) the gap and trace width are minor than those on design (a). Increasing the numbers of turns from 6 to 9 yields to obtain the desired inductance occupying just the half area. The drawback will be the lower quality factor due to higher resistance associated with the more turns and the minor path trace width.

Two different coil inductors for the HF band have been fabricated by screen, Figure 30c and inkjet printing, Figure 30d. Special care has been taken when designing the corners of the inductors. First, we designed round corners

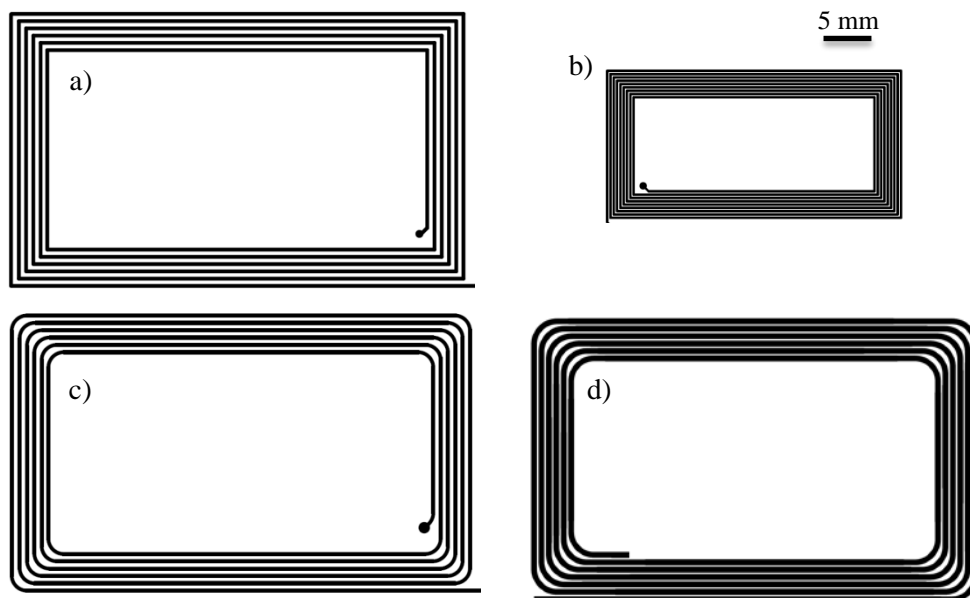


Figure 30. Layouts of the final antenna designs for milling on FR-4 substrate (a) (b), screen printing (c) and inkjet printing (d).

trying to minimize the equivalent resistance of the manufactured coil inductor. Second, the inter-spacing was increased on the corners to avoid short-circuits. In general, printing techniques present challenges when printing complicated layout such as 90 degrees junction and direction shifts.

The manufactured inkjet printed inductor included 6 turns of a 979 μm wide conductor with inter-spacing of 300 μm and a total surface area of 77.0 mm x 49.0 mm. The thickness was 1.57 μm , equivalent to 4 printed layers. Full frequency response until 50 MHz for the inkjetted printed inductor can be appreciated in Figure 32b. Simulated and measured values are in good agreement in a wide range close to the 13.56 MHz operating frequency, although differences appear as the frequency rises (see Figure 32).

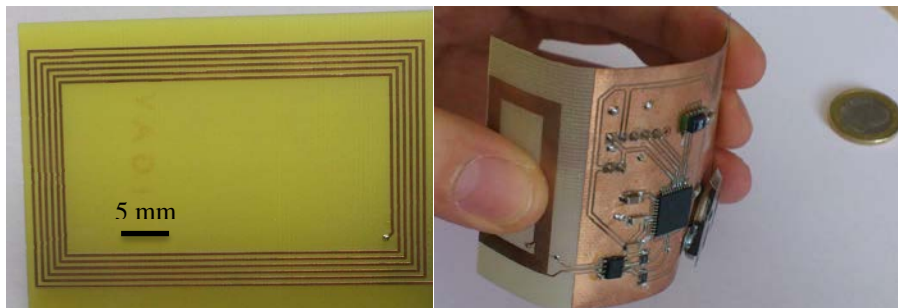


Figure 31. Pictures of the fabricated coil inductors on FR-4 substrate.

Screen printed inductors were manufactured on PI substrate. Sheet resistance,

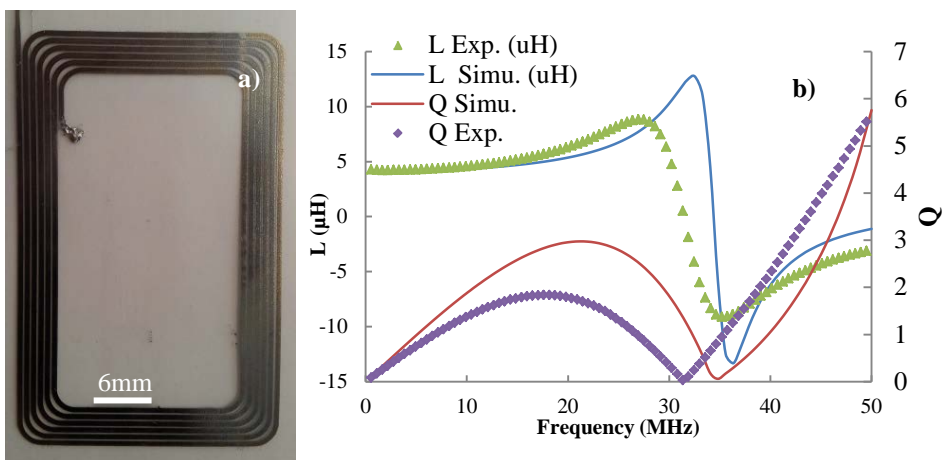


Figure 32. (a) Printed coil for 13.56 MHz RFID tag. (b) Simulated and measured frequency response of the 4 layers inkjet printed coil.

resistivity and RF performance of screen printed patterns were quite similar for PI and PEI substrates as shown Chapter 2. The reason to choose PI substrate over PEI is the better screen printability. Screen printed coil inductors with 6 turns and surface area of 75.0 mm x 45.0 mm have been fabricated using 90 (T/cm) and 140 (T/cm) mesh densities; their thickness, 9.32 μm in the case of 140 (T/cm) mesh density and 19.3 μm in the case of 90 (T/cm) mesh density, corresponded to one single layer. Both, the lines width and the inter-spacing between them, are 600 μm . Frequency responses of both antennas with different mesh can be observed on Figure 33.

Table 11 shows the simulated and measured values for the set of fabricated antennas at the frequency of interest. The data are obtained from measuring four specimens, taking the standard deviation as uncertainty.

Table 11. Simulated and measured inductance (L) and quality factor (Q) at 13.56 MHz.

Substrate	Technique	Simulation		Measurements	
		L (μH)	Q	L (μH)	Q
FR-4	Milling Design (a)	4.69	75.78	5.13 \pm 0.44	45.26 \pm 1.44
	Milling Design (b)	4.19	59.27	4.86 \pm 0.7	38.2 \pm 0.9
PI	Screen printing 90 T/cm	5.82	5.47	5.15 \pm 0.44	5.13 \pm 0.64
	Screen printing 140 T/cm	6.13	2.88	5.08 \pm 0.08	2.51 \pm 0.08
PEI	Inkjet printing	4.11	2.20	4.68 \pm 0.15	1.68 \pm 0.12

As shown in Table 11, screen printed inductors fabricated with lower mesh densities present better quality factor due to their higher thickness and corresponding lower sheet resistance. In this concrete case, the change from 140 (T/cm) to 90 (T/cm) mesh density led to an increment of the quality factor from 2.51 \pm 0.08 to 5.13 \pm 0.64 at 13.56 MHz.

Table 11 shows that the measured quality factor was lower than expected in all the cases. A similar behavior was observed on the inductance value. This mismatch could be explained by the reduction with frequency of the metallization layer conductivity. Moreover, the measured self-resonant frequency of the inductors, around 32 MHz, was slightly lower than the simulated one, around 35 MHz, as shown in Figure 32b.

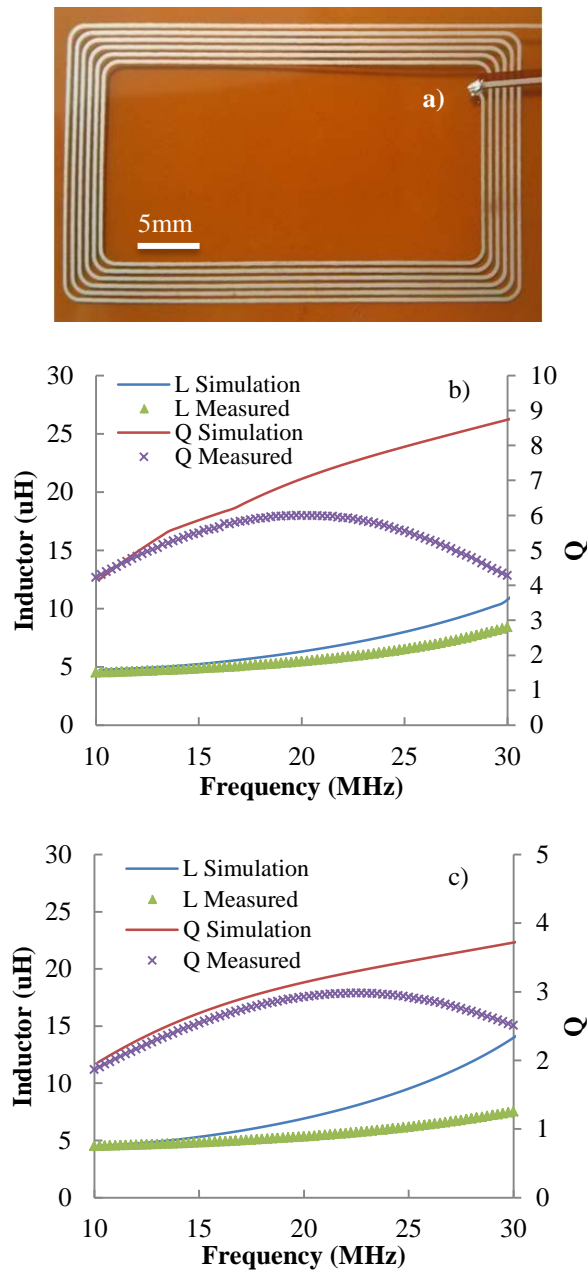


Figure 33. (a) Screen-printed coil for 13.56 MHz RFID tag. Simulated and measured frequency response of the screen printed coil with 90 T/cm (b) and 140 T/cm (c).

Analogous differences in the transmission parameter have already been pointed out in the CPW response on Chapter 2. The printing process introduced certain repeatability issues such as drops miss-placement, real

dimensions inaccuracy, different curing conditions, coffee ring effect, etc., (Derby 2010, Kim, Nogi and Suganuma 2012, Lee, Oh and Bae 2010, Singh et al. 2010) that can be the reason of the aforementioned differences between simulation and experimental measurements. In the case on FR-4 antennas, the aforementioned differences between simulated and measured could be attributed to an effective conductivity of the copper layer minor than those indicated by the manufacturer.

Operation of the antenna tags has been tested with the commercial RFID reader with a reading range of around 12.6 cm for big FR-4 design, 7.8 cm for small FR-4 design, 5.6 cm in the case of the screen printed inductor with 90 T/h mesh and 4.2 cm for the inkjetted antenna. The proper operation of the tags has been satisfactorily tested through the development of the Visual Basic application.

3.3.3 Ultra High Frequency Band Antennas

Our main contribution in this field has been to propose a novel procedure to calibrate tags by means impedance measurements. This methodology is presented in this section. With the aim of compare the proposed calibration setup, S-parameter measurements of the fabricated standards (Short, Open and Load) on the range 0- 2 GHz are shown on Figure 34.

Analogous differences in the transmission parameter have already been pointed out in the CPW response on Chapter 2. The printing process introduced certain repeatability issues such as drops miss-placement, real dimensions inaccuracy, different curing conditions, coffee ring effect, etc., (Derby 2010, Kim et al. 2012, Lee et al. 2010, Singh et al. 2010) that can be the reason of the aforementioned differences between simulation and experimental measurements. In the case on FR-4 antennas, the aforementioned differences between simulated and measured could be attributed to an effective conductivity of the copper layer minor than those indicated by the manufacturer.

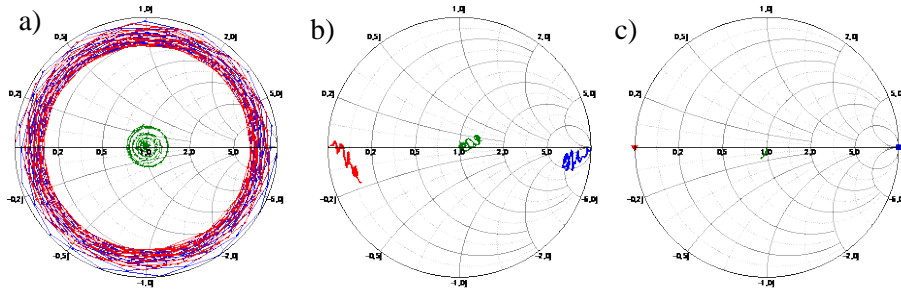


Figure 34. Smith chart representation showing the S-differential parameter measurement of the standards using the proposed test fixture. Short standard in red, load in green and open in blue. a) no-calibration b) port-extension calibration c) calibration proposed in this work.

Three smith charts representation are used to illustrate the effect of no calibration at all, Figure 34a, calibration using port-extension technique, Figure 34b and custom calibration presented in this work, Figure 34c. Ideally standards on smith chart should be “points” on the left position (short), center (load) and right (open). Before calibration, the frequency responses of the three standards are circles whose ratio changes as frequency rises. After port-extension is applied, standards responses are close to the ideal positions but they become more non-ideal as frequency rises. Performing the proposed calibration open and short standards are mostly concentrated on the left and right positions of the smith chart whilst load response is a narrow arc in the center.

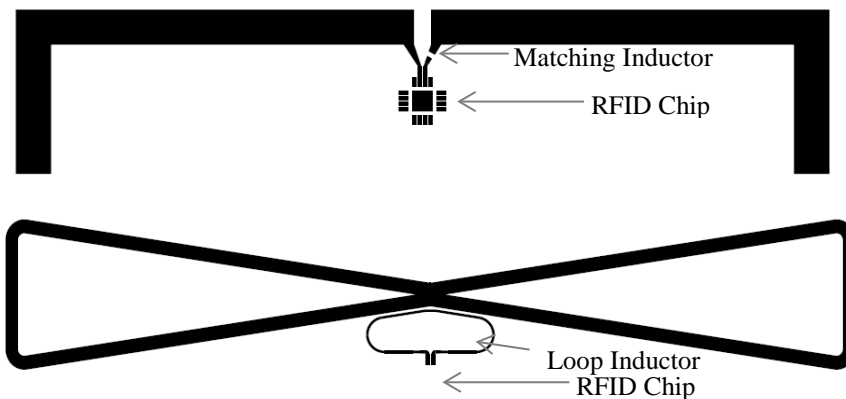


Figure 35. Schematic layout of the two proposed RFID Antennas for the UHF band.

Two types of antennas are characterized in this work, see Figure 35. Dipole antennas were chosen due to their almost omnidirectional 3D radiation. This characteristic provides the advantage that the RFID tag could be read almost in any relative position to the RFID reader. First, we present the typical dipole antenna based on the FR4 development kit designed and recommended for SL900A chip by the manufacturer (AG 2014). In this case, a RF Surface Mount Device (SMD) inductor is used to match the imaginary part of chip input impedance whilst the antenna is designed to get the same real part. Final dimensions of the FR-4 dipole antenna arms are 5.1 mm width and 70 mm length. In case of the screen printed dipole, antenna arms are 5.5 mm width and 79 mm length. Inkjet printing dipole have not been manufactured due to this concrete design involves large amount of ink and long printing times. Second, we propose an antenna design composed by a main radiator with a “bow-tie” shape in conjunction with a loop feed strategy. In order to minimize the amount of spent ink and printing time by inkjet fabrication, the “bow tie” antenna layout is designed with the two dipole arms having empty inner parts, see Figure 35. Loop matching networks are appropriated when the chip input impedance presents large absolute difference between real and imaginary part as in the present work. The desired impedance can be achieved taking into account that the loop size and shape have great influence on the imaginary part whereas the separating distance of the main radiator mainly controls the real part (Marrocco 2008).

Furthermore, including the matching network in the antennas' layout instead of using SMD inductors reduces the tag cost. The bow-tie antenna fabricated on FR-4 is 2 mm width, 118.2 mm long and 22.2 mm high at the arms endings (widest part of the design). The loop shape is 0.8 mm wide in an area of 6.8 mm x 20.1 mm and the gap between the bow tie antenna and the loop inductor is 0.25 mm. In a similar way, the screen printed tag dimensions are 2 mm width, 129.8 mm total length and 20.8 mm height at arms endings. The loop inductor dimensions are 0.8 mm width in an area of 7.2 mm x 24.9 mm and the gap distance to the antenna is 2.8 mm. In the case of the inkjet printed tag dimensions (Figure 32) are 2 mm width, 135.7 mm total length and 22.2 mm height at arms endings. The loop inductor dimensions are 0.7 mm width in an area of 31.8 mm x 9.9 mm and the gap distance to the antenna is 3.6 mm. It should be noted that the obtained dimensions of the printed tags are larger than those on FR-4 substrate. Moreover, in case of the

printed bow-tie antenna, loops need a larger gap with main radiator to get the same real part of the impedance. It could be attributed to the different resistivity/thickness of both technologies that leads to a different sheet resistance.

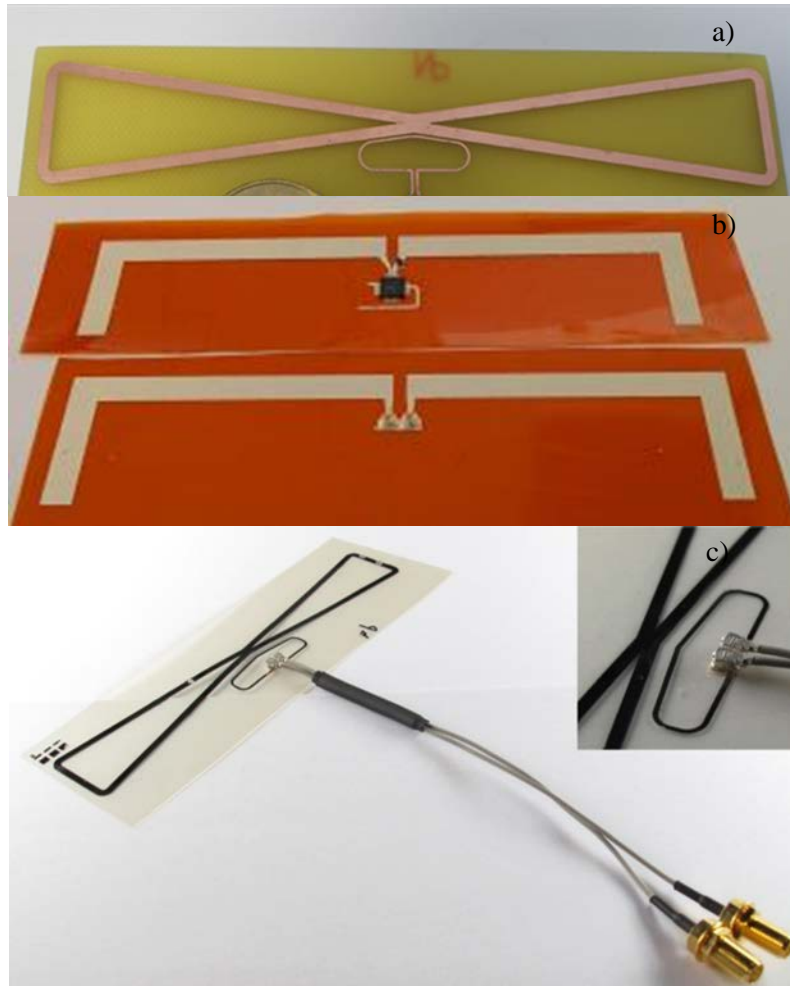


Figure 36. Pictures showing a) bow-tie antenna fabricated on FR-4 substrate, b) screen printed dipole including RFID chip and SMD inductance for matching and screen printed dipole showing the U.FL connectors on antenna feed point and c) Inkjet printed loop antenna showing the U.FL connectors and the U.FL-SMA cable adaptor.

Frequency responses of the dipoles are shown in Figure 37. Measurements and simulated features of antennas are in good agreement. As can be seen, differences with simulated values are smaller at low frequencies, below 800 MHz whereas the difference increases when frequency rises. This could be attributed to the custom calibration kit and the non-ideal character of the different standards. Basically, open standard can be modeled as shunt capacitor and resistor whose values will be larger as frequency rises. The same behavior can be applied to the short standard, equivalent to a series resistance and inductance. Thus, the error introduced by the calibration will be larger at upper frequencies explaining these results. Resonance frequency is fulfilled for the two fabrication techniques, being close to the designed value of 868 MHz. Measured input impedance of the dipole at 868 MHz was $30 + j10.9 \Omega$. This dipole impedance was designed to get the same real part as the RFID chip impedance, $31.1 + j286 \Omega$, whilst the necessary large inductive part was achieved with a SMD inductor series 3650 of 51 nH and a quality factor of 60 at 900 MHz (TE Connectivity, Ltd., Schaffhausen, Switzerland) placed on one of its arms. In a similar way, the screen printed dipole response impedance was $30 + j9.9 \Omega$ and a 40 nH SMD inductor was used as matching network to get the complex conjugate RFID chip impedance, $29.9 + j226 \Omega$. Power reflection coefficient value at resonance for FR-4 dipole is slightly larger in simulation than experimental result. On EM simulations, we set FR-4 copper conductivity to $4.6 \cdot 10^7$ S/m and loss tangent

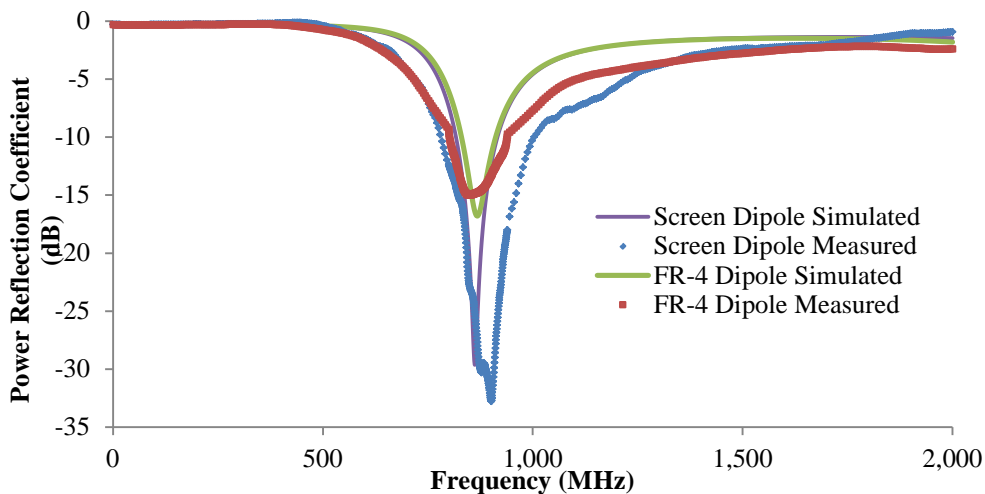


Figure 37. Measured and simulated power reflection coefficient for the set of fabricated dipole antennas: FR-4 substrate using milling techniques and Kapton PI substrate using screen printing techniques.

to 0.02 instead of manufacturer data, conductivity of $5.8 \cdot 10^7$ S/m and loss tangent of 0.015. EM simulations with manufacturer data resulted on more inaccuracy results. This fact shows how a rigorous characterization as performed on chapter 2 leads to more accurate results. In case of screen printed dipole, power reflection coefficient was slightly larger in measured results than simulated. Two loss mechanisms play a role on antenna response: dielectric substrate losses and ohmic losses. Due to the thin film employed on screen printing tag fabrication, the loss on metallic layer became significantly more important than these of the substrate, therefore differences are associated to ohmic loss of the silver printed layer.

The power reflection coefficient as well as the input impedance of both bow-tie antennas can be seen in Figure 38. FR-4 fabricated tags shows similar differences between simulated and measured features than screen printed antennas, in a similar manner to dipole comparison results. In both case, the real part was higher than expected, whereas the imaginary part was smaller: FR-4 bow-tie simulated impedance value was $34 + j286 \Omega$ whereas measured value was $41 + j282 \Omega$. In case of screen printed one, simulated value was $25.5 + j224 \Omega$ whilst measured one was $37.3 + j220.8 \Omega$. In the case of inkjet printed bow-tie antenna, the real part was slightly higher than expected, whereas the imaginary part was smaller: simulated value was $31 + j295 \Omega$ whereas measured value was $34 + j280 \Omega$.

Table 12 shows the calculated maximum read range using Eq. 51 according to the setup explained previously. The RFID chip sensitivity is -15 dBm, G_{tag} refers to the tag antenna gain whose values were obtained by electromagnetic simulation with ADS and can be seen in Table 10. P_{reader} is the effective radiated power by the reader and G_{reader} is the reader antenna gain. The transmission power was 26 dBm and the reader antenna gain was 7 dBi at 868 MHz according to the manufacturer. The reading range is shown in first column in Table 12 and it was calculated assuming ideal conditions ($\tau = 1$) in Eq. 51. In this estimation, the cable (N6314A Type N cable from Agilent Technologies) and adaptors losses were taken into account.

The *PLF* factor takes in account lossless due to polarization mismatch (linear vs. circular) between reader and tag antenna value is 0.5 (3dB). In this calculation, we assume an ideal matching condition between RFID chip and antenna, $\tau=1$. The two antennas designs show a very similar reading range, although the loop antenna presents the advantage of no additional component to implement the matching network. Comparison between fabrication techniques shows that printed antennas have a shorter read range than expected. These differences could be associated to the lower DC conductivity and the non-ideal behavior of the metallic layers in printed electronics. Both factor leads to a lower performance than the expected one affecting the gain

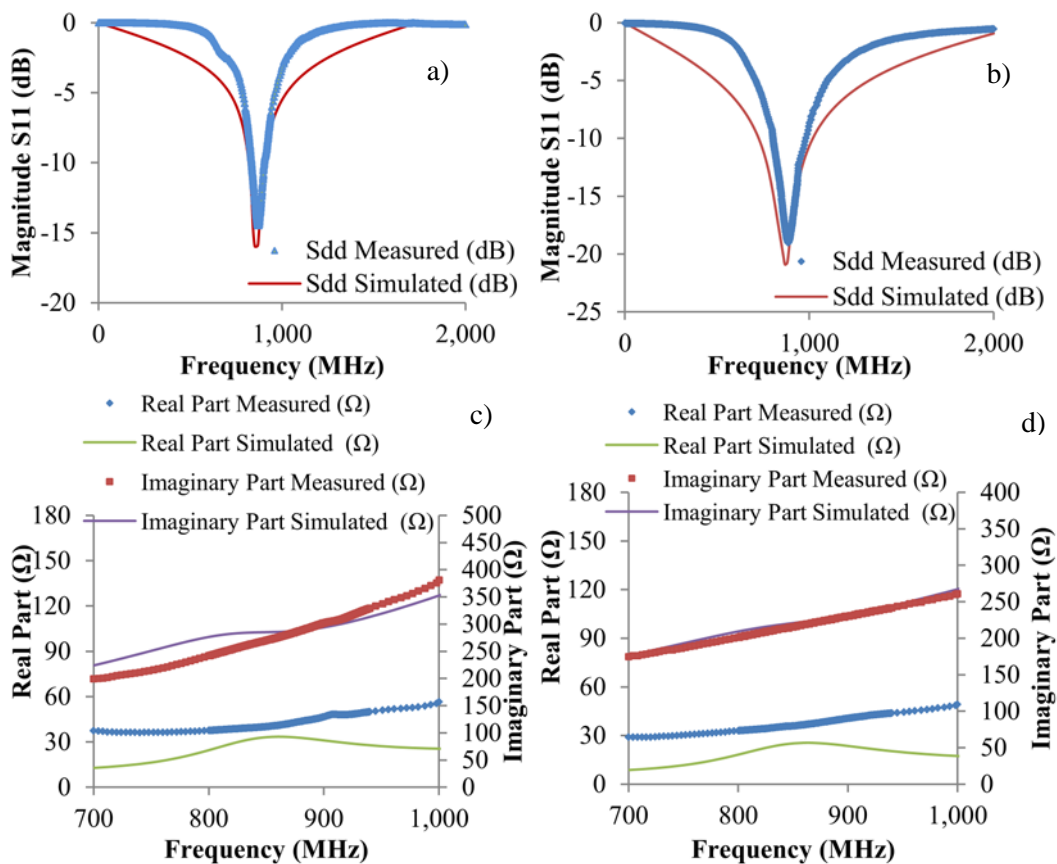


Figure 38. Measured and simulated responses of the UHF bow-tie antennas: a) S-parameter response of the antenna fabricated on FR-4 substrate, b) S-parameter response of the screen printed antenna, c) impedance of the antenna fabricated on FR-4 substrate and d) impedance of the screen printed antenna.

and efficiency of the fabricated antennas. Furthermore, extra losses are introduced by the mismatching between the IC's and antenna impedance because of the variation of the RFID chip impedance with both working frequency and different input powers levels. The inkjet printed antenna shows only a read range of 0.7 m. This could be attributed to the different thicknesses, 4.3 μm for inkjet antenna and 13 μm for screen printed one. In the case of thickness being equal to or thinner than the skin depth, around 10 μm for the measured conductivity, the total resistance will be inversely proportional to the conductor thickness. Conductor thickness should not be too thin to avoid the degradation of the antenna radiation efficiency. Lower performance of inkjetted antenna compared to screen printed one is associated thus to an increase in ohmic loss due to the different thickness (Björninen et al. 2009, Merilampi et al. 2010b, Koski et al. 2012). Printing more than twelve layers will however involve very long printing times. Hence, we consider that other printing techniques are more suitable for manufacturing tag antennas (Merilampi et al. 2010a, Janeczek et al. 2012, Virtanen et al. 2010a). Anyway, several strategies could still be used to improve the performance of the inkjet printed antennas.

Table 12. Main Characteristic of the designed RFID antennas.

Antenna	Calculated Read Range Passive Mode (m)	Maximum Read Range Passive Mode (m)	Maximum Read Range Active Mode (m)	Simulated Gain (dBi)	Simulated Directivity (dBi)	Simulated Efficiency
Dipole FR4	2.7	2.2	-	1.02	2.19	77.58
Dipole Screen Printing	2.6	1.6	-	0.66	2.40	66.97
Bow-Tie FR-4	2.8	2.2	3.1	1.31	3.00	72.20
Bow-Tie Screen Printing	2.7	1.8	2.8	0.91	2.17	63.20
Bow-Tie Inkjet Printing	1.8	0.7	1.2	-2.25	3.010	29.80

3.3.4 Comparison of fabrication techniques for UHF RFID tags

Figure 39 shows the obtained line-profiles for the set of benchmarked fabrication techniques. The line-profiles are 7 mm length comprising three sections of the basetta design meander lines; see red line on Figure 25.

Inkjet printed profile shows how the optimized sintering process avoids printing defects and gets smooth surfaces. A thickness around 8.8 μm has been achieved printing 20 layers; enough to not degrade antenna performance compare with other techniques. We have detected the edge effect drop causing that the obtained line-width is bigger compare with the other cases. Looking at the screen printed line profiles it can be observed the roughness already reported on chapter two and the obtained thickness of $\sim 10 \mu\text{m}$.

Solid-ink wax based process shows how the etching process affects the copper layer. The protection of the mask is not ideal and causes that some holes to appear on copper surface. We have observed that the 35 μm -thick copper layer suffers of holes or spot around 8 μm depths as mean value. Anyway this effect should not degrade antenna performance due the low number of observed holes.

Adhesive copper surface is practically ideal but the definition of the line width suffers from low resolution. Discrepancy between widths of the different lines increases in this case. The measured thickness is around 115 μm thick but adhesive layer is included on this measurement explaining the thick profile obtained.

Figure 39 shows the impedance frequency response of the set of fabricated tags on a smith chart representation. The red point is the targeted antenna impedance of $34+j154$. As can be seen for design comparison, basetta design gets closer to the desired impedance while thin-propeller one far away. This should cause a penalty on maximum read range due to the higher mismatching between RFID chip and antenna, and then thin propeller design must be modified to get the desired impedance.

Comparison among fabrication techniques shows a little dependence of the fabrication technique with impedance frequency response. Indeed both designs show very similar trends. Resonance, see circle radius around resonant frequency, are slightly broader on the case of 35- μm thick copper layers (wax-based and cutting plotter fabrication techniques) while printed antennas suffers for a narrower resonance. This can be explained due to the lower conductivity of the silver printed layer compared with the copper one.

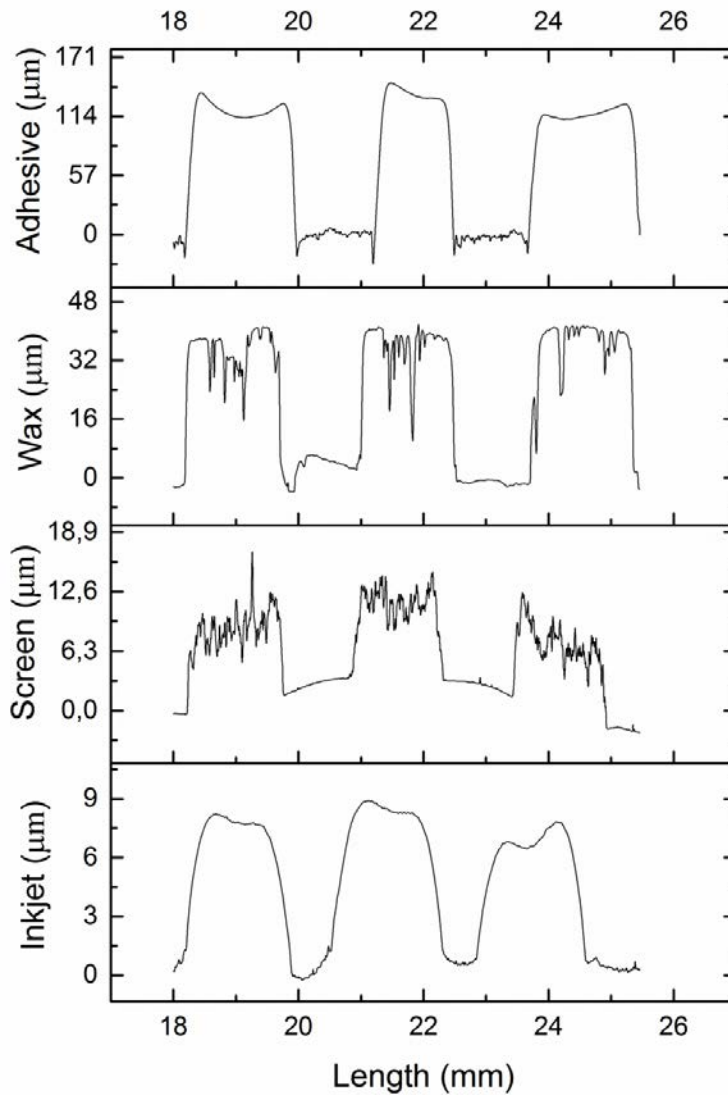


Figure 39. Thickness line-profiles of the basetta antennas along the red line depicted in Figure 25 for the four fabrication techniques.

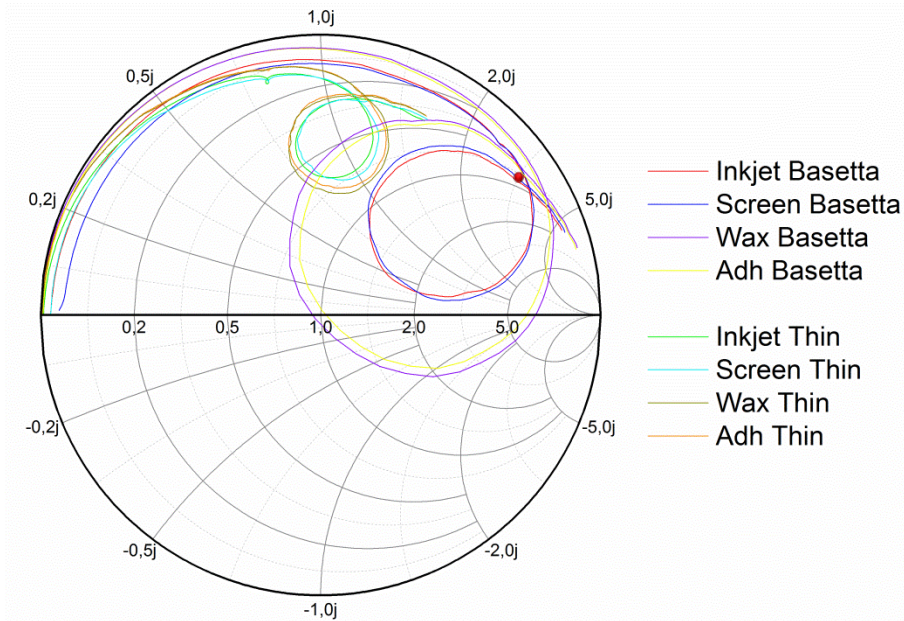

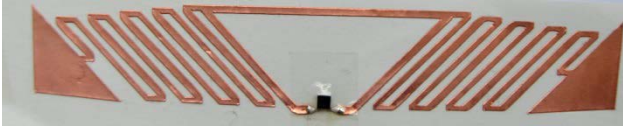








Figure 40. Smith Chart representation showing the impedance frequency response for the set of prototyped RFID tags. Red point indicated the designed antenna impedance.

Finally on Table 13 we have indicated the maximum read range for each tag and a picture of the manufactured prototype. The obtained gain for the thin-propeller design is 0.73 dBi, directivity is 2.02 dBi and efficiency is 74.3 %. In the case of the basetta design, the gain is 0.92 dBi while directivity is 1.98 dBi and efficiency is 78.3 %. According to Equation 51, theoretical read ranges are 6.8 meters for thin-propeller design and 7 meters for basetta design. Read ranges comparison between antenna designs confirms the penalty introduced due the non-matched condition with the RFID chip of the thin propeller design. Comparison between techniques shows better performance of copper layers antennas; although the performance is practically comparable among techniques. Printed antennas suffer of a more limited read-range but in any case it is comparable to the copper ones. Finally, the inkjet printed antennas gets a read range almost equal to the screen printing one whilst in the case of “bow-tie” antenna comparison the differences were significant larger. Must be take in account that the obtaniend thicknes now is twice the 4 μm -thcik “bow-tie” antenna being now the thickness of both printing techniques almost equal.

Table 13. Maximum read ranges for the set of fabricated RFID tags showing pictures of all prototypes obtained with each design/technique

Tag	UHF Tags Thin-Propeller and Basetta	Read Range (m)
Cutting Plotter		3.53
		4.11
Wax Based		4.04
		4.47
Screen Printing		3.49
		4.20
Inkjet Printing		3.48
		4.19

3.4 Conclusions

Using the optimal parameters obtained from chapter 2, antennas were fabricated to be used in RFID tags.

To manufacture the antennas using inkjet printing, SunTronic ink on PEI substrate has been used due to its better RF performance and printability. The number of printed layers must be enough to provide the required thickness in order not to degrade the quality factor of the RFID tag. In the particular case of the HF inductor, four printed layers were enough to fabricate the working RFID antenna with a quality factor of 1.68 ± 0.12 . Screen printed inductors presents better quality factors and therefore best antenna performance.

Regarding UHF antennas, a technique for impedance measurement of balanced UHF RFID antennas based on S-parameter study has been showed. A differential probe with U.FL connectors together a custom SOLT calibration kit composes the measurement tools. In all the investigated cases, the experimental results and numerical simulations have shared very similar trends, although real part present bigger differences than imaginary part suggesting that real part is the critical factor to get RFID chip matched antenna impedance. It has been pointed out how a rigorous characterization of fabrication technology leads to more accurate results. Both antenna designs exhibit similar read ranges while screen printed antennas suffer from a reduced reading range compared to the copper ones but benefited from an extended reading range compared to the inkjet printed ones.

About printing techniques comparison, screen printing with mesh densities between 90 and 140 threads per centimeter resulted in a more advantageous technique to manufacture antennas for RFID tags due to their lower sheet resistance and higher antenna performance compared to inkjet printed ones. Anyway, inkjet printed antennas can be fabricated with enough numbers of printed layers to get a performance comparable to the screen printed ones, although the drawback are long printing times and a carefully sintering process to avoid undesired printing defects.

Finally, the comparison of fabrication techniques shows that printing techniques can achieve performances comparables antennas manufactured with to 35 μm -thick copper metallization layers.

4. Design and characterization of smart RFID Tags

In this chapter four smart RFID tags with sensing capabilities are presented both in HF and UHF frequency bands.. The aim is to design and demonstrated valuable low-cost passive and semi-passive tags architectures to interface sensors. The previously designed RFID tags are now combined with commercial sensors and digital architectures making up RFID systems able to detect and monitor some environmental parameters of interest: temperature, relative humidity, light intensity and atmospheric pressure.

4.1 Smart RFID tags with commercial sensors

4.1.1 Material, methods and designs

The full set of manufactured RFID tags are those shown in Table 14. The chosen combination of materials, silver ink and printing conditions are those reported on Chapter 2 due to best demonstrate performance. Some requirements have been taken into account for the design of the tags: minimizing the number of components, the feasibility of transferring packaged chips on printed flexible PCBs, and operation at very low power

Table 14. Summary of Main Characteristic of the fabricated smart RFID.

Tag	Energy Mode	Antenna Type- RFID Band	Printing Technique	Substrate	Sensors
1	Semi-Passive	Inductor-HF	-	PI	Temperature Humidity
2	Passive	Dipole-UHF	-	PI	Temperature Light intensity
3	Semi-Passive	Bow Tie-UHF	3.1	PEI	Temperature Pressure
4	Semi-Passive	Bow Tie-UHF	2.8	PI	Temperature Pressure

A block diagram of the proposed HF RFID tag number 1 is presented in Figure 41. It is a microcontroller-based system designed to measure the

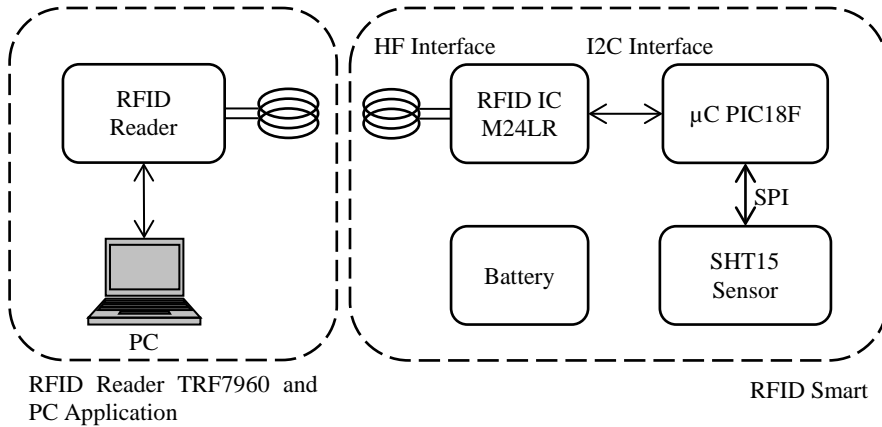


Figure 41. Block diagram of smart RFID tag with temperature and humidity sensors.

temperature and humidity obtained from a commercial sensor. The microcontroller used for this prototype is a PIC18F46J50 (Microchip Technology Inc., USA) which has been selected because of its low power consumption (nanoWatt XLP Technology). The availability of inter-integrated circuit (I2C) and serial port interface (SPI) ports also allows easy communication with the RFID chip and the commercial sensor, respectively. A SHT15 (Sensirion AG, Staefa ZH, Switzerland) has been chosen as the sensor. This is a multi-sensor module that can be configured to measure either relative humidity with an accuracy of $\pm 2\%$ or temperature with an accuracy of $\pm 0.5^\circ\text{C}$. It provides calibrated and digital data to the microcontroller via a serial interface.

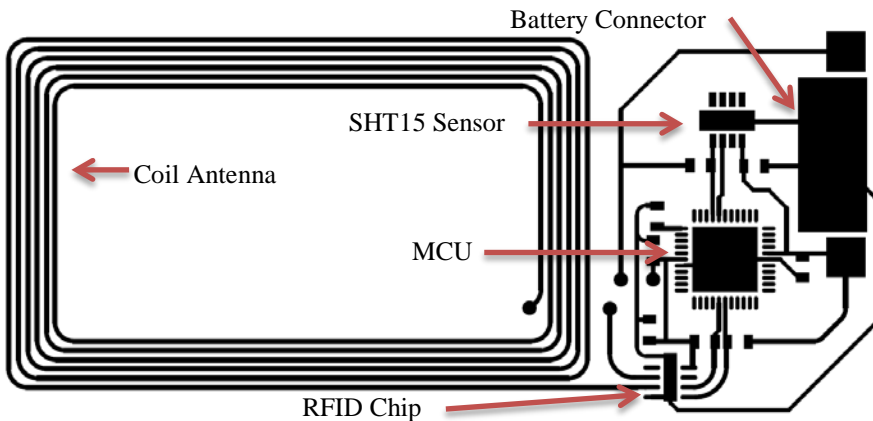


Figure 42. Schematic layout of the designed RFID Smart tags number 1.

An M24LR64 (STMicroelectronics Inc, Geneve, Switzerland) has been selected as the RFID chip. In RF mode, using the ISO15693 protocol, the RFID chip is accessed via a 13.56 MHz carrier electromagnetic wave on which incoming data are demodulated from the received amplitude modulated signal. Apart from the RF interface, this chip works with the I2C interface which allows access to its EEPROM memory through the microcontroller. In this regard, it is possible to store data on the RFID chip memory that could be read out easily by a commercial RFID reader. Logging mechanism is implemented using a watch dog timer (WDT) mechanism to periodically awake the MCU, drive the sensor module and the obtained store sensor information on RFID chip EEPROM memory. A commercial button battery model 2032 has been used to power on the tag. All these components have been labeled on Figure 42. A HF band commercial reader, TRF7690_EVM (Texas Instrument Inc, Dallas, TX, USA) fully compatible with the protocol ISO15693, has been used to test the developed RFID tag. A Visual Basic application (Microsoft Corp., Redmond, WA, USA) has been developed to configure and read out the manufactured RFID tag.

The final RFID tag prototype number 1 has been manufactured on a PI substrate by screen printing with 120 (T/cm) mesh density. The coil antenna design is that presented on Chapter 3 for screen printing manufacturing. The inner and outer ends of the coil have been connected through a small “bridge” manufactured by inkjet printing on PI substrate and IC chips has been attached using the bonding process presented in Chapter 2..

The RFID tags prototypes numbers 2, 3 and 4 are manufactured to work in the RFID band of 868-915 MHz (UHF band) and use the EPC Gen 2 protocol. UHF RFID chips usually provide EPC Gen 2 compatibility, but some extra functions are required to include sensing capabilities. These functions are mainly Serial Port Interface (SPI) to provide full access to the RFID chip EEPROM memory, and the integration of built-in sensors or signal conditional stages to interface external sensors. There are only few UHF RFID chips that able to provide these functions. RFID chips with SPI capability are, for example, the D18BLO1 from Delta Company. The EM4325 provided by EM Microelectronics-Marin and the WM72016 from Ramtron Corporate also include on-chip temperature sensor. Besides these features, the RFID chip SL900A (AMS AG, Unterpemstaetten, Austria)

integrates a very complete SFE. This extra circuitry can be used to interface different type of current-output, resistive and capacitive sensors to be easily read out by an EPC Gen 2 RFID reader. This feature has motivated the choice of the SL900A chip for the design of the RFID smart tags developed in this work.

To carry out an exhaustive characterization of the mentioned chip, we have investigated on one hand its interface to ultra-low power sensors by designing a passive tag and, on the other hand, its interface to other sensor with extra power requirement obtained from a battery in a semi passive tag.

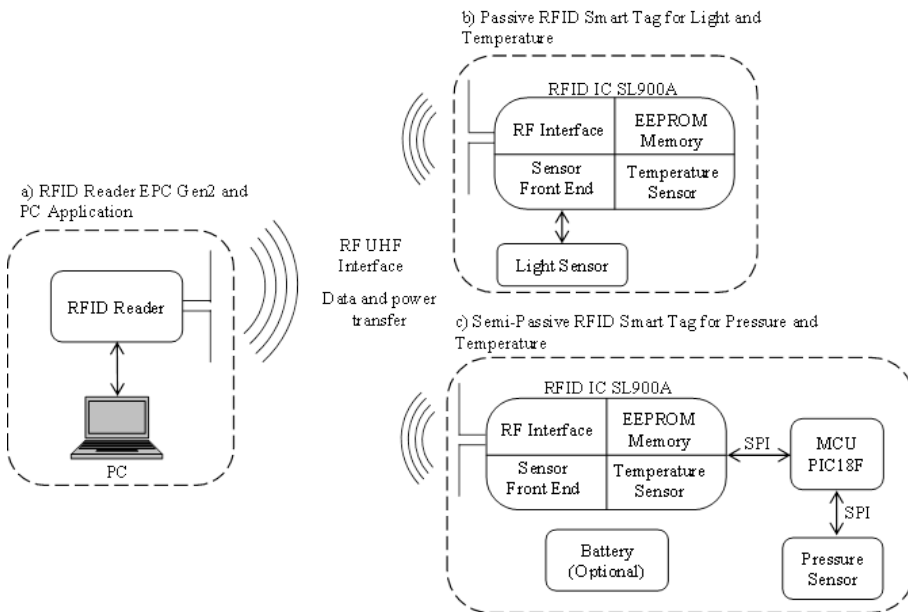


Figure 43. Block Diagram of the developed RFID sensing systems showing the two different tag architectures. a) RFID reader and PC application, b) light and temperature passive smart tag, manufactured in this work by screen printing technique and c) semi-passive smart tag showing the pressure sensor and the microcontroller interfaces, manufactured in this work by screen and inkjet printing techniques.

The system level designs including both architectures of the RFID tags are shown in Figure 43. The first design is a passive tag with the RFID chip, and the second one is a semi passive tag which includes an additional microcontroller unit (MCU). With the aim to minimize the occupied area, the low power microcontroller used in the latter design is a PIC18LFK22 (Microchip Technology Inc., USA). It has been selected because of its low

power consumption (NanoWatt XLP Technology) and the availability of serial port interfaces (SPI) to communicate with both RFID chip and external sensors.

In the passive tag number 2 the SFE of the RFID chip has been set up to sense light by using a passive photodiode as sensor. In the semi-passive architecture number 3 and 4 containing the RFID chip and the MCU, a commercially available pressure sensor has been implemented. Moreover, for all the tags, temperature measurements have been obtained directly from the built-in temperature sensor in the UHF SL900A chip.

In Figure 44 the two types of printed tag architectures are displayed including the footprints of all components. For the passive architecture, we used the dipole antenna based on the FR4 development kit designed and recommended for the SL900A chip by the manufacturer and presented in Chapter 2 (AG 2014). In this case, a RF Surface Mount Device (SMD) inductor is used to match the chip input impedance. For the semi-passive strategy and to investigate the RF versatility of the RFID chip, we propose the novel “bow-tie” antenna design presented in chapter 3. Furthermore, including the matching network in the antennas’ layout instead of using SMD inductors reduces the tag cost.

Figure 44a depicts the passive RFID tag layout to measure temperature and light intensity. The SL900A RFID chip includes an in-built temperature sensor that can be accessed by the RF or SPI interfaces. Temperature value comes from a conversion in the on-chip 10 bits A/D converter. Two voltage references, V_{ref1} and V_{ref2} individually selectable in steps of 50 mV, define the lower and upper limits of this converter. These limits are defined as $2 \cdot V_{ref2} - V_{ref1}$ and V_{ref2} . The difference between them determines the input voltage range, $V_{ref2} - V_{ref1}$, and the operation limits. These reference voltages can be chosen in the user application and, therefore, a concrete resolution and range can be selected by the user. The minimum resolution is 0.18°C in a range of 189.9°C while a resolution of 0.232°C is obtained with the widest range of 237.2°C.

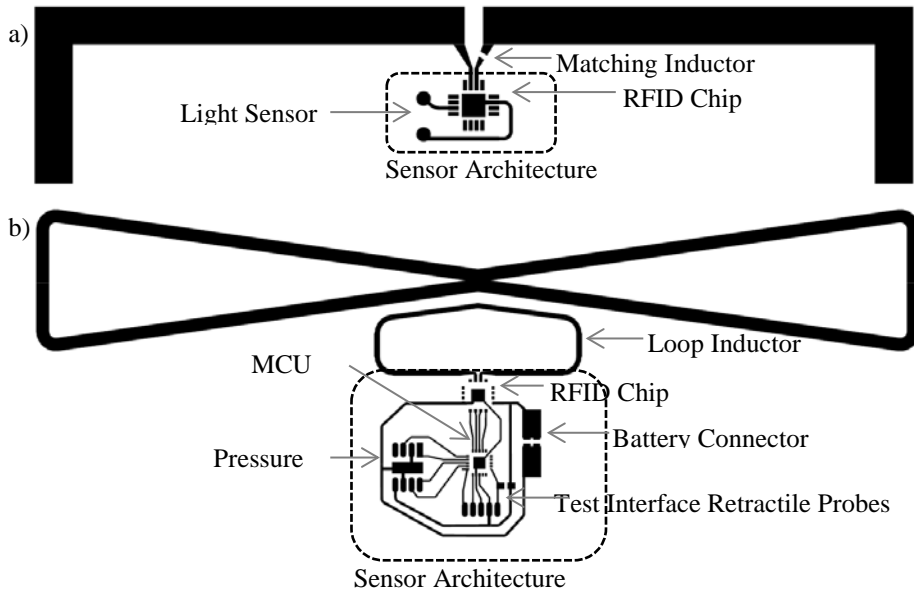


Figure 44. Schematic layout of the designed RFID Smart tags: a) a passive temperature and a light sensor tag based on dipole antenna; b) a semi-passive pressure and a temperature sensor tag based on loop antenna.

Light intensity is obtained through a S1227 photodiode (Hamamatsu Photonics K. K., Hamamatsu City, Japan). The photodiode is packaged in a 6 mm x 7.6 mm plastic body whereas the window size of the photosensitive area is 2.4 mm x 2.4 mm covered by a resin potting. The spectral response to the incident light ranges from 300 to 1000 nm with a peak value at 720 nm of 0.43 A/W. The photodiode is directly connected to the SFE of the RFID chip. Basically, it is a current-voltage amplifier whose gain is selectable by choosing the value of the on-chip feedback resistor. In this work, the light sensor is configured as a threshold sensor, capable of detecting if the proposed RFID tag is exposed to light or not. A calibration process is carried out at three different levels of ambient light: complete dark, cloudy day and sunny day. A light meter model 180-7133 (RS Amidata S.A., Madrid, Spain) is used to estimate the incident light.

The layout of the second proposed semi passive tag can be seen in Figure 44b. The chosen microcontroller includes the peripheral interfaces to communicate with the RFID chip and the pressure sensor. The microcontroller drives the pressure sensor and saves the data in the RFID

chip EEPROM memory on a specific location known by the reader. The commercial MEMS pressure sensor MS5803 (Measurement Specialties TM, Hampton, USA) is a digital temperature and pressure sensor with 24 bits of precision and capable of measuring from 0 to 6 bars and -40°C to 85°C . We have selected this sensor because of its ultralow power consumption of $1\ \mu\text{A}$ (standby $< 0.15\ \mu\text{A}$) and no need of external components to operate. In this semi-passive tag, battery is only necessary to drive the pressure sensor and the microcontroller and store pressure data on the RFID chip memory. We have used a flexible rechargeable ultra-thin polymer lithium-ion battery, PGEB01 (General Electronics Battery Co, Shenzhen, P.R. China) with a capacity of 200 mAh at 3.7V. Digital electronics in charge of driving pressure sensor only occupies an area of 10 mm x 20 mm.

Moreover, for testing and debugging purposes, retractile probes were mounted on a small FR-4 PCB board. These probes were used to provide electrical contact to the power (battery voltage or rectifier voltage) and to in-circuit debugging interface of the microcontroller. In this respect, we had full access to the digital architecture and we were able to measure the power consumption.

There are two ways of operation for the proposed UHF smart tags: direct measurement from the RFID reader or logging mechanism. In the former case, the RFID reader power up the tag and read out directly the values of temperature, light or pressure from the RFID chip using EPC Gen 2 commands. Logging mechanism is implemented in two ways. In the case of single-chip architecture, Cool-LogTM protocol implemented in the RFID chip can be used for logging purposes. In the case of the micro-controlled RFID tags, the logging procedure uses a watch dog timer (WDT) mechanism to periodically awake the MCU.

UHF RFID tag tests were performed using a commercial RFID reader compatible with EPC Gen2, DK-UHF RFID HP2 (IDS Microchip AG, Wollerau, Switzerland). This RFID reader was used to check the maximum distance to detect and read out the manufactured RFID tags through a Visual Basic application running in a PC. The devices were tested in an anechoic chamber. The RFID reader antenna was placed in a tripod. It consists of a circular polarized patch antenna A0025 (Poynting antenna, Samrad, South

Africa). The tags were attached to a foam structure to simulate free space conditions and placed in front of the reader antenna at the same height.

4.1.2 Experimental Results

Table 15 summarizes the magnitude, sensor capabilities and characteristic of the manufactured smart RFID tags. Power from RFID reader column refers the possibility for the tag to operate in passive mode, no battery required to access sensor information.

Table 15. Main characteristics of the sensor capabilities of the fabricated smart tags.

Magnitude	Tag Number Architecture	Power from RFID reader	Number of samples in memory	Range/Accuracy/resolution
Temperature	Tag 1 SHT15 Sensor	No	2000	-40 °C to 123.8 °C/±0.5 °C/0.01°C
Humidity	Tag 1 SHT15 Sensor	No	2000	0 to 100 % RH/ 0.2 % RH /0.05 % RH
Temperature	Tags 2,3 and 4 RFID Chip	Yes	841	-20 to 60 °C/±1 °C/0.15°C
Light (Photocurrent)	Tag 2 RFID Chip Photodiode	Yes	841	45.1 to 125 µA/±0.4 µA /78 nA
Pressure	Tags 3 and 4 RFID Chip MCU MEMS Sensor	No	350	0-6 bar/±120 mbar/0.036 mbar

Operation of the smart tag number 1 for temperature and humidity has been tested with the commercial HF RFID reader with a reading range of around 12.0 cm in vertical direction and 11.2 cm in horizontal one. The proper operation of the label has been satisfactorily tested through the development of the Visual Basic application. Battery power was not necessary to access the data stored on the sensor, making the label a semi-passive smart tag for sensing applications. Furthermore, any commercial sensor could be integrated in the design only with minor changes. Figure 45 shows the manufactured tag and a screen capture of the Visual Basic application. The power consumption of the RFID tag is only $34 \pm 5 \mu\text{A}$ in idle mode and $957 \pm 5 \mu\text{A}$ in sensing mode. A complete measurement cycle drives the digital sensor and stored the read out sensor data on the RFID chip memory. The whole process took around 1.7 s, mostly due to ISO15693 protocol delay specifications and the sensor measurement time

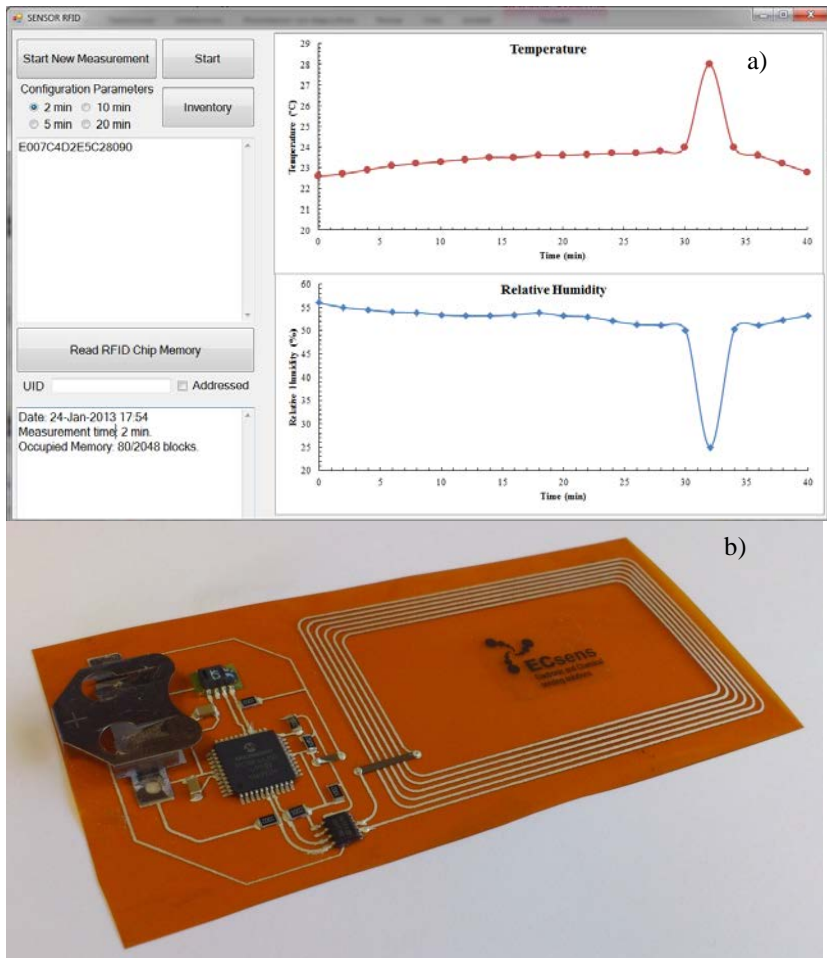


Figure 45. (a) Capture image of the Visual Basic application to configure and read-out the Smart RFID tag and (b) picture of the prototype number 1, a HF RFID tag capable of measuring temperatura and humidity manufactured on PI substrate by screen printing.

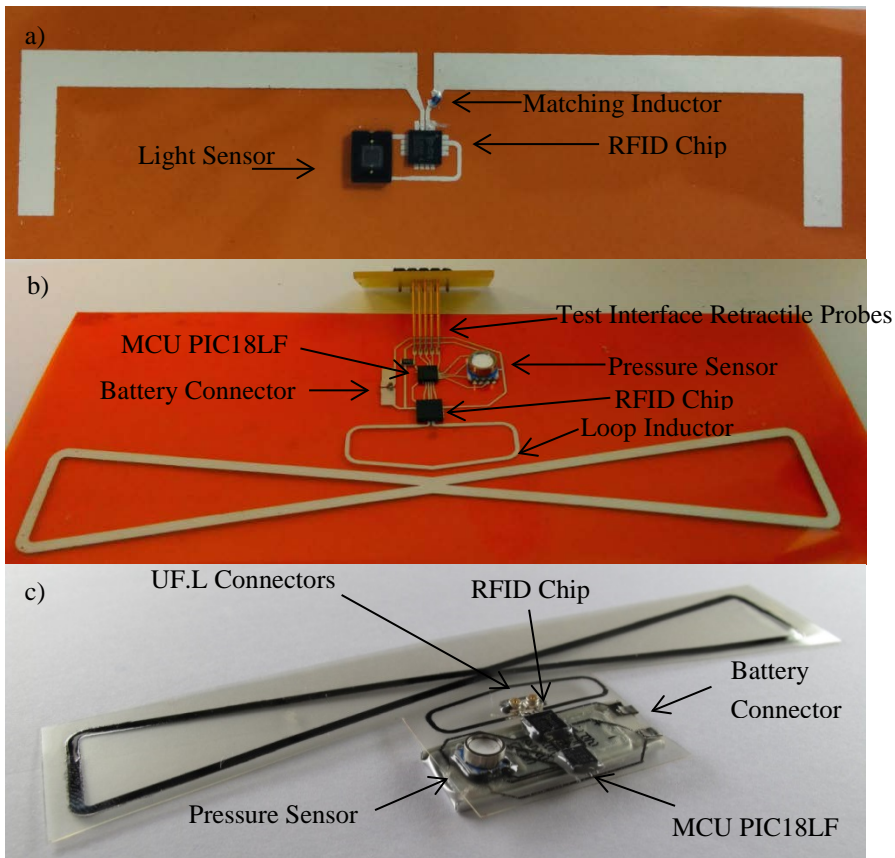


Figure 46. Images showing the fabricated RFID smart tags: a) smart tag number 2, passive dipole-based antenna tag fabricated by screen printing with temperature and light sensors, b) the smart tag number 3, a semi-passive loop-based tag also fabricated by screen printing with pressure and temperature sensors and showing the test interface retractile probes and c) the semi-passive tag number 4 as in b) but inkjet-printed and showing the mounted thin battery.

The main characteristics of the implemented sensor capabilities in tags number 2, 3 and 4 are presented in Table 15. A picture of these tags can be seen Figure 46, where the different components have been labeled for better understanding. Temperature measurements present different errors and accuracies depending on the selected measurement range. The calibration process was carried out for the light sensor. A response of 0 counts was observed for all the performed measurements when the smart tag was in the black box (complete dark environment). Smart tag exposition to natural light in a sunny day at 12:00 h in Andalusia, Spain (1220 lux measured with the light meter) produced a saturated response; consecutive measurements produce 1023 as digital output. The exposition in the same conditions but in

a cloudy day (670 lux measured with the light meter) generated 496 as digital output. An uncertainty of ± 5 LSB was observed in both cases. The pressure sensor stage was validated as an altimeter. The pressure smart tag was transported from CITIC research center in Granada, 667 m over sea level; to Güejar-Sierra at 1491 m. Pressure values were stored every 5 minutes in the RFID chip memory. Temperature measurements using the pressure sensor module were also carried out for compensating the acquired pressure information, as recommended by the manufacturer. Environmental pressure information was correlated with altitude obtained by GPS information showing a good agreement. The measured pressure ranging from 941 mbar to 852 mbar corresponded to a change in altitude of 818 m. Accuracy and errors associated with this sensor stage can be seen in Table 15.

Regarding tag number 2, no power consumption from battery is needed to measure light and temperature when the tag is in the vicinity of a RFID reader. In this respect, the light and temperature smart tag works in a full passive way, reducing the final cost of the fabricated label. However, if logging mechanism is required, a battery could be included as shown in the pressure sensor design. In this latter case, the battery consumption of the RFID chip is $870 \mu\text{W}$ using the SFE to collect sensor data and $4.8 \mu\text{W}$ in idle mode. The Cool-LogTM protocol implemented in the RFID chip by the manufacturer could be easily configured and no microcontroller unit is necessary for logging purposes. The proposed RFID tag number 2 composed only by a single silicon chip and a light sensor provides a cost-effective solution.

For the semi-passive tags number 3 and 4, the extreme low-power architecture requires a power of only $2.1 \mu\text{W}$ in sleep mode and $426 \mu\text{W}$ in sensing mode working with the WDT. A complete measurement cycle including storing measured information in the RFID chip takes around 100 ms. These power consumptions are similar to those reported by others microcontroller based RFID tags (Unander et al. 2011, Fernandez et al. 2012, Kassal et al. 2013). The associated battery life time will be dependent on the set sensing period. A battery life time of several years is estimated for a sensor sampling period of 1 hour. The maximum available current from the RF rectifier is $200 \mu\text{A}$ that could be used to recharge the battery or power out external components. In this regard, the life time of the tag will be extended

but an extra chip managing the battery charge process would be necessary. Finally, the manufacturer provides a mechanism to measure the voltage level of the battery, so it is possible to set an alert if this voltage drops below the required operation level.

4.2 Smart RFID tag with harvesting capabilities

4.2.1 Material, methods and design

RFID tags with sensing capabilities normally requires extra circuitry and battery to be able to acquire and process data increasing the cost the tag and requiring change the battery time to time. In addition to this, batteries are also essential when RFID tags monitor its parameters in autonomous mode.

One solution to reduce the tag cost and the inconveniences of changing batteries is the inclusion of energy harvesting module in the tag. This module takes advantage of the available environmental energy (solar energy, RF energy, mechanical vibrations and so on), collecting it and storing it for future access.

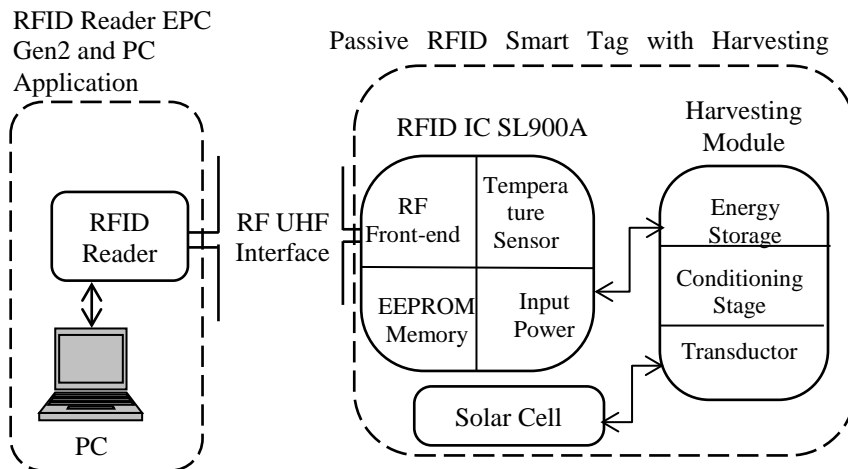


Figure 47. Block diagram of the setup for testing the Smart RFID tag with harvesting capabilities.

Figure 47 shows the RFID systems composed by the EPC Gen 2 RFID reader and the smart RFID tag. The tag presents a passive architecture based on SL900A RFID chip (AMS AG, Unterpremstaetten, Austria) compatible with EPC Gen 2 RFID standard. As previously explained, the chip includes and

SFE an on-chip temperature sensor. In this case, we are going to perform only temperature tracking but the monitoring of other magnitudes would be a direct integration by adding properly the chosen sensor to the chip SFE. Temperature value comes from a conversion in the on-chip A/D converter of the SL900A. The design chosen to manufacture this UHF tag was the FR-4 dipole antenna designed on chapter 3 whose arms were bended to reduce the occupied area.

The energy harvester module makes use of the integrated circuit LTC3588-1 (Linear Technology, USA) which is designed to harvest energy from solar cells and piezoelectric generators with virtually the same configuration. In order to operate properly, the output voltage of the harvester device must be between 5 V and 16 V.

In our case, we chose a solar panel to test the performance of this chip. The solar cell used was SA-0640 from Solarex (Istanbul, Turkey) whose dimensions are 152x55x2 mm. This solar cell was tested in outdoor and indoor conditions, showing an open-circuit voltage (V_{oc}) of about 8V and 6.5 V, respectively. These voltages are enough high to provide 1.8 V to the RFID chip and they also agree with the harvester circuit constrains. Other smaller cells can be used but we selected this one for testing purposes.

Figure 48 presents the configuration used to collect solar energy and provide power to the RFID chip. Four capacitors and one inductor are required to condition the EH chip. Output of the harvester module is directly connected to power pin of the RFID chip making the RFID tag active, that is, it is capable of autonomous communicating. In order to verify the autonomy of the system, the RFID chip was programmed to acquire and store temperature data every second and the tag was tested in three different scenarios:

- RFID chip powered by a commercial RFID reader (IDS Microchip AG, Wollerau, Switzerland).
- RFID chip powered by the energy harvesting module.
- RFID chip powered by both commercial RFID reader and energy harvesting module.

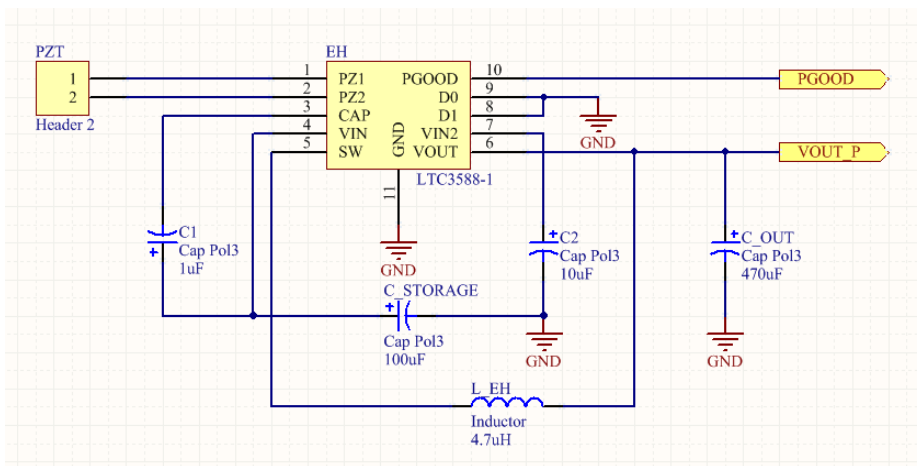


Figure 48. Schematics of the harvester module.

4.2.2 Experimental Results

Figure 49 shows the fabricated and mounted RFID tags. The size of this tag can be reduced by not including the test points and reallocating the components.

RFID module and energy harvesting module share the ground plane, although the ground plane does not totally cover the RFID module in order to not degrade antenna performance.

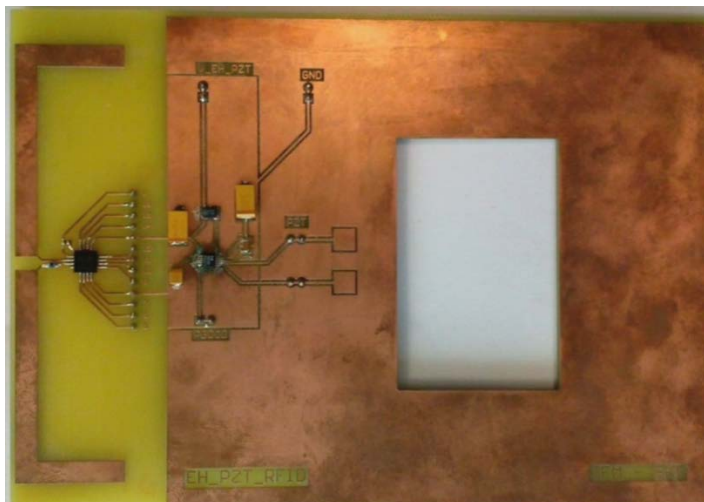


Figure 49. RFID tag with energy harvesting module.

Figure 50 presents temperature data during 6 min in the scenarios described above. As can be observed, all scenarios show virtually the same tendency. Taking into account that the room temperature was 28 °C, all measurements are within the error of the sensor ($\pm 1^\circ\text{C}$). The mean value obtained in each scenario was 27.3 °C (RFID reader), 28.6 °C (EH module) and 28.2 °C (RFID reader and EH module).

After that, we monitored the battery level (V_{BAT}). As expected, this voltage is constant when RFID reader is activated; therefore we only monitored the autonomous scenario: only EH module provides the energy to the tag.

Figure 51 illustrates the monitoring of the battery level. This voltage is constant (1.85 V) the first 90 s. During this period the EH module is capable of providing enough energy to the RFID chip. After that we disconnected the EH module, forcing the capacitor discharging. The result is the decay of battery level during 60 s up to 1.77 V where the RFID chip cannot work and, therefore, the autonomy is over. In case of not being able to collect enough energy from the environment, we have 1 min to recover the system with a capacitor of 470 μF . This time could be easily enlarged by increasing this capacitance.

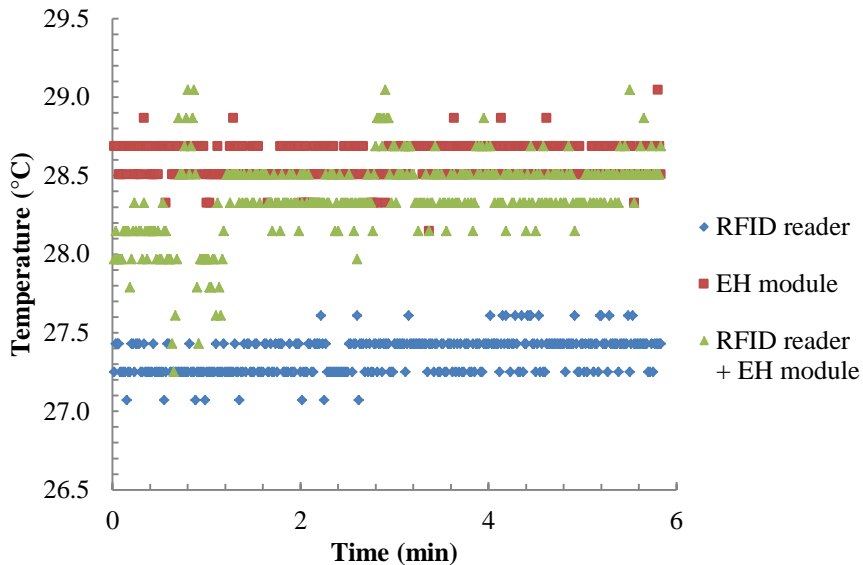


Figure 50. Temperature monitoring in 3 different scenarios of power providing.

Another alternative use of the EH module is to increase the read range, that is, to increase the maximum distance between reader and tag to communicate successfully. In order to test this increase, we defined two operation modes: detection and monitoring. Detection mode refers to only identify the tag through its EPC command whilst the tag also tracks temperature in monitoring mode. In the latter case, the tag requires more power than the former case. Firstly, we measured the read range in both scenarios without connecting the EH module. Then, we repeated the experiments connecting this module. Results are summarized in Table 16.

Table 16. Read range for identification and temperature measurement in passive mode and active (harvester powered) modes.

		Mode		
		Identification	Monitoring	Difference
Read range (cm)	RFID reader	125	111.5	13.5
	RFID reader + EH module	189.5	164.3	25.2
	Difference	64.5	52.8	

On one hand, as expected, the read range is larger in detection mode than in monitoring mode since the chip consumes more energy to get temperature value.

On the other hand, the read range is enlarged about 50% in both modes with EH module. We can take advantage of this result especially in environments with difficult access.

Finally, we have monitored both temperature and battery level in autonomous mode Figure 52. The time between consecutive measurements was 10 s. The tag was introduced in the climatic chamber VCL 4006 (Vötsch Industrietechnik GmbH, Germany) that was programmed to decrease temperature from 30 °C to 20 °C in 10 min.

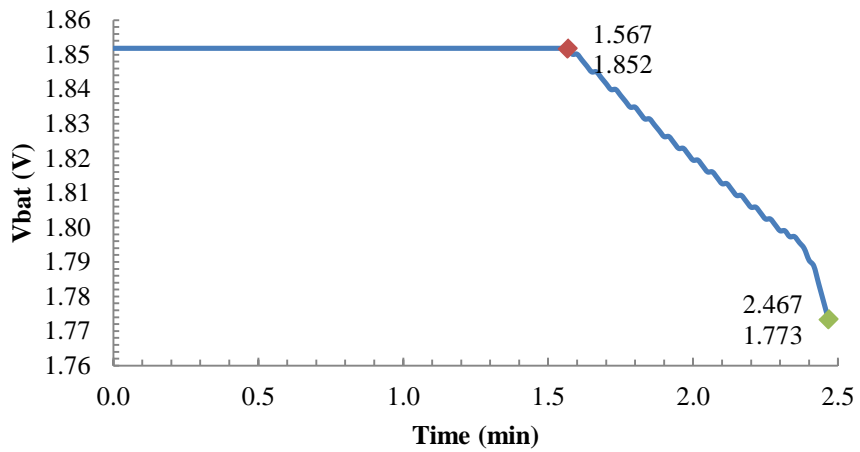


Figure 51. Monitoring battery level with the harvester module operating until 1.5 min, then battery capacitor discharges in one minute.

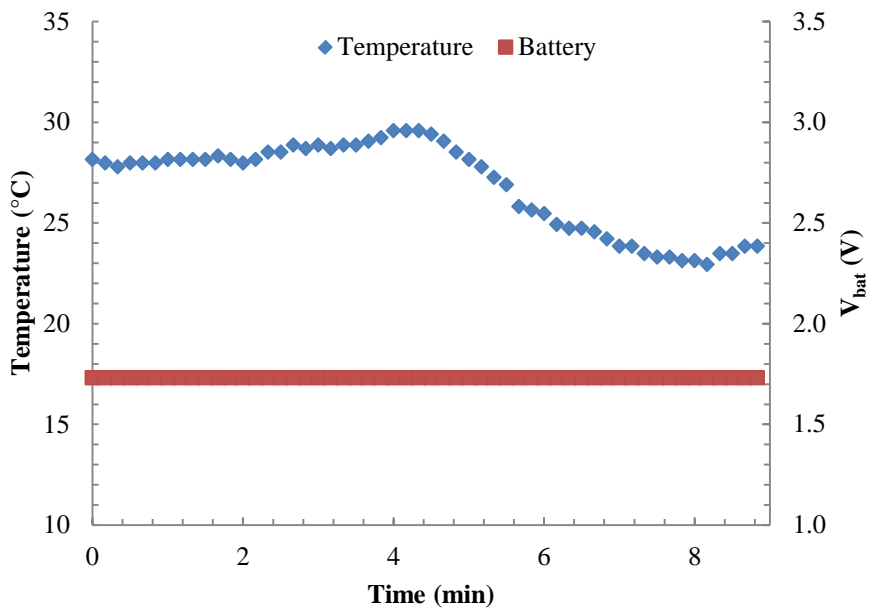


Figure 52. Temperature and battery level monitoring in autonomous mode.

Battery level was constant during the test with a mean value of 1.77 V. Temperature decayed from about 29 °C to 22 °C which fits with the accuracy of the climatic chamber and its stabilization time.

4.3 Conclusions

First, we have shown the development of a semi-passive HF RFID tag with temperature and humidity sensing capabilities. An ultra-low power architecture composed by a dual-interface RFID chip, an ultra-low power MCU and a commercial sensor has been fabricated on flexible substrate and its operation has been demonstrated.

Second, the features of the SL900A RFID chip to include novel sensing capabilities have been investigated in printed UHF RFID tags compatible with EPC Gen 2 protocol. Environmental parameters such as temperature, light and atmospheric pressure have been acquired with the presented printed RFID tags. First, a dipole-based passive RFID tag which is capable of measuring temperature and light intensity has been designed, fabricated by screen printing, and characterized. This proposed RFID tag composed only by a single silicon chip and a light sensor provides a cost-effective solution. Second, a loop-shaped antenna semi-passive tag has been implemented to read out the environmental pressure and temperature. In this case, an ultra-low power architecture based on a microcontroller unit has been developed resulting in a very compact device. Although the smart tag needs a battery to drive out the pressure sensor and store the information in the RFID chip memory, the battery can be electromagnetically recharged and it is not needed to access the stored data in the RFID chip memory.

Finally, a harvester approach to the RFID tags has been tested. A solar cell has been used to power up the tag, extending the maximum read range of the tag and providing to use the sensor capabilities without needing external battery.

To sum up, we have demonstrated valuable low-cost passive and semi passive tags architectures to interface sensors that can be implemented for different applications.

5. Design and characterization of smart RFID tags with printed sensors

5.1 Smart HF tag: Oxygen Monitoring

In previous works, the authors presented portable instrumentation for the determination of gaseous oxygen based on the quenching of luminophore platinum octaethylporphyrin (PtOEP) (Demas and DeGraff 2001, Quaranta, Borisov and Klimant 2012). The use of photodiodes coated with a stabilized polystyrene membrane containing PtOEP makes it possible to sense O₂ using an analytical parameter similar to lifetime (Martinez-Olmos et al. 2011, Palma et al. 2007) and also the intensity of the luminescence in a stationary excitation state which is quantified by a color measurement (Lopez-Ruiz et al. 2012). Here, this luminophore is used to create a tag for smart packaging oriented to the monitoring of oxygen in a modified atmosphere.

5.1.1 Material and methods

The chosen substrate was 125 μm thick polyethylene naphthalate (PEN, Kaladex[®] PEN Film, Dupont Teijin Films[™], Japan). The film must present a high transparency to visible light due to application requirements. Polyethylene terephthalate (PET) is widely used in packaging applications, so we considered it in the first place. PEN polyester is chemically quite similar to PET but is more temperature resistant and certified for long term electrical use. Although both materials have a high optical transmission (>85%) in the visible spectrum, PEN was finally selected because of its better adherence. It is, however, more expensive and have a lower flex life.

Manufacturing of the prototypes was performed with the optimal conditions reported previously to manufacture HF smart tags: a 120 (T/cm) mesh was used with SunTronic CRSN 2442 silver ink (Sun Chemical, Parsippany, NJ, USA). Placement and attaching of the chips were carried out with process described on Chapter 3.

For the electrical characterization of the system, the following instrumentation was used: a mixed signal oscilloscope (MSO4101, Tektronix, Beaverton, OR, USA), an 8½-bit Digital Multimeter 3158A (Agilent Technologies, Santa Clara, CA, USA), a 15 MHz waveform generator 33120A (Agilent Technologies, Santa Clara, CA, USA), an E5071C network analyzer, a N4431A kit (Agilent Technologies, Santa Clara, CA, USA), a Precision Impedance Analyzer 4294A and an impedance probe kit (4294A1) (Agilent Technologies, Santa Clara, CA, USA), a DC power supply E3630A (Agilent Technologies, Santa Clara, CA, USA) and a RFID reader TRF7960 (Texas Instruments, Dallas, TX, USA). A user interface made in Visual Basic© was used in a computer for calibration purposes. All chemicals were weighed with a DV215CD balance (Ohaus Co., Pine Brook, NJ, USA) with a precision of ± 0.01 mg.

The chemicals used were as follows: platinum octaethylporphyrin complex (PtOEP, Porphyrin Products Inc., Logan, UT, USA), 1,4-diazabicyclo[2.2.2]octane (DABCO, 98%), tetrahydrofuran (THF) and polystyrene (PS, average MW 280,000, Tg: 100 °C, GPC grade). All three supplied by Sigma–Aldrich Química S.A. (Madrid, Spain). The gases O₂ and N₂ (>99%) were supplied in gas cylinders by Air Liquid S.A. (Madrid, Spain).

The standard mixtures for instrument calibration and characterization were prepared using N₂ as the inert gas by controlling the flow rates of the different high purity gases O₂ and N₂, entering a mixing chamber using a computer-controlled mass flow controller (Air Liquid España S.A., Madrid, Spain) operating at a total pressure of 760 Torr and a flow rate of 500 cm³·min⁻¹.

A thermostatic chamber, with a lateral hole for the connection to a computer and gas tubing entrance, made possible to maintain a controlled temperature between -50 °C and +50 °C with an accuracy of ± 0.1 °C for thermal characterization of the tag.

The cocktail for the preparation of the oxygen-sensitive membrane were made by dissolving 0.5 mg of PtOEP and 12 mg of DABCO in 1 mL of a solution of 5% (w/v) of PS in freshly distilled THF. The sensitive membrane was cast by placing a volume of 10 μ L of the cocktail on a flexible substrate using spin-coating technique under ambient atmospheric conditions. After

the deposition of the sensing membranes, the substrate containing them was left to dry in darkness in a THF atmosphere for 1 h. The obtained membranes were homogeneous, transparent and pink colored. The sensing membranes containing PtOEP in PS are recommended to be cured in darkness for 9 days before their use (Perez de Vargas-Sansalvador et al. 2009) . When they are not in use, they must be kept in darkness to extend their lifetime.

5.1.2 Tag architecture

The monitoring system for intelligent packaging presented here determines the concentration of gaseous O₂ by means of the measurement of the intensity of the luminescent emission generated in the membrane which is quenched by O₂. Classically, the scheme for the intensity measurement consists of a photo detector such a photodiode that generates a current proportional to the incident light. Nevertheless, it is possible to substitute this kind of photo detectors by color detectors, whose output is a signal proportional to the color of the incident light and the intensity of this color (Capitan-Vallvey et al. 2007) This strategy for the quantification of light intensity has proven to be highly sensitive and allows discarding external interferences (Lopez-Ruiz et al. 2012, Park, Hong and Kim 2010, Schaferling et al. 2003). Therefore, here it is used instead of the classical light measurement through photodiodes.

This intensity is quantified using the red (R) coordinate of the RGB color space obtained directly as the output of a digital color detector when it is reached by the light of the luminophore previously described. The system can be considered to be formed by two blocks: the sensing module, which excites the oxygen sensitive membrane and detects the luminescence, and the transmitting module formed by a RFID tag for the remote reading of the measurement.

The sensing module is schematized in Figure 53. This block is formed by the excitation and detection electronics together with the oxygen sensing membrane. The optical excitation of the membrane is carried out using a surface-mount LED (OCU-400UE390, OSA Opto Light, Berlin, Germany) with peak emission at 385 nm. The luminescence generated by the luminophore when it is optically excited is dynamically quenched by oxygen,

thus causing changes both in phosphorescence intensity and lifetime (Schaferling et al. 2003). In this case, luminescence intensity is selected to be related to the concentration of the surrounding gaseous oxygen. This emission is registered by means of a color detector model S9706 (Hamamatsu Photonics, Japan). This colour detector has been already used on the determination of virgin olive colour in our previous work (Salmerón et al. 2012). This device is a digital color sensor sensitive to red ($\lambda_p=615$ nm, the wavelength of maximal sensitivity), green ($\lambda_p=540$ nm) and blue ($\lambda_p=465$ nm) spectral regions, which makes possible the simultaneous measurement of RGB color coordinates. The detected signals are a 36-bit serial word, which make it possible to connect directly the sensors to the microcontroller. To enable measurement over a wide range of illuminants, the S9706 detector has two configuration parameters to select its active area and integration time. Internally, the active area of each detector (with dimensions of 1.2×1.2 mm) consists of 9×9 silicon photodiode elements in a mosaic, alternating red, blue and green sensitivity, and it can be configured in a high sensitivity mode, where the full area collects the incident light, or in a low sensitivity mode, where a 3×3 center area is chosen to be active. In this work, a high sensitivity mode was always chosen to cover a wide membrane surface. The integration time can be modified by software, and it determines the temporal window in which the detector is collecting the incident light. The response time and resolution of the system are depending on this parameter, as it will be explained below.

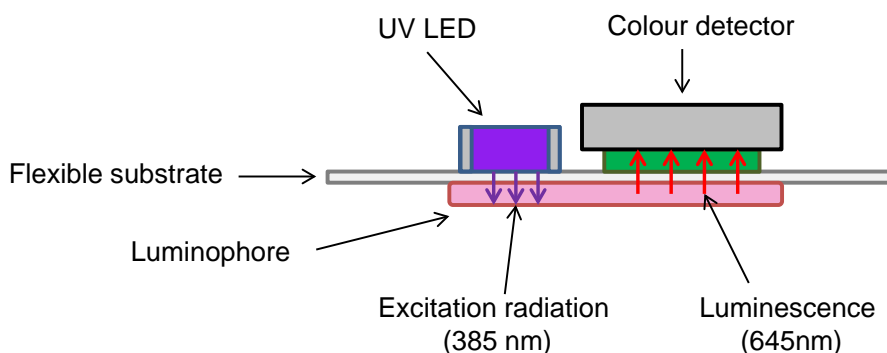


Figure 53. Side view of the sensing module.

Although simultaneous reading of the RGB components in the incident light is provided, only the red and blue coordinates are considered in this case, being the green value irrelevant. When the system is optically isolated to avoid external light interference, the R value corresponds exclusively to the luminescence generated by the PtOEP complex and its value depends on the intensity of this emission and, therefore, on the O₂ concentration (Lopez-Ruiz et al. 2012, Park et al. 2010). The B value of the reading is related to the visible emission of the LED and it is used as a reference signal to correct fluctuations in the source illumination (Wang et al. 2010).

As it can be seen in Figure 54, the layout of these components is as follows: the luminophore is deposited on the inner surface of flexible substrate (PEN). In this way, this is the only element of the system that is placed inside the package, whereas the full electronics is printed on the outer side of the substrate. The LED for the optical excitation as well as the color detector are placed very close one to another, and facing directly the membrane from the external side of the substrate. Although in the literature similar dispositions of the sensing elements are reported, it is common to manipulate the substrate in an effort to make out of it a waveguide to transport the excitation and response emissions (Courbat et al. 2011, Mayr et al. 2009, Saini 1995). It inevitably implies optical losses in the propagation of the light (Courbat et al. 2011). In order to avoid these losses, we have treated the package surface merely as a substrate for the system, and both the exciting emission as the response luminescence travel directly from the LED to the membrane, and from the membrane to the color detector, as depicted in Figure 53.

Both the LED and the S9706 detector are connected directly to a PIC18F46J50 microcontroller (Microchip Technology Inc., Chandler, AZ, USA) which has been selected because of its low power consumption (nanoWatt XLP Technology). In order to avoid thermal drifts, the LED is biased in a pulsed mode by the microcontroller, which introduces a pulse train of a high frequency (500 kHz) and 3.3V between its terminals. This biasing configuration eliminates the use of a current source in the design, thus simplifying the system, as it will be exposed below.

The block diagram of the proposed RFID tag is presented in Figure 54. It is a microcontroller-based system designed for a wireless transmission of the

oxygen concentration within the package. This diagram is similar to HF smart tag for humidity and temperature monitoring presented in the previous chapter. This scheme is aimed to transmit the measured data using the protocol ISO15693 which operates in the High Frequency (HF) band (13.56 MHz). The objective is to print the designed antenna and all the electronics on a flexible substrate which makes the package.

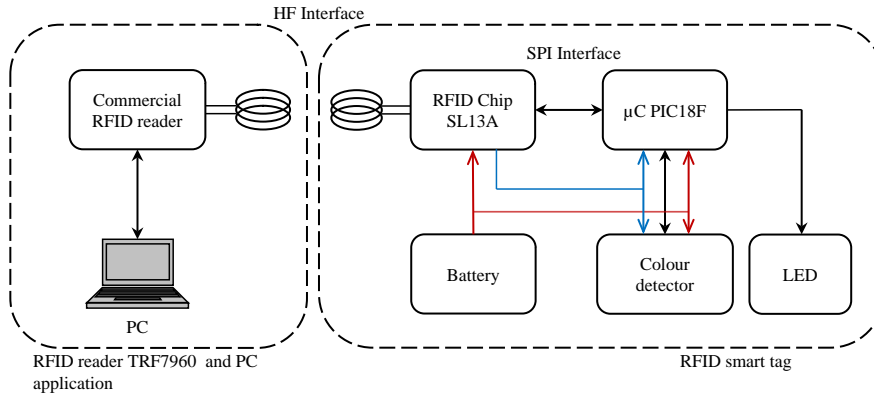


Figure 54. Block diagram of the developed RFID tag. Black connections represent data lines, red connections are principal power lines and blue connections are secondary power lines.

The SL13A (IDS Microchip AG, Wollerau, Switzerland) has been selected as the RFID chip. This device includes, apart from the RF interface, an on-chip 8k bit EEPROM and an on-chip temperature sensor. Apart from the RF ISO 15693 interface, this chip works with the SPI interface which allows access to its EEPROM memory and temperature data through the microcontroller. In this regard, it is possible to store data on the RFID chip memory that could be read out easily by a commercial RFID reader. In addition, the IDS-SL13A is supplied from either the battery or through the RF field from a reader, making possible to operate in passive or active mode. The chip has an internal regulator capable of providing a voltage output of 3.4 V and a maximum current of 4 mA for the rest of the circuitry when it is supplied from the reader. Therefore, it is possible to configure the system as a passive tag that only measures the oxygen when the user requires a reading, with no need of additional power supplying (blue powering lines in Figure 54). However, we have included a battery to give the option of a periodic oxygen measurement and data storing when the external RFID reader is not present (red lines in Figure 54). In this second operation mode, the measured

values of oxygen and temperature including a timestamp in UTC format are stored on the system memory. Furthermore, the system can be configured to store the information only when the acquired data is out of threshold values by setting the highest and lowest values of oxygen detection.

The antenna is a custom-designed screen printed inductor. The chosen RFID chip has a capacitance of about 25 pF at the frequency of interest. HF antennas presented on chapter 2 were designed for M24LR64 RFID chip whose capacitance is 30 pF. Then a re-design of the antenna was carried out in a similar way that described on Chapter 2. Resonance occurs when $\omega_0=1/\sqrt{LC}$, thus a value of 5.5 μH for the coil antenna must be achieved to resonate at the desired frequency without including external capacitances. The printed coil inductor is finally designed with 7 turns and dimensions of 75 mm \times 45 mm. The width of the conductor and the inter-spacing between the lines are each 600 μm .

A polymer Lithium-ion battery PGEB01 (General Electronics Co, Shenzhen, P.R. China) has been used to power on the tag when it is used in active mode. This is a rechargeable battery of 3.7V and a charge of 40 mAh. A HF band commercial reader, TRF7690EVM (Texas Instrument Inc, USA) fully compatible with ISO15693 protocol, has been used to test the developed RFID tag. A Visual Basic application (Microsoft Corp., Redmond, WA, USA) has been developed to configure and read out the manufactured RFID tag.

5.1.3 Experimental Results

Figure 55 presents photography of the full system, where all the components described in the previous section are marked. It is to be noted that the sensing block must be darkened in order to avoid external light interference. This can be done by covering the sensing module with adhesive black insulating tape.

As we have already explained above, the luminophore is excited with a radiation of 385 nm generated using an UV LED. This corresponds to one of the absorption peaks of the PtOEP complex, being the other peak at 537 nm wavelength which has been used in other works (Capitan-Vallvey et al. 2007, Pérez de Vargas-Sansalvador et al. 2010). Nevertheless, in those previous

cases the measurement of the gaseous oxygen was based on the lifetime of the luminescence generated in the sensing membrane. In this work, a relationship between oxygen concentration and luminescence intensity is searched, and this intensity is quantified by means of color measurements. For that reason, an excitation in the UV range is selected in order to avoid environmental light interferences in the color detection (Lopez-Ruiz et al. 2012).

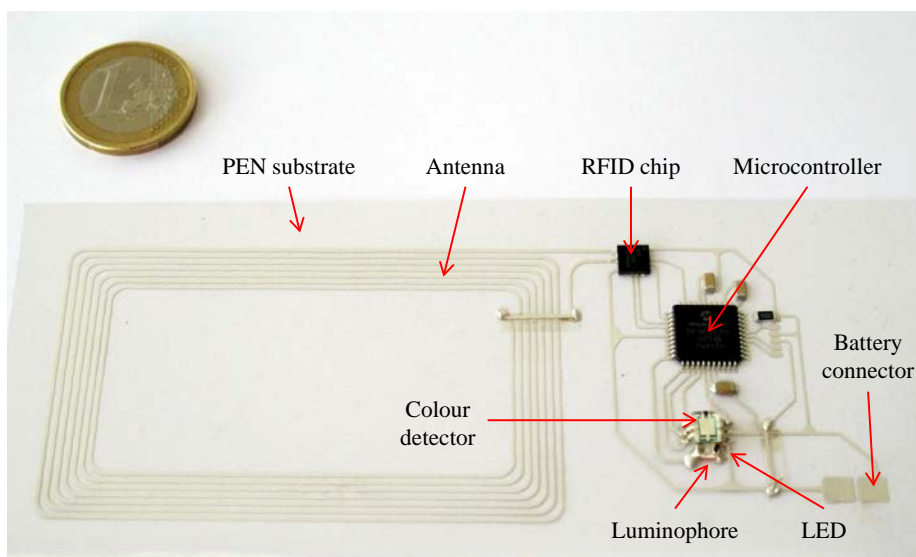


Figure 55. Photography of the system. The sensing module has been uncovered to show its structure.

System calibration

The color detection is carried out after the membrane is excited by the UV radiation emitted by the LED. In previous work, this LED was biased using a custom-designed current source that led the LED to a steady state in which it drove a fixed current. In this state, the precise moment to take the measurement became critical, since the excitation with the UV radiation produces an increase in the temperature over time that affects the intensity of the emitted luminescence (Lopez-Ruiz et al. 2012). To overcome this situation, we have directly biased the LED through the microcontroller, which introduces a voltage pulse train between the terminals of the LED of 3.3V high and 500 kHz. In consequence, the current source is not necessary and the number of components in the electronics and, thus, the consumption

of the systems are reduced. The high frequency in the biasing of the LED implies a period of alternation between on and off states for the LED of $2 \mu\text{s}$, much lower than the response time of the luminophore which is in the range of hundreds of microseconds (Pérez de Vargas-Sansalvador et al. 2010). Therefore, the sensing membrane is not affected by this LED commutation, and thermal drifts are minimized. In addition, the integration time of the color detector S9706 varies in the range of hundreds of milliseconds, as will be exposed below; in this period of time the detector is collecting incident light, and variations of the luminescence due to the LED commutation are minimized by the integration of the total incident light in this period. In this situation, the color measurement can be carried out at any moment after the LED is polarized. However, a small delay of 0.5 seconds is elapsed before the measurement in order to get a stabilized state of the LED. Moreover, fluctuations of the emitted radiation of the LED can appear if the power line of the microcontroller is not completely stable. These fluctuations can introduce variations in the membrane response with deeper effects than those due to the LED commutation. In order to correct this effect, the R coordinate given by the color detector is normalized by the B coordinate, whose value corresponds to the LED radiation captured by the color detector. Consequently, the oxygen concentration is related to the ratio R/B, being R and B the values of the red and blue coordinates given by the color detector S9706.

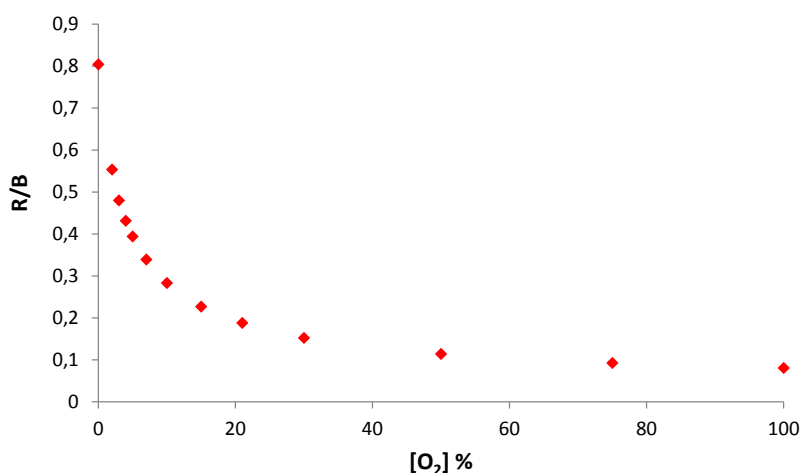


Figure 56. Response curve of the oxygen RFID tag (21 °C).

The relationship between oxygen concentration and the value of the R/B coefficient is shown in Figure 56, where the response curve of the system in the full range 0 to 100 % O₂ is presented. These data include six replicas at room temperature (21 °C) and the integration time of the color detector was set to 200 ms. Although error bars are included in this figure (and following ones), they are too small to be appreciated.

As it can be seen, the intensity of the luminescence decreases with the oxygen concentration. The response curve in Figure 56 can be fitted to a Freundlich isotherm for luminescence, see Figure 57, which models a non-linear Stern-Volmer behavior and can be represented in the simplest form as (Carraway et al. 1991):

$$\frac{I_0}{I} - 1 = \alpha [O_2]^\beta \quad (53)$$

Where I is the intensity of the emitted luminescence, I_0 the intensity in the absence of oxygen, and α and β are fitting parameters. The fitting curve for the response of the sensor is presented in Figure 53, for which $\alpha = 0.30$ and $\beta = 0.7635$ (correlation factor $r^2 = 0.995$).

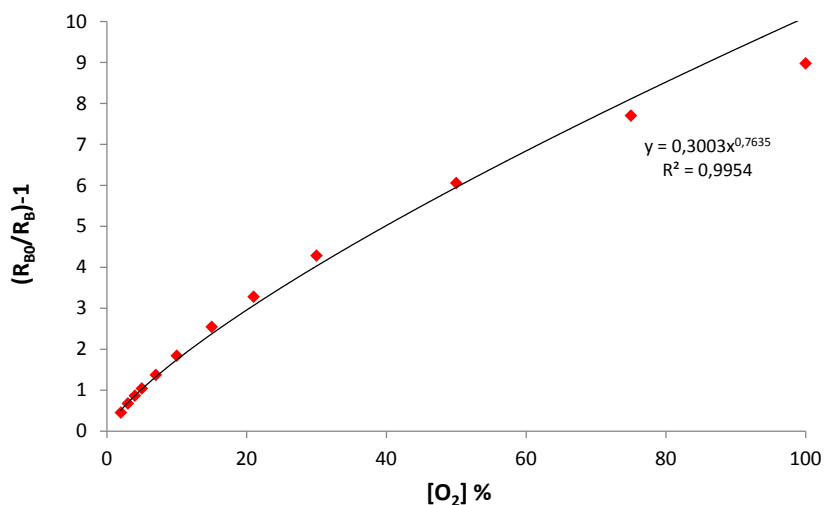


Figure 57. Calibration curve of the oxygen RFID tag.

The parameters R_B and R_{B_0} denote the ratios R/B and R_0/B_0 , respectively, which correspond to the measurement of the intensity of the luminescence in presence and absence of oxygen, as explained above.

The technical specifications of the system, such as resolution and response time depends directly on the integration time selected for the measurement. This parameter establishes the period of time in which the color detector is collecting the incident light. It is evident that the output data of the detector is higher if this time is longer, resulting in better characteristics of the system. In Figure 58 several response curves of the sensitive membrane, corresponding to different integration times, are depicted. As it can be seen, the higher the integration time, the broader the range of the R coordinate, which implies a better resolution, as it will be exposed in the following figure.

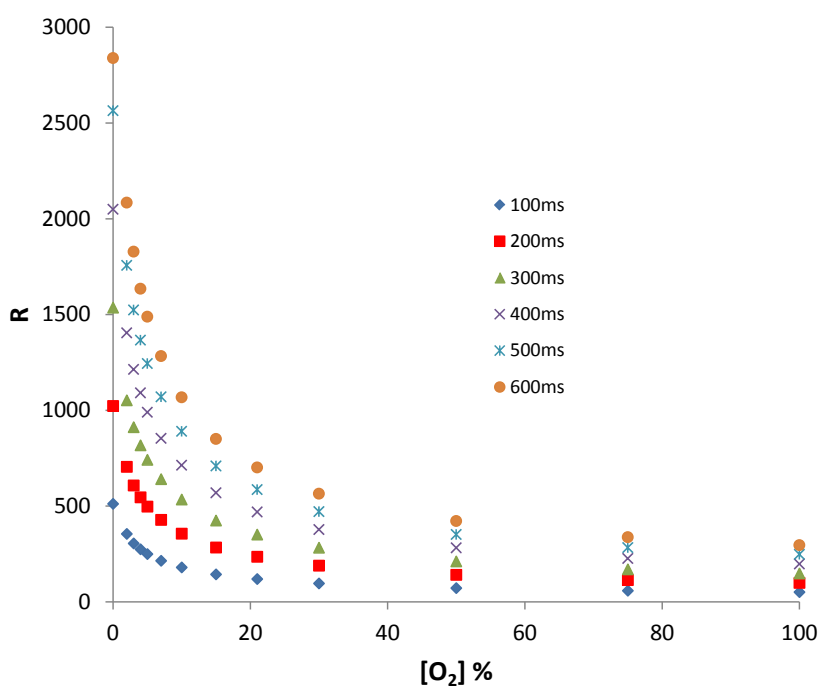


Figure 58. Response curves for different integration times.

The theoretical resolution of this system can be derived from the fitting curve of Equation 53 by taking derivatives in both sides, approximating these derivatives to increments and reorganizing the terms, so that the theoretical resolution is obtained as:

$$\Delta O_2 = \frac{I_0 \left(\frac{I - I_0}{I\alpha} \right)}{I\beta(I - I_0)} \Delta I \quad (54)$$

where ΔI is the maximum resolution in the measurement of the light. This parameter is related to the resolution of the color detector. Although it is not specified in the datasheet of the S9706, it is common to take a reading error of ± 4 LSB for the internal analog to digital converter in these devices. Therefore, taking into account that the resolution of the color detector is 12 bits, the value for ΔI is 0.19%. From Eq. 54, the results of resolution for the different integration times of Figure 58 are calculated at several oxygen concentrations and presented in Table 17. These data confirm that better values of the resolution are achieved when higher integration times are used, being the maximum reachable without producing a saturation of the detector of 0.07 ppm of O_2 , which is a very low value. This value improves significantly the resolution obtained in previous works (Palma et al. 2007, Pérez de Vargas-Sansalvador et al. 2010) where the resolution was 5000 and 500 ppm, respectively. These results demonstrate that quantifying the intensity of the luminescence by a high resolution color detector is a good alternative to classical measuring approaches where the intensity of the signal is registered by simple photo detectors. The accuracy achieved with the RFID tag depends on the oxygen concentration, being 0.02% and 0.14% at 2% and 21% of O_2 respectively.

Table 17. Theoretical resolution of the system in ppm at different O_2 concentrations.

Integration Time (ms)	2% O_2	10% O_2	21% O_2
100	0.4	2.4	6.6
200	0.2	1.2	3.3
300	0.2	0.8	2.2
400	0.1	0.6	1.7

Another important technical datum is the limit of detection (LOD). This parameter was obtained using the standard criteria: $LOD = y_b + 3s_b$, where y_b is the average blank signal and s_b is the standard deviation of the blank, which is determined using at least 10 replicas. In this case, the LOD is independent of the integration time and takes a value of 50 ppm of O_2 , which

confirms that the system here presented is suitable for smart packaging where the food are preserved at very low oxygen concentrations.

As discussed in previous works, the temperature has a notable influence on the quenching produced by the oxygen in the light emission of a luminophore (Lopez-Ruiz et al. 2012, Pérez de Vargas-Sansalvador et al. 2010). Therefore, this effect has to be characterized and corrected. With this aim, we carried out a study of the instrument response for different temperatures. Figure 59 represents the instrument response at different temperatures. The curves were obtained using six replicas for each oxygen concentration at a given temperature. As it can be seen, the increase in the temperature reduces the intensity of the luminescence generated by the membrane causing a lower red signal. This effect was modeled introducing the thermal dependence in the fitting parameters α and β which can be expressed as a polynomial function of the temperature in the form $\alpha = -1.09 \cdot 10^{-5} \cdot T^3 + 5.14 \cdot 10^{-4} \cdot T^2 - 4.35 \cdot 10^{-3} \cdot T + 0.198$ ($r^2 = 0.981$), $\beta = 8.22 \cdot 10^{-6} \cdot T^3 - 3.85 \cdot 10^{-4} \cdot T^2 + 3.39 \cdot 10^{-3} \cdot T + 0.797$ ($r^2 = 0.987$) with T in Celsius degrees.

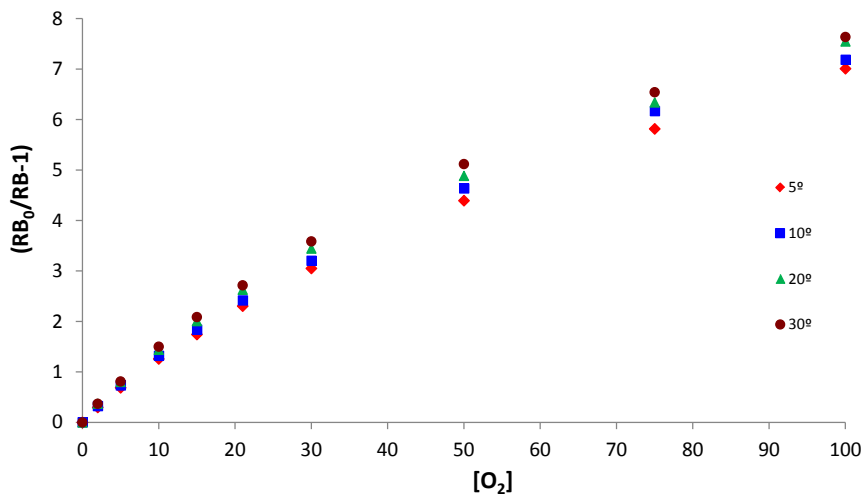


Figure 59. Thermal dependence of the oxygen RFID tag.

As we have exposed above, the RFID chip used in this work has an on-chip temperature sensor which is able to obtain temperature readings in the range -40 °C to 60 °C, with an accuracy of 0.5 °C. The 10 bits temperature value is obtained from the RFID chip through an on-chip A/D converter which uses a

calibrated bandgap reference as reference voltage. Through this feature, it is possible to correct the measurement of the oxygen including the previous modeling of the fitting parameters α and β in the microcontroller.

RF characterization

Due the new antenna designed for the SL13A RFID chip, a fully characterization of the antenna has been carried out by means of simulations and experimental analysis, showing a good concordance in the results and proving that flexible RFID tags are recommendable for this application. The RF electrical characterization for the fabricated coil inductors has been performed by measuring their inductance quality factor and equivalent circuits. The values obtained by simulation for the induction and quality factor are $5.62 \mu\text{H}$ and 2.676 , respectively, whereas the experimental values are $5.8 \mu\text{H}$ and 3.5 at the resonance frequency of 13.56 MHz . Although these values are in concordance, we have detected a reduction of the self-resonant frequency of the inductors, 32 MHz , was slightly lower than the simulated one, 35 MHz , as shown in Figure 56. These results are in concordance with the obtained in chapter 2 and confirm that the inductance value of the coil is hardly affected by the substrate.

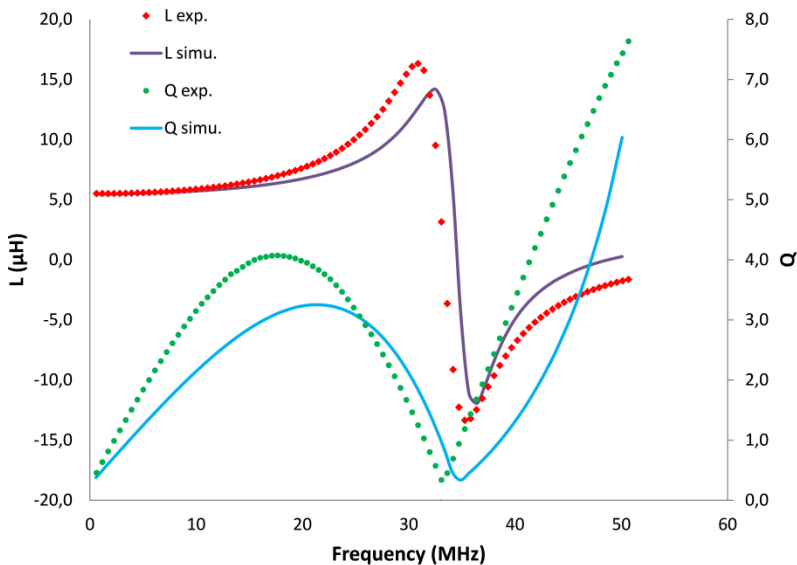


Figure 60. Simulated (lines) and measured (symbols) frequency response of the antenna.

The operation of the antenna tag has been tested with the commercial RFID reader TRF7960 with a read range of around 15 cm in vertical direction and 13.2 cm in horizontal one in passive operation mode. The resonance frequency of the full system antenna-RFID chip has been evaluated through an impedance analyzer. In Figure 60 the impedance of the tag is presented, where it has been decomposed in phase and module. As it can be observed on Figure 61, the impedance reaches a value of 1.6 k Ω at the resonance frequency, that is the one at which the phase is null, in this case 13.6 MHz. Although this value is not exactly the working frequency searched of 13.56 MHz, it is perfectly valid for a wireless operation following the ISO15693 protocol specification related to anti-collision mechanism that establishes a tolerant range of ± 7 kHz around this center frequency.

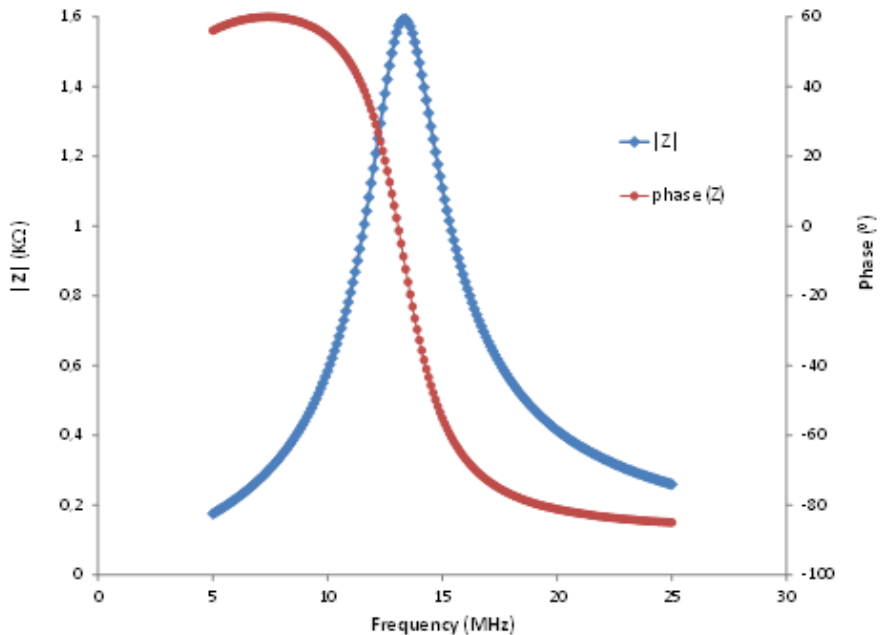


Figure 61. Impedance of the tag as a function of the frequency.

The proper operation of the label has been tested satisfactorily through the developed Visual Basic application. Battery power is not necessary to access the stored data on the RFID chip making the label a semi-passive smart tag for sensing applications. The power consumption of the RFID tag is only 34.4 μ A in idle mode and 3.55 mA in sensing mode. This value is low enough (below 4 mA) to be provided by the internal regulator of the SL13A

RFID chip, which makes possible to operate as a passive tag with no need of an extra battery.

5.1.4 Conclusions

We have shown a high resolution, long-life system for the determination of the oxygen concentration which allows users (producer, distributor, seller or consumer) to monitor the content of O₂ inside the package. The reading of the oxygen concentration inside the envelope can be carried out with an external RFID reader using a wireless communication. This means that the packaging remains completely closed, with no need of perforations for probes or wires. Thanks to its high resolution, readings of O₂ can be realized at concentrations as low as 40 ppm of O₂ with very low error levels in the order of 0.1 ppm of O₂. Temperature drift is corrected through the on-chip temperature sensor. Therefore, this system is highly suitable for its application in the measurement of oxygen concentration in modified atmosphere packaging with a reduced oxygen concentration.

5.2 Single-chip passive UHF tag for humidity monitoring

Here, we present the design, fabrication and characterization of two printed RFID tags with temperature and relative humidity sensors. These passive tags are screen-printed on a flexible substrate and each one includes a different printed capacitive structure which enables to measure the relative humidity.

The first tag contains a new Serpentine (SRE) electrode configuration due to their higher sensitivity than the conventional interdigitated (IDE) electrodes (Rivadeneira et al. 2014b). The drawback of this approach is the fact that this sensor is defined by inkjet-printing to achieve better pattern resolution and, therefore, two different printing processes are implicated. In order to ease the manufacturing process, we present the second tag. In this particular case, the sensor is fabricated by screen printing but, due to the lower resolution of this printing technique, the sensor size is significantly bigger in order to get a similar capacitance value. As remarkable features, the architecture is based on printing technologies as fabrication process and with

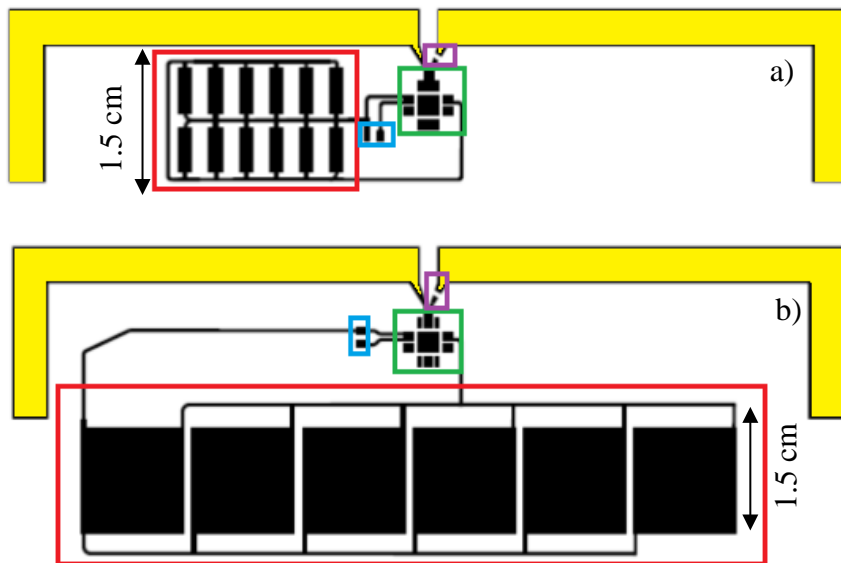


Figure 62. Schematics of the two RFID tags with (a) array of capacitive humidity sensors by inkjet printing and (b) array of capacitive sensor by screen printing (highlighted in red). Both tags include the same antenna design (in yellow) and the same chip RFID (in green). The external matching network has been remarked in purple and the reference capacitance in blue.

only a single chip architecture, where the sensor data, in digital form, can be reliably delivered to the UHF RFID reader. Material, methods and design

Figure 62 shows the architecture of the two types of printed tag, including the footprints of the different components required. Both tags present a passive architecture based on SL900A RFID chip (AMS AG, Unterpremstaetten, Austria) compatible with EPC Gen 2 RFID standard. The RFID chip was chosen due to the integration of a Sensor Front End (SFE) that includes a capacitive sensor conditioning stage and 10-bits Analog to Digital Converter (ADC). This extra circuitry has been used to interface the relative humidity capacitive sensor. Furthermore includes an on-chip temperature sensor. In this regard we will be able to measure capacitance values of the humidity sensor and, if necessary, perform thermal compensation to the acquired values.

Two types of printed humidity sensors are presented and they can also be seen in Figure 62. In both cases, humidity sensors consist of several capacitive elements in parallel with the aim of achieving a total capacitance

of around 36 pF, well above the parasite capacitance of the RFID chip connections which is about tenths of picofarad. The only difference between these layouts is the footprint of the array of printed sensors, fabricated with different printing techniques, and placed in parallel to sum up a bigger sensor capacitance. The radiofrequency interface consists on the dipole antenna resonating at 868 MHz and a RF Surface Mount Device (SMD) inductor used to match the chip input impedance already described on chapter two (Rao et al. 2005).

Temperature value comes from a conversion in the on-chip A/D converter of the SL900A. The minimum resolution is 0.18 °C in a range of 189.9 °C while a resolution of 0.23 °C is obtained with the widest range of 237.2 °C.

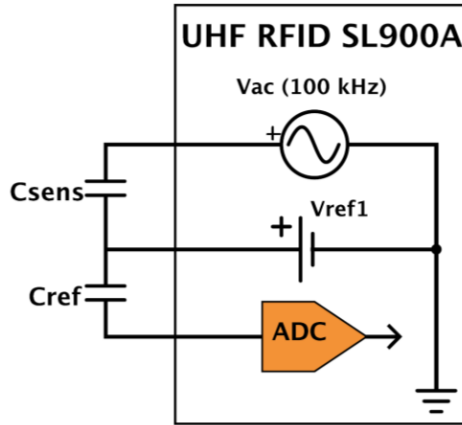


Figure 63. Diagram showing the external capacitive sensor mode of the RFID chip with AC signal excitation.

Two internal voltage references, V_{ref1} and V_{ref2} individually selectable in steps of 50 mV between 160 and 610 mV, set the lower and upper limits of the ADC converter. These limits are defined as $2 \cdot V_{ref1} - V_{ref2}$ and V_{ref1} . The difference between them defines the input voltage range, $V_{ref2} - V_{ref1}$, and the limits of operation. These voltage references can be set in the user application and, therefore, a concrete resolution and range can be selected by the user.

The printed humidity sensor is directly connected to the SFE of the RFID chip. To read out the capacitance value, the SFE is configured in capacitance mode. In this mode, an external reference capacitor has to be placed in series

with the printed sensor as shown in Figure 63. The sensor capacitance is excited with a 100 kHz square wave signal whose amplitude is equal to V_{ref1} voltage. This AC signal is generated with a voltage offset of V_{ref1} so the amplitude signal goes from 0 to $2 \cdot V_{ref1}$. The input voltage on the ADC associated with the capacitance value is:

$$V_{ADC} = V_{REF1} \frac{C_{REF}}{C_{REF} + C_{SENS}} + V_{REF1} \quad (55)$$

There is no auto ranging capability on the ADC; therefore the reference capacitor has to be properly chosen according to the expected sensor capacitance. According to Eq. 55, the term composed by the division of C_{ref} and $C_{ref}+C_{sens}$ governs the input voltage change. At maximum sensing capacitance value ($C_{sens} \gg C_{ref}$) the input voltage should be close to V_{ref1} whereas at minimum sensing capacitance value ($C_{sens} \ll C_{ref}$) the input should be close to $2 \cdot V_{ref1}$. In our concrete case, we are interested in reading a small change in capacitance between two known values, the sensor capacitance at 0% and 100% levels of relative humidity (RH). Sensor capacitance shift causes a change in the $C_{ref}/C_{ref}+C_{sens}$ term. The reference capacitance should be chosen to maximize this change: the sensor capacitance value at 50% of RH. The selection will cause not to cover the full input range; the term $C_{ref}/C_{ref}+C_{sens}$ will not be never 0 (lower limit) or 1 (upper limit). Taking advantage of V_{ref2} the upper limit of the ADC can be settled to a lower value to maximize the performance of the ADC.

All the patterns were printed on a polyimide substrate with 75 μm thickness (Kapton® HN, Dupont™, Wilmington, DE, USA). With regard to the humidity sensors, no sensing layer was deposited onto the electrodes, being the substrate the only element which changes with the relative humidity. This polyimide is a well-known and broadly used material (Harrey et al. 2002, Rivadeneyra et al. 2014a, Virtanen et al. 2010b) whose electrical permittivity, ϵ_r shows a high sensitivity to the relative humidity according to the following expression given by the manufacturer of the substrate:

$$\epsilon_r = 3.05 + 0.008 \cdot RH(\%) \quad \text{at } 1 \text{ kHz, } 23 \text{ }^\circ\text{C} \quad (56)$$

where RH (%) is the relative humidity in percentage...

The first tag design incorporated an inkjetted printed SRE sensor, see Figure 64a, to measure the relative humidity. For its fabrication, a DMP-2831™ Dimatix printer (Fujifilm Dimatix Inc, Santa Clara, USA) was used for inkjet printing of the electrodes. The employed silver ink was U5603 (SunTronic Technology, San Diego, USA) with a solid content of 20% of silver nanoparticles dispersed in ethanol/ethanediol. The substrate temperature was fixed at 40°C while printing with the DMP-2831. For minimum area, a drop space of 25 μm was settled in the printer for 50 μm landed diameter drops followed by a sintering step at 120°C for 60 min. Sintering took place in two different stages; a ramping of the temperature from room temperature to 160°C at 3°C/minute, followed by an hour at constant 180 °C temperature. According to the thickness model presented, the obtained thickness is $0.43 \pm 0.05 \mu\text{m}$ and the resistivity $23 \pm 0.8 \mu\Omega\cdot\text{cm}$.

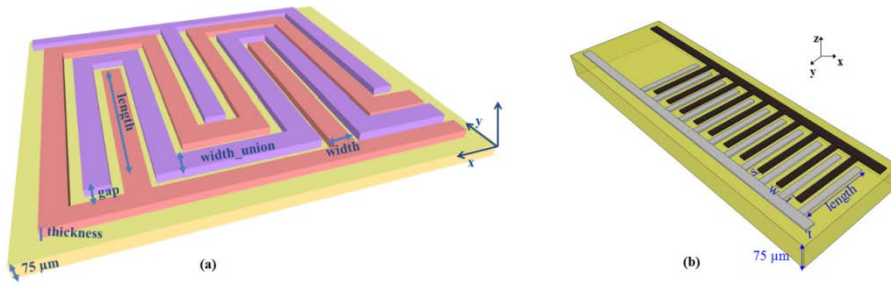


Figure 64. (a) Layout of the designed SRE capacitor indicating the notation of the dimensions and the Cartesian axes and (b) Layout of the designed IDE sensor (w = width, s = distance, i = interspacing, t = thickness).

Alternatively, the second tag design will test a screen printed IDE sensor. Screen printed patterns were manufactured with a Serfix III screen printing machine (Seglevint SL, Barcelona, Spain). The screen used to manufacture the tags had a mesh density of 120 Nylon thread per centimeter (T/cm) to fabricate them with only a single-layer screen printed of conductive silver ink CRSN 2442 (Sun Chemical Corporation, Parsippany, USA). With the same criterion as the former case, the minimum spatial resolution for a reliable fabrication process was 150 μm. Sintering took place at constant 120 °C of temperature for 20 minutes.

Dipole antennas and chip interconnections were manufactured by screen printing on both tags design. Therefore, the second tag has been completely

printed by screen printing, reducing the number of fabrication steps. Finally, we carried out the three-step process to do the assembly of the chip.

The difference between the two tags is the capacitive structure and the printing technique and, as consequence of this latter, the dimensions. The first prototype includes an array of capacitive sensors based on the serpentine electrodes presented in (Rivadeneira et al. 2014b). We chose this design because it has been shown a higher performance than the traditional interdigitated electrodes. The manufacturing process is inkjet printing because it provides better resolution, saving area. The dimensions of each array element are presented in Table 18 for a targeted nominal capacitance (for one printed layer) of 2 pF and the final area was 11.65 mm^2 ($L = 1.85 \text{ mm} \times W = 6.3 \text{ mm}$) composed of 62 fingers (31 fingers for each electrode) with $50 \mu\text{m}$ width and inter-spacing (see Figure 60a).

On the other hand, the second tag incorporates an array of interdigitated electrodes manufactured by screen printing. We chose this design for the complete screen printed tag because the manufacturing yield is higher than the serpentine electrodes. The array element dimensions are presented in Table 19 for a targeted nominal capacitance (for one printed layer) of 6 pF and the final area was 2.25 cm^2 ($L = 1.5 \text{ cm} \times W = 1.5 \text{ cm}$) composed of 26 fingers (13 fingers for each electrode) with $150 \mu\text{m}$ width and inter-spacing (see Figure 64b).

Table 18. Physical dimensions of each of the inkjet-printed serpentine structures.

Parameter	Value	Description
Length	1.1 mm	Length of each finger (y-axis)
Width	$50 \mu\text{m}$	Width of each finger (x-axis)
Thickness	$0.5 \mu\text{m}$	Thickness of electrodes (1 layer) (z-axis)
Number	31	Total number of fingers of the larger electrode
Interspacing	$50 \mu\text{m}$	Distance between consecutive fingers (y-axis)
Distance	$50 \mu\text{m}$	Distance between fingers of one electrode and the backbone of the other electrode (x-axis)

Table 19. Physical dimensions of each of the screen printed interdigitated structures

Parameter	Value	Description
Length	1.5 cm	Length of each finger (y-axis)
Width	$150 \mu\text{m}$	Width of each finger (x-axis)

Thickness	10 μm	Thickness of electrodes (1 layer) (z-axis)
Number	13	Total number of fingers of the larger electrode
Interspacing	150 μm	Distance between consecutive fingers (y-axis)
Distance	150 μm	Distance between fingers of one electrode and the backbone of the other electrode (x-axis)

The AC electrical characterization for the different fabricated capacitors has been performed by measuring their capacitance and dissipation factor, using the four-wires measurement technique with a precision Impedance Analyzer 4294A and an impedance probe kit (4294A1) (Agilent Tech., Santa Clara, CA, USA). The excitation voltage applied in all measurements was $V_{DC} = 0$ and $V_{AC} = 500$ mV at 100 kHz. We have considered this frequency because it is the frequency of the excitation signal of the RFID chip for measuring capacitance. The stationary humidity and temperature responses of the tags have been measured in a climatic chamber VCL 4006 (Vötsch Industrietechnik GmbH, Germany). The humidity range varied from 10% RH to 98% RH in a temperature range of + 10 °C to + 95 °C. The humidity deviation in time was $\pm 1\%$ to $\pm 3\%$, whereas the temperature deviation in time was ± 0.3 °C to ± 0.5 °C. In the climatic chamber, we included two commercial sensors to monitor the temperature and humidity close to the sensors. These sensors are an analogue humidity sensor HIH4000 (Honeywell International Inc., Illinois, USA) with accuracy of $\pm 2.5\%$ and a digital thermometer RS Series A1 (RS Amidata S.A., Madrid, Spain) with resolution of 0.1 °C.

5.2.1 Experimental Results

Figure 65 shows the two smart RFID tags fabricated. Regarding dipole antenna characterization, dimensions and performance are those obtained in Chapter 3: final dimensions of the screen printed dipole antenna arms are 5.5 mm width and 79 mm length each one and dipole was designed to get the same real part of the impedance as the RFID chip, whilst the necessary large inductive part is achieved with a SMD inductor. The obtained parameters of the antennas by EM simulation at 868 MHz are gain of 0.661 dBi, directivity of 2.401 dBi and efficiency of 66.97%.

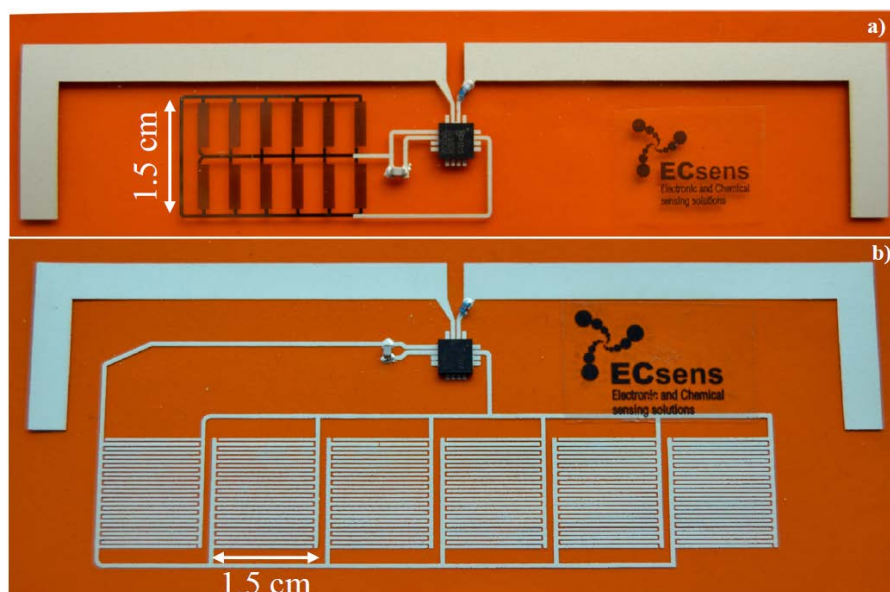


Figure 65. (a) RFID tag with inkjetted serpentine sensors and (b) RFID tag with interdigitated sensors by screen printing.

The measured read range is the maximum distance in which the reader was able to read out the tag including the sensing functionalities. It should be noted that the sensitivity of the RFID chip has a penalty. Chip sensitivity to answer identification inquiries of EPC protocol is -15 dBm whereas the sensitivity for reading out capacitance value is -2.21 dBm. The reason is to the required extra-power to drive the SFE that needs to be collected from the radiated EM field of the reader. According to Equation 51, the read range assuming ideal conditions (perfect matching between chip, $\tau = 1$, and the dipole antenna gain obtained by EM simulation, $G_{\text{tag}}=0.66$ dBi) should be 2.2 meters. The measured ranges for the printed tags are smaller than the simulated ones, 1.6 meters. These differences could be due to the non-ideal behavior of the metallic layers in printed electronic as already pointed out on previous chapters.

The capacitance of the serpentine electrodes has been measured at 100 kHz for different values of relative humidity in ascending and descending mode. The response of one sensor to changes in the relative humidity is directly extracted from the curves obtained with the impedance analyzer (Figure 66).

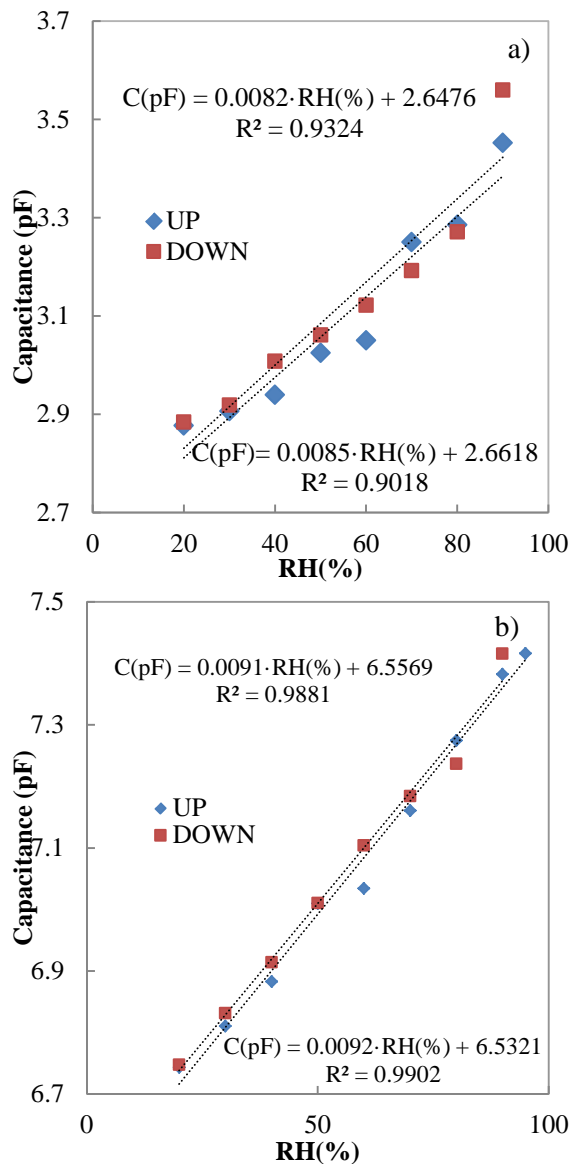


Figure 66. (a) Capacitance vs. Relative humidity for a single inkjetted printed serpentine capacitor and (b) Capacitance vs. Relative humidity for a single screen printed interdigitated capacitor.

Let's remember that we have built an array of sensors connected in parallel. Then, the total capacitance is the sum of the individual contributions. A total of 12 serpentine capacitors have been printed, therefore, the total expected capacitance is 32.4 pF at dry atmosphere. The sensitivity would also be multiplied by 12, resulting in 100 fF/%RH. The total measured capacitance

of the serpentine array at room conditions was 36 pF. The reference capacitance for this array was selected of 33 pF. An SMD capacitor size 0805 with 2% tolerance from Vishay (Vishay Intertechnology, Inc. PA, USA) was employed for this purpose. A preliminary manufacturing yield of 80% was reported for SRE capacitors (Rivadeneira et al. 2014b). In contrast to IDE capacitor, any printing error in the serpentine structure totally breaks the capacitor due to the higher complexity of this structure. This complexity also explains the lower fabrication yield in comparison with the IDE design (90%) (Rivadeneira et al. 2014a). In addition, broken fingers in IDE structure only results in a lower sensor performance but the sensor still works; whereas just one finger broken in SRE leads to the sensor uselessness.

The same characterization was carried out for the interdigitated electrodes manufactured by screen printing. The response of one sensor to changes in the relative humidity is directly extracted from the curves obtained with the impedance analyzer. As indicated before, an array of sensors connected in parallel has been implemented. Then, the total capacitance is the sum of the individual contributions. A total of 6 interdigitated capacitors have been printed, therefore, the total expected capacitance is 34.8 pF at dry atmosphere. The sensitivity would be multiplied by 6 as well, resulting in 54 fF/%RH. The number of screen printed IDE sensors was chosen to get a capacitance value similar to the inkjetted sensors array. We measured a total capacitance for this array of 38 pF at room conditions. The SMD 0805 reference capacitance (Vishay Intertechnology, Inc. PA USA) for this tag was selected of 39 pF as an optimum value after studying different capacitors of reference.

Temperature measurements are obtained directly from the on-chip sensor and present different errors and accuracy depending on the selected measurement range as mentioned above.

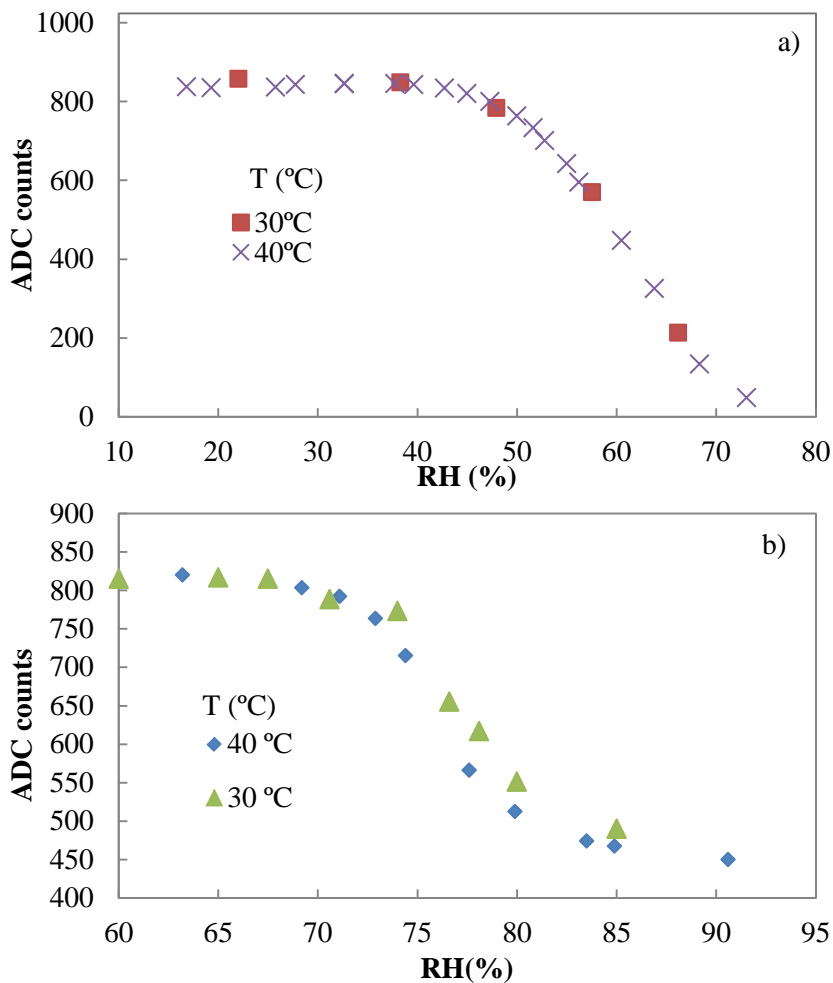


Figure 67. (a) ADC counts of tag with inkjetted serpentine sensor and (b) ADC counts of screen printed tag with IDE sensors.

After setting the voltages configuration, we characterized both tags varying the relative humidity at different temperatures. We stored 30 ADC data to know the deviation between measurements. This deviation was lower than 2 LSB of the ADC in all the studied cases. Figure 67 illustrates the average data obtained by the ADC on both tags. As can be seen in both graphs, the range of sensitivity is concentrated on a range of RH; that is, the whole range of RH cannot be read by just one tag. Looking at the prototype with SRE capacitors, it is not possible to distinguish values below 42.5% and above 75% RH. In the other tag, these limits are 57.5% and 87.5% RH. Therefore,

we can assume that the measurement range is about 30% RH independently on the sensor sensitivity neither the reference capacitance.

Figure 67a shows an output range approximately from 850 to 85, that is to say, more than 750 counts to be associated to a variation of the 30% RH. Whereas the values in Figure 67b change from about 820 to 450 counts, then only 370 counts can be used to discriminate this variation of the 30% RH. This result is coherent taking into account that the sensitivity to humidity is almost twice for serpentine sensors compared to IDE sensors.

Regarding the tuning of the tag, we can easily select the range of humidity where the tag is going to discriminate values by selecting the suitable value of reference capacitance. For example, we designed the tags for similar values of capacitance at room temperature but their ranges of discriminations are different: the central span of the inkjetted sensors is 58.5 % RH with a reference capacitance of 33 pF whereas this point is found at 72.5% RH for a reference capacitance of 39 pF.

With respect to the thermal drift, these values are 0.024 %RH/°C for the inkjetted serpentine structure and 0.044 %RH/°C for the screen-printed interdigitated structure. This results is in agreement with the results shown in our previous works (Rivadeneyra et al. 2014a) (Rivadeneyra et al. 2014b), where printed sensors on the same substrate had negligible thermal drifts.

5.2.2 Conclusions

The fabrication and characterization of full printed passive UHF RFID tags based on SL900A RFID chip including two different humidity capacitive sensors have been investigated. These tags have been printed on polyimide substrate (Kapton HN as humidity sensitivity element) comprising, apart from the printed sensors, a dipole antenna, a series inductance to match the RFID chip impedance, a reference capacitor necessary for capacitance measurements and the RFID chip. Both tags were able to provide temperature and relative humidity environmental parameters.

Taking advantage of the known behavior of polyimide with relative humidity, two different printed relative humidity sensors, fabricated by inkjet printing and screen printing respectively, have been interfaced to the RFID

chip. Capacitance values are obtained in digital form (10 bits) from the integrated ADC of the RFID chip. The tag with the inkjetted printed sensor presents a performance higher than the one obtained with the array of screen printed sensors. The former covers 800 counts of 1024 for a shift in RH from 37% to 70%. The latter covers 220 counts of 1024 for a shift in RH from 57% to 86%. Between these limits of RH, the obtained resolution and associated error are acceptable while out of these range the performance is reduced. The different performance among tags can be explained by the different number of devices (12 inkjetted vs. 6 screen-printed) that affects directly the obtained sensitivity of each array. The different obtained range of RH can be associated with the choice of the reference capacitor, 36 and 39 pF respectively. These capacitors can be tuned to monitor a concrete range of RH. The lack of performance of the ADC can be explained by the fact that the SFE of the RFID chip has been designed to interface different type of sensors, e. g., resistive, and not specific for capacitance.

The drawback of the inkjetted sensor approach is the need of mixing techniques, inkjet and screen printing, implying a complex fabrication with different sintering process and alignment. The screen printed sensors approach can be fabricated with just one step but a much bigger area is required. Therefore, the tag choice will depend on the restrictions of each application, basically in terms of sensitivity and area. Energy to power up the tag and drive the sensor stage is extracted from the radiated field of the RFID reader. Thus, the proposed tags are passive and composed by a single silicon chip providing a cost-effective solution to monitor environmental properties.

5.3 Single-chip passive HF tag for humidity monitoring

Here, we present the development of a several RFID tags on the HF band whose resonance frequency directly shifts with the relative humidity in the environment. Resonance peak would be then associated with a concrete level of relative humidity.

5.3.1 Material, methods and design

The tag has been designed to resonate at 13.56 MHz (HF band). The first approach that we developed was to add to the architecture of HF band presented in chapter 4 a printed capacitor in order to know how this new element affects the antenna behaviour. The RFID chip M24LR64 (STMicroelectronics, Geneva, Switzerland) has a capacitance of approximately 30 pF. Without including the parasitic resistance, a value of 4.6 μ H for the coil antenna must be achieved to enable resonance at the desired frequency.

Now, we will add a sensor capacitance in parallel with the RFID chip capacitance to study the behaviour of this tag. Therefore, the analytical expression of the resonance frequency is given by:

$$f_o = \frac{1}{2\pi} \sqrt{\frac{1}{L(C_{chip} + C_{sens})} - \frac{R^2}{L}} \quad (57)$$

Screen printed and inkjet printed RFID tags have been manufactured using the optimal conditions already reported on chapter 3. The AC electrical characterization for the different fabricated tags has been performed by measuring their impedance, both magnitude and phase, using the four-wire measurement technique with a precision Impedance Analyser 4294A and an impedance probe kit (4294A1) (Agilent Tech., Santa Clara, CA, USA). The excitation voltage applied in all measurements was $V_{DC} = 0$ and $V_{AC} = 500$ mV from 5 MHz to 40 MHz. We have considered this frequency range because it contains the work frequency of the RFID chip (13.56 MHz) and enough frequencies around it to perceive shifts on the resonance frequency due to variations in the relative humidity. The stationary humidity and temperature responses of the tags have been measured in a climatic chamber VCL 4006 (Vötsch Industrietechnik GmbH, Germany). In the climatic chamber, we included two commercial sensors to monitor the temperature and humidity close to the sensors: an analogue humidity sensor HIH4000 (Honeywell International Inc., Illinois, USA) with accuracy of $\pm 2.5\%$ and a digital thermometer RS Series A1 (RS Amidata S.A., Madrid, Spain) with resolution of 0.1 °C. RFID tag tests were carried out using a commercial

RFID reader compatible with ISO 15693, HF TRF7960 (Texas Instruments). The RFID reader power up and drives the tags using ISO15693 commands.

5.3.2 Experimental Results

Firstly, we measured the change in impedance of every single element, coil and capacitor, for each printing technique. After this study, we characterize the different LC printed tags.

Single elements

Figure 68 presents the two coil inductors fabricated. As can be seen, the only difference between them is the printing technique. Figure 69 and Figure 70 show the screen printed coil response to changes in humidity and temperature, respectively. As can be seen, the only appreciable change is in the amplitude of the response with a maximum change of 20 Ω in humidity and 12 Ω in temperature but no frequency shift is perceived.

Figure 70 and Figure 72 present the resonance frequency as a function of humidity and temperature curves. There is a small shift in the resonance frequency due to changes in humidity and temperature. The resonance frequency decreases when both magnitudes increases but the maximum change perceived is less than 2 kHz in the ranges of RH and temperature studied.

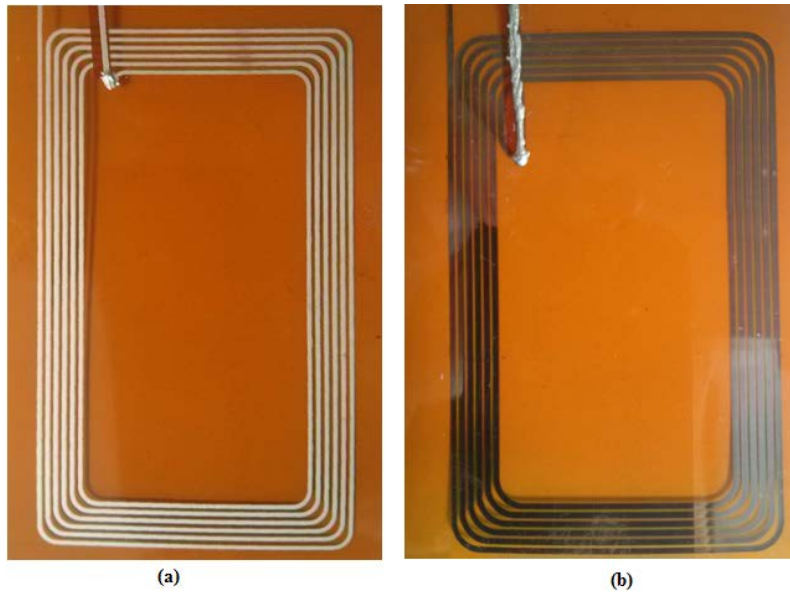


Figure 68. Printed coil inductor by (a) screen printing, (b) inkjet printing.

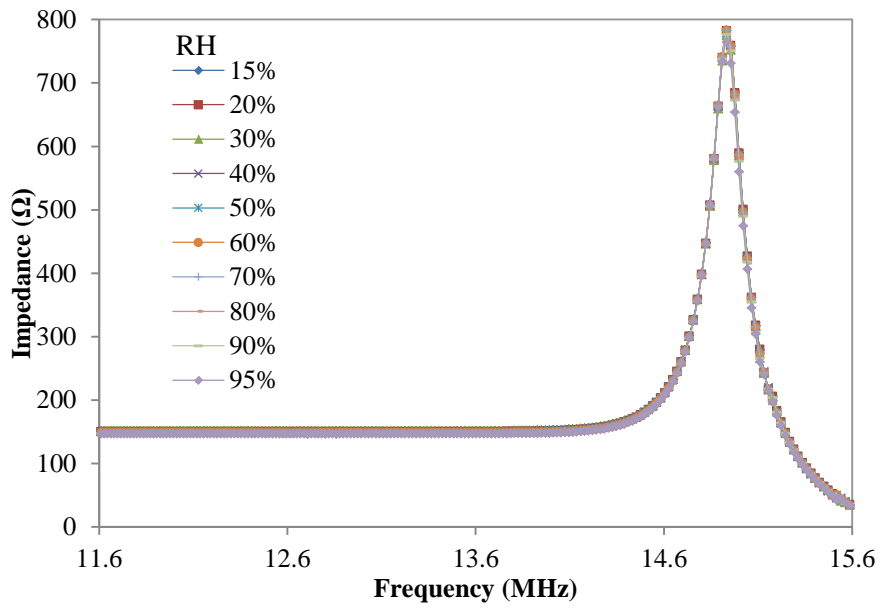


Figure 69. Coil impedance by screen printing as function of frequency at different values of RH.

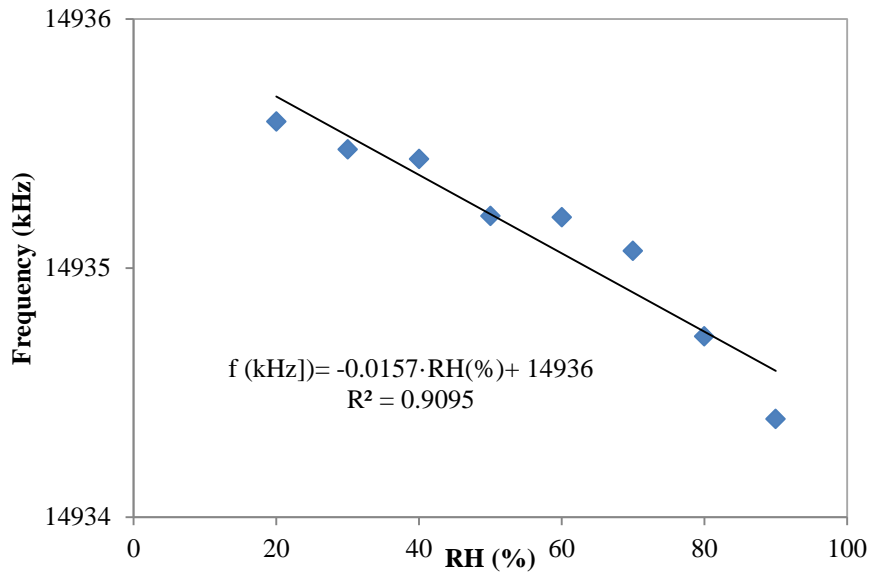


Figure 70. Coil resonance frequency by screen printing as a function of relative humidity.

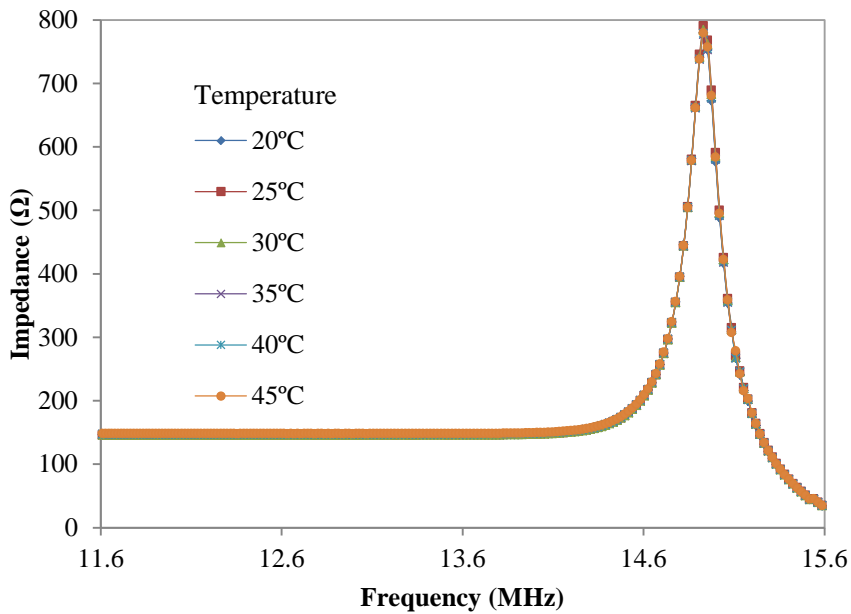


Figure 71. Coil impedance by screen printing as a function of frequency at different temperature values.

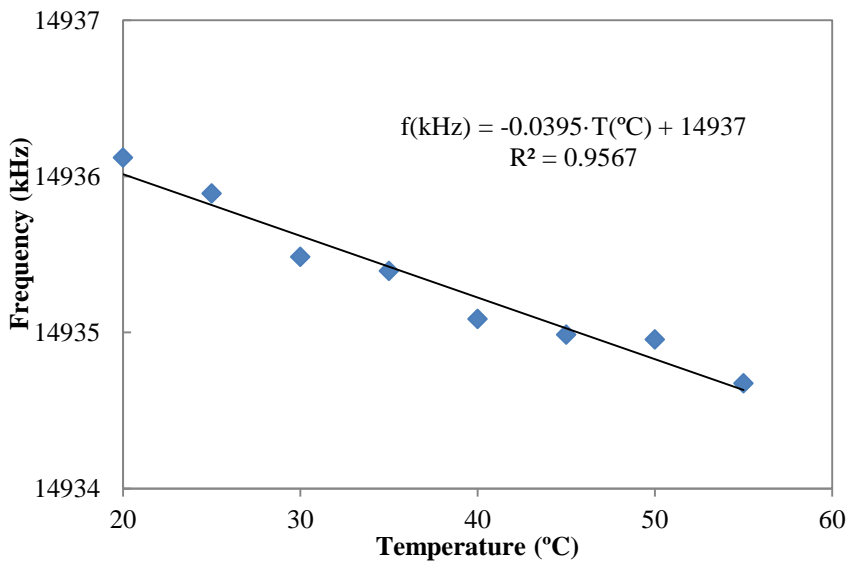


Figure 72. Coil resonance frequency by screen printing as a function of temperature.

Figure 73 presents the impedance of the inkjetted coil as a function of frequency at different values of relative humidity. As we can see, the magnitude not only has reduced its value but also the peak has been widened in comparison with Figure 69. For this reason, we dismissed this option and therefore, the LC tag has been fabricated with screen printed inductances.

On the other hand, the screen printed capacitor was designed in order to get a capacitance value high enough to interfere in the frequency response of the tag. For its ease of fabrication, we chose the interdigitated electrodes. Table 20 contains the physical dimensions of the capacitor with a modelled capacitance of 8 pF at dry atmosphere.

Figure 74 and Figure 75 present the screen printed capacitor curves in humidity and temperature, respectively. The sensitivity decreases from 11 fF/%RH at 1 MHz to 7.5 fF/%RH at 100 MHz. The thermal dependence is less than -1 fF/°C in the whole frequency range. The inkjet-printed capacitor is based on serpentine electrodes whose characterization has been already described.

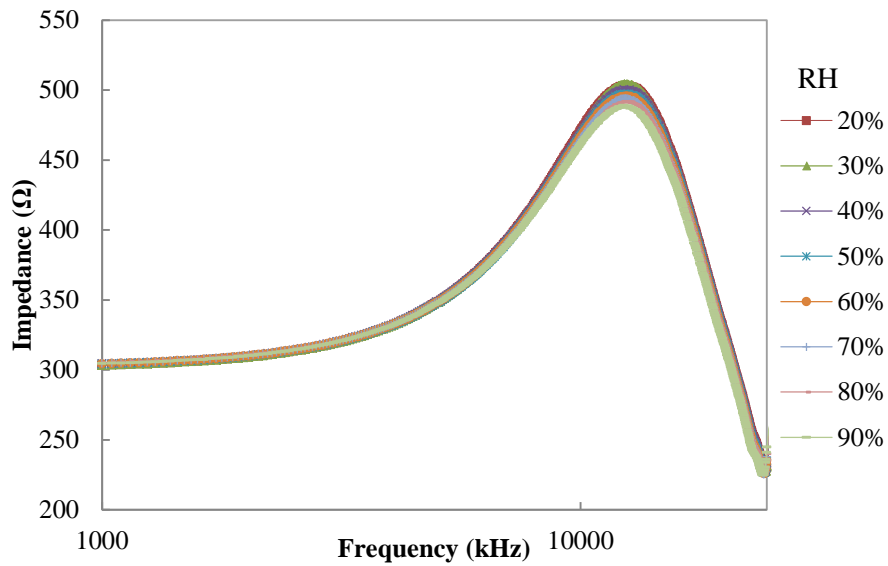


Figure 73. Coil impedance by inkjet printing as a function of frequency at different values of RH.

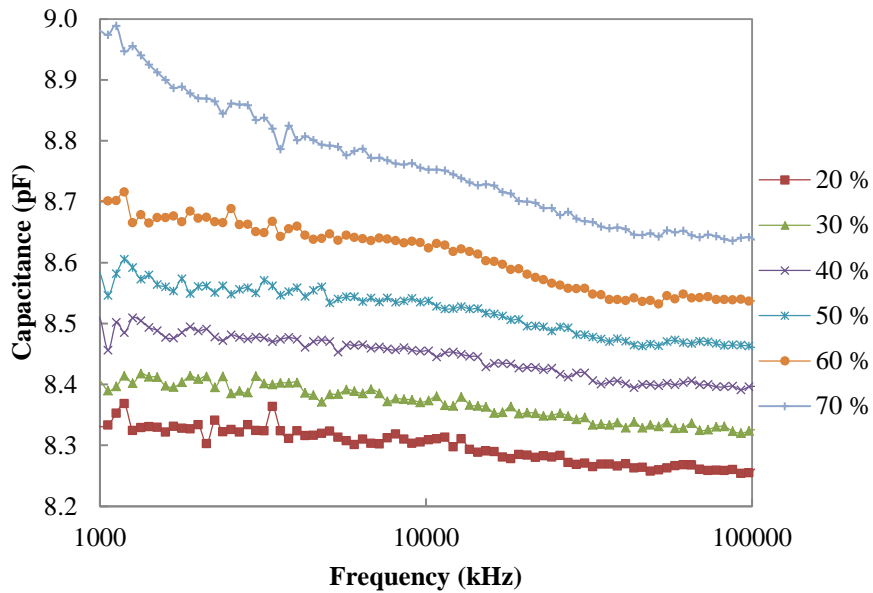


Figure 74. Screen printed capacitance as a function of frequency at different RH values.

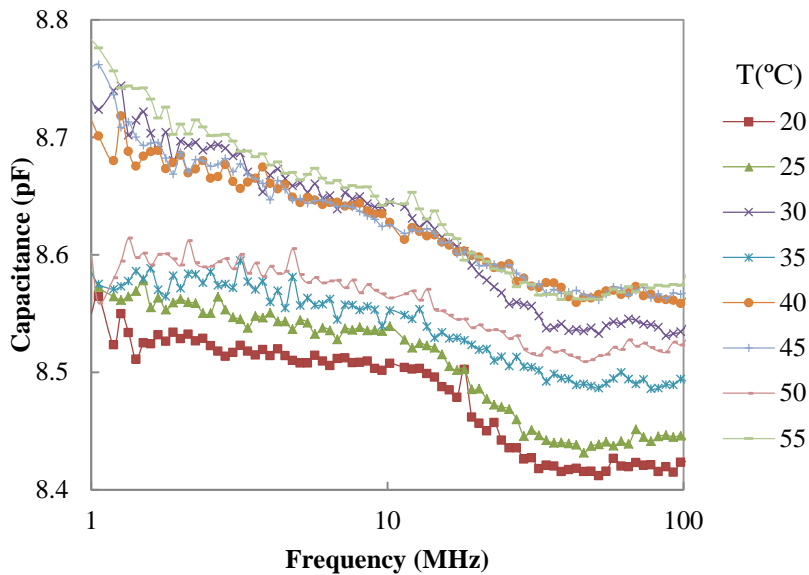


Figure 75. Screen printed capacitance as a function of frequency at different temperature values.

Table 20. Physical dimensions of the screen printed interdigitated structure

Parameter	Value	Description
Length	1.0 cm	Length of each finger (y-axis)
Width	200 μm	Width of each finger (x-axis)
Thickness	10 μm	Thickness of electrodes (1 layer) (z-axis)
Number	20	Total number of fingers of the larger electrode
Interspacing	200 μm	Distance between consecutive fingers (y-axis)
Distance	200 μm	Distance between fingers of one electrode and the backbone of the other electrode (x-axis)

LC tags

Then, we characterized a LC tag completely fabricated by screen printing (including one IDE capacitor with specifications in Table 20 as shown in Figure 76). As any of the tag components showed a remarkable variation induced by temperature, we have just studied the tag as a function of RH.

The impedance of the screen printed tag at different values of RH is shown in Figure 77. In order to better appreciate the resonance frequency shift, we have zoomed the area where the peak is located and normalized the response, see Figure 78. The resonance frequency is shifted to about 12 MHz because

of the added capacitor and the change in the resonance frequency varying RH is about 80 kHz (see Figure 79).

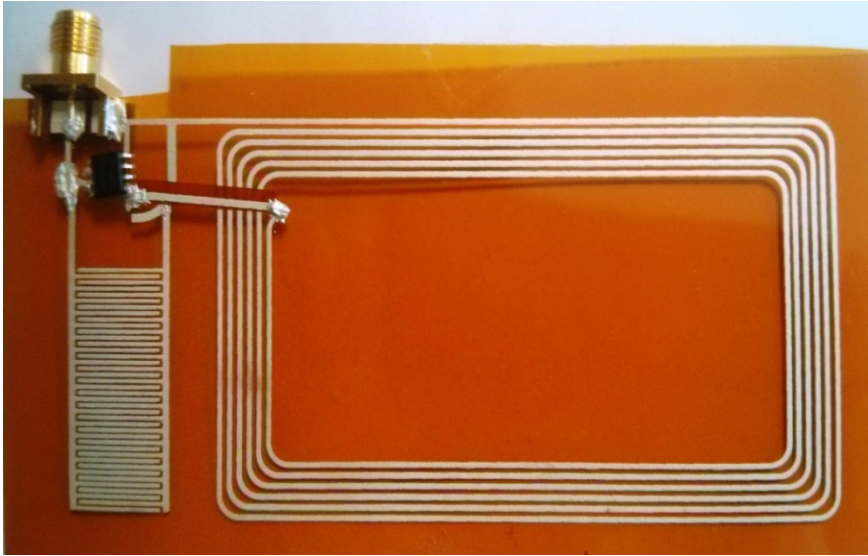


Figure 76. LC tag by screen printing.

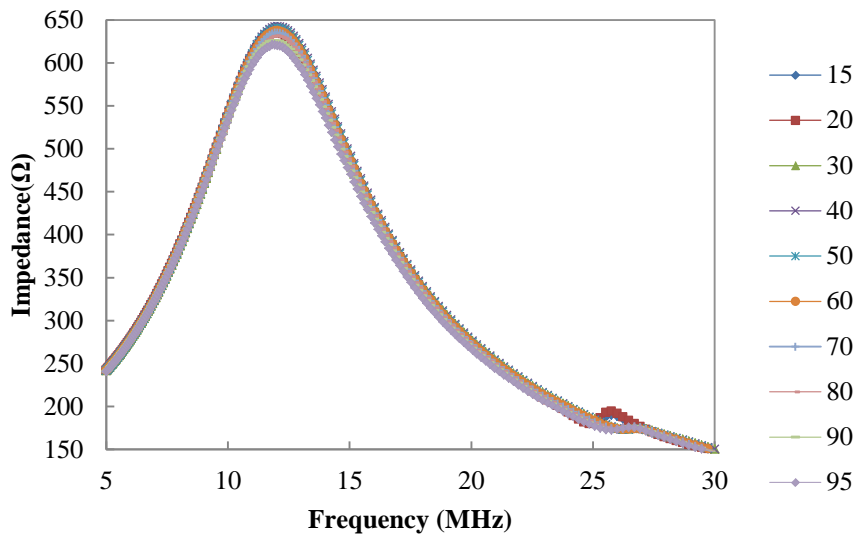


Figure 77. Impedance of the screen printed LC tag as a function of frequency for different RH values.

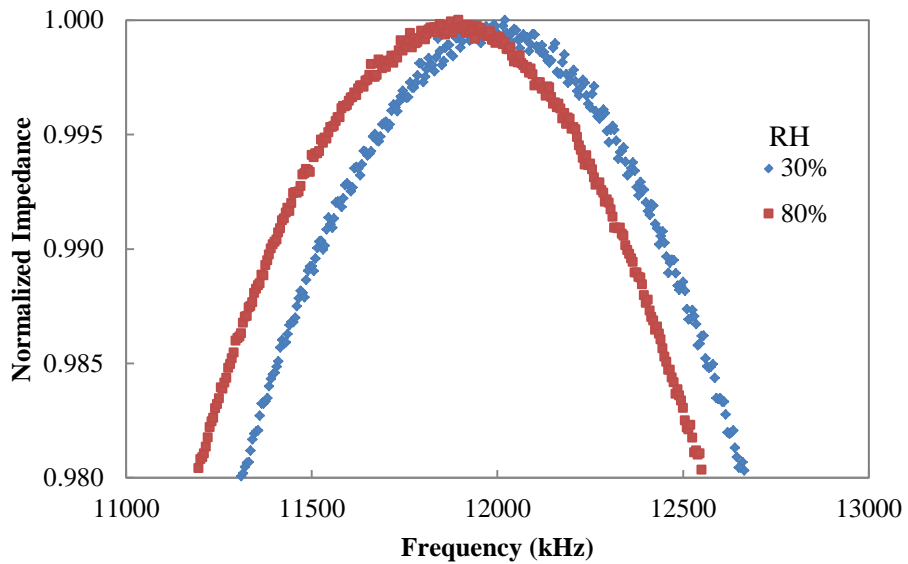


Figure 78. Normalized impedance as a function of frequency for two RH values.

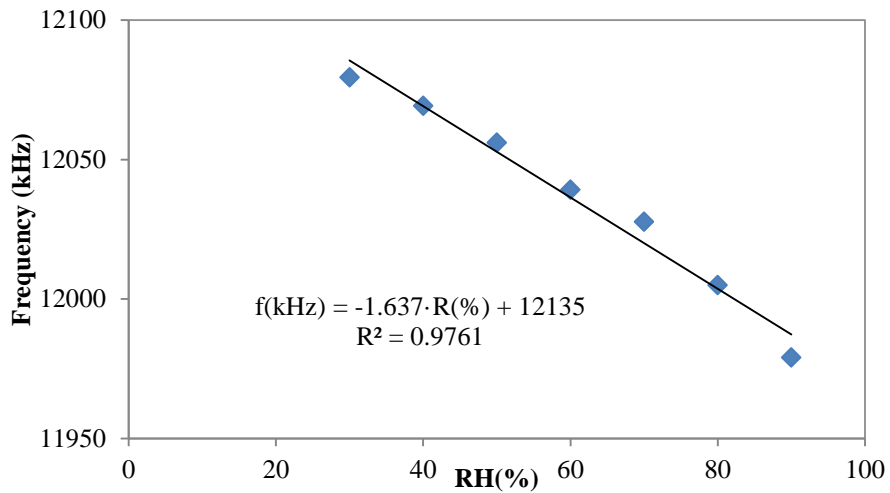


Figure 79. Resonance frequency of the screen printed LC circuit as a function of RH.

Finally, we characterized a hybrid LC tag where the coil inductor was fabricated by screen printing and an array of SRE capacitor was manufactured by inkjet printing (including 12 replicas of SRE capacitor associated in parallel, with specifications in Table 18) as shown in Figure 80. Here, we have just studied the tag as a function of RH due to the low influence of temperature of each single element. The impedance of the screen

printed tag at different values of RH is shown in Figure 81 and Figure 82. In order to better appreciate the resonance frequency shift, we have zoomed the area where the peak is located and normalized the response, see Figure 82. The resonance frequency is shifted to about 9.5 MHz because of the added capacitors. The change in the resonance frequency varying RH is about 300 kHz (see Figure 83).

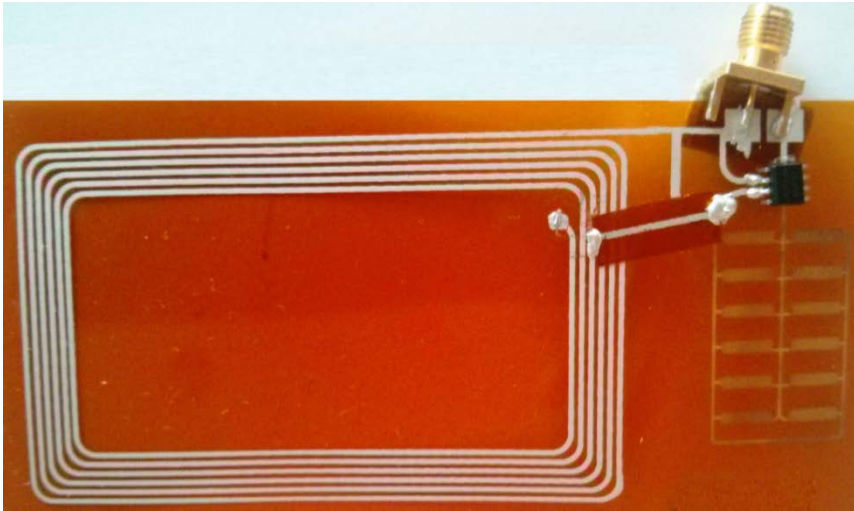


Figure 80. Hybrid LC tag by screen printing (coil) and inkjet printing (capacitors).

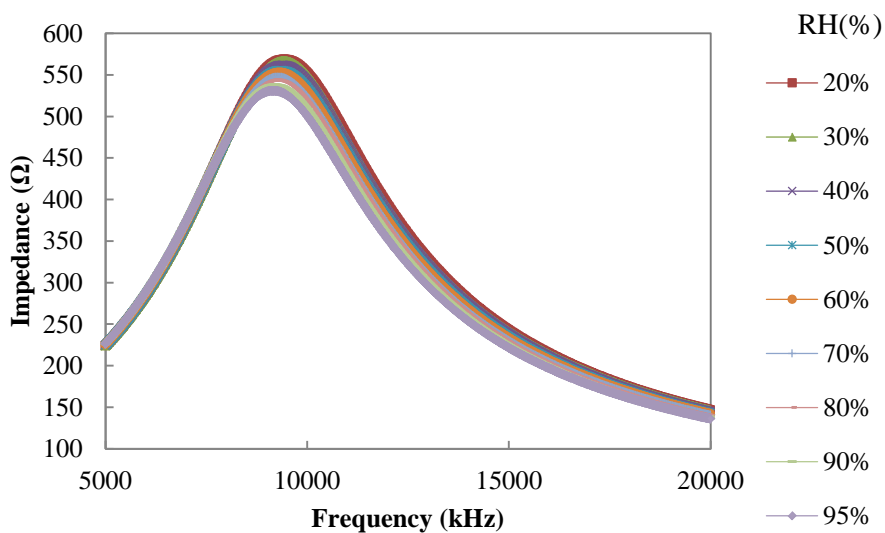


Figure 81. Impedance of the hybrid LC tag as a function of frequency for different RH values.

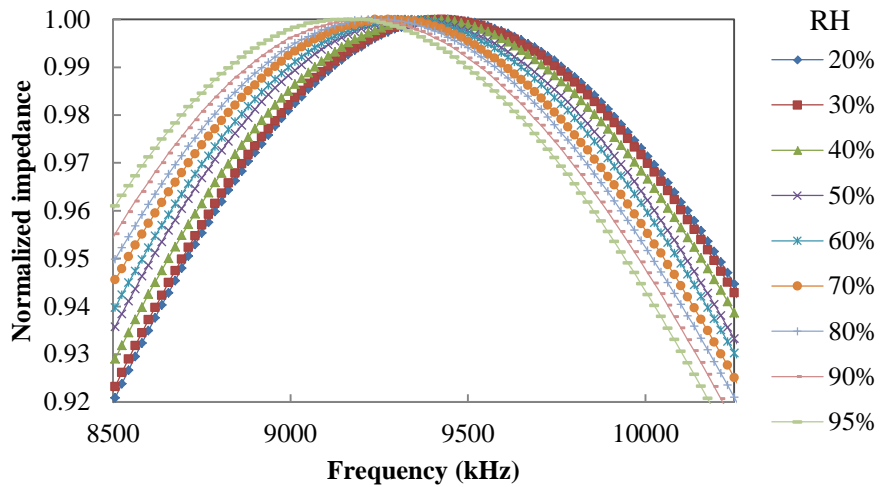


Figure 82. Normalized impedance of hybrid LC tag as a function of frequency for two RH values.

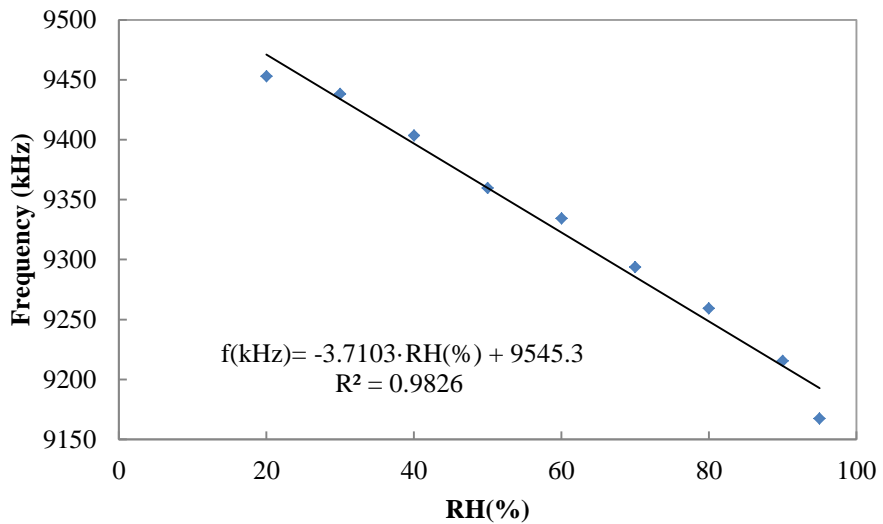


Figure 83. Resonance frequency of the hybrid printed LC circuit as a function of RH.

Further investigation has to be carried out to complete this study but we have obtained a significant change in the resonance frequency. Next steps will be the enhancement of this frequency shift as well as in tuning the tag for the desired RH range. Anyway, this design could be directly used as a resonance humidity sensor by directly measuring the resonance frequency by analog measurements. Actually, we have disconnected the RFID chip to the hybrid

LC tag and the shift in the resonance frequency is about 700 kHz in this latter case.

5.3.3 Conclusion

Finally, a RFID tag has been studied as a threshold humidity sensor. The idea is shifting the resonance frequency of the RFID tag to tune the antenna within a specific humidity range. The reader could not read the tag out of this range. For this purpose, we have manufactured an inductor coil and an interdigitated capacitor by screen printing and inkjet printing. Then, we have studied the behaviour of every single element, coil and capacitor, as a function of frequency at different relative humidity (RH) values. The response of coil inductors to humidity were virtually negligible but the quality factor of the inkjetted coil was much lower than the screen printed one and it was strongly affected by RH; therefore we have rejected this option for the final tag. Then, we have characterized a full screen printing LC tag. We found a shift of 100 kHz in the resonance frequency for the whole RH range studied. A hybrid tag with screen printed coil and an array of inkjetted capacitor has also been analysed. In this case, a shift of about 300 kHz in the resonance frequency has been found. Further investigation should be carried out to complete this study but we have obtained a significant change in the resonance frequency. Next steps should be addressed in the enhancement of this frequency shift as well as in tuning the tag for the desired RH range. Anyway, this design could be directly used as a resonance humidity sensor by directly measuring the resonance frequency. Actually, a shift of 700 kHz has been found in the hybrid tag by only disconnecting the RFID chip.

5.4 Single-chip passive UHF RFID tag with multiple sensors capabilities

Here, we present the design, fabrication and characterization of a printed RFID tag with sensing capabilities. This passive tag is printed on a cardboard with the aim of monitor the packaging conditions. The tag includes a commercial force sensor and a printed opening detector. In this sense, the mass applied to the packaging can be monitored as well as the detection of

the opening of the box. As remarkable features, the architecture is based on screen printing technology as fabrication process and with only single chip architecture. In addition, a simple switch is implemented to be able to measure in the same access both sensor magnitudes without including microcontroller neither battery. Moreover, the chip used here integrates a temperature sensor, and therefore, these tags provide three parameters in every reading.

5.4.1 Material, methods and design

Figure 84 shows the architecture of the printed tag, including the footprints of the different components required. This tag present a passive architecture based on SL900A RFID chip (AG 2014) (AMS AG, Unterpremstaetten, Austria) compatible with EPC Gen 2 RFID standard. The RFID chip was chosen due to the integration of a Sensor Front End (SFE) and 10-bits Analog to Digital Converter (ADC). The extra circuitry has been used to interface the resistive sensors. Furthermore includes an on-chip temperature sensor, so we can also measure temperature without extra circuitry.

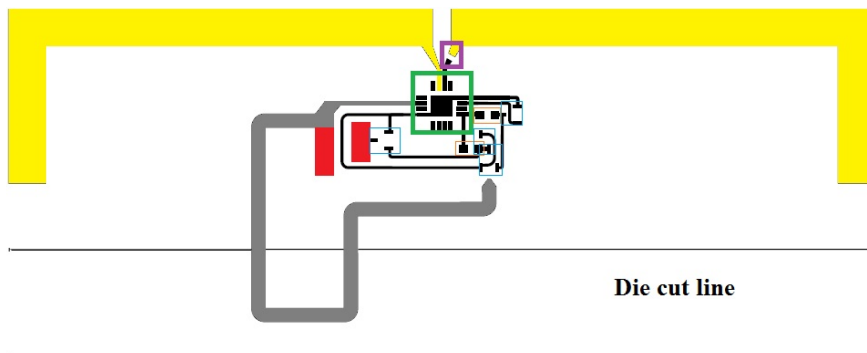


Figure 84. Schematics of the RFID tag with the dipole antenna (in yellow) and the chip RFID (in green). The external matching network has been remarked in purple. The resistors and transistors to switch the sensors are highlighted in orange and blue, respectively. The opening sensor is shown in grey and the pads for the force sensor are presented in red.

The radiofrequency interface consists on a typical dipole antenna resonating at 868 MHz (European Band for RFID UHF) and a RF Surface Mount Device (SMD) inductor used to match the chip input impedance (Rao et al. 2005).

Two resistive sensors are integrated in this tag: a force sensor and an opening detector (Figure 84). In order to measure the vertical force applied to the packaging, we selected the force sensor FlexiForce A201 (Tekscan, Inc., USA). This sensor presents an error lower than 3% and its hysteresis is lower than 4.5%. The time response is below 5 μ s. As opening detector, we printed a pattern through the die cut line of the package. In this sense, we are able to measure a low resistance value when the package is closed, whereas when it is opened this printed pattern is broken and, therefore, an open circuit is detected.

Temperature value comes from a conversion in the on-chip A/D converter of the SL900A. The minimum resolution is 0.18 $^{\circ}$ C in a range of 189.9 $^{\circ}$ C while a resolution of 0.23 $^{\circ}$ C is obtained with the widest range of 237.2 $^{\circ}$ C.

Two internal voltage references, V_{ref1} and V_{ref2} individually selectable in steps of 50 mV between 160 and 610 mV, set the lower and upper limits of the ADC converter. These limits are defined as $2 \cdot V_{ref1} - V_{ref2}$ and V_{ref1} . The difference between them defines the input voltage range, $V_{ref2} - V_{ref1}$, and the limits of operation. These voltage references can be set in the user application and, therefore, a concrete resolution and range can be selected by the user.

The resistive sensors are directly connected to the SFE of the RFID chip. To read out the resistance value, the SFE is configured in resistive mode. In this mode, it is no required any external component but, in our case, we want to measure in the same access two different values. For this purpose, a simple switch has been implemented, see Figure 85. The transistors are BSS138LT1 NMOS (Semiconductor Components Industries LLC, USA) with a resistance value in on-region $R_{DS(on)} = 3.5 \Omega$; and resistors are surface mounted devices (SMD) of 4.7 k Ω (Panasonic, Japan).

The sensor resistance is polarized with a configurable current source (I_{SENS}) whose amplitude can be selected from 0 to 7.75 μ A, in steps of 25 μ A. The input voltage on the ADC associated with the resistance value is:

$$V_{ADC} = I_{SENS}(R_{SENS,i} + R_{DS(on)}) \quad (58)$$

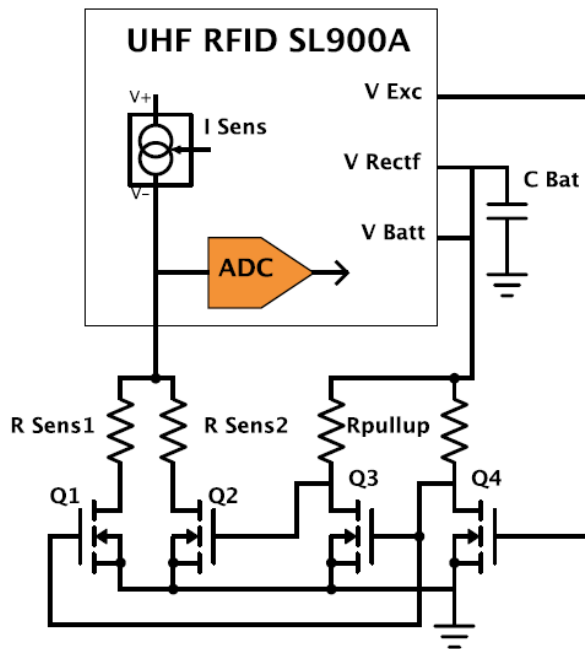


Figure 85. Diagram showing the external resistive sensor mode of the RFID chip, including the extra circuitry to read each resistive sensor.

In order to measure both sensors is necessary to properly select the current value; the opening detector was measured with a current equal to $I_{\text{SENS}} = 7.00 \mu\text{A}$, whilst the force sensor was configured with $I_{\text{SENS}} = 7.75 \mu\text{A}$. This difference in current is given by the range of resistance variation; in the former case is enough to detect a change from few Ω (close state) to $50 \text{ k}\Omega$ (open state). In the latter case, the resistance varies from some $\text{M}\Omega$ to $40 \text{ k}\Omega$ and we are also interested in the specific value of force applied.

In order to control which sensor is being measured, transistor Q3 and Q4 are in inverse configuration, so as, when Q3 is ON, there is no current through Q4 and vice versa. Transistor Q1 and Q2 are controlled by this inverter, therefore only one sensor is read each time, as well as, the resistance of the active transistor. As the transistor resistance is connected in series with the resistive sensor, its effect is neglectable in comparison with the expected values. In both cases the ADC reference configuration is $V_{\text{REF1}} = 210 \text{ mV}$ and $V_{\text{REF2}} = 260 \text{ mV}$.

All the patterns were directly printed on a commercial cardboard box (Sociedad Estatal Correos y Telégrafos, S.A., Spain). Screen printed patterns were manufactured with a Serfix III screen printing machine (Seglevint SL, Barcelona, Spain). The screen used to manufacture the tag had a mesh density of 120 Nylon thread per centimetre (T/cm) to fabricate it with only a single-layer screen printed of conductive silver ink CRSN 2442 (Sun Chemical Corporation, Parsippany, USA). The minimum spatial resolution for a reliable fabrication process was 150 μm . Sintering took place at constant 80 °C of temperature for 20 minutes.

Finally, the assembly of the chips and external components to the cardboard was carried out with the previous described three-step process.

5.4.2 Experimental Results

Figure 86 presents the manufactured RFID tag with its different components labelled for better understanding. Final dimensions of the screen printed dipole antenna arms are 5.5 mm width and 79 mm length and its characterization can be found on chapter 3.

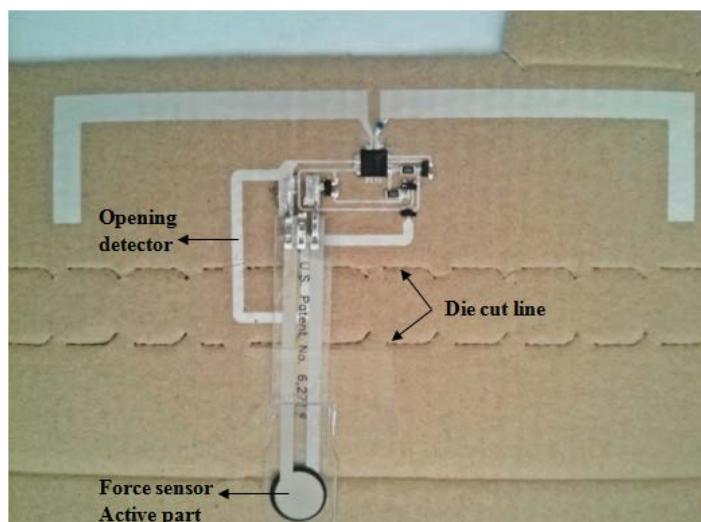


Figure 86. Fabricated RFID tag with all components.

The measured read range is the maximum distance in which the reader was able to read out the tag including the sensing functionalities. It should be noted that the sensitivity of the RFID chip has a penalty. Chip sensitivity to

answer identification inquiries of EPC protocol is -15 dBm whereas the sensitivity for reading out resistance value is -2.21 dBm. The reason is to the required extra-power to drive the SFE that needs to be collected from the radiated EM field of the reader. According to Eq. 51, the read range assuming ideal conditions (perfect matching between chip, $\tau = 1$, and the dipole antenna gain obtained by EM simulation, $G_{\text{tag}}=0.66$ dBi) should be 2.2 meters. The measured range for the printed tag is smaller than the simulated ones, 1.1 meters. Differences between simulated and measured read ranges were already reported on previous chapter and are attributed to two factors: the non-ideal behavior of the metallic layers in printed electronic that leads to a lower gain and efficiency of the fabricated antennas and extra losses introduced by the mismatching between the RFID chip and antenna impedances.

But in this case the read range has been reduced approximately in two thirds compared with the same antenna fabricated on PI substrate. This reduction could be associated to the thicker cardboard substrate that will introduce extra loss and also detuning of the RFID antenna (Vyas et al. 2009). Moreover, there is non-direct sight between RFID reader and RFID antenna which is printed on the inner side of the cardboard box. To justify this reduction, a commercial UHF RFID Raflatac tag from UPM RFID (SMARTRAC N.V., Amsterdam, The Netherlands) has been detected on the same conditions: direct sight with RFID reader on free air condition and attached on the inner side of the cardboard. Those values were 3.3 m and 2.28 m respectively. Measured read ranges are larger due to the lower sensitivity of these RFID tags, but the reading range is penalized in a similar way that our dipole antenna explaining the results encountered.

Figure 87 shows the cardboard with the printed RFID tag. Regarding force sensor, its active part has been placed just in the junction part of the cover and lateral of the box (see Figure 87a). When weight is placed on top of the box, the pressure force is distributed on the junction between cover and laterals side of the box. In respect to the opening detector, it has been defined through the die cut line in such a way that once the box is closed, to open it again, it is necessary to stripe the die cut line off. Therefore, the opening detector has memory.



Figure 87. a) Close cardboard with RFID tag; (b) view of the RFID tag before closing the box.

After setting the current configuration, we characterized both sensors varying the mass on top of the force sensor and opening the box. We stored 30 ADC data to know the deviation between measurements. This deviation was lower than 2 LSB of the ADC in all the studied cases. Figure 88 presents the average data obtained by the ADC for the force sensor.

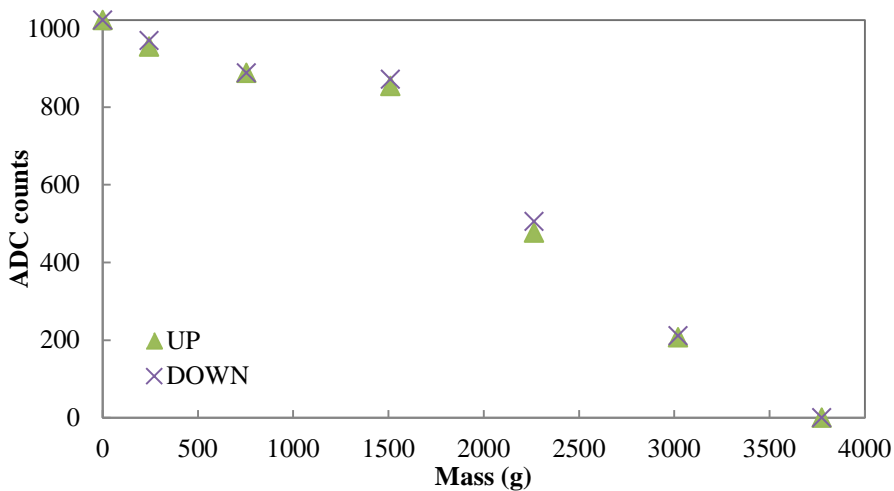


Figure 88. ADC counts for the force sensor measurements.

The output range for the force sensor is equal to the maximum resolution of the internal ADC, that is to say, 1024 counts can be associated to a variation of about 3.75 kg, Figure 78. This force sensor achieved some $M\Omega$ when there is no mass on it, decreasing its value while increasing the mass. With respect to the hysteresis in measurements, the maximum error found is 30 counts.

Regarding the opening detector, the maximum ADC count is read when the packaging is opened. On contrary, zero level is returned while the box is closed. No error was observed in any of the test performed.

5.4.3 Conclusion

A dipole-based UHF RFID tag with multiple sensor capabilities integrated on a cardboard package has been presented. Two resistance sensors are comprised on the design: one pressure force to measure when weight is placed on top of the package and a silver trace crossing the package die cut line to detect if the package has been opened. To connect both sensors to the single-sensor interface of the RFID chip, a simple switch has been integrated on the design. Operation of the tag has been demonstrated successfully although the force sensor is more indicated to be used as threshold sensor instead of being able of measure absolute weight.

6. Conclusiones

Este trabajo se ha centrado en el diseño, simulación, fabricación y validación de distintas etiquetas de radiofrecuencia con capacidades sensoras basadas en tecnología RFID. Dichas etiquetas se han fabricado mediante técnicas de impresión integrando en las mismas distintos sensores de interés para monitorización ambiental o para la preservación de bienes empaquetados. Las principales conclusiones que se pueden extraer son:

1. Se han caracterizado dos procesos de fabricación mediante técnicas de electrónica imprimible: inyección por chorro de tinta y serigrafía. Distintas combinaciones de materiales y tintas han sido caracterizadas a través del diseño y fabricación de distintos patrones impresos. La finalidad es obtener por un lado las principales características geométricas y eléctricas para cada caso estudiado y por otro lado, establecer una comparación entre los distintos materiales en términos de rendimiento en radiofrecuencia para la fabricación de etiquetas RFID impresas.

En el caso de impresión por chorro de tinta, dos tintas de nano partículas de plata, DGP y Suntronic, se han impreso sobre tres sustratos diferentes, PET, PEI y PI. Adicionalmente, se ha mostrado un modelo simple para estimar el espesor en patrones impresos mediante esta técnica. Las medidas experimentales muestran una gran concordancia con los datos predichos por el modelo. El espesor obtenido con la tinta de plata DGP es de 0.105-0.180 μm mientras que con la tinta Suntronic es de 0.355-0.430 μm , si bien existen ligeras diferencias dependiendo del sustrato empleado. Los resultados experimentales muestran que varias capas se pueden imprimir consecutivamente sin degradar la reproducción del patrón ni la rugosidad superficial obtenida. La resolución de esta técnica viene determinado por el diámetro de gota, $\sim 50 \mu\text{m}$ para la tinta Suntronic y $\sim 100 \mu\text{m}$ para DGP. La combinación de la tinta DGP junto con el sustrato PEI presentan la menor resistividad, $8.6 \pm 0.8 \mu\Omega \cdot \text{cm}$, comparado con el resto de casos analizados aunque el mejor resultado en términos de rendimiento, resolución y espesor alcanzado por una única capa impresa corresponde a la combinación de tinta Suntronic en sustrato PEI con una resistividad de $24.4 \pm 1.1 \mu\Omega \cdot \text{cm}$. Más aún, se ha observado un incremento en la resistividad obtenido para

patrones impresos con un espesor menor a las 0.3 μm , probablemente debido a un incremento de la contribución de los mecanismos de dispersión, el denominado “*grain boundary scattering*” que se produce en las fronteras de grano.

En el caso de serigrafía, una única tinta ha sido impresa en los tres sustratos propuestos: PET, PEI y PI. Para ello se han empleado mallas con distintas densidades, es decir, distinto número de hilos por centímetro. Los espesores obtenidos han sido 9.2 μm para 140 hilos por centímetro (h/cm), 19 μm para 90 h/cm y 30 μm para 43 h/cm. Los límites de impresión para serigrafía obtenidos experimentalmente son 800 μm en el caso de la malla de 90 h/cm y 600 μm para 140 h/cm. La resistividad mínima medida es de $39 \pm 4 \mu\Omega \cdot \text{cm}$ obtenida en los sustratos PEI y PI. Como se esperaba, estos patrones con un mayor espesor presentan una resistencia laminar menor que la obtenida con inyección de tinta. Las resistencias laminares en el caso de serigrafía son $15.0 \pm 0.7 \text{ m}\Omega/\square$ para 43 h/cm, $21 \pm 2 \text{ m}\Omega/\square$ para 90 h/cm y $41 \pm 4 \text{ m}\Omega/\square$ para 140 h/cm, mientras que en los mejores casos de inyección de tinta la menor resistencia laminar encontrada es de $54 \pm 6 \text{ m}\Omega/\square$ (12 capas impresas con la tinta DGP) y $153 \pm 8 \text{ m}\Omega/\square$ (4 capas impresas con la tinta Suntronic) ambas en el sustrato PEI. No obstante, los patrones de serigrafía presentan peor resolución, bordes de los patrones impresos más irregulares y una mayor rugosidad superficial que los patrones fabricados mediante inyección.

Para estudiar el rendimiento a las frecuencias de operación de la tecnología RFID, se han diseñado y fabricado líneas de transmisión de tipo coplanar con las distintas combinaciones de materiales y técnicas. Dichas líneas de transmisión se han fabricado en cada caso concreto con dos diferentes longitudes presentando los resultados finales como pérdidas por unidad de longitud. Los resultados demuestran que en el caso de inyección, Suntronic presenta menores pérdidas que DGP, demostrando que en el caso de patrones impresos solo el estudio de la resistividad no es suficiente para asegurar un buen rendimiento en radiofrecuencia. La printabilidad, es decir, la correcta reproducción de los patrones en términos de resolución y precisión, también juega un papel muy importante. La comparación entre sustratos muestra el compartimiento esperado de acuerdo a la información de pérdidas indicada para cada sustrato por los fabricantes: PEI presenta las menores pérdidas

seguido de PI y PET. En resumen, se ha demostrado que el substrato PEI con la tinta Suntronic es la combinación indicada para la fabricación de antenas RFID mediante técnica de chorro de tinta mientras que en el caso de serigrafía ambos substratos, PEI y PI pueden ser empleados para este fin donde la elección de la densidad de malla determina de la resolución y espesor obtenidos.

2. Usando las condiciones óptimas de fabricación, diversas antenas RFID para las bandas HF y UHF han sido diseñadas, simuladas y validadas. En el caso de la simulación numérica, los parámetros introducidos en el simulador numérico son aquellos obtenidos en la caracterización de la tecnología.

Debido a la mejor printabilidad y mejor rendimiento en radiofrecuencia, la combinación de tinta Suntronic impresa en el substrato PEI ha sido usado para la fabricación de antenas por medio de chorro de tinta. Se ha presentado la optimización del proceso de curado, obteniéndose que los mejores resultados se producen cuando la temperatura de curado se eleva gradualmente desde la temperatura ambiente, ~ 25 °C, hasta 180 °C con una rampa de 3°C/min. Los cambios abruptos de la temperatura de curado conllevan a que el solvente de la tinta no se evapore homogéneamente, acarreando problemas como el “*coffee ring*” en líneas estrechas o una gran rugosidad superficial. Para las antenas fabricadas mediante serigrafía, se ha usado una malla de 120 h/cm en substrato PI debido a su mejor printabilidad en comparación con otras densidades de malla.

En el caso de antenas para la banda HF, el número de capas impresas de las bobinas fabricadas debe ser suficiente para obtener un espesor mínimo. El espesor logrado debe ser suficiente para no degradar el factor de calidad Q de la antena debido al alto valor de la resistencia serie asociada con el inductor. En nuestro caso particular, 4 capas impresas han sido suficientes para conseguir un factor de calidad de 1.68 ± 0.12 . Las antenas HF fabricadas mediante serigrafía con mallas de 90 h/cm y 140 h/cm obtienen mejores factores de calidad y, por lo tanto, mejor rendimiento como antenas RFID.

En el caso de antenas UHF, se ha presentado una nueva técnica para la medida de la impedancia de entrada diferencial de dichas antenas. Esta medida es crítica en el diseño de las etiquetas UHF para garantizar la condición de máxima transferencia de potencia entre el chip RFID y la

antena. Para realizar esta medida se han fabricado de forma personalizada una sonda diferencial con conectores U.FL y un kit de calibración SOLT para dicha sonda que, junto con un analizador de redes de gama media, permite obtener la impedancia de entrada a partir del estudio de los parámetros de dispersión (S-parameters). Para obtener dicha medida no es necesario ningún post-procesado de los datos obtenidos, pudiendo realizarse las medidas directamente. En todos los casos investigados, las medidas experimentales y las simulaciones numéricas muestran una gran concordancia y respuestas en frecuencia muy similares, si bien la parte real de la impedancia presenta mayores diferencias con los valores simulados que la parte imaginaria. Esto sugiere que la parte real de la impedancia es el factor crítico para obtener la condición de adaptación de impedancias y que una correcta caracterización de las resistencia laminar (resistividad y espesor) de las capas metálicas impresas conlleva unos resultados con menores errores. Dos diseños de antenas han sido mostrados, un dipolo tradicional con los brazos doblados para optimizar el área ocupada, usando una inductancia SMD con red de adaptación, y un nuevo diseño compuesto por una estructura dipolo modificado en forma de pajarita junto con un inductor “loop” impreso para la adaptación. Ambos diseños de antenas presentan rangos de lectura comparables.

En cuanto a comparación de técnicas de fabricación, las antenas serigrafiadas presentan rangos de lectura mayores que las realizadas por medio de técnicas de inyección aunque sufren de un rango ligeramente menor que las realizadas con cobre de 35 μm de espesor, en cualquier caso los rangos obtenidos de las antenas serigrafiadas son comparables a las de cobre. La razón para el menor rendimiento de las antenas inyectadas es su mayor resistencia laminar por lo que las pérdidas óhmicas degradan las características de radiación de las antenas. De cualquier forma, las antenas de inyección pueden obtener rangos comprables siempre que se impriman suficientes capas para mejorar su rendimiento. En nuestro caso particular, la impresión de 20 capas conlleva que el rendimiento entre las antenas de inyección y serigrafía sean equiparables, si bien la fabricación mediante de las mismas implica tiempos de impresión muy largos, entorno a varias horas.

3. La integración de sensores en etiquetas RFID se ha llevado a cabo mediante el diseño, prototipado y validación de distintas arquitecturas. La

lectura de la información de los sensores se ha realizado mediante lectores RFID comerciales compatibles con los protocolos ISO o EPC, ampliamente usados en RFID. De esta forma no es necesario ningún lector RFID especial para estas aplicaciones.

Primero, se ha demostrado como el uso de chips RFID junto con microcontroladores de ultra bajo consumo puede ser explotado para integrar sensores en las etiquetas. En un primer prototipo valores de temperatura y humedad ambiental han sido obtenidos por un microcontrolador de un sensor comercial STH15. Esta información es almacenada en el chip RFID gracias a la interfaz I²C que puede ser utilizada por el microcontrolador para acceder a la memoria EEPROM. Se ha mostrado tanto la realización de la etiqueta en la banda HF en sustrato flexible como el desarrollo del software necesario del lector RFID para la correcta adquisición de los datos mediante el protocolo ISO15693.

Ya en la banda de UHF se han presentado dos arquitecturas. Ambas hacen uso del chip RFID SL900A. La configuración y acceso a las funciones especiales de este chip son controladas mediante comandos del estándar EPC Gen2. De forma similar el primer prototipo, un microcontrolador ha sido integrado junto con un sensor de presión ambiental MEMS. Las mejoras de esta arquitectura semi-pasiva frente al primer prototipo descrito son: menor número de componentes, empaquetados de los chips de menores dimensiones, la arquitectura ha sido integrada en un área menor y se hace uso de baterías flexibles. La segunda arquitectura utiliza las ventajosas características del chip RFID SL900A para crear arquitecturas pasivas. Valores de temperatura y luz ambiental han sido obtenidos mediante una etiqueta RFID pasiva, sin necesidad de baterías. La etiqueta integra una antena tipo dipolo junto con un fotodiodo. Los valores de temperatura son obtenidos del sensor integrado en el chip RFID. El convertidor analógico-digital integrado también en el chip RFID es utilizado para medir la fotocorriente generada. Esta etiqueta representa una solución de reducido coste compuesta por un fotodiodo y un chip RFID como únicos elementos no impresos.

Por último, se ha mostrada una aproximación al cosechado de energía o “*harvesting*”. Una placa solar junto con la circuitería necesaria para el

acondicionamiento de la señal entregada se ha integrado en un prototipo de etiqueta RFID en la banda UHF. Los beneficios frente a la solución han sido un rango de lectura de la etiqueta incrementado incluyendo las funciones sensoras. Además dicha fuente de energía puede ser aprovechada para alimentar las arquitecturas sensoras cuando las etiquetas RFID pasivas no están en presencia del lector RFID y, por lo tanto, no pueden estar operativas.

Para resumir, se han mostrado arquitecturas pasivas y semi-pasivas de bajo coste que pueden ser utilizadas para la integración de sensores en etiquetas RFID en distintas aplicaciones.

4. Se ha fabricado y validado una etiqueta RFID semi-pasiva para la determinación de la concentración de oxígeno. Una membrana sensible al oxígeno es excitada ópticamente por un LED mientras que un detector de color analiza la intensidad de la señal generada por luminiscencia en dicha membrana. El sistema es de alta resolución y con un tiempo de vida largo permitiendo al usuario (productor, distribuidor, vendedor o consumidor) monitorizar el contenido de O_2 dentro de un contenido empaquetado. La lectura del oxígeno es realizada mientras el paquete permanece completamente cerrado sin necesidad de perforaciones para sondas. Además la alta resolución conseguida permite detectar concentraciones de oxígeno muy bajas, en torno a 40 ppm de O_2 con un error del orden de 0.01 ppm de O_2 . La deriva térmica del sensor ha sido estudiada y corregida gracias al sensor de temperatura integrado en el chip RFID. Por lo tanto este sistema está especialmente indicada para aplicaciones de envasado inteligente donde la atmósfera ha sido modificada para que la concentración de oxígeno presente sea extremadamente baja.

5. Se han fabricado y caracterizado dos etiquetas RFID UHF para la medida de humedad relativa en el ambiente. Las etiquetas han sido completamente impresas sobre una poliamida, Kapton HN, cuya permitividad eléctrica se incrementa con la humedad. Dos tipos diferentes de sensores capacitivos, fabricados por inyección y serigrafía respectivamente, han sido caracterizados completamente en de temperatura y humedad. Los valores de capacidad son obtenidos por el chip RFID SL900A. Aparte del chip RFID, la arquitectura está formada por una antena dipolo impresa por serigrafía, una inductancia SMD como red de adaptación y una capacidad SMD de

referencia necesaria para la medida de la capacidad. . Ambas etiquetas presentan una arquitectura pasiva con un único chip, capaz de devolver a un lector RFID estándar valores de humedad y temperatura ambientales de forma digital (10 bits) usando comandos EPC Gen 2.

La etiqueta con los sensores impresos por inyección está formada por 12 estructuras serpentinadas en paralelo mientras que la etiqueta fabricada por serigrafía por 6 estructuras interdigitales. El número que componen estos arrays ha sido elegido para alcanzar un valor nominal de capacidad en torno a 30 pF. La etiqueta con los sensores fabricados por inyección presenta un mejor rendimiento que la etiqueta fabricada por serigrafía. La primera cubre un rango de 800 cuentas de las 1024 posibles para un cambio de humedad relativa del 37% al 70%. La segunda cubre un rango de 220 cuentas de 1024 para un cambio de humedad relativo del 57% al 86%. Entre estos valores de humedad la resolución y el rendimiento obtenidos son aceptables, fuera de estos límites se ven degradados. La diferencia obtenida entre las etiquetas puede ser explicada por el distinto número de dispositivos, 12 en el caso de inyección y 6 en el caso de serigrafía, que afectan directamente a la sensibilidad de cada array de sensores. La diferencia en el rango de humedad obtenido puede explicarse por el distinto valor de la capacidad de referencia usada, 36 pF para los sensores fabricados por inyección y 39 pF por serigrafía, por lo que este valor puede ser escogido para monitorizar un rango de humedad concreto. La falta de rendimiento fuera de estos rangos puede ser explicada porque las interfaces capaces de medir sensores del chip RFID no están diseñadas específicamente para medir capacidad, sino que son de propósito general.

La desventaja de la aproximación con sensores impresos por inyección es la necesidad de usar dos técnicas de fabricación distintas elevando la complejidad de la fabricación con más procesos de sinterizado y necesidad de alineamiento. En cambio, la etiqueta por serigrafía se realiza con un solo paso de fabricación aunque el área ocupada por los sensores es mucho mayor. Por lo tanto dependiendo de los requerimientos de sensibilidad y área uno de las dos aproximaciones sería la más adecuada para una aplicación en concreto.

6. Una etiqueta RFID en la banda de HF ha sido estudiada como sensor de humedad umbral. La idea es estudiar el cambio en la frecuencia de resonancia de la etiqueta pasiva sintonizada en 13.56 MHz al introducir en el circuito LC resonante que constituye la antena los sensores de humedad capacitivos. Sintonizando apropiadamente las etiquetas se podría conseguir que estas etiquetas fueran detectadas por un lector RFID solo si la humedad relativa es inferior o superior a un valor umbral. Para ello primero se ha estudiado el comportamiento en frecuencia de las inductancias fabricadas tanto por inyección como para distintos niveles de humedad relativa. El cambio en el valor nominal de las inductancias a distintos niveles de humedad ha sido despreciable pero los factores de calidad de las bobinas se ven seriamente afectados, posiblemente debido a un aumento de la resistividad de la capa de plata impresa. Este efecto se aprecia aun de forma más severa en la bobina fabricada por inyección, por lo que se rechazó esta opción para la etiqueta final. La caracterización de una etiqueta RFID fabricada completamente fabricada por serigrafía incluyendo un sensor interdigital capacitivo y el chip RFID conectado mostró un cambio de la frecuencia de resonancia de 100 kHz para el rango completo de humedad relativa estudiado. En las mismas condiciones pero con un array de sensores serpentina fabricado por inyección en lugar del sensor interdigital serigrafiado el cambio de resonancia fue de 300 kHz. Es necesario un estudio en mayor profundidad para sintonizar las etiquetas en las frecuencias deseadas a valores concretos de humedad, si bien se ha obtenido un significativo cambio en la frecuencia de resonancia fácilmente detectable. De hecho, este último diseño podría ser utilizado como un sensor de humedad de tipo resonante.

7. Se ha diseñado y fabricado una etiqueta UHF RFID pasiva impresa directamente en una caja de mensajería comercial. La etiqueta presenta una arquitectura pasiva con un único chip, el SL900A, siendo capaz de adquirir de forma digital los valores de varios sensores. Dos sensores resistivos se han usado. Uno es un sensor de fuerza directamente integrado en la parte superior cuya función es detectar el peso depositado encima del paquete. El segundo es una línea de plata impresa atravesando la línea pre-perforada de apertura del paquete para detectar si este ha sido abierto. Para conectar ambos sensores a al chip RFID que en principio es hábil para un único sensor, un simple conmutador se ha diseñado e integrados en el diseño. Se ha

demostrado el correcto funcionamiento de la etiqueta, si bien el sensor de peso está más indicado para operar como sensor umbral que para adquirir medidas absolutas.

7. Scientific Contributions

Journals Papers

Almudena Rivadeneyra, **José Fernández-Salmerón**, Jesús Banqueri, Juan A. López-Villanueva, Luis Fermín Capitan-Vallvey, Alberto J. Palma. “*A novel electrode structure compared with interdigitated electrodes as capacitive sensor*”. Sensors and Actuators B: Chemical. August 2014.

José F. Salmerón, Francisco Molina-Lopez, Almudena Rivadeneyra, Andrés Vásquez Quintero, L. F. Capitán-Vallvey, Nico F. de Rooij, Jesús Banqueri Ozáez, Danick Briand and Alberto J. Palma. “*Printed UHF RFID Smart Tags for Sensing Applications*”. IEEE Sensors. July 2014.

Almudena Rivadeneyra, **José Fernández-Salmerón**, Manuel Agudo, Juan A López-Villanueva, Luis Fermín Capitan-Vallvey, Alberto J Palma. “*Design and characterization of a low thermal drift capacitive humidity sensor by inkjet-printing*”. Sensors and Actuators B: Chemical. 2014. 195: 123-131.

José F. Salmerón, Francisco Molina-Lopez, Danick Briand, Jason J. Ruan, Almudena Rivadeneyra, Miguel A. Carvajal, L. F. Capitán-Vallvey, Nico F. de Rooij, Alberto J. Palma. “*Properties and Printability of Inkjet and Screen-Printed Silver Patterns for RFID Antennas*”. Journal of Electronic Materials. 2014. Vol. 43, 2: 604-617.

A Martínez-Olmos, **J. Fernández-Salmerón**, N. Lopez-Ruiz, A. Rivadeneyra Torres, L. F. Capitan-Vallvey, A. J. Palma. “*Screen printed flexible radiofrequency identification tag for oxygen monitoring*”. Analytical Chemistry. 2013. Vol. 85, 22: 11098-11105.

José F. Salmerón, Luis Gómez-Robledo, Miguel Á. Carvajal, Rafael Huertas, María José Moyano, Belén Gordillo, Alberto J. Palma, Francisco J. Heredia, Manuel Melgosa. “*Measuring the colour of virgin olive oils in a new colour scale using a low-cost portable electronic device*”. Journal of Food Engineering. 2012. Vol. 111, 2: 247-254.

Journal papers submissions

José F. Salmerón, Almudena Rivadeneyra, L. F. Capitán-Vallvey, Jesús Banqueri Ozáez, Alberto J. Palma and Miguel A. Carvajal. “*A Technique for Impedance Measurement of Balanced UHF RFID Antennas*”. Transactions on Antennas and Propagation. August, 2014.

José F. Salmerón, Almudena Rivadeneyra, Manuel Agudo-Acemel, Luis Fermín Capitan-Vallvey, Jesús Banqueri, Miguel A. Carvajal, Alberto J. Palma. “*Printed Single-chip UHF Passive Radiofrequency Identification Tags with Sensing Capability*”. Sensors and Actuator: A. July, 2014.

Almudena Rivadeneyra, **José Fernández-Salmerón**, Manuel Agudo-Acemel, Alberto J. Palma, Luis Fermín Capitan-Vallvey, Juan A. López-Villanueva. “*Cantilever fabrication by a printing and bonding process*”. Journal of Microelectromechanical Systems. March, 2014

International Conferences

Almudena Rivadeneyra-Torres, **José Fernández-Salmerón**, Juan Antonio Lopez-Villanueva, Luis Fermín Capitán-Vallvey, Alberto J. Palma-López. “*Novel capacitive structure: A comparison with Interdigitated Electrodes*”. The Swiss Conference on Printed Electronics and Functional Materials (21-22 November 2013, Basel, Switzerland)

Almudena Rivadeneyra-Torres, **José Fernández-Salmerón**, Juan Antonio Lopez-Villanueva, Luis Fermín Capitán-Vallvey, Alberto J. Palma-López. “*Ink-jet printed humidity sensor on Kapton HN for UHF RFID tags*”. Large-area, Organic & Printed Electronics Convention (LOPE-C). (11-13 June 2013, Munchen, Germany)

José F. Salmerón, Almudena Rivadeneyra Torres, Jesus Banqueri, Migue A Carvajal, Manuel Agudo. “*Design and Characterization of Ink-Jet and Screen Printed HF RFID Antennas*”. 2012 Fourth International Workshop on RFID Technology (EURASIP RFID) (27-28 September 2012, Torino, Italy)

José F. Salmerón, Luis F. Capitan-Vallvey, Alberto J Palma, Francisco Molina-Lopez, Danick Briand, Nico F de Rooij. “*Physical and electrical properties of ink-jet and screen printed patterns for RFID HF antennas*”.

IEEE International Conference on RFID-Technologies and Applications (5-7 November 2012, Nice, France)

Manuel Melgosa-Latorre, Luis Gómez-Robledo, Rafael Huertas, María Dolores Huete, **José F. Salmerón**, Miguel A. Carvajal, Alberto J. Palma, María Jose Moyano, Belén Gordillo, Francisco J. Heredia. "*The Modified Uniform Oil Colour Scale (MUOCS)*". Interim Meeting of the International Colour Association (22-25 September 2012, Taipei, Taiwan)

Appendix I. Smart RFID Chip SL900A

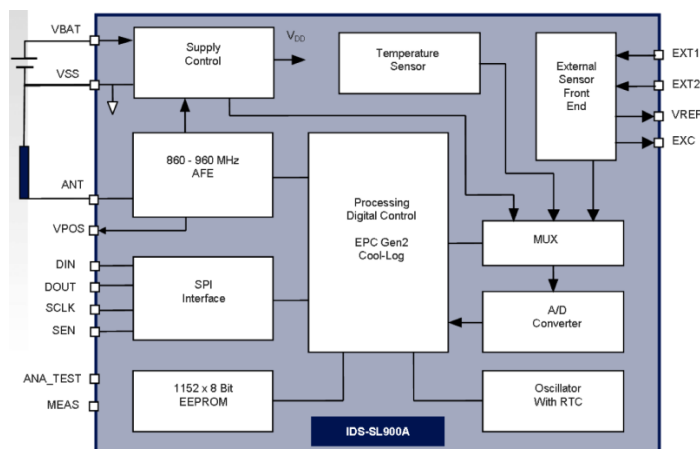
The SL900A is an EPC global Class 3 tag chip optimised for single-cell and dual-cell, battery-assisted smart labels with sensor functionality. The chip is ideal for applications using thin and flexible batteries but can also be powered from the RF field (electromagnetic waves from an RFID reader).

The chip has a fully integrated temperature sensor with a typical nonlinearity of $\pm 0.5^{\circ}\text{C}$ over the specified temperature range. The external sensor interface provides a flexible way of adding additional sensors to the system and supports up to 2 external sensors.

Key Features

- High Temperature Range: -40°C to $+110^{\circ}\text{C}$
- Frequency: 860 to 960 MHz
- Battery supply: 1.5V or 3V
- Data logging from:
 - On-chip temperature sensor
 - external sensors
- EPC Class 1 and Class 3 Compliant
- Compatible to EPC Gen.2
- Real-time clock for data logging
- External sensor interrupt capability
- Serial peripheral interface
- On-chip 9k bit EEPROM
- Integrated dynamic shelf life calculation
- Advanced logging with 4 user-selectable limits

Block Diagram



Supply Arrangement

The SL900A is supplied from either the battery or through the electromagnetic waves from a reader. The device is normally supplied from the battery unless there is no battery attached (passive label), or when the battery is drained.

Analogue Front End (AFE)

The analogue front end is designed according to EPC Gen 2. The forward link (reader to tag) is amplitude modulated and the backward link (tag to reader) is amplitude modulated (load modulation is used).

Processing and Digital Control

The SL900A is fully EPC Class 1 compliant, with additional custom commands for extended functions. The maximum transponder to interrogator data rate according to Class 1/Gen.2 is 640 Kbit/s. The maximum interrogator to transponder data rate is 160 Kbit/s.

Serial Interface (SPI)

The integrated serial interface (SPI) can be used to initialize the chip and to set the parameters. The logging procedure can be started and stopped with the SPI. The SPI bus can also be used for the communication between a microcontroller that is attached to the SL900A and the RFID reader.

Real-Time Clock (RTC)

The on-chip real-time clock (RTC) is started through the START LOG command in which the start time is programmed in UTC format. The interval for sensing and data logging can be programmed in the range from 1 second up to 8 hours. The accuracy of the timer is $\pm 3\%$.

Temperature Sensor

The on-chip temperature sensor can measure the temperature in the range from -20°C to 60°C with a typical accuracy of $\pm 0.5^{\circ}\text{C}$.

External Sensors

The on-chip external sensor front end provides a flexible interface for analogue external sensors. It has an auto-range and interrupts function. It supports various types of analogue sensors from pressure, humidity, temperature, light ...

Analogue to Digital Converter

The chip has an integrated 10-bit analogue to digital converter with selectable voltage references. It is used for conversion of temperature, external sensors and battery voltage.

External Sensor Interrupt

The external sensor inputs EXT1 and EXT2 can be used for event-triggered logging. In this mode the logging is not triggered in predefined time intervals from the internal timer, but can be triggered externally, either with a sensor, switch or a microcontroller.

The interrupt source can be the EXT1, EXT2 input or both, were the EXT1 input has the higher priority. The user application can select which measurements are triggered by the interrupt event.

In the interrupt mode the sensor value is stored together with the 32-bit real time clock value. For a correct real-time clock value the correct Start time has to be supplied. The interrupt mode is started with the START LOG command and the correct setting in the registers (SET LOG MODE command).

Data Protection

Additional to the Gen2 lock protection, the SL900A offers read/write protection using 3 password sets for 3 memory areas. Each 32-bit password is divided into 2 16-bit passwords, where the lower 16 bits are reserved for the Write protection and the higher 16 bits are reserved for the Read/Write protection.

Shelf Life

The SL900A device has an integrated shelf life algorithm that can dynamically calculate the remaining shelf life of the product. It has an automatic alarm function for the shelf life expiration. This can be used to directly drive a LED or as an interrupt for an external microcontroller.

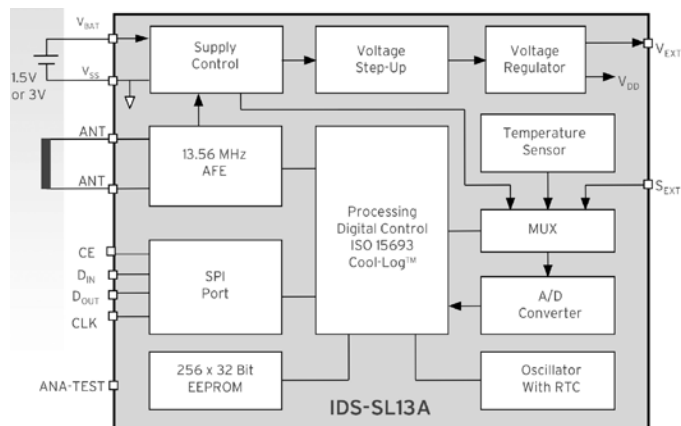
Appendix II. Smart RFID Chip SL13A

The IDS-SL13A is an active/semi-passive tag chip optimised for single-cell, battery-powered smart labels with sensor functionality and data logging. The chip is ideal for applications using thin and flexible batteries but can also be powered from the RF field (electromagnetic waves from an RFID reader). The chip has a fully integrated temperature sensor with a maximum accuracy of 0.5°C. The external sensor interface (SEXT) is an analogue input and allows the connection of an external sensor. The SPI port provides direct access to the EEPROM from external circuits.

Key Features

- High Temperature Range: -40°C to +110°C.
- Frequency: 13.56 MHz.
- Battery supply: 1.5V or 3V.
- Data logging from:
 - On-chip temperature sensor.
 - External sensor.
- ISO 15693 and cool-Log™ compliant
- Real-time clock for data logging
- Parameter setting and access to EEPROM via serial bus (SPI)
- On-chip 8k bit EEPROM
- Anti-collision capability
- Backup through supply from RF field for EEPROM readout after battery is exhausted

Pin-out and Block Diagram



Supply Arrangement

The IDS-SL13A is supplied from either the battery or through the electromagnetic waves from a reader. The device is normally supplied from the battery unless the battery voltage is too low - in this case the device is powered from the RF field. This functionality enables the read out of the log data even in case the battery is exhausted. The chip automatically detects whether a 1.5V or 3V battery is connected and adapts accordingly. The voltage step-up converter provides an input voltage for the voltage regulator, which provides a regulated voltage of 2V nominal (internal digital supply). The maximum current available from VEXT for external circuitry is 4mA (only when RF field is present) and is regulated to 3.4V.

Analogue Front End (AFE)

The analogue front end is designed for 13.56 MHz according to ISO 15693. The incoming data are demodulated from the received ASK (Amplitude Shift Keying) signal, which is 10 ~ 30% or 100% modulated. Outgoing data are generated by the IDS-SL13A load variation using Manchester coding with one or two sub-carrier frequencies of 423.75 KHz ($f_c/32$) or 484.28 KHz ($f_c/28$).

Processing and Digital Control

The IDS-SL13A is fully ISO 15693 compliant. Additional data logging commands are handled by the cool-Log™ protocol. Both data coding modes (1 out of 256 and 1 out of 4) are supported by the IDS-SL13A. The reader (interrogator) makes mode selection within the SOF (Start of Frame). The 1-of-256 data coding mode has a data rate of 1.65 Kbit/s ($f_c/8192$) meaning that the transmission of one byte takes 4.833 ms. The 1-of-4 coding has a rate of 26.48 Kbit/s ($f_c/512$) with the transmission of one byte taken 302.08 μ s.

Serial Interface (SPI)

The integrated serial interface (SPI) can be used to read and write the embedded EEPROM and to set the parameters. The SPI interface is a secondary and test interface - the main interface is the RF ISO15693 interface.

Real-Time Clock (RTC)

The on-chip real-time clock (RTC) is started through the START-LOG command in which the start time is programmed in UTC format. The interval for sensing and data logging can be programmed in the range from 1 second up to 9 hours. The accuracy of the timer is $\pm 3\%$.

Temperature Sensor

The on-chip temperature sensor can measure the temperature in the range from -20°C to 60°C with an accuracy of $\pm 0.5^{\circ}\text{C}$. The reference voltage for the A/D conversion is supplied from an on-chip calibrated band gap reference.

A/D Converter

An integrated 10-bit dual slope A/D converter is used for the temperature, battery and external sensor voltage conversions.

EEPROM Organization and Security

The EEPROM is organized into 3 areas - the System area, User area and Measurement area. The System area has a fixed size and can be accessed only by the proprietary commands. It is protected by the Level 1 password - the System password. The User and Measurement areas reside in the same address space (256 blocks), but have separated passwords - the User password and the Measurement password. The User and Measurement areas can be accessed by the standard ISO15693 read and write commands. The User area size can be set by the Initialize command. The minimum size of the User area is 1 block, the maximum is 256 blocks. The size of the Measurement area is 256 blocks minus User area. All blocks are 32 bits wide.

The password protection restricts only the write- type commands. Read commands are always open. The password protection can be activated for every area individually by writing a value not equal to 0 to the password blocks.

The chip also supports a one-time-use secure mode. When this mode is used, the chip with the Start Log command automatically locks all Measurement blocks. Those blocks cannot be unlocked anymore even if the Level 3 (Measurement) password is known. This mode is intended for high security applications where the 32-bit password does not provide sufficient protection.

References

- Abad, E., F. Palacio, M. Nuin, A. G. d. Zárate, A. Juarros, J. M. Gómez & S. Marco (2009) RFID smart tag for traceability and cold chain monitoring of foods: Demonstration in an intercontinental fresh fish logistic chain. *Journal of Food Engineering*, 93, 394-399.
- AG, A. 2014. Demo Kit for the SL900A smart EPC sensor tag IC.
- Akyildiz, I. F., W. Su, Y. Sankarasubramaniam & E. Cayirci (2002) Wireless sensor networks: a survey. *Computer networks*, 38, 393-422.
- Allen, M., C. Lee, B. Ahn, T. Kololuoma, K. Shin & S. Ko (2011) R2R gravure and inkjet printed RF resonant tag. *Microelectronic Engineering*, 88, 3293-3299.
- Allen, M. L., K. Jaakkola, K. Nummila & H. Seppa (2009) Applicability of Metallic Nanoparticle Inks in RFID Applications. *Ieee Transactions on Components and Packaging Technologies*, 32, 325-332.
- Amin, Y., Q. Chen, L. Zheng & H. Tenhunen (2012) Development and Analysis of Flexible UHF RFID Antennas For "Green" Electronics. *Progress In Electromagnetics Research-PIER*, 130, 1-15.
- Amin, Y., R. K. Kanth, P. Liljeberg, A. Akram, Q. Chen, L.-R. Zheng & H. Tenhunen. 2013. Printable RFID Antenna with Embedded Sensor and Calibration Functions. In *Progress In Electromagnetics Research Symposium Proceedings, Stockholm, Sweden, Aug. 12-15, 2013*, 567-570. Electromagnetics Academy.
- Andersson, H., A. Manuilskiy, T. Unander, C. Lidenmark, S. Forsberg & H. Nilsson (2012) Inkjet printed silver nanoparticle humidity sensor with memory effect on paper. *Sensors Journal, IEEE*, 12, 1901-1905.
- Artunc, N., M. D. Bilge & G. Utlu (2007) The effects of grain boundary scattering on the electrical resistivity of single-layered silver and double-layered silver/chromium thin films. *Surface & Coatings Technology*, 201, 8377-8381.
- Atsushi, O. & Y. Kentaro (2006) A temperature-managed traceability system using RFID tags with embedded temperature sensors. *Nec Technical Journal*, 1, 82-86.
- Atzori, L., A. Iera & G. Morabito (2010) The internet of things: A survey. *Computer Networks*, 54, 2787-2805.
- Babar, A. A., S. Manzari, L. Sydanheimo, A. Z. Elsherbeni & L. Ukkonen (2012) Passive UHF RFID Tag for Heat Sensing Applications. *Antennas and Propagation, IEEE Transactions on*, 60, 4056-4064.
- Balanis, C. A. 2012. *Antenna theory: analysis and design*. John Wiley & Sons.
- Bhattacharyya, R., C. Floerkemeier & S. Sarma (2010) Low-Cost, Ubiquitous RFID-Tag-Antenna-Based Sensing. *Proceedings of the IEEE*, 98, 1593-1600.

- Björninen, T., S. Merilampi, L. Ukkonen, L. Sydänheimo & P. Ruuskanen (2009) The Effect of Fabrication Method on Passive UHF RFID Tag Performance. *International Journal of Antennas and Propagation*, 2009, 1-8.
- Blakistone, B. A. 1998. *Principles and applications of modified atmosphere packaging of foods*. Springer.
- Briand, D., A. Oprea, J. Courbat & N. Barsan (2011) Making environmental sensors on plastic foil. *Materials Today*, 14, 416-423.
- Brody, A. L., B. Bugusu, J. H. Han, C. K. Sand & T. H. McHugh (2008) Scientific status summary. Innovative food packaging solutions. *J Food Sci*, 73, R107-16.
- Broutas, P., H. Contopanagos, E. D. Kyriakis-Bitzaros, D. Tsoukalas & S. Chatzandroulis (2012) A low power RF harvester for a smart passive sensor tag with integrated antenna. *Sensors and Actuators a-Physical*, 176, 34-45.
- Calvert, P. (2001) Inkjet printing for materials and devices. *Chemistry of Materials*, 13, 3299-3305.
- Capitan-Vallvey, L. F., L. J. Asensio, J. Lopez-Gonzalez, M. D. Fernandez-Ramos & A. J. Palma (2007) Oxygen-sensing film coated photodetectors for portable instrumentation. *Anal Chim Acta*, 583, 166-73.
- Carraway, E. R., J. N. Demas, B. A. Degraff & J. R. Bacon (1991) Photophysics and Photochemistry of Oxygen Sensors Based on Luminescent Transition-Metal Complexes. *Analytical Chemistry*, 63, 337-342.
- Catarinucci, L., M. Cappelli, R. Colella & L. Tarricone (2008) A novel low-cost multisensor-tag for RFID applications in healthcare. *Microwave and Optical Technology Letters*, 50, 2877-2880.
- Catarinucci, L., R. Colella & L. Tarricone (2009) A Cost-Effective UHF RFID Tag for Transmission of Generic Sensor Data in Wireless Sensor Networks. *Ieee Transactions on Microwave Theory and Techniques*, 57, 1291-1296.
- (2012) Smart Prototyping Techniques for Uhf Rfid Tags: Electromagnetic Characterization and Comparison with Traditional Approaches. *Progress in Electromagnetics Research-Pier*, 132, 91-111.
- (2013) Enhanced UHF RFID Sensor-Tag. *IEEE Microwave and Wireless Components Letters*, 23, 49-51.
- Cazeca, M. J., J. Mead, J. Chen & R. Nagarajan (2013) Passive wireless displacement sensor based on RFID technology. *Sensors and Actuators a-Physical*, 190, 197-202.
- Courbat, J., D. Briand, J. Wollenstein & N. F. de Rooij (2011) Polymeric foil optical waveguide with inkjet printed gas sensitive film for colorimetric sensing. *Sensors and Actuators B-Chemical*, 160, 910-915.

- Chen, S. L., K. H. Lin & R. Mittra (2010) A Measurement Technique for Verifying the Match Condition of Assembled RFID Tags. *Ieee Transactions on Instrumentation and Measurement*, 59, 2123-2133.
- Chiolerio, A., M. Cotto, P. Pandolfi, P. Martino, V. Camarchia, M. Pirola & G. Ghione (2012) Ag nanoparticle-based inkjet printed planar transmission lines for RF and microwave applications: Considerations on ink composition, nanoparticle size distribution and sintering time. *Microelectronic Engineering*, 97, 8-15.
- Chu, H., G. Wu, J. Chen, F. Fei, J. D. Mai & W. J. Li (2013) Design and simulation of self-powered radio frequency identification (RFID) tags for mobile temperature monitoring. *Science China Technological Sciences*, 56, 1-7.
- da Costa, F. C., E. R. de Lima, R. T. Yoshioka, J. E. Bertuzzo & J. Koeppe. 2013. Impedance measurement of dipole antenna for EPC Global compliant RFID tag. In *Microwave & Optoelectronics Conference (IMOC), 2013 SBMO/IEEE MTT-S International*, 1-5.
- Daliri, A., A. Galehdar, S. John, C. H. Wang, W. S. T. Rowe & K. Ghorbani (2012) Wireless strain measurement using circular microstrip patch antennas. *Sensors and Actuators a-Physical*, 184, 86-92.
- De Donno, D., L. Catarinucci, A. Di Serio & L. Tarricone (2013) A Long-Range Computational RFID Tag for Temperature and Acceleration Sensing Applications. *Progress In Electromagnetics Research C*, 45, 223-235.
- De Donno, D., L. Catarinucci & L. Tarricone (2014) A Battery-Assisted Sensor-Enhanced RFID Tag Enabling Heterogeneous Wireless Sensor Networks. *IEEE Sensors Journal*, 14, 1048-1055.
- Demas, J. N. & B. A. DeGraff (2001) Applications of luminescent transition platinum group metal complexes to sensor technology and molecular probes. *Coordination Chemistry Reviews*, 211, 317-351.
- Derby, B. 2010. Inkjet Printing of Functional and Structural Materials: Fluid Property Requirements, Feature Stability, and Resolution. In *Annual Review of Materials Research, Vol 40*, eds. D. R. Clarke, M. Ruhle & F. Zok, 395-414.
- Eom, K. H., M. C. Kim, S. Lee & C. w. Lee (2012) The Vegetable Freshness Monitoring System Using RFID with Oxygen and Carbon Dioxide Sensor. *International Journal of Distributed Sensor Networks*, 2012, 1-6.
- Evans, R. C., P. Douglas, J. A. Williams & D. L. Rochester (2006) A novel luminescence-based colorimetric oxygen sensor with a "traffic light" response. *J Fluoresc*, 16, 201-6.
- Faddoul, R., N. Reverdy-Bruas & A. Blayo (2012) Formulation and screen printing of water based conductive flake silver pastes onto green ceramic tapes for electronic applications. *Materials Science and Engineering B-Advanced Functional Solid-State Materials*, 177, 1053-1066.

- Faustman, C. & R. G. Cassens (1990) The Biochemical Basis for Discoloration in Fresh Meat: A Review. *Journal of Muscle Foods*, 1, 217-243.
- Feng, Y., M. Mueller, J. Liebeskind, O. Chen, L.-R. Zheng, W. Schmidt & W. Zapka. 2011. Characterization of Inkjet Printed Coplanar Waveguides for Flexible Electronics. In *NIP & Digital Fabrication Conference*, 454-457. Society for Imaging Science and Technology.
- Fernandez, I., A. Asensio, I. Gutierrez, J. Garcia, I. Rebollo & J. de No (2012) Study of the communication distance of a MEMS Pressure Sensor Integrated in a RFID Passive Tag. *Advances in Electrical and Computer Engineering*, 12, 15-18.
- Finkenzeller, K. & D. Müller. 2010. *RFID Handbook: Fundamentals and Applications in Contactless Smart Cards, Radio Frequency Identification and Near-Field Communication*. Wiley.
- Gao, J., J. Siden, H.-E. Nilsson & M. Gulliksson (2013) Printed Humidity Sensor With Memory Functionality for Passive RFID Tags. *IEEE Sensors Journal*, 13, 1824-1834.
- Griffin, J. D. & G. D. Durgin (2009) Complete link budgets for backscatter-radio and RFID systems. *Antennas and Propagation Magazine, IEEE*, 51, 11-25.
- Grosinger, J., C. F. Mecklenbräuker & A. L. Scholtz. 2010. UHF RFID Transponder Chip and Antenna Impedance Measurements. In *The Third International EURASIP Workshop on RFID Technology*, 1-4. La Manga del Mar Menor, Murcia, Spain.
- Hailong, Z., Y. C. A. Ko & T. T. Ye. 2010. Impedance measurement for balanced UHF RFID tag antennas. In *Radio and Wireless Symposium (RWS), 2010 IEEE*, 128-131.
- Han, J. H. 2005. *Innovations in Food Packaging*. Elsevier Science.
- Harrey, P., B. Ramsey, P. Evans & D. Harrison (2002) Capacitive-type humidity sensors fabricated using the offset lithographic printing process. *Sensors and Actuators B: Chemical*, 87, 226-232.
- Jacquemod, G., M. Nowak, E. Colinet, N. Delorme & F. Conseil (2010) Novel architecture and algorithm for remote interrogation of battery-free sensors. *Sensors and Actuators a-Physical*, 160, 125-131.
- Janeczek, K., M. Jakubowska, G. Koziół, A. Młodziak & A. Araźna (2012) Investigation of ultra-high-frequency antennas printed with polymer pastes on flexible substrates. *IET Microwaves, Antennas & Propagation*, 6, 549.
- Jung, H. C., S. H. Cho, J. W. Joung & Y. S. Oh (2007) Studies on inkjet-printed conducting lines for electronic devices. *Journal of Electronic Materials*, 36, 1211-1218.
- Kassal, P., I. M. Steinberg & M. D. Steinberg (2013) Wireless smart tag with potentiometric input for ultra low-power chemical sensing. *Sensors and Actuators B: Chemical*, 184, 254-259.

- Kattumenu, R., M. Rebros, M. Joyce, P. D. Fleming & G. Neelgund (2009) Effect of substrate properties on conductive traces printed with silver-based flexographic ink. *Nordic Pulp & Paper Research Journal*, 24, 101-106.
- Kerry, J. P., M. N. O'Grady & S. A. Hogan (2006) Past, current and potential utilisation of active and intelligent packaging systems for meat and muscle-based products: A review. *Meat Sci*, 74, 113-30.
- Kim, C., M. Nogi & K. Sukanuma (2012) Electrical conductivity enhancement in inkjet-printed narrow lines through gradual heating. *Journal of Micromechanics and Microengineering*, 22, 035016.
- Kim, J. W., Y. C. Lee, J. M. Kim, W. Nah, H. S. Lee, H. C. Kwon & S. B. Jung (2010a) Characterization of direct patterned Ag circuits for RF application. *Microelectronic Engineering*, 87, 379-382.
- Kim, Y., H. Kim & H. J. Yoo (2010b) Electrical Characterization of Screen-Printed Circuits on the Fabric. *Ieee Transactions on Advanced Packaging*, 33, 196-205.
- Koski, K., E. Koski, J. Virtanen, T. Bjorninen, L. Sydanheimo, L. Ukkonen & A. Z. Elsherbeni (2012) Inkjet-printed passive UHF RFID tags: review and performance evaluation. *International Journal of Advanced Manufacturing Technology*, 62, 167-182.
- Kuo, S.-K., S.-L. Chen & C.-T. Lin (2008) An accurate method for impedance measurement of RFID tag antenna. *Progress In Electromagnetics Research*, 83, 93-106.
- Lacy, F. (2011) Developing a theoretical relationship between electrical resistivity, temperature, and film thickness for conductors. *Nanoscale Res Lett*, 6, 636.
- Lee, D. J. & J. H. Oh (2010) Inkjet printing of conductive Ag lines and their electrical and mechanical characterization. *Thin Solid Films*, 518, 6352-6356.
- Lee, D. J., J. H. Oh & H. S. Bae (2010) Crack formation and substrate effects on electrical resistivity of inkjet-printed Ag lines. *Materials Letters*, 64, 1069-1072.
- Li, X. Y. & E. C. Kan (2010) A wireless low-range pressure sensor based on P(VDF-TrFE) piezoelectric resonance. *Sensors and Actuators a-Physical*, 163, 457-463.
- Lim, N., J. Kim, S. Lee, N. Kim & G. Cho (2009) Screen Printed Resonant Tags for Electronic Article Surveillance Tags. *Ieee Transactions on Advanced Packaging*, 32, 72-76.
- Lopez-Ruiz, N., A. Martinez-Olmos, I. M. P. de Vargas-Sansalvador, M. D. Fernandez-Ramos, M. A. Carvajal, L. F. Capitan-Vallvey & A. J. Palma (2012) Determination of O-2 using colour sensing from image processing with mobile devices. *Sensors and Actuators B-Chemical*, 171, 938-945.

- Magdassi, S., M. Grouchko, O. Berezin & A. Kamyshny (2010) Triggering the sintering of silver nanoparticles at room temperature. *ACS Nano*, 4, 1943-8.
- Mamishv, A. V., K. Sundara-Rajan, F. Yang, Y. Du & M. Zahn (2004) Interdigital sensors and transducers. *Proceedings of the IEEE*, 92, 808-845.
- Manzari, S., C. Occhiuzzi, S. Nawale, A. Catini, C. Di Natale & G. Marrocco (2012) Humidity Sensing by Polymer-Loaded UHF RFID Antennas. *IEEE Sensors Journal*, 12, 2851-2858.
- Marrocco, G. (2008) The art of UHF RFID antenna design: impedance-matching and size-reduction techniques. *IEEE Antennas and Propagation Magazine*, 50, 66-79.
- Marsh, K. & B. Bugusu (2007) Food packaging--roles, materials, and environmental issues. *J Food Sci*, 72, R39-55.
- Martinez-Olmos, A., I. M. P. de Vargas-Sansalvador, A. J. Palma, J. Banqueri, M. D. Fernandez-Ramos & L. F. Capitan-Vallvey (2011) Multisensor probe for soil monitoring. *Sensors and Actuators B-Chemical*, 160, 52-58.
- Mats, L., J. T. Cain & M. H. Mickle (2009) The in-situ technique for measuring input impedance and connection effects of RFID tag antenna. *IEEE transactions on automation science and engineering*, 6, 4-8.
- Mattoli, V., B. Mazzolai, A. Mondini, S. Zampolli & P. Dario (2010) Flexible tag datalogger for food logistics. *Sensors and Actuators a-Physical*, 162, 316-323.
- Mayr, T., T. Abel, B. Enko, S. Borisov, C. Konrad, S. Kostler, B. Lamprecht, S. Sax, E. J. List & I. Klimant (2009) A planar waveguide optical sensor employing simple light coupling. *Analyst*, 134, 1544-7.
- Merilampi, S., T. Björninen, L. Ukkonen, P. Ruuskanen & L. Sydänheimo (2011) Embedded wireless strain sensors based on printed RFID tag. *Sensor Review*, 31, 32-40.
- Merilampi, S., T. Laine-Ma & P. Ruuskanen (2009) The characterization of electrically conductive silver ink patterns on flexible substrates. *Microelectronics Reliability*, 49, 782-790.
- Merilampi, S. L., T. Björninen, L. Ukkonen, P. Ruuskanen & L. Sydänheimo (2010a) Characterization of UHF RFID tags fabricated directly on convex surfaces by pad printing. *The International Journal of Advanced Manufacturing Technology*, 53, 577-591.
- Merilampi, S. L., T. Björninen, Vuorima, x, A. ki, L. Ukkonen, P. Ruuskanen & L. Sydanheimo (2010b) The Effect of Conductive Ink Layer Thickness on the Functioning of Printed UHF RFID Antennas. *Proceedings of the IEEE*, 98, 1610-1619.
- Metrology, V. P. 1999. WYKO Surface Profiler Technical Reference Manual. Tucson, AZ.

- Meys, R. & F. Janssens (1998) Measuring the impedance of balanced antennas by an S-parameter method. *Antennas and Propagation Magazine, IEEE*, 40, 62-65.
- Mills, A. (2005) Oxygen indicators and intelligent inks for packaging food. *Chem Soc Rev*, 34, 1003-11.
- Mills, A. & D. Hazafy (2008) A solvent-based intelligence ink for oxygen. *Analyst*, 133, 213-8.
- Mills, A., K. Lawrie, J. Bardin, A. Apedaile, G. A. Skinner & C. O'Rourke (2012) An O₂ smart plastic film for packaging. *Analyst*, 137, 106-12.
- Mohan, S. S., M. D. Hershenson, S. P. Boyd & T. H. Lee (1999) Simple accurate expressions for planar spiral inductances. *Ieee Journal of Solid-State Circuits*, 34, 1419-1424.
- Molina-Lopez, F., D. Briand & N. F. de Rooij (2012) All additive inkjet printed humidity sensors on plastic substrate. *Sensors and Actuators B-Chemical*, 166, 212-222.
- Nikitin, P. V., K. S. Rao, S. F. Lam, V. Pillai, R. Martinez & H. Heinrich (2005) Power reflection coefficient analysis for complex impedances in RFID tag design. *IEEE Transactions on Microwave Theory and Techniques*, 53, 2721-2725.
- Nikitin, P. V., K. S. Rao, R. Martinez & S. F. Lam (2009) Sensitivity and impedance measurements of UHF RFID chips. *Microwave Theory and Techniques, IEEE Transactions on*, 57, 1297-1302.
- Nilsson, H.-E., T. Unander, J. Siden, H. Andersson, A. Manuilskiy, M. Hummelgard & M. Gulliksson (2012) System Integration of Electronic Functions in Smart Packaging Applications. *Components, Packaging and Manufacturing Technology, IEEE Transactions on*, 2, 1723-1734.
- Ning, Z. & L. Xiuping. 2010. RFID tag antenna design and its EM simulation based measurement method. In *Communication Technology (ICCT), 2010 12th IEEE International Conference on*, 644-647.
- O'Riordan, T. C., H. Voraberger, J. P. Kerry & D. B. Papkovsky (2005) Study of migration of active components of phosphorescent oxygen sensors for food packaging applications. *Analytica Chimica Acta*, 530, 135-141.
- Oprea, A., J. Courbat, N. Bârsan, D. Briand, N. F. de Rooij & U. Weimar (2009) Temperature, humidity and gas sensors integrated on plastic foil for low power applications. *Sensors and Actuators B: Chemical*, 140, 227-232.
- Palma, A. J., J. Lopez-Gonzalez, L. J. Asensio, M. D. Fernandez-Ramos & L. F. Capitan-Vallvey (2007) Microcontroller-based portable instrument for stabilised optical oxygen sensor. *Sensors and Actuators B-Chemical*, 121, 629-638.

- Palmer, K. D. & M. W. van Rooyen (2006) Simple broadband measurements of balanced loads using a network analyzer. *Instrumentation and Measurement, IEEE Transactions on*, 55, 266-272.
- Palukuru, V. K., K. Sanoda, V. Pynttari, T. Hu, R. Makinen, M. Mantysalo, J. Hagberg & H. Jantunen (2011) Inkjet-Printed RF Structures on BST-Polymer Composites: An Application of a Monopole Antenna for 2.4 GHz Wireless Local Area Network Operation. *International Journal of Applied Ceramic Technology*, 8, 940-946.
- Papkovsky, D. B., N. Papkovskaia, A. Smyth, J. Kerry & V. I. Ogurtsov (2000) Phosphorescent sensor approach for non-destructive measurement of oxygen in packaged foods: Optimisation of disposable oxygen sensors and their characterization over a wide temperature range. *Analytical Letters*, 33, 1755-1777.
- Park, J., W. Hong & C. S. Kim (2010) Color Intensity Method for Hydrogel Oxygen Sensor Array. *Ieee Sensors Journal*, 10, 1855-1862.
- Perelaer, J., P. J. Smith, D. Mager, D. Soltman, S. K. Volkman, V. Subramanian, J. G. Korvink & U. S. Schubert (2010) Printed electronics: the challenges involved in printing devices, interconnects, and contacts based on inorganic materials. *Journal of Materials Chemistry*, 20, 8446-8453.
- Perez de Vargas-Sansalvador, I. M., M. A. Carvajal, O. M. Roldan-Munoz, J. Banqueri, M. D. Fernandez-Ramos & L. F. Capitan-Vallvey (2009) Phosphorescent sensing of carbon dioxide based on secondary inner-filter quenching. *Anal Chim Acta*, 655, 66-74.
- Pérez de Vargas-Sansalvador, I. M., A. Martinez-Olmos, A. J. Palma, M. D. Fernández-Ramos & L. F. Capitán-Vallvey (2010) Compact optical instrument for simultaneous determination of oxygen and carbon dioxide. *Microchimica Acta*, 172, 455-464.
- Pletersek, A., M. Sok & J. Trontelj (2012) Monitoring, control and diagnostics using RFID infrastructure. *J Med Syst*, 36, 3733-9.
- Potyrailo, R. A., N. Nagraj, Z. Tang, F. J. Mondello, C. Surman & W. Morris (2012) Battery-free radio frequency identification (RFID) sensors for food quality and safety. *J Agric Food Chem*, 60, 8535-43.
- Pozar, D. M. 2009. *Microwave engineering*. John Wiley & Sons.
- Qing, X., C. K. Goh & Z. N. Chen (2009) Impedance characterization of RFID tag antennas and application in tag co-design. *Microwave Theory and Techniques, IEEE Transactions on*, 57, 1268-1274.
- Quaranta, M., S. M. Borisov & I. Klimant (2012) Indicators for optical oxygen sensors. *Bioanal Rev*, 4, 115-157.
- Rao, K. V. S., P. V. Nikitin & S. F. Lam (2005) Antenna design for UHF RFID tags: a review and a practical application. *Antennas and Propagation, IEEE Transactions on*, 53, 3870-3876.
- Reininger, F., C. Kolle, W. Trettnak & W. Gruber. 1996. Quality control of gas-packed food by an optical oxygen sensor. In *Proceedings of the*

international symposium on food packaging: Ensuring the safety and quality of foods.

- Restuccia, D., U. G. Spizzirri, O. I. Parisi, G. Cirillo, M. Curcio, F. Iemma, F. Puoci, G. Vinci & N. Picci (2010) New EU regulation aspects and global market of active and intelligent packaging for food industry applications. *Food Control*, 21, 1425-1435.
- Rida, A., L. Yang, R. Vyas & M. M. Tentzeris (2009) Conductive inkjet-printed antennas on flexible low-cost paper-based substrates for RFID and WSN applications. *Antennas and Propagation Magazine, IEEE*, 51, 13-23.
- Rivadeneira, A., J. Fernández-Salmerón, M. Agudo, J. A. López-Villanueva, L. F. Capitan-Vallvey & A. J. Palma (2014a) Design and characterization of a low thermal drift capacitive humidity sensor by inkjet-printing. *Sensors and Actuators B: Chemical*, 195, 123-131.
- Rivadeneira, A., J. Fernández-Salmerón, J. Banqueri Ozaez, J. A. López-Villanueva, L. F. Capitan-Vallvey & A. J. Palma (2014b) A novel electrode structure compared with interdigitated electrodes as capacitive sensor. *Sensors and Actuators B: Chemical*, Article in press.
- Roberson, D. A., R. B. Wicker & E. MacDonald (2012) Ohmic Curing of Printed Silver Conductive Traces. *Journal of Electronic Materials*, 41, 2553-2566.
- Rooney, M. (1995) Active food packaging.
- Rouse, C. D., M. R. Kurz, B. R. Petersen & B. G. Colpitts (2013) Performance Evaluation of Conductive-Paper Dipole Antennas. *Antennas and Propagation, IEEE Transactions on*, 61, 1427-1430.
- Saini, D. P. 1995. Chip level waveguide sensor. Google Patents.
- Salmerón, J. F., L. Gómez-Robledo, M. Á. Carvajal, R. Huertas, M. J. Moyano, B. Gordillo, A. J. Palma, F. J. Heredia & M. Melgosa (2012) Measuring the colour of virgin olive oils in a new colour scale using a low-cost portable electronic device. *Journal of Food Engineering*, 111, 247-254.
- Sangoi, R., C. G. Smith, M. D. Seymour, J. N. Venkataraman, D. M. Clark, M. L. Kleper & B. E. Kahn (2005) Printing radio frequency identification (RFID) tag antennas using inks containing silver dispersions. *Journal of dispersion science and technology*, 25, 513-521.
- Schaferling, M., M. Wu, J. Enderlein, H. Bauer & O. S. Wolfbeis (2003) Time-resolved luminescence imaging of hydrogen peroxide using sensor membranes in a microwell format. *Applied Spectroscopy*, 57, 1386-1392.
- Schoo, C. & M. Knoll (2014) Self-writing smart labels for humidity monitoring. *Sensors and Actuators A: Physical*, 205, 1-5.

- Shin, D. Y., Y. Lee & C. H. Kim (2009) Performance characterization of screen printed radio frequency identification antennas with silver nanopaste. *Thin Solid Films*, 517, 6112-6118.
- Siegel, A. C., S. T. Phillips, M. D. Dickey, N. S. Lu, Z. G. Suo & G. M. Whitesides (2010) Foldable Printed Circuit Boards on Paper Substrates. *Advanced Functional Materials*, 20, 28-35.
- Singh, M., H. M. Haverinen, P. Dhagat & G. E. Jabbour (2010) Inkjet printing-process and its applications. *Adv Mater*, 22, 673-85.
- Smolander, M., E. Hurme & R. Ahvenainen (1997) Leak indicators for modified-atmosphere packages. *Trends in Food Science & Technology*, 8, 101-106.
- Sondheimer, E. H. (2001) The mean free path of electrons in metals. *Advances in Physics*, 50, 499-537.
- Starke, E., A. Turke, M. Krause & W.-J. Fischer. 2011. Flexible polymer humidity sensor fabricated by inkjet printing. In *Solid-State Sensors, Actuators and Microsystems Conference (TRANSDUCERS), 2011 16th International*, 1152-1155. IEEE.
- Steinberg, M. D., P. Kassal, B. Tkalčec & I. Murković Steinberg (2014) Miniaturised wireless smart tag for optical chemical analysis applications. *Talanta*, 118, 375-381.
- Suganuma, K. (2014) Introduction to printed electronics.
- Svensson, C. & G. Dermer (2001) Time domain modeling of lossy interconnects. *IEEE Transactions on Advanced Packaging*, 24, 191-196.
- Tanabe, M., M. Nishitsuji, Y. Anda & Y. Ota (2000) A low-impedance coplanar waveguide using an SrTiO₃ thin film for GaAs power MMIC's. *Ieee Transactions on Microwave Theory and Techniques*, 48, 872-874.
- Tao, F., M. E. Grass, Y. Zhang, D. R. Butcher, J. R. Renzas, Z. Liu, J. Y. Chung, B. S. Mun, M. Salmeron & G. A. Somorjai (2008) Reaction-driven restructuring of Rh-Pd and Pt-Pd core-shell nanoparticles. *Science*, 322, 932-4.
- Technologies, A. 2002. Applying Error Correction to Network Analyzer Measurements. AN 1287-3. Agilent Technologies
- Unander, T. & H.-E. Nilsson (2009) Characterization of Printed Moisture Sensors in Packaging Surveillance Applications. *IEEE Sensors Journal*, 9, 922-928.
- Unander, T., J. Siden & H.-E. Nilsson (2011) Designing of RFID-Based Sensor Solution for Packaging Surveillance Applications. *IEEE Sensors Journal*, 11, 3009-3018.
- Virtanen, J., T. Björninen, L. Ukkonen & L. Sydänheimo (2010a) Passive UHF Inkjet-Printed Narrow-Line RFID Tags. *IEEE Antennas and Wireless Propagation Letters*, 9, 440-443.
- Virtanen, J., L. Ukkonen, T. Björninen, A. Z. Elsherbeni & L. Sydänheimo (2011) Inkjet-Printed Humidity Sensor for Passive UHF RFID

- Systems. *IEEE Transactions on Instrumentation and Measurement*, 60, 2768-2777.
- Virtanen, J., L. Ukkonen, T. Bjorninen & L. Sydanheimo. 2010b. Printed humidity sensor for UHF RFID systems. In *Sensors Applications Symposium (SAS), 2010 IEEE*, 269-272. IEEE.
- Virtanen, J., L. Ukkonen, A. Z. Elsherbeni, V. Demir & L. Sydänheimo. 2010c. Comparison of different electromagnetic solvers for modeling of inkjet printed RFID humidity sensor. In *2010 ACES Conference The 26th Annual Review of Progress in Applied Computational Electromagnetics, Tampere, Finland, April 25th-29th, 2010*.
- Virtanen, J., J. Virkki, A. Z. Elsherbeni, L. Sydänheimo & L. Ukkonen (2012) A Selective Ink Deposition Method for the Cost-Performance Optimization of Inkjet-Printed UHF RFID Tag Antennas. *International Journal of Antennas and Propagation*, 2012, 1-9.
- Vyas, R., V. Lakafosis, A. Rida, N. Chaisilwattana, S. Travis, J. Pan & M. M. Tentzeris (2009) Paper-Based RFID-Enabled Wireless Platforms for Sensing Applications. *IEEE Transactions on Microwave Theory and Techniques*, 57, 1370-1382.
- Wang, X. D., R. J. Meier, M. Link & O. S. Wolfbeis (2010) Photographing oxygen distribution. *Angew Chem Int Ed Engl*, 49, 4907-9.
- Weremczuk, J., G. Tarapata & R. S. Jachowicz (2012) The ink-jet printing humidity sorption sensor—modelling, design, technology and characterization. *Measurement Science and Technology*, 23, 014003.
- Wilson, C. L. (2007) Intelligent and active packaging for fruits and vegetables.
- Yang, L., A. Rida & M. M. Tentzeris (2009) Design and Development of Radio Frequency Identification (RFID) and RFID-Enabled Sensors on Flexible Low Cost Substrates. *Synthesis Lectures on RF/Microwaves*, 1, 1-89.
- Yang, L., A. Rida, R. Vyas & M. M. Tentzeris (2007) RFID tag and RF structures on a paper substrate using inkjet-printing technology. *Microwave Theory and Techniques, IEEE Transactions on*, 55, 2894-2901.
- Yi, X., C. Cho, J. Cooper, Y. Wang, M. M. Tentzeris & R. T. Leon (2013) Passive wireless antenna sensor for strain and crack sensing—electromagnetic modeling, simulation, and testing. *Smart Materials and Structures*, 22, 085009.
- Yin, J., J. Yi, M. K. Law, Y. X. Ling, M. C. Lee, K. P. Ng, B. Gao, H. C. Luong, A. Bermak, M. Chan, W. H. Ki, C. Y. Tsui & M. Yuen (2010) A System-on-Chip EPC Gen-2 Passive UHF RFID Tag With Embedded Temperature Sensor. *IEEE Journal of Solid-State Circuits*, 45, 2404-2420.
- Zampolli, S., I. Elmi, E. Cozzani, G. C. Cardinali, A. Scorzoni, M. Cicioni, S. Marco, F. Palacio, J. M. Gómez-Cama, I. Sayhan & T. Becker

- (2007) Ultra-low-power components for an RFID Tag with physical and chemical sensors. *Microsystem Technologies*, 14, 581-588.
- Zhang, W., S. H. Brongersma, O. Richard, B. Brijs, R. Palmans, L. Froyen & K. Maex (2004) Influence of the electron mean free path on the resistivity of thin metal films. *Microelectronic Engineering*, 76, 146-152.
- Zhu, X., S. K. Mukhopadhyay & H. Kurata (2012) A review of RFID technology and its managerial applications in different industries. *Journal of Engineering and Technology Management*, 29, 152-167.